

ISSN 2187-2260

**Proceedings of the 14th Meeting of
Japan CF Research Society,
JCF14**

**December 7 - 8, 2013
Tokyo Institute of Technology, Japan**

Japan CF-Research Society

Edited by Akira Kitamura

Copyright © 2014 by Japan CF-Research Society

All rights reserved. No part of this publication may be reproduced, stored in a retrieval system, or transmitted, in any form or by any means, electronic, mechanical, photocopying, recording or otherwise, without the prior permission of the copyright owner.

PREFACE

This is the Proceedings of the 14th Meeting of Japan CF-Research Society (JCF14) held at Tokyo Institute of Technology on December 7 - 8, 2013. In this meeting were given 16 oral presentations, out of which 14 papers were submitted for this Proceedings to the editorial board. The submitted papers have been peer-reviewed by referees, and accepted for publication either as-is or after some revision.

For all meetings, JCF1 through JCF13, we published the Proceedings. For the meetings after JCF4, we published electronic versions of the Proceedings on our web-site http://jcfrs.org/proc_jcf.html in addition to their printed versions. In view of low efficiency and low effectiveness in distributing information, we decided to discontinue the printed version for the meetings, JCF12. Only the electronic versions have been, and are to be published thereafter. Needless to say, any responses from the world scientists will be welcomed.

We, Japan CF-Research Society members, started the research of the cold fusion more than two dozens of years ago. The cold fusion has a potential ability to establish a small-scale, radiationless nuclear reactor, and hopefully to shorten half-lives of radioactive wastes by nuclear transmutation. We believe that our approach is one of the most challenging ways not only to realize an environmentally-sound nuclear power system with zero emission of the greenhouse gases and other harmful oxides, but also to develop a novel technique for disposal of the nuclear wastes produced by fission reactors.

Recently, not a few entrepreneurs have entered into this field, condensed matter nuclear physics (CMNS), and have attended various meetings including international conferences, especially ICCF18 held at University of Missouri, 2013, where several presentations were made on their own articles or commercial products. These activities would certainly promote progress in the science and technology of CMNS, provided that they are based on scientifically reliable experimental results. We believe that priority has to be given to clarification of the underlying physics.

Finally, we would like to thank all the participants and the people who have collaborated in organizing this meeting. We also would appreciate support by The Thermal & Electric Energy Technology Inc. Foundation.

Editor-in-Chief

Akira Kitamura, Technova Inc.

June 2014

CONTENTS

Preface: A. Kitamura	i
JCF14-1. Study on Anomalous Heat Evolution from H-Ni Nanoparticle System at Elevated Temperature with Mass-Flow Calorimetry <i>A. Kitamura, A. Takahashi, R. Seto, Y. Fujita, A. Taniike and Y. Furuyama</i>	1
JCF14-2. Recent Advances in Transmutation Experiments Induced by Deuterium Permeation Using Nano-Structured Pd/CaO/Pd Multilayer Thin Film <i>S. Tsuruga, T. Itoh and Y. Iwamura</i>	14
JCF14-3. Deuterium permeation experiment using Pd/Ni multi-layered sample <i>T. Takahashi, R. Omi and S. Narita</i>	26
JCF14-4. Bound states of the nucleus-monopole system <i>T. Sawada</i>	34
JCF14-5. Atomic Nucleus and Neutron — Nuclear Physics Revisited with the Viewpoint of the Cold Fusion Phenomenon <i>H. Kozima and K. Kaki</i>	47
JCF14-6. Nuclear Transmutation in Actinoid Hydrides and Deuterides <i>H. Kozima</i>	77
JCF14-7. Synthesis of nano-Pd particles in Y-zeolite pores by ultrasonic irradiation <i>X. F. Wang, T. Mizuno and Y. Arata</i>	95
JCF14-8. Impressive Increase in Number of Etch Pit Occasionally Produced on CR-39 in Light and Heavy Water Electrolysis Using Ni Film Cathode <i>H. Yamada, K. Mita, H. Aizawa and Y. Shida</i>	101
JCF14-9. D(H)-Cluster Langevin Code and Some Calculated Results <i>A. Takahashi and D. Rocha</i>	113
JCF14-10. Computer Simulation of Hydrogen States around T-site in Ni, Pd and Cu Metals <i>H. Miura</i>	141
JCF14-11. Numerical simulation of vortex appeared on electrode surface under long-term evolution of deuterium in 0.1 M LiOD – Vortex formation triggered by pillar current initiation <i>H. Numata</i>	151
JCF14-12. The Quantum States of the System Including Two Species of Charged Bosons in Ion Traps - III	

<i>K. Tsuchiya, A. Okuzumi and A. Watanabe</i> -----	161
JCF14-15. Nuclear Transmutations (NTs) in Cold Fusion Phenomenon (CFP) and Nuclear Physics	
<i>H. Kozima</i> -----	168
JCF14-16. The Cold Fusion Phenomenon – What is It?	
<i>H. Kozima</i> -----	203

Study on Anomalous Heat Evolution from H-Ni Nanoparticle System at Elevated Temperature with Mass-Flow Calorimetry

A. Kitamura^{#1,2}, A. Takahashi^{1,3}, R. Seto¹, Y. Fujita¹,
A. Taniike², Y. Furuyama²

¹ Technova Inc., Tokyo 1000011, Japan

² Graduate School of Maritime Sciences, Kobe University, Kobe 6580022, Japan,

³ Osaka University, Suita 5650871, Japan

[#] kitamuraakira3@gmail.com

Abstract – A new mass-flow calorimetry system has been installed to investigate the excess-power phenomena at elevated temperatures up to several hundred degrees C with an increased amount of the Ni-based nano-composite sample. The first trial runs with a silica-included Cu-Ni nano-composite sample (CNS) containing 4.1 gram of Ni showed an implication of a few-days-lasting excess power of 5 W/g-Ni. Next, a Cu-Ni-Zr oxide nano-composite sample (CNZ4) containing 61 gram of Ni has been examined to show excess power of 15 W lasting for 3 days and that gradually increasing at a rate of 10 W per 3 weeks. Each corresponds to 30 eV/atom-Ni and 100 eV/atom-Ni, which implies a nuclear origin of the excess energy.

Index Terms – oil-cooling mass-flow calorimetry, hydrogen gas absorption, Cu-Ni-Zr oxide nano-composite, excess energy, 100 eV/atom-Ni.

I. INTRODUCTION

There have been increasing interests in hydrogen-gas charged Ni-based samples for excess energy generation owing to broader accessibility of nickel than palladium. A successful work using a Ni-Cu-Mn alloy thin wire has been published in a scientific publication [1]. In addition, a number of entrepreneurs are publicizing their own “products” on web sites with undisclosed details [2 – 4].

We have been studying phenomena of anomalous heat evolution from hydrogen-isotope-loaded nano-composite samples at elevated temperatures as well as at room temperature using an A₁-A₂ twin H(D)-absorption and calorimetry system [5,6]. Recent experiments have utilized Ni-based nano-composite samples supported by zirconia, Pd₁Ni₇/ZrO₂ (“PNZ”), Ni/ZrO₂ (“NZ”), Cu_{0.081}Ni_{0.36}/ZrO₂ (“CNZ”), Cu_{0.21}Ni_{0.21}/ZrO₂ (“CNZ2”) and a Ni-based nano-composite sample supported by silica, Cu_{0.007}Ni_{0.03}/SiO₂ (“CNS”). The results have been described in the 12th Annual Meeting of the Japan CF-Research Society (JCF12), the 17th International Conference on Condensed Matter Nuclear Science (ICCF17), the 13th Annual Meeting of the Japan CF-Research Society (JCF13) and the 18th International Conference on Condensed Matter Nuclear Science (ICCF18), and have been / will be published in [7], [8], [9] and [10], respectively.

The results from the ZrO₂-supported materials, PNZ, NZ, CNZ and CNZ2, are summarized, and the time-dependent data are re-analysed in a paper by A. Takahashi in ICCF18 [11] for speculating a mechanism for heat release during the several-weeks-lasting phase of D(H)-loading into the nano-composite samples. As are shown there, a lot of interesting, even astonishing, features are involved; namely, burst-like heat release with anomalously high values of differential heat of sorption (η) reaching about 600

eV/atom-H, large values of integrated heat reaching about 800 eV/atom-Ni from the CNZ sample absorbing (and weakly releasing) H, and abrupt large desorption with absorbed energy of 50 - 80 eV/atom-Ni observed almost exclusively in the first 573-K run for each sample.

To confirm the interesting phenomena, repeated measurements with improved signal-to-noise ratio, especially in calorimetry, are required. The improved H-absorption/calorimetry experimental system, C₁, having a reaction chamber (RC) with a ten-times-larger volume and capable of a mass-flow calorimetry using an oil coolant with a boiling point of 390 °C, was fabricated for this purpose, and applied first to the CNS sample to show repeated excess heat evolution [10].

In the present paper, we show the H-absorption and heat-power producing characteristics of the CNZ4 sample having a similar composition to the CNZ, after describing calibration runs for calorimetry using a blank alumina sample.

II. DESCRIPTION OF THE SYSTEM

The improvement has been done by reforming the A₂ part of the A₁·A₂ twin system. The reaction chamber (RC) with a capacity of 50 cc of A₂ has been replaced with one with a capacity of 500 cc, and a flow-calorimetry system has been modified to work at elevated temperatures up to 300°C. A schematic of the C₁ system named after the modification is shown in Fig. 1.

On the outer surface of the RC, a coolant pipe and a 1-kW sheath heater are spirally wound alternately for heat removal and sample heating, respectively. These are enclosed by a thin sheet of stainless steel for the purpose of thermal shield and close contact of the sheath heater to the side surface of the RC. All of these are supported by a stainless-steel pipe feeding H₂ gas to the sample in the RC, and surrounded again by a thermal shield made of ceramic fiber (Isowool 14C; Isolite Insulating Products, Co., Ltd.) not only on the side but also on the top and the bottom. The power to the heater is fed from a finely regulated DC power supply in a constant-current mode.

The coolant oil is an aromatic hydrocarbon (Barreltherm-400 (BT400); Matsumura oil Co., Ltd.), which has a boiling point of 390 °C and practically-usable maximum temperature of 330 °C. The coolant is driven by a digital liquid tubing pump (Masterflex peristaltic pump) with a constant flow rate of 20 cc/min in the present work. Material of the plastic tube in the squeezing section is either Tygon or Viton. The coolant is fed to the RC from the bottom, and heated by the heater and the H-absorbing sample. After emerging from the top flange, the oil is flowing to an external heat exchanger of water chiller, set up outside the air-temperature-regulated cabin, and cooled down to the ambient temperature, and fed back to the tubing pump through a water bath kept at a temperature of 24.0 ±0.1 °C (summertime) or 20.0 ±0.1 °C (wintertime).

Seven thermocouples (TC) are deployed; 5 points on the surface of the coolant pipe; TC1, TC2, TC3, TC5 and TC6, 1 point on the gas feed pipe TC4, and TC0 for monitoring the ambient temperature. For flow calorimetry measure, the difference of temperatures between TC2 just at the outlet from the RC for the outlet oil temperature and TC6 for the inlet oil temperature is used. In addition to the TC's, four resistance temperature detectors (RTD) are deployed inside the RC to directly measure the sample temperature. The positions in the RC expressed as [radial position (mm), height (mm)]

from the bottom flange] are [10, 30], [0, 60], [10, 60] and [10, 90], respectively for RTD1, RTD2, RTD3 and RTD4.

The amount of H atom absorbed in the sample is deduced from decrease in the number of H₂ molecules calculated from pressure values at the storage tank (ST), P_s , and that at the RC, P_r , both measured with piezoelectric elements. Since it is one of the most important matters of concern whether excess heat, if any, originates in nuclear effects or not, neutron and γ -ray counting rates are monitored steadily with a ³He-dosimetry-counter and an NaI scintillation detector, respectively. Energy spectra of γ -rays including natural events are also recorded.

The measurements with the CNS sample [10] were done using this system C₁. In the course of the runs, necessity of an additional heater on the axis of the RC and monitoring the flow rate of the coolant BT400 was noticed. The C₁ system has been modified further to meet these requirements. For the former, a 200-W cartridge heater (#2 heater) was installed at the centre of the bottom flange of the RC, and the RTD's were moved to the positions [10, 30], [10, 60], [10, 90] and [10, 120], respectively for RTD1, RTD2, RTD3 and RTD4. For the latter, the pipe arrangement around the level monitor was changed to make a section where the BT400 free-falls and makes droplets, which enables counting of the dropping rate of the BT400. Figure 1 shows the system after these improvements.

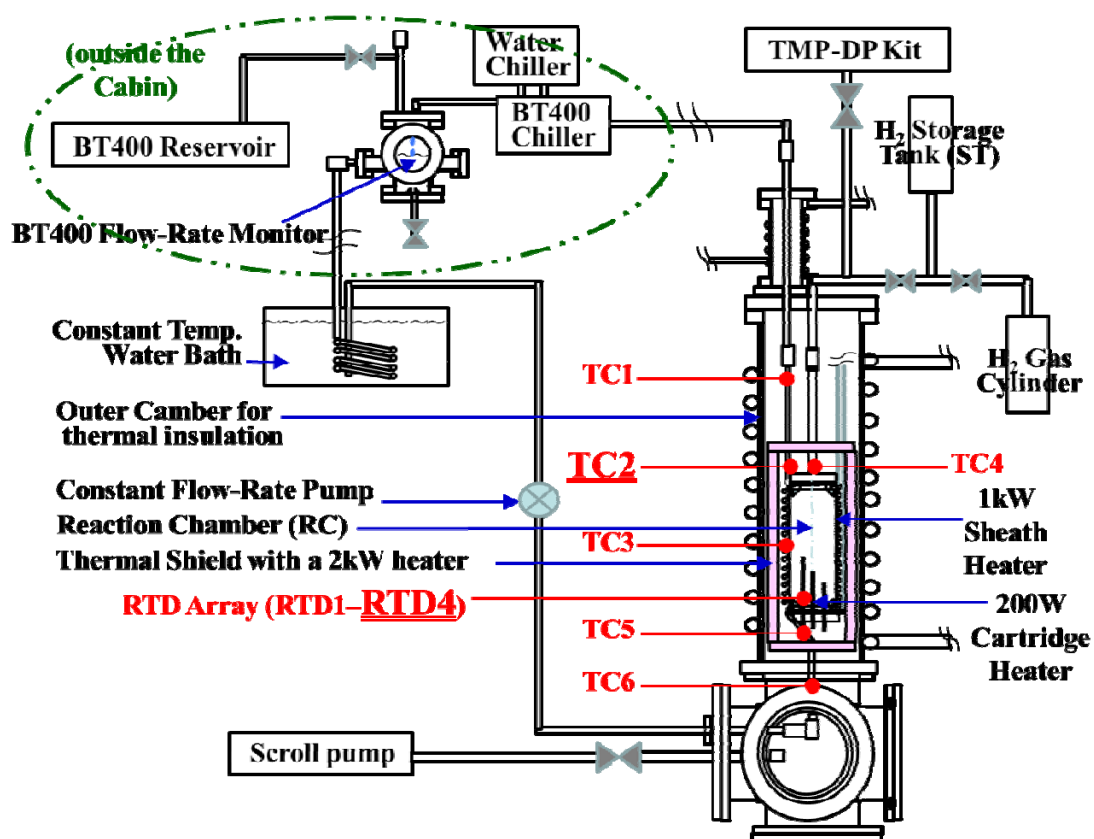


Fig. 1. Schematic of the C₁ absorption system after modification of the flow-rate-monitor and addition of the 200-W cartridge heater.

The BT400 has rather strong temperature dependence of the viscosity. Although this might affect the flow rate of the coolant, the tubing pump is tough enough to send out the oil forcibly by squeezing rotors. The temperature dependence of the density and the specific heat are approximated by linear functions of temperature for the purpose of calculation of heat balance, *etc.*

All of the measured values mentioned above are processed with a “Measurement and Automation Explorer (MAX)” system, National Instruments. We are planning to make feedback control of the heater input power and the flow rate of the coolant to enable constant temperature operation that will be needed in future.

III. CALIBRATION

We have to know the heat conversion coefficient (dW/dT) and the heat recovery rate (R_h) beforehand using a dummy powder. We used the same kind of powder of alumina Al_2O_3 (“ Al_2O_3 2”) with an average size of $60 \mu m$ as that used in the calibration runs for the system before adding the #2 heater [10]. Figure 2 shows temperature history during the calibration runs operated at a variety of combination of heater input powers of $(W_1+W_2) = (0+26) W$ to $(69+78) W$ with a coolant flow rate of 20 cc/min. Here, W_1 denotes the outer (#2) heater power and W_2 does the inner (#1) heater power.

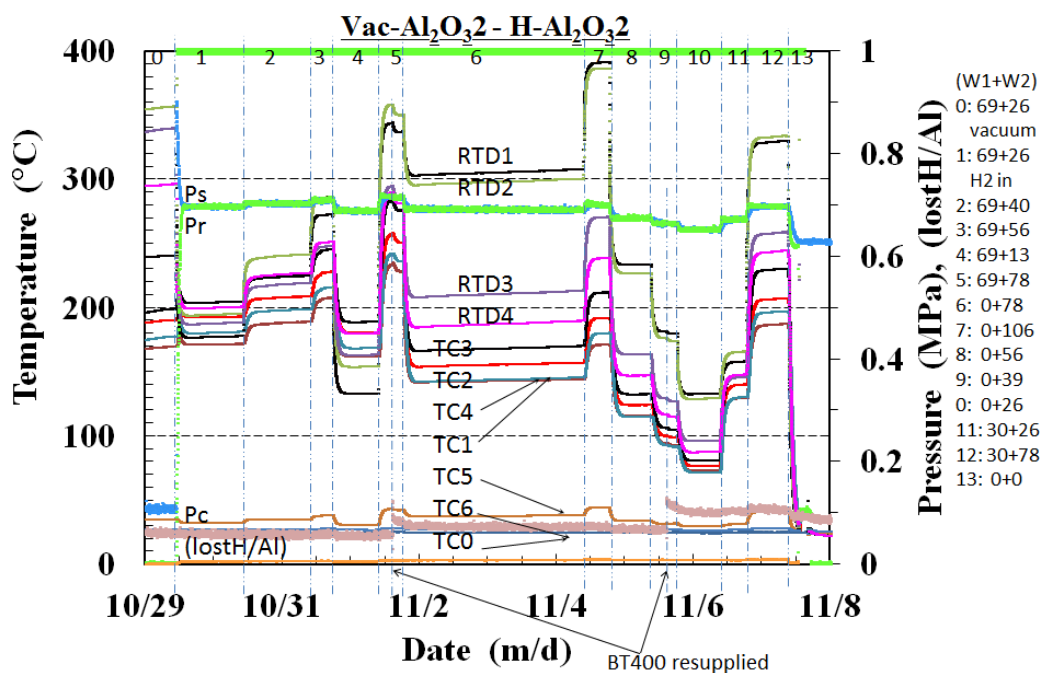


Fig. 2. Calibration run using H-filled Al_2O_3 powder, Al_2O_3 2, which serves also as a control run; H- Al_2O_3 2.

In the figure, “lost H/Al” denotes the decrease in the number of H atoms in the gas phase both in the ST and the RC normalized to the number of Al atoms in the sample. The decrease, if any, might be absorption/adsorption by the sample and/or accidentally happening leak out of the system. Figure 2 shows a constant and very small “lost H/Al”, which means that the sample Al_2O_3 absorbs/adsorbs very few hydrogen atoms, and also that there is no leak in the system.

With the heater power set at (69+26) W, H₂ gas was introduced into the evacuated RC from the storage tank (ST) on Oct. 29. The pressures P_r and P_s began to increase and decrease, respectively, and then the temperatures began to converge to approach the uniform distribution; temperatures at RTD's located near the #2 heater decreased and those at TC's increased by a few degrees C. This is because the heat transfer coefficient was substantially increased by the introduction of the H₂ gas through enhanced conduction and convection. Looking at the TC temperatures just after the gas introduction, we notice small humps of about 10 °C. This is explained as follows. Compared to the sample in the steady state well after the gas introduction, the sample before introducing the gas has more energy stored near the #2 heater and the RTD's. After introducing the gas, the stored energy is released quickly to the coolant as a result of the increased heat transfer coefficient, which forms the humps in the TC temperatures. We call this effect the “enhanced-heat-transfer effect”. Magnitude of the effect depends on the difference in the RTD temperatures before and after the introduction of the gas, on the gas pressure and on the powder material.

The steady-state temperatures at TC2 in each power phase are plotted in Fig. 3 as a function of the total input power, $W_1 + W_2$, making three groups having the same value of W_1 . The temperatures in each group can be fitted by a linear function. However, the three lines do not coincide; the slopes and the intercept values for the three groups are different from each other. For a given total power, the temperature at TC2 could differ by up to 20 °C depending on the value of W_1 . This is a result of the fact that a heat loss through the bottom flange with the heater #2 and RTD's is not negligible compared with the loss to the coolant whose pipe the TC's are attached on.

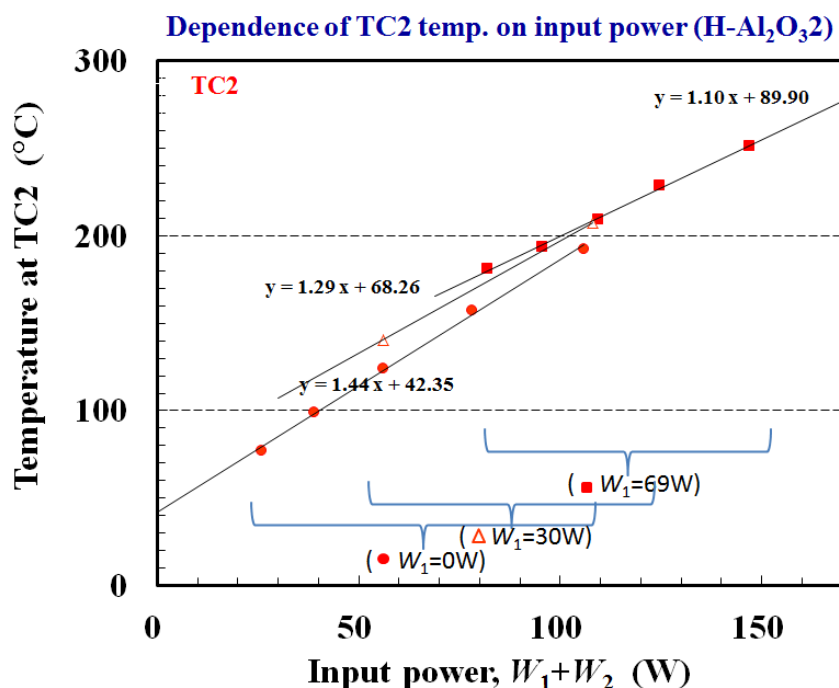


Fig. 3. TC2 temperatures plotted vs. input power in the calibration run, H-Al₂O₃2.

The coefficient of temperature-to-power conversion, dW/dT , is approximated by $\Delta W/\Delta T$ calculated from the change in the input power, ΔW , divided by the change in the

steady-state temperature, ΔT , in each phase of power change. The heat recovery rate, $R_h = F \cdot \rho \cdot C \cdot \Delta T / \Delta W$ is calculated also by using ΔW and ΔT , where F , ρ and C are the flow rate, the mass density and the specific heat capacity, respectively, of the coolant BT400. The conversion coefficient and the recovery rate are plotted in Fig. 4 with no distinction of the ratio of W_1 and W_2 . They can be approximated by $dW/dT = 1.05 \pm 0.05$ W/°C and $R_h = 0.85 \pm 0.06$. The errors or the scattering around the mean values correspond to the difference in the slopes of the fitting functions in Fig. 3. The parameters thus deduced are very similar to and consistent with those for the C_1 system before the addition of the cartridge heater #2; $dW/dT = (9.74 \pm 0.76) \times 10^{-1}$ W/°C and $R_h = (8.82 \pm 0.26) \times 10^{-1}$ [10]. Rather high value of the heat recovery rate is owing to high degree of thermal insulation for the RC even with the heater #2 added on the bottom flange.

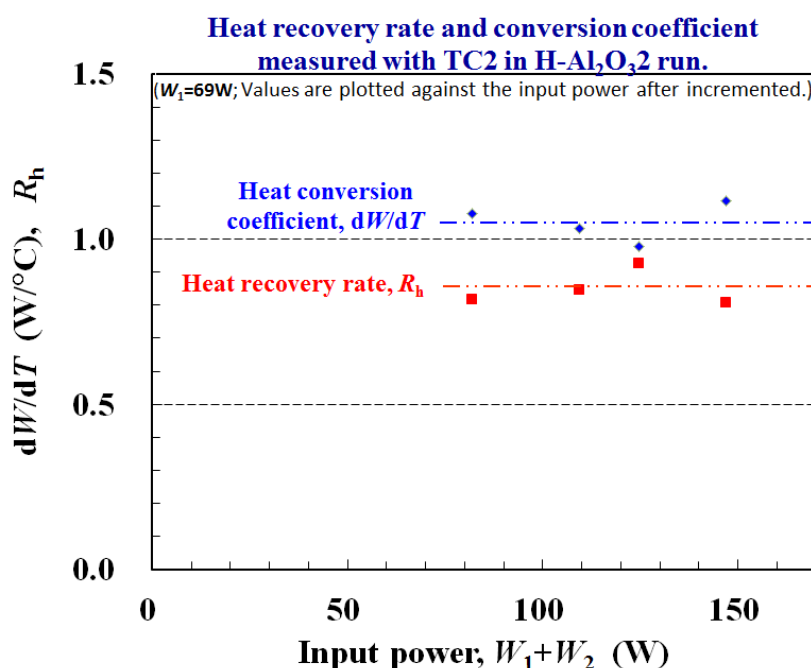


Fig. 4. Temperature-to-power conversion coefficient and heat recovery rate measured in the calibration run H- Al_2O_3 .

IV. H-ABSORPTION RUN OF THE CNZ4 SAMPLE

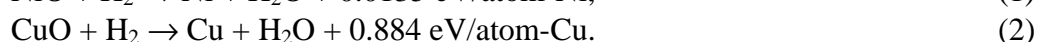
Absorption runs were performed on a 293.6-g powder of $Cu_{0.076}Ni_{0.364}/ZrO_2$ nanocomposite (“CNZ4”, Santoku Corp.), which contains 61.4 g (1.05 mol) of Ni and 13.8 g (0.217 mol) of Cu with crystalline diameter of 25.5 nm and 6.5 nm, respectively. XRD measurements done in Santoku Corp. showed that almost all Cu and Ni atoms are oxidized, and that the specific surface area is 42.1 m^2/g . Since the CNZ4 sample occupied a volume of only about 300 cc in the RC, the RC was filled up by adding a 120-g powder of Al_2O_3 which is the same material as that used for the calibration/control run.

The CNZ4/ Al_2O_3 powder was subjected first to vacuum baking at a heater input power of up to (69+27) W with the ratio of W_1 to W_2 giving optimum one for the temperature distribution to be uniform. This sample seems to contain very much water

or adsorbed molecules on the surface, and the baking for about one week was necessary to purge the adsorbed molecules. Two hours before introducing the H₂ gas to start the H-CNZA/Al₂O₃#1 run, the heater power was adjusted to (0+39) W. The histories of the temperature and the pressure before and after the gas introduction are shown in Fig. 5 and Fig. 6. Similarly to the case of H-Al₂O₃2 run, the number of H atoms lost from the gas phase is normalized to the number of Ni atoms in the sample, and designated as (H/Ni).

Just after introducing the H₂ gas, humps are recorded in the temperatures at RTD2, RTD1 and TC's. The hump of about 10 W × 4 hr at TC2 is time-integrated to give an emerging energy of 35 kJ (0.35 eV/atom-Ni). One of the possible mechanisms for this heat evolution is the enhanced-heat-transfer effect, or transient release of the energy stored in the preceding phase in the thermally-insulated sample, that was discussed in the preceding section for the Al₂O₃ sample.

Other mechanisms responsible for the hump formation could be reduction of the oxides, NiO and CuO, and hydride formation or absorption/adsorption. Since the formation enthalpy of the oxides, NiO (2.49 eV) and CuO (1.62 eV) are rather high, it is difficult to remove oxygen from NiO and CuO by simple vacuum baking. It is known that the easiest way to reduce these oxides is to expose the sample to H₂ gas, anticipating the exothermic reactions;



If we assume the number of H atoms used for these reactions is equal to the “loading ratio” at the end of the hump, (H/Ni) ~ 0.4, then the emerging energy from the reduction reactions is 2.7 - 18 kJ (0.027 - 0.18 eV/atom-Ni) depending on the ratio of the number of NiO atoms to that of CuO to be deoxidized.

Thus, the energies due to the enhanced-heat-transfer effect and the reduction reactions could be rather large and be the major parts of the hump energy. Moreover, it is difficult to factor out the amount of H atoms used for the reduction reaction; it is difficult to know the number of absorbed/adsorbed atoms from the measured value of (H/Ni). It is therefore difficult to experimentally determine the hydride formation energy, or the absorption/adsorption energy, from the present data. In the following, we discuss the excess energy mainly in the steady state, or the “S (saturation) -phase”.

In the S-phase of #1-1, the temperatures at TC2 and TC3 have steady values, while those at RTD's and (H/Ni) are gradually increasing. When the H₂ gas was refilled at #1-2, only a little increase in (H/Ni) was observed, while (H/Ni) increased substantially, when the input power was increased at #1-3. It should be noted that the hydrogen loss did saturate at (H/Ni) ~ 0.95, which remained even when the power was increased further in #1-4 through #1-6. After an evacuation phase #1-7 at some elevated temperature, the #2 run was started with #2-8 phase, where the loss (H/Ni) did not grow more than 0.13. Even in the #3 run after more elaborate baking for two days (see Fig. 6 and Fig. 7 later), the hydrogen loss remained at (H/Ni) ~ 0.1.

These facts imply the following: (a) It is natural to attribute (H/Ni) ~ 0.13 in the #2 run to absorption/adsorption by the sample. (b) The difference of the loss in #1-3 through #1-6 and that in #2-1, Δ(H/Ni) ~ 0.82, should correspond to the number of H atoms necessary for the reduction reaction. (c) Temperature of about 180 °C is necessary for the reduction reaction to proceed, and is sufficient for absorption /

adsorption to proceed. (d) There is no leak of gas out of the system at least at this stage of the runs.

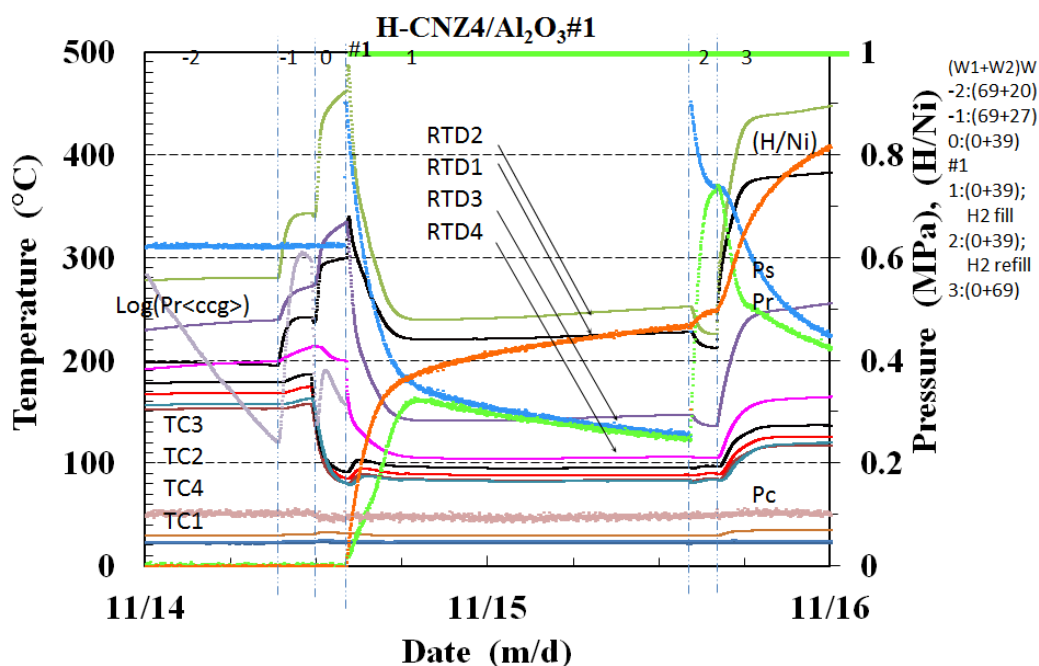


Fig. 5. Transition from baking process to H-absorption run H-CNZ4/Al₂O₃#1.

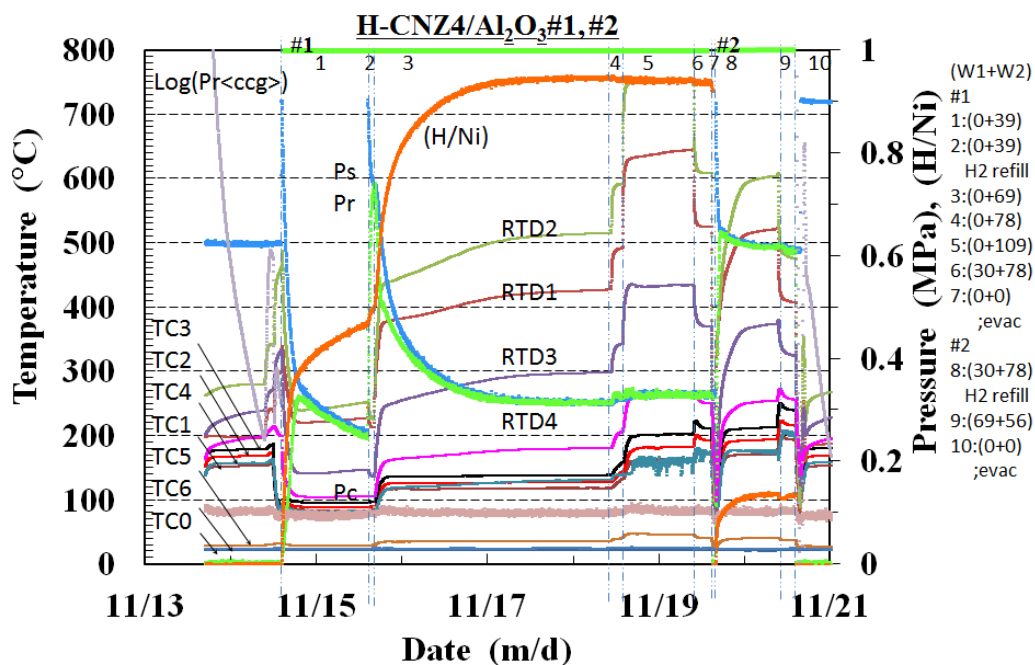


Fig. 6. H-absorption runs H-CNZ4/Al₂O₃#1 followed by evacuation and H-CNZ4/Al₂O₃#2 run.

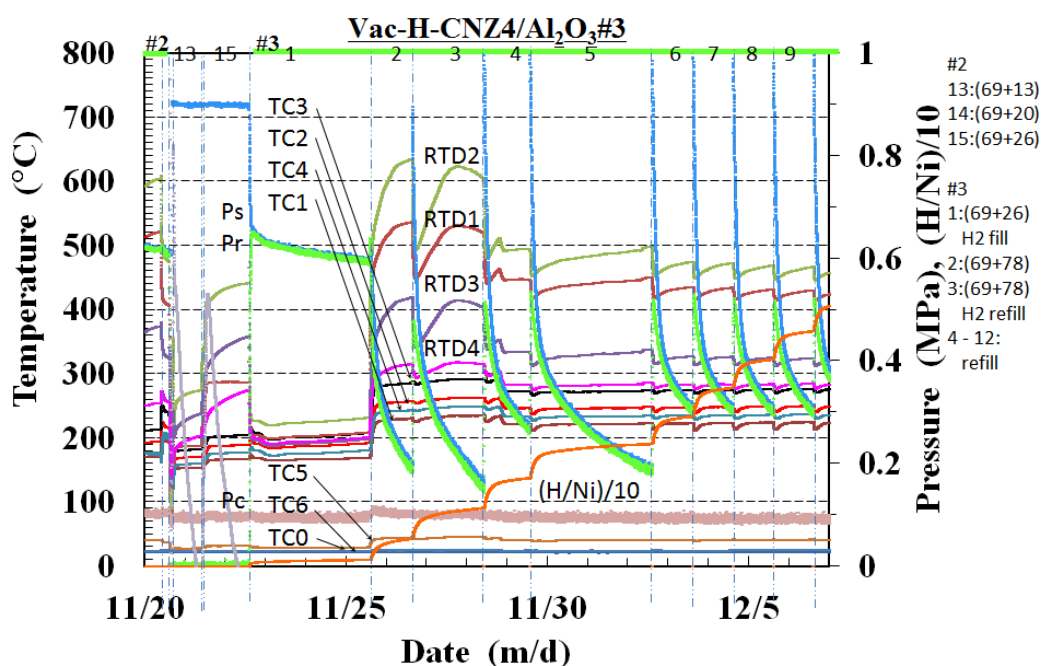


Fig. 7. Temperature, pressure and H-loss (H/Ni) in the run H-CNS/Al₂O₃#3.

To check whether the outgas condition in the #1-7 phase was adequate or not, baking with much harder condition was performed in the #2-10 through #2-15 before the #3 runs are started. The initial several phases of the #3 run are shown in Fig. 7. Just after the transition from the #2-15 (vacuum) phase to the #3-1 (H₂-filled) phase, we see the humps which must be of the same origin with those found at the #1-1 phase. As has been mentioned earlier, the value of (H/Ni) remains modest in the #3-1 phase.

However, (H/Ni) suddenly grows to about 0.5 at the beginning of the #3-2 phase, when the gas is refilled with a pressure of 0.9 MPa. This remains essentially the same thereafter for many weeks, accompanying negative spikes in the temperatures at TC's and RTD's. These are discussed later in the present paper.

Looking at the temperatures in the phases #3-2 through #3-4, we notice long-term humps in the RTD's and TC's. If we take the base (zero-power) line for the TC2 as the temperature at TC2 in the case of the calibration/control run using Al₂O₃2, we can express the excess power as a function of time, which is shown in Fig. 8 as the thick red line. Note that the excess power is multiplied by 10 in the figure for the purpose of easy view.

The excess power grows to the maximum value of 15 W (0.25 W/g-Ni), and is quenched suddenly at midnight of Nov. 28, forming an 80-hours hump. Integrating the power, we obtain an excess energy of 3 MJ/mol-Ni (30 eV/atom-Ni). This is several to ten times larger than the energy generated by any chemical reaction. If we assume that the increase in (H/Ni) (~ 1.5) during this 80-hr period was entirely related to the excess phenomena, the excess energy is expressed as 20 eV/atom-H at least. This is more than one order of magnitude larger than the energy produced in, *e.g.*, the water producing reaction; $\text{H}_2 + (1/2)\text{O}_2 \rightarrow \text{H}_2\text{O} + 2.97 \text{ eV}$. It is inferred that a nuclear process is involved in this excess energy production.

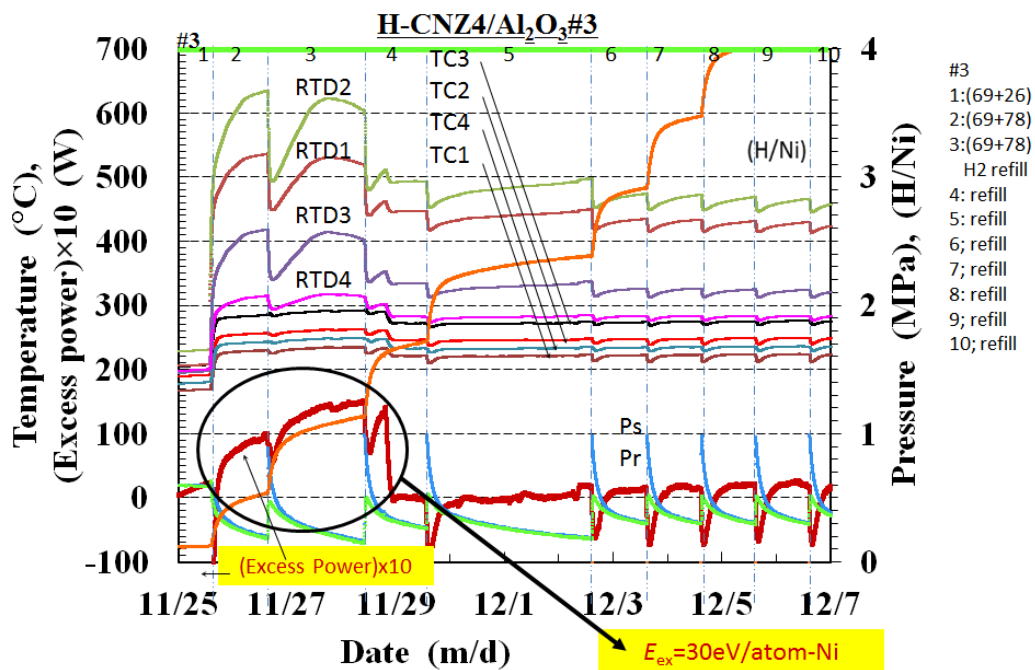


Fig. 8. Excess power in the H-CNS/Al₂O₃#3 run. The excess is calculated as the deviation in TC2 temperature from that in the control run H-Al₂O₃2.

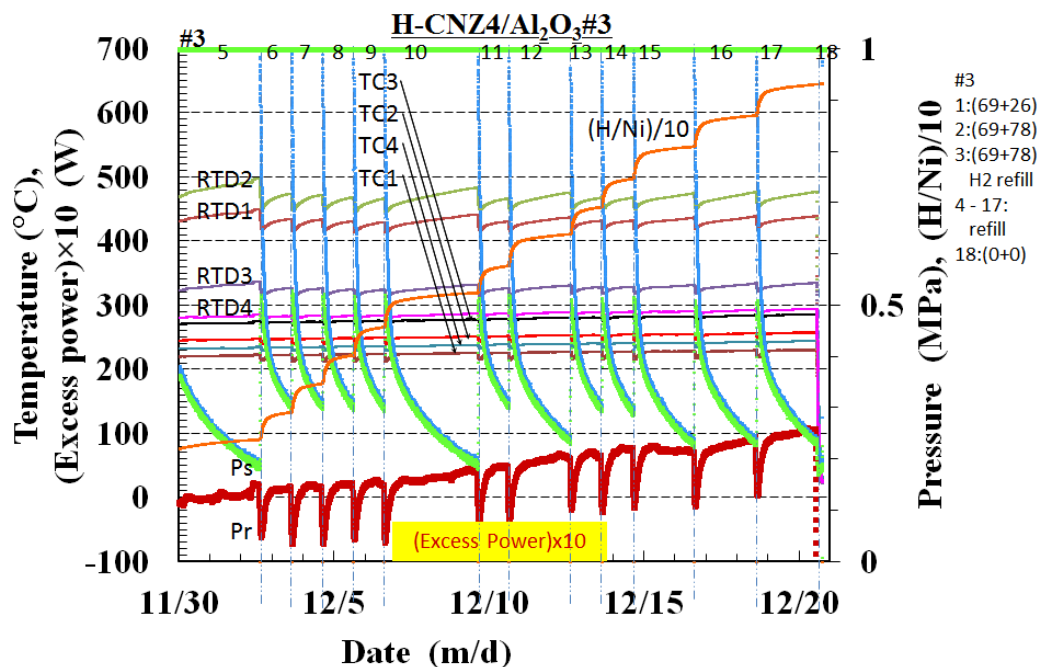


Fig. 9. Gradually increasing excess power reaching 10 W.

The excess power was retrieved. Figure 9 shows a three-week-long excess power approaching 10 W (0.17 W/g-Ni), which gives an integrated energy of 10 MJ/mol-Ni (100 eV/atom-Ni).

The above values of the excess power of the order of 10 W (10^{-1} W/g-Ni) are one order of magnitude smaller than that we expected for the present sample of CNZ4. They are one order of magnitude smaller than that claimed for the CNZ sample yielding an excess power of 2 W/g-Ni using the A₁-A₂ system [6]. We still need one-order-of-magnitude larger temperature change to claim excess heat with absolute certainty. Nevertheless, it is also true that it is difficult to find a reasonable cause other than excess heat for the temperature change at the present stage.

Now we discuss the stepwise increase in (H/Ni) accompanied by the negative spikes in the temperature observed in every phase of gas refill. The stepwise increase $\Delta(H/Ni) \sim 0.5$ corresponds to a loss of 0.25-mol H₂, while the negative spike in temperature corresponds to a lost/absorbed energy of the order of 0.01 eV per one atom contained in the system. However, when we look for the source of this energy, we have to evaluate the energy divided by the number of atoms concerned in the source reaction. It is 1.3 eV/atom-Ni or 2.6 eV/atom-H, if only Ni atoms or H atoms are assumed to be concerned in the loss/absorption.

These values are not very large as a chemical reaction energy, while they are too large as a gas-dynamical reaction energy or even as the absorption/adsorption energy. The negative energy introduced to the hot (~ 300 °C) system by supplying the H₂ gas at room temperature, 0.025 eV/H₂, is more than two orders of magnitude smaller than the value 2.6 eV/atom-H.

We now know that there has been some leak of H₂ gas from the system; after the nine-weeks run, we detected H₂ gas by a portable hydrogen leak checker at the outlet of the scroll pump evacuating the outer chamber. However, the leak cannot be the major origin of the endotherm of 2.6 eV/atom-H, since the thermal energy of the H₂ molecule at 300 °C, 0.05 eV/H₂, is again two orders of magnitude smaller. Further investigation is necessary to solve this paradox of absorbed energy.

- a three-week-long excess power approaching 10 W (0.17 W/g-Ni), which gives an integrated energy of 10 MJ/mol-Ni (100 eV/atom-Ni).
- (B4) Stepwise increase of $\Delta(H/Ni) \sim 0.5$ accompanied by the negative spikes in the temperature corresponding to 1.3 eV/atom-Ni was observed in every phase of gas refill. Further investigation is needed to find a possible cause of this phenomenon.

Acknowledgement

The authors thank T. Tahara and T. Murota, Santoku Corp. for providing the CNZ4 sample and its XRD analysis.

References

- [1] Francesco Celani, E. F. Marano, A. Spallone, A. Nuvoli, E. Purchi, M. Nakamura, B. Ortenzi, S. Pella, E. Righi, G. Trenta, S. Bartalucci, A. Ovidi, G. L. Zangari, F. Micciulla, S. Bellucci; Cu-Ni-Mn alloy wires, with improved sub-micrometric surfaces, used as LENR device by new transparent, dissipation-type, calorimeter; to be published in Proc. ICCF17
- [2] F. Piantelli / Nichenergy; <http://e-catsite.com/2012/06/15/piantelli-moves-closer-to-commercialization/>
- [3] A. Rossi / Leonardo Corporation; <http://ecat.com/>
- [4] J. Hadjichristos / Defkalion Green Technologies; <http://www.youtube.com/watch?v=J006idrZEcw>
- [5] Akira Kitamura, Yu Sasaki, Yuki Miyoshi, Akira Taniike, Akito Takahashi, Reiko Seto and Yushi Fujita; Heat Evolution from Pd Nanopowders Exposed to High-Pressure Hydrogen Isotopes and Associated Radiation Measurements; J. Condensed Matter Nucl. Sci. **4** (2011) 56-68.
- [6] Y. Miyoshi, H. Sakoh, A. Taniike, A. Kitamura, A. Takahashi, R. Seto and Y. Fujita; Effect of Forced Oxidation on Hydrogen Isotope Absorption / Adsorption Characteristics of Pd·Ni·Zr Oxide Compounds; J. Condensed Matter Nucl. Sci. **10** (2013) 46-62.
- [7] Y. Miyoshi, H. Sakoh, A. Taniike, A. Kitamura, A. Takahashi, R. Seto and Y. Fujita; Gas-phase hydrogen isotope absorption/adsorption characteristics of a Ni based sample; Proc. JCF12 (2012) 1-9.
- [8] H. Sakoh, Y. Miyoshi, A. Taniike, Y. Furuyama, A. Kitamura, A. Takahashi, R. Seto, Y. Fujita, T. Murota, T. Tahara; Hydrogen isotope absorption and heat release characteristics of a Ni-based sample; to be published in Proc. ICCF17.
- [9] H. Sakoh, Y. Miyoshi, A. Taniike, Y. Furuyama, A. Kitamura, A. Takahashi, R. Seto, Y. Fujita, T. Murota, T. Tahara; Heat release characteristics of Ni-based samples absorbing hydrogen isotopes at high temperature; Proc. JCF13 (2013) 214-229.
- [10] A. Kitamura, A. Takahashi, R. Seto, Y. Fujita, A. Taniike and Y. Furuyama; Mass-Flow-Calorimetry System for Scaled-up Experiments on Anomalous Heat Evolution at Elevated Temperatures; to be published in Proc. ICCF18
- [11] A. Takahashi, A. Kitamura, R. Seto, Y. Fujita, H. Sakoh, Y. Miyoshi, A. Taniike, Y. Furuyama, T. Murota and T. Tahara; Anomalous Exothermic and Endothermic Data Observed by Nano-Ni-Composite Samples; to be published in Proc. ICCF18.

Recent Advances in Transmutation Experiments induced by Deuterium Permeation using Nano-Structured Pd/CaO/Pd Multilayer Thin Film

S. Tsuruga, T. Itoh, Y. Iwamura

Advanced Technology Research Center, Mitsubishi Heavy Industries, Ltd., Japan
E-mail: shigenori_tsuruga@mhi.co.jp

Abstract-- Low energy nuclear transmutations have been observed in the nano-sized Pd complexes, which are composed of Pd and CaO thin film and Pd substrate, induced by D₂ gas permeation. In order to increase the transmutation products, an electrochemical method was applied to increase deuterium density near the surface of the nano-structured Pd multilayer film. Transmutation products were successfully increased by this approach. These recent experimental methods gave us increased transmutation products, gamma-ray emissions, and new implications on Deuterium Permeation Induced Transmutation.

Index Terms—Transmutation, Increase of Reaction Products, Deuterium Permeation Induced Transmutation, nano-structured Pd multilayer thin film.

I. INTRODUCTION

Transmutation reactions in nano-structured material have been observed in nano-structured Pd multilayer thin film which is composed of Pd and CaO thin film and Pd substrate, induced by D₂ gas permeation[1]-[5]. Experimental data that indicates the presence of transmutation have been accumulated and experimental conditions for inducing low energy transmutation reactions are gradually becoming clear, although systematic experimental study is still insufficient. Replication experiments have been performed by some researchers and similar results have been obtained [6]-[8]. Potential applications would be expected as an innovative nuclear transmutation method of radioactive waste and a new energy source.

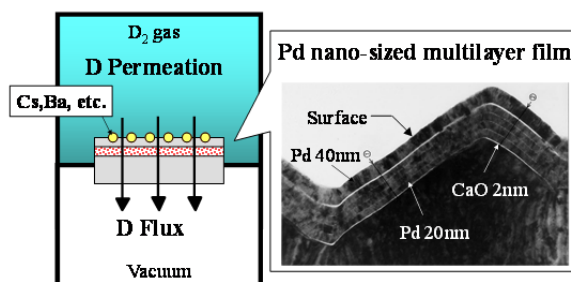


Fig.1. Experimental Method for Permeation Induced Nuclear Transmutation.

Figure 1 shows schematic of our experimental method. Our approach can be characterized by the permeation of D₂ gas through the nano-structured Pd complex and the addition of an element that is specifically targeted to be transmuted. Permeation of deuterium is attained by exposing one side of the Pd multilayer thin film to D₂ gas while

maintaining the other side under vacuum conditions. The surface of the foil was covered by layers of CaO and Pd, which were obtained by five times alternately sputtering 2-nm-thick CaO and 20-nm-thick Pd layers. Then a 40nm-thick Pd layer was sputtered on the surface of the CaO and Pd layers. These processes were performed by the Ar ion beam sputtering method. After fabricating a Pd complex, Cs, Ba, or other element is deposited on the surface of the top thin Pd layer. The added elements are expected to be transmuted.

Reactions observed so far in our group are shown in TABLE I. Based on these experimental results, alkali elements seem to be transmutable by our method. In other words, chemically active elements that can easily emit electrons might be transmutable. And the obtained experimental results so far suggest that a certain rule seems to exist. We can notice that 2d, 4d or 6d look like reacting with deposited elements. Multi-body reactions like 2d, 4d and 6d require sufficient number of d. Reaction probability particularly depend on d density. Therefore we can see that sufficient deuterium density would be important to induce transmutation reactions.

TABLE I [1]-[5]
TYPICAL REACTIONS OBSERVED SO FAR

Elements		Assumed Reactions
Cs	4d	$^{133}_{55}\text{Cs} \xrightarrow{4d(2\alpha)} ^{141}_{59}\text{Pr}$
Ba	6d	$^{138}_{56}\text{Ba} \xrightarrow{6d(3\alpha)} ^{150}_{62}\text{Sm}$, $^{137}_{56}\text{Ba} \xrightarrow{6d(3\alpha)} ^{149}_{62}\text{Sm}$
W	4d or 2d	$^{182}_{74}\text{W} \xrightarrow{4d(2\alpha)} ^{190}_{78}\text{Pt}$, $^{186}_{74}\text{W} \xrightarrow{2d(\alpha)} ^{190}_{76}\text{Os}$

TABLE II shows correlation between intermediate material in Pd multilayer film and transmutation results. If we replaced CaO with MgO, we did not obtain any positive transmutation products; we could not observe any transmutation reactions. It means that MgO cannot work instead of CaO. Three cases out of the three experiments using MgO show no Pr by ICP-MS measurements, although D₂ gas Flow rates in the case of using MgO were the same as the flow rate in the case of using CaO or Y₂O₃ in all cases. However, if we replaced CaO with Y₂O₃, we could observe transmutation reactions from Cs to Pr. Y₂O₃ works like CaO. Work functions for MgO, Y₂O₃ and CaO are shown in the Table II. Although it is difficult to make conclusive results, the existence of low work function of intermediate material might have some effects to induce transmutation.

TABLE II
CORRELATION BETWEEN INTERMEDIATE MATERIAL IN Pd MULTILAYER FILM AND
TRANSMUTATION RESULTS

Intermediate Material	Work Function (eV)	Results for analysis after permeation
CaO	1.2	Pr detected >100cases
Y ₂ O ₃	2.2	Pr detected >10cases
MgO	3.3	No Pr (3cases)

The permeation induced transmutation technology would be expected as an innovative nuclear transmutation method for radioactive waste and a new energy source. However, it is necessary to increase the amount of transmutation products for commercialization.

The author is now assuming that the following two conditions are important to increase up transmutation products based on the experimental results.

- i) Local deuterium density is sufficiently high.
- ii) Electron rich state is important.

We tried to increase the amount of transmutation products by the increase of deuteron density, especially according to i) assumption.

II. INCREASE OF DEUTERON DENSITY USING AN ELECTROCHEMICAL METHOD

Figure 2 shows the transmutation products dependence on D₂ gas pressure in the case of Cs transmutation into Pr. Conversion rate means how much portion of initial Cs was transmuted into Pr. Amount of Pr is expressed as the mass of Pr divided by the permeated surface area. Permeated surface area is about 1.0cm².

It is possible to see that the amount of Pr and conversion rate increase as the D₂ gas pressure increase. It is reasonable that multi-body reactions observed in the permeation induced transmutation require sufficient number of deuterium. Therefore we need high D₂ gas pressure to induce the transmutation effectively since it gives much deuterium near the surface.

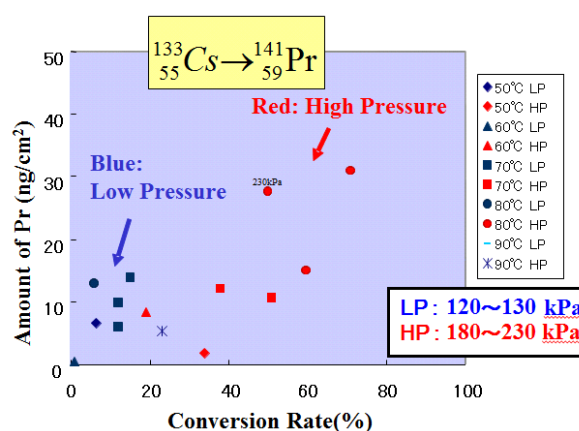


Fig.2. Dependence on D₂ gas pressure in Pr production.

An electrochemical method is applied to increase deuterium surface density as shown in Fig.3. A photo of our apparatus is shown also in the Fig.3. If we apply this method, we can provide very high deuterium density by controlling applied voltage between the Pd/CaO multilayer thin film and the anode made of Platinum. Simple pressurization is, off course, one of the solutions which give high deuterium density, however, it needs relatively large-scale apparatus. Therefore we choose this electrochemical method for giving high deuterium density to the Pd surface, taking into the consideration of future commercialization.

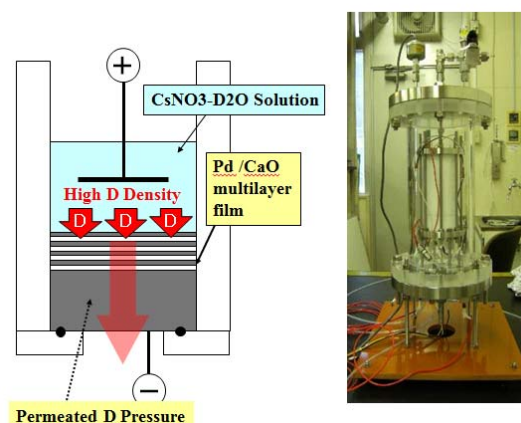


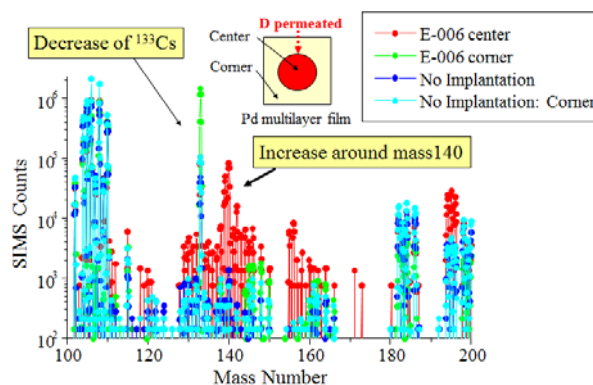
Fig.3. Electrochemical Deuterium Permeation Apparatus aiming the Increase of Deuterium Density.

An example of experimental results is shown in Figure 4 and 5. A 0.1M CsNO₃-D₂O solution was used for this experiment. Purity for both CsNO₃ and D₂O is more than 99.9%. Mass spectra by SIMS (Secondary Ion Mass Spectrometry) are plotted in the Fig.4 and mass distributions by ICP-MS (Inductively Coupled Plasma Mass Spectrometry) for the same sample: E006 are shown in Fig.5.

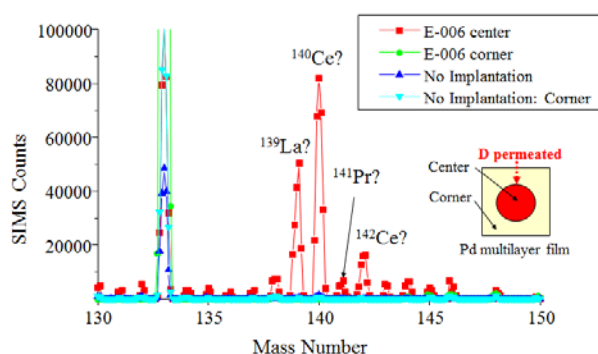
We can postulate that nuclear transmutation reactions occur at the permeated part of the Pd multilayer sample (center), however, no reactions occur at the part where no D permeated (corner). In advance, Cs ion implantation (20kV, 10¹⁶ ions/cm²) were applied to Pd multilayer.

SIMS counts are plotted in a logarithmic scale in Fig. 4(a). SIMS analysis was performed by O²⁺ ions and the analyzed area was circle in 60μm diameter. Mass 133 corresponds to Cs and SIMS counts for mass 133 of E006-corner are larger than those of E006-center as shown in Fig. 4(a). It means that ¹³³Cs decreased at the center of E006. On the contrary, SIMS counts around mass 140 of E006-center are larger than those of E006-corner. It means that elements or molecular compounds that have mass number around 140 increased at the deuterium permeated point where SIMS analysis was performed. As a reference, SIMS mass distributions for no Cs implantation sample are plotted for both center and corner. The increase of SIMS counts around mass 140 cannot be seen as for the no implantation sample.

The magnified mass spectra from mass 130 to mass 150 is shown in Fig 4(b) where SIMS counts are plotted in a linear scale. It can be seen that SIMS counts around mass 140 are greatly increased only for the E006-center.



(a) Wide SIMS Spectra in a logarithmic scale



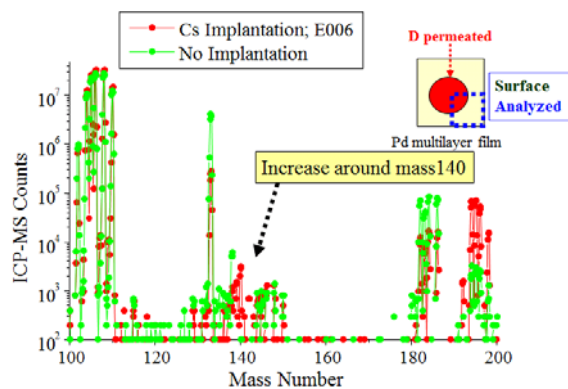
(b) Magnified SIMS Spectra from mass 130 to mass 150 in a linear scale.

Fig.4. Comparison of SIMS Mass Spectra between E006 and No Cs Implantation sample.

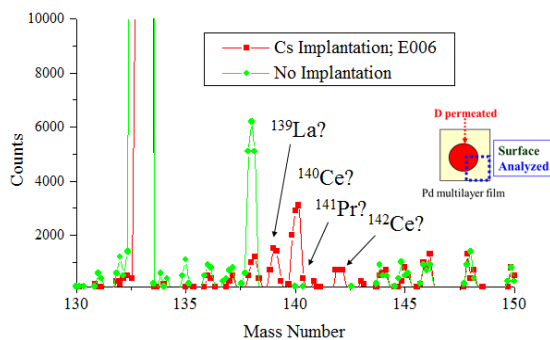
We performed ICP-MS analysis to confirm the obtained results by SIMS analysis. Basically, the mass information obtained by SIMS is at the analyzed small point. In contrast, the information obtained by ICP-MS is from the sample surface because mass distribution was analyzed for the HNO_3 solution that contains the surface of Pd multilayer thin film. In the ICP-MS analysis, we cut a permeated Pd multilayer sample into 1/4 size and put it into 68% high purity HNO_3 solution and analyzed the HNO_3 solution that contained the surface part of it.

Figure 5 (a) shows ICP-MS results for E006 and the no Cs implantation and D permeated sample. ICP-MS counts around mass 140 of E006 are larger than those of no Cs implantation sample. It means that elements or molecular compounds that have mass number around 140 increased on the dissolved surface by HNO_3 . The magnified mass spectra from mass 130 to mass 150 are shown in Fig 5(b) where ICP-MS counts are plotted in a linear scale. It would be possible to say that Fig.4 and Fig.5 are similar around mass 140, although the difference of signals between E006 and no Cs

implantation is smaller for Fig.5. It is reasonable because SIMS data is taken from the **spot** where transmutation reactions were supposed to occur, however, ICP-MS results contained corner part where no D was permeated and therefore no transmutation reactions were supposed to occur.



(a) Wide ICP-MS Spectra in a logarithmic scale



(b) Magnified SIMS Spectra from mass 130 to mass 150 in a linear scale

Fig.5. Comparison of ICP-MS Mass Spectra between E006 and No Cs Implantation sample.

Next we examined the formations of compound species for mass 139 and 140 that large increases were observed. Possible compounds for mass 139 and 140 are shown in TABLE III. If we carefully examine and take natural abundances for each element into consideration, mass 139 and 140 cannot be explained by these compounds. Therefore mass 139 and 140 would be ^{139}La and ^{140}Ce , respectively.

TABLE III
POSSIBLE COMPOUNDS FOR MASS 139 AND 140

Possible compounds for mass 140		
$^{138}\text{Ba}(71.7\%)\text{D}$	$^{133}\text{Cs}(100\%)^7\text{Li}(92.4\%)$	$^{110}\text{Pd}^{30}\text{Si}(3.1\%)$
$^{106}\text{Pd}^{34}\text{Si}(4.3\%)$	$^{109}\text{Ag}(48.1\%)^{31}\text{P}(100\%)$	$^{104}\text{Pd}^{36}\text{Ar}(0.33\%)$
$^{102}\text{Pd}^{38}\text{Ar}(0.06\%)$	$^{110}\text{Pd}^{28}\text{Si}(92.3\%)\text{D}$	$^{108}\text{Pd}^{30}\text{Si}(3.1\%)\text{D}$
$^{105}\text{Pd}^{33}\text{Si}(0.8\%)\text{D}$	$^{102}\text{Pd}^{36}\text{Si}(0.02\%)\text{D}$	$^{102}\text{Pd}^{36}\text{Ar}(0.3\%)\text{D}$
Possible compounds for mass 139		
$^{137}\text{Ba}(11.2\%)\text{D}$	$^{133}\text{Cs}(100\%)^6\text{Li}(7.6\%)$	$^{110}\text{Pd}^{29}\text{Si}(4.7\%)$
$^{106}\text{Pd}^{33}\text{Si}(0.8\%)$	$^{104}\text{Pd}^{35}\text{Cl}(75.8\%)$	$^{102}\text{Pd}^{37}\text{Cl}(24.2\%)$
$^{110}\text{Pd}^{27}\text{Al}(100\%)\text{D}$	$^{106}\text{Pd}^{31}\text{P}(100\%)\text{D}$	$^{105}\text{Pd}^{32}\text{S}(94.9\%)\text{D}$
$^{104}\text{Pd}^{33}\text{Si}(0.8\%)\text{D}$	$^{105}\text{Pd}^{32}\text{Si}(94.9\%)\text{D}$	$^{102}\text{Pd}^{35}\text{Cl}(75.8\%)\text{D}$

We also performed XPS analysis to cross-check the products. Figure 6 shows XPS result for E006. Weak two binding energy peaks of Pr $3d_{5/2}$ and $3d_{3/2}$ were observed, it was thought that Pr would formed on the surface of Pd multilayer film. Other elements should be cross-checked by the other analysis methods, for example, XRF or XPS, too.

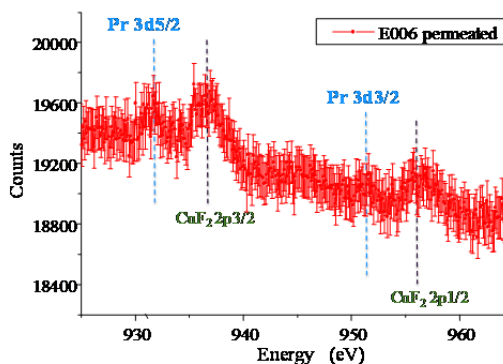


Fig.6. XPS Spectrum of Pr for E006.

According to our experimental results using D_2 gas permeation, we usually observed transmutation of Cs into Pr, in other words, mass 133 decreased and mass 141 increased. In this new apparatus, however, mass 139, 140, 141 and 142 increased while mass 133 decreased. The differences between D_2 gas permeation and electrochemical D permeation can be attributed to the effective deuterium density and/or source of deuterium.

Let us consider about contamination due to the $\text{CsNO}_3\text{-D}_2\text{O}$ solution. If we analyzed the $\text{CsNO}_3\text{-D}_2\text{O}$ solution, we could not see any mass numbers of 139, 140, 141, 142 (La, Ce, Pr). Furthermore, we make comparison between E006 and the D permeated sample.

The D permeated sample was contacted with CsNO₃-D₂O solution and almost the same current was applied. The other experimental conditions except Cs implantation were all the same. However, the only permeated part of E006 has different mass distribution as shown in Fig.4 and 5. So it is very difficult to assume that obtained mass difference between D₂ gas permeation and electrochemical D permeation are derived from the contamination of CsNO₃-D₂O solution. Therefore we might consider the effective deuterium density make effects on the transmutation reaction pass. Anyway, we should make more experiments using the other measurement methods and improve the reliability of our experiments.

III. GAMMA-RAY EMISSION CAUSED BY THE INCREASE OF TRANSMUTATION PRODUCTS

We describe an example of gamma-ray detection during an electrochemical D permeation experiment. In the Fig.7, applied voltage and corresponding current between Pd multilayer thin film and Pt anode, pressure at the evacuated side of Pd multilayer cathode are plotted as a function of time. Deuterium permeation rate is proportional to the pressure described here. At the beginning of the experiment, applied voltage was 3V and the current was low. If we increased the voltage up to 4 V, the current increased and permeated D increased correspondingly, as shown in Fig.7. If we increased the voltage up to 4.5V, current amounted to 70mA and deuterium permeation increased, however, the current and D permeation decreased gradually even though we did not change the applied voltage.

In this experiment, Pd/Y₂O₃/Pd multilayer thin film with Cs implantation and 0.5M CsNO₃-D₂O solution were used.

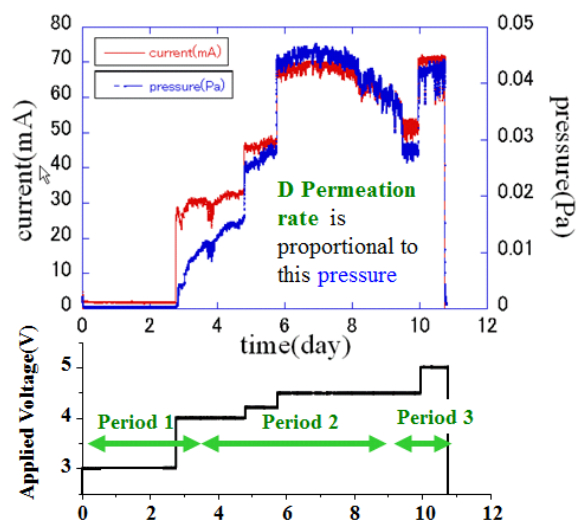


Fig.7. Time variation of Applied Voltage, Current and Pressure during an experiment E16.

Gamma-ray measurements using a Germanium detector were performed during electrochemical D permeation experiments. In this experiment (E16), gamma-ray energy spectra were obtained for 3 periods shown in Fig.7. We deducted background energy spectra from obtained gamma-ray spectra during period 1, 2 and 3.

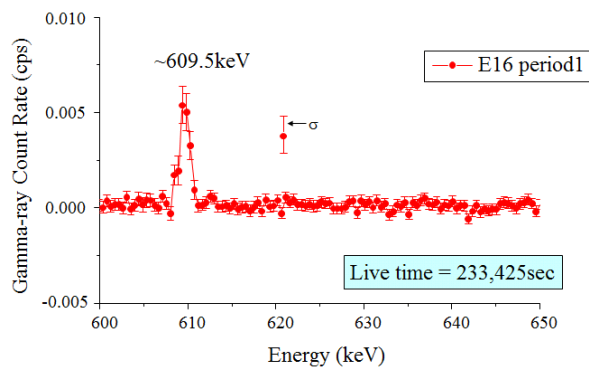
Emitted gamma-ray spectra are plotted in Fig.8 (a), (b) and (c), which correspond to period 1, 2 and 3, respectively. Standard deviations are also plotted for each point in all

spectra. During period 1, very low current and low permeation rate, a clear gamma-ray peak around 609keV exceeding statistic error was detected. During period 2 and 3, relatively high current and large amount of D permeation, the 609keV gamma-ray vanished and a peak around 511keV was detected. There was no 511keV peak during period 1.

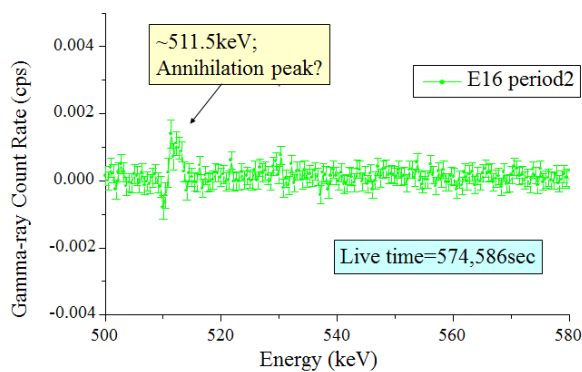
Gamma-rays were not always detected. Energy spectra, in most cases, were exactly the same as background spectra, which were taken several times using the same set-up without D permeation. In the case of experiment E16, as well as a few experiments, gamma-rays exceeding statistical errors were detected. Ge detector and experimental apparatus were fixed during the experiments, of course.

We could not observe clear gamma-ray emissions for D₂ gas permeation experiments for long time. What does it mean that we can observe weak gamma-ray emissions recently from the electrochemical D permeation? The electrochemical D permeation method gives us more transmuted products than D₂ gas permeation method. Detection of gamma-ray might be correlated to the increase of the transmuted products. The 511keV gamma-ray is closed to annihilation energy and we might have some unstable nuclear species that emit positron. Further study is necessary to identify the source of the gamma-ray emitter.

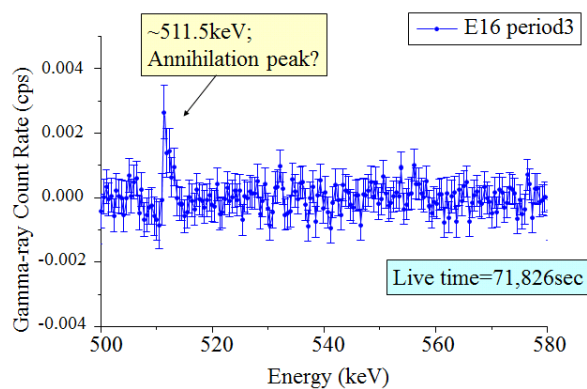
We performed XPS analysis of E16 sample. Figure 9 shows XPS result for E16. Clear two binding energy peaks of Pr 3d_{5/2} and 3d_{3/2} were observed. We also performed ICP-MS analysis to cross-check, but clear peak was not observed at mass 141. We suppose that this discrepancy may be caused by sample preparation process for ICP-MS. By dissolving the film surface too much by HNO₃, Pr concentration would be diluted to lower than detection limit of ICP-MS. It is a future work to improve the pretreatment process of ICP-MS analysis for high sensitive detection.



(a) Gamma-ray Energy Spectrum emitted during Period 1



(b) Gamma-ray Energy Spectrum emitted during Period 2



(c) Gamma-ray Energy Spectrum emitted during Period 3

Fig.8. Gamma-ray Emissions during an electrochemically D permeation experiment E16.

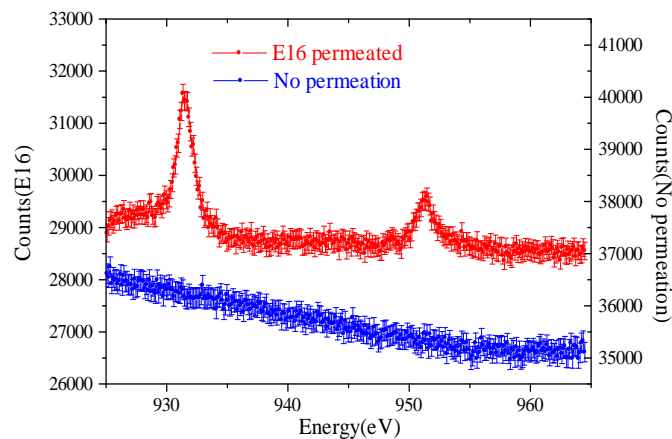


Fig.9. XPS Spectrum of Pr for E16.

IV. CONCLUDING REMARKS

We tried the electrochemical method in order to increase the surface deuterium density near the surface of the nano-structured Pd multilayer film. The electrochemical deuterium permeation method gave us increased transmutation products. Many kinds of transmuted products were obtained and gamma-ray emissions were observed by the electrochemical deuterium permeation method. It is necessary to perform more experiments from different viewpoints using the other measurement methods and improve the reliability of our experiments.

REFERENCES

- [1] Y. Iwamura, M.Sakano and T.Itoh, "Elemental Analysis of Pd Complexes: Effects of D₂ Gas Permeation", *Japanese Journal of Applied Physics*, Vol.41, (2002) pp. 4642-4650.
- [2] Y. Iwamura, T. Itoh, N.Yamazaki, J. Kasagi, Y. Terada, T. Ishikawa, D. Sekiba, H. Yonemura and K. Fukutani, "Observation of Low Energy Nuclear Transmutation Reactions Induced by Deuterium Permeation through Multilayer Pd and CaO thin Film", *J. Condensed Matter Nucl. Sci.* vol.4 (2011) pp.132–144.
- [3] Y. Iwamura, T. Itoh, M. Sakano, S. Kuribayashi, Y. Terada and T. Ishikawa, "Observation of Surface Distribution of Products by X-ray Fluorescence Spectrometry during D₂ gas permeation through Pd Complexes", *Condensed Matter Nuclear Science*, ed. by A. Takahashi et.al, World Scientific, New Jersey, (2006) pp.178-187.
- [4] Y. Iwamura, T. Itoh, M. Sakano, S. Sakai and S. Kuribayashi, "Low Energy Nuclear Transmutation in Condensed Matter induced by D₂ Gas Permeation through Pd Complexes: Correlation between Deuterium Flux and Nuclear Products", *Condensed Matter Nuclear Science*, ed. by P. H. Hagelstein and S. Chubb, World Scientific, New Jersey, (2006) pp.435-446.
- [5] Y. Iwamura, T. Itoh, N. Yamazaki, N. Watari, H. Yonemura, K. Fukutani, D. Sekiba, "Recent Advances in Deuterium Permeation Transmutation Experiments", *Proc. of ICCF16*, to be published.

- [6] T. Hioki, N. Takahashi, S. Kosaka, T. Nishi, H. Azuma, S. Hibi, Y. Higuchi, A. Murase and T. Motohiro, "Inductively Coupled Plasma Mass Spectrometry Study on the Increase in the Amount of Pr Atoms for Cs-Ion-Implanted Pd/CaO Multilayer Complex with Deuterium Permeation", *Japanese Journal of Applied Physics*, Vol.52, (2013) 107301.
- [7] T. Higashiyama, M Sakano, H. Miyamaru and A. Takahashi, "Replication of MHI Transmutation Experiment by D₂ Gas Permeation Through Pd Complex", Proceedings of 10th International Conference on Condensed Matter Nuclear Science, edited by P. H. Hagelstein et al., Condensed Matter Nuclear Science, World Scientific, New Jersey (2006) pp.447-454.
- [8] H. Yamada et.al., Producing Transmutation Elements on Plain Pd-foil by Permeation of Highly Pressurized Deuterium Gas, Proceedings of 12th International Conference on Condensed Matter Nuclear Science, ed. by A. Takahashi et al., Condensed Matter Nuclear Science, World Scientific, New Jersey (2006)pp.196-205.
- [9] D. Letts and D. Cravens. "Laser Stimulation of Deuterated Palladium: Past And Present", *Proc. of ICCF10*, 2003. Cambridge, World Scientific, Inc (2006) pp.159-170.

Deuterium permeation experiment using Pd/Ni multi-layered sample

T. Takahashi, R. Omi, S. Narita

Department of Electrical Engineering and Computer Science,
Iwate University
Morioka, Iwate, 020-8551, Japan
†t2313017@iwate-u.ac.jp

ABSTRACT

We performed a deuterium permeation experiment using a multi-layered Pd/Ni sample on which ^{133}Cs was deposited, and we investigated the occurrence of selective nuclear transmutation reactions from ^{133}Cs to nuclides with masses of 137, 141, and 145. Transmutation products from ^{133}Cs were not confirmed thus far. Improving deuterium permeation efficiency may be necessary for effectively inducing the reaction. In addition, we searched for newly produced elements from nuclear reactions over a wide mass range result.

Keywords: multi-layered metal samples, deuterium permeation, transmutation

1. Introduction

The observation of a transmutation phenomenon in deuterium permeation using a Pd/CaO multi-layered complex by the MHI group is an outstanding report in the study of low energy nuclear reactions in condensed matter. In particular, a selective transmutation from ^{133}Cs , which is deposited onto the sample surface, to ^{141}Pr was found and verified by various methods. The multi-layered sample structure is expected to be key for triggering the reaction, especially because it contains nano-scaled thin Pd membrane and CaO layer with a lower work function [1,2].

Anomalous heat evolution was found in deuterium loading/unloading with Pd-Ni binary nano-particles by Kobe-Technova group [3] and also in deuterium unloading with a multi-layered complex Pd-Ni sample [4]. In those experiments, the fine-structure of the sample as well as specific properties of Ni in deuterium loading could be related to the anomalous phenomenon. We may expect higher deuterium density at the interface between Pd and Ni layers for a Pd-Ni binary metal because Pd has a much higher deuterium diffusion coefficient than Ni.

Considering these results, we performed a deuterium permeation experiment using a Pd-Ni multi-layered sample on which Cs atoms are deposited, as shown in Fig. 1. We searched for a selective transmutation resulting in the production of an element with a mass number of 137/141/145, as has been predicted by the MHI group results.

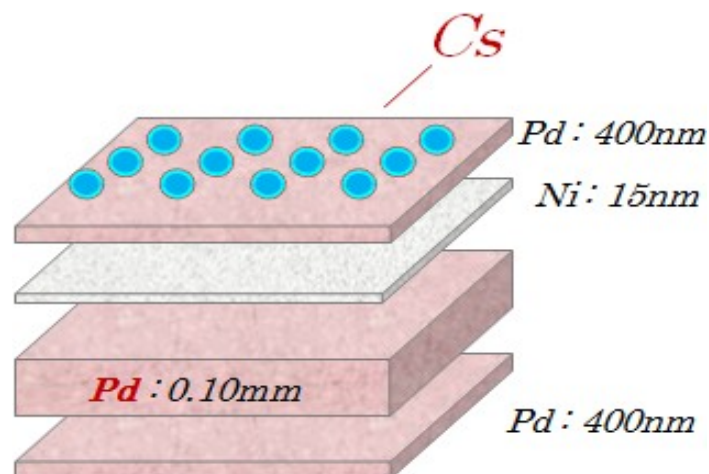


Figure 1. Sample structure.

In addition, we investigated the possibility of the production of other elements as evidence of a nuclear reaction.

2. Experiment

2.1 Sample preparation

A Pd foil $12.5 \times 12.5 \times 0.1$ mm in size was washed in acetone for 30 min, annealed for 10 h at 900°C , and washed with aqua regia to remove metallic impurities, and then subjected to ultrasonic cleaning in ultra-pure water. Ni and Pd membranes were deposited on one side of the Pd foil by Ar ion beam sputtering. The thickness of the Ni and Pd films were 15 nm and 400 nm, respectively.

It is known that a multi-layered structure of crystalline bulk Pd and non-crystalline Pd membrane has a unique property in hydrogen absorption and desorption [5]. In our past desorption experiments, we found that such samples promote out-diffusion of deuterium [4,6]. Therefore, in this study, we deposited a 400-nm-thick Pd membrane on the other side of the Pd foil to enhance deuterium permeability. Figure 1 shows the Pd/Ni multi-layered sample used in this study.

After forming the multi-layered structure, a small amount of Cs was electrochemically deposited on the uppermost surface of the sample. The sample and Pt anode were placed in a 1 mM $\text{CsNO}_3/\text{H}_2\text{O}$ solution, and we applied a potential difference of 1 V to the electrodes for 10 s.

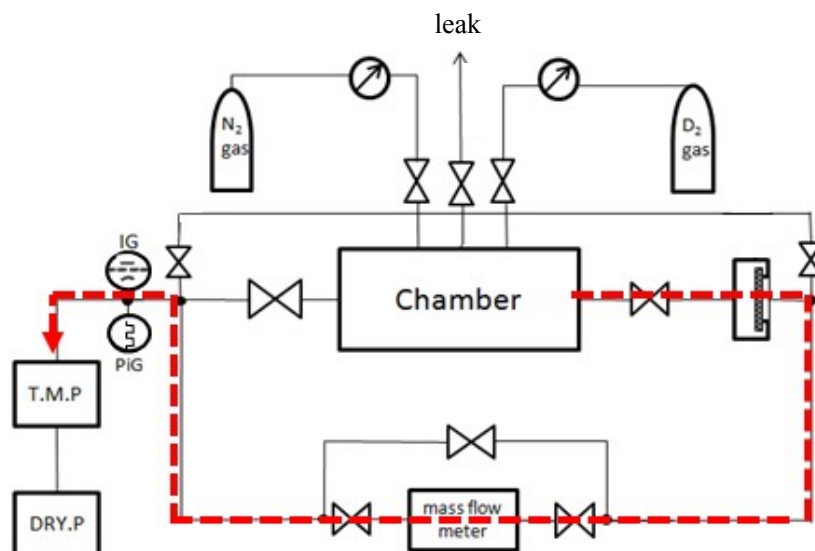


Figure 2. Deuterium permeation system.

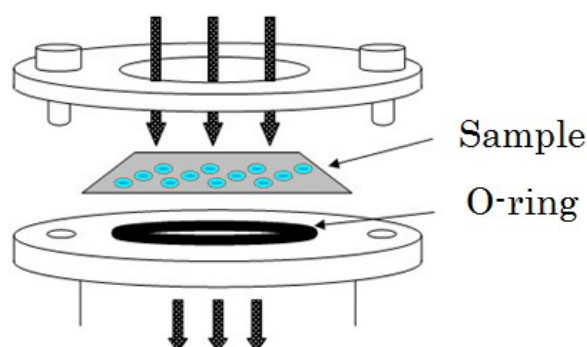


Figure 3. Sample holder

2.2 Permeation experiment.

Figure 2 shows the deuterium permeation system used in this experiment. A schematic view of the sample holder is shown in Fig. 3. After setting the sample in the holder, the system was evacuated by a dry-scroll pump and a turbo-molecular pump, following which deuterium gas was introduced into the main chamber until the inside pressure reached 0.2 MPa. The Pd/Ni multi-layered side was exposed to deuterium gas, and the other side faced an evacuated space. Deuterium permeated from the chamber through the sample to the evacuated side because of the pressure gradient. The temperature of the sample holder was maintained at 70°C throughout the experiment, which typically ran for a week. The flow rate was measured using a mass flow meter

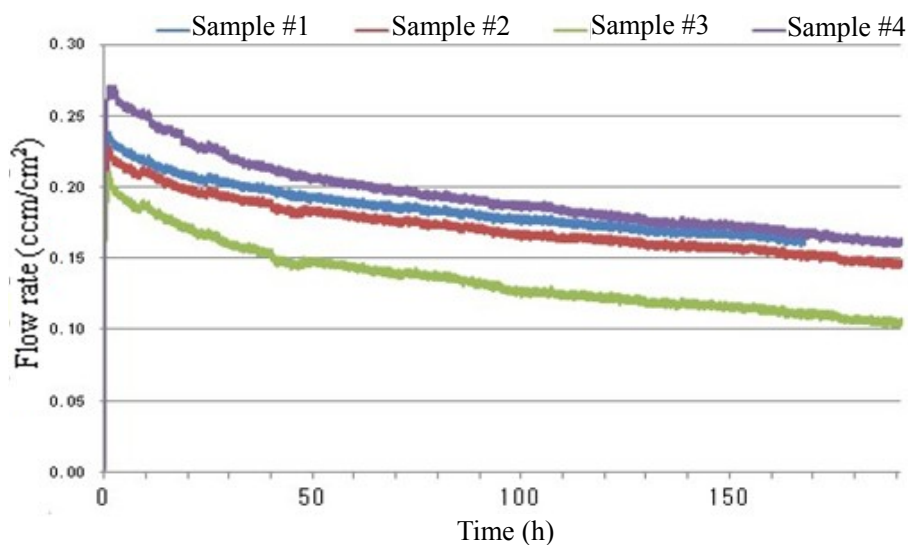


Figure 4. Deuterium flow rate.

(STEC, SEF-7330M) placed downstream of the sample. Four permeation experiments were conducted.

After each permeation experiment, the sample was heated and the chamber evacuated for a few days to purge the remaining deuterium atoms. Then, the sample was taken out from the sample and the elemental composition on the surface was analyzed by time-of-flight secondary ion mass spectrometry (TOF-SIMS; ULVAC-PHI PHI TRIFT V nano-TOF). A pulsed Bi⁺ beam was used as the source of primary bombarding ions and three spots, each of area 40 μm × 40 μm, randomly selected on the sample were analyzed. We analyzed the surface area on each spot as well as a somewhat deeper region within the same spot, where contaminants were removed by sputtering with a DC Bi⁺ beam for 30 s (sputter cleaning process). In order to evaluate the effect of environmental contaminations, we prepared a control sample following the same procedure but not permeated deuterium.

3. Results and Discussion

3.1 Deuterium flow rate

Figure 4 shows the flow rates measured in the 4 permeation experiments. The maximum flow rates were found to be 0.1~0.3 ccm/cm², and these flow rates gradually decreased. We fabricated samples #1-3 simultaneously, and they were subjected to the permeation experiment in order. This may be why the total flow rate was smaller for sample #3. We expect that the flow rate is very sensitive to the sample treatment process

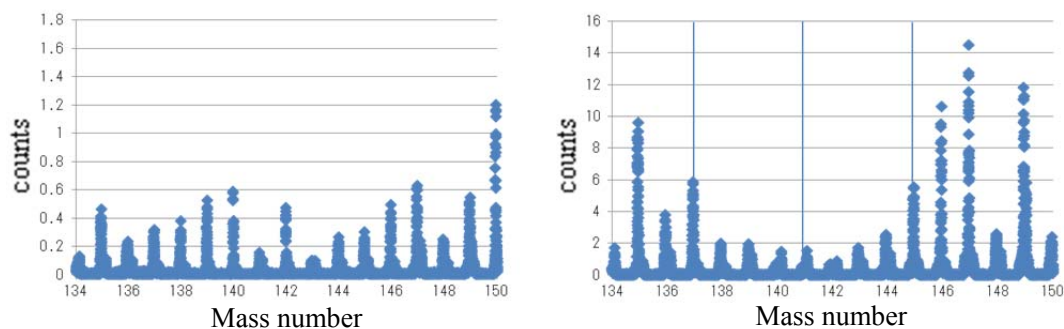


Figure 5. TOF-SIMS mass spectra for control sample (left) and permeation sample (right).

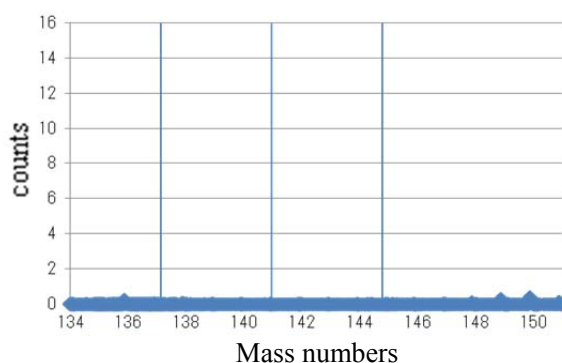


Figure 6. TOF-SIMS mass spectrum for permeation sample analyzed after sputter cleaning.

and contamination of the sample surface. It is possible that the surface was polluted between fabrication and use, although we stored the sample in a dry cabinet before the experiment. For sample #4, we tested immediately after fabrication, which may be why its flow rate was higher than that of the other samples.

3.2 Elemental analysis

Figure 5 shows the mass-spectra for mass numbers ranging from 134 to 150. The spectra were obtained by TOF-SIMS analysis without sputter cleaning, for a control and a permeation sample. Note that the signal intensities of the control and the permeation samples are significantly different in those spectra. Since signal intensity of a mass spectrum obtained by TOF-SIMS depends on various effects such as type of contaminants on the sample, the surface condition, and so on. We are assuming that there were more various elements and their compounds on the control sample, so that

the signals on each nominal mass became relatively smaller comparing with those for the permeation sample.

We expected a selective transmutation reaction that produces elements of mass numbers 137, 141, and 145, as mentioned above. However, we did not observe a significant signal in the mass spectrum. The mass spectrum for a permeation sample after sputter cleaning is shown in Fig. 6, and no signals corresponding to the expected mass numbers were found in that case either.

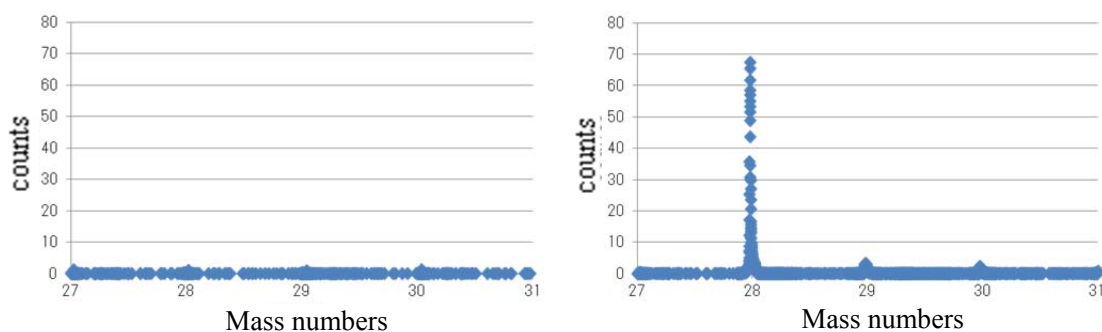


Figure 7. TOF-SIMS mass spectra for mass numbers around 30 for the control sample (left) and permeation sample (right).

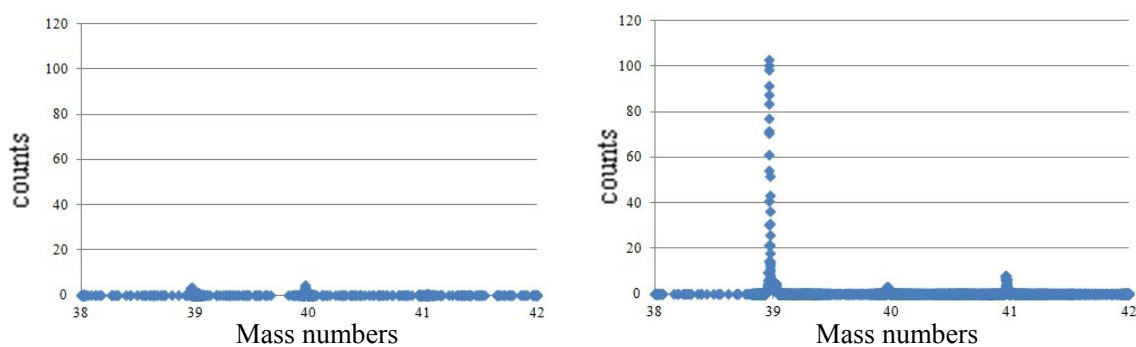


Figure 8. TOF-SIMS mass spectra for mass numbers around 40 for the control sample (left) and permeation sample (right).

We did not observe any expected signals in all 4 runs. One possible reason was that the yields of the transmutation products were quite low because the deuterium flow rate was insufficient to effectively induce the reaction. Therefore, we have considered

modifying some experimental conditions, such as the procedure to deposit membranes, their thickness, the densities of deposited Cs, to improve the flow rate. In addition, we should conduct the experiment under much cleaner environments because the flow rate can be greatly affected by contaminants on the sample surface. Moreover, it may be helpful to extend the permeation period to enhance the yields of reaction products.

Besides, MHI group has claimed that the sample should consist of a material with a lower work function to induce a transmutation effectively. They used a Pd/CaO complex sample and the work function of CaO is 1.0-1.5 eV. In contrast, it is 5.1 eV for Ni. This difference in work function might be a reason why we did not observe the transmutation so far.

Si	Mass	28	29	30
	Abundance by TOF-SIMS signal intensity (%)	87.2	9.7	3.1
	Natural abundance (%)	92.2	4.7	3.1
K	Mass	39	40	41
	Abundance by TOF-SIMS signal intensity (%)	88.4	3.6	8.0
	Natural abundance (%)	93.3	0.01	6.7

Table 1. Natural isotopic abundance of elements compared to the signals of TOF-SIMS mass spectra.

We found some significant signals in TOF-SIMS analysis for permeation samples. Figure 7 and 8 show spectra around mass numbers 30 and 40, respectively. We can observe significant signals for mass numbers 28 and 39 that did not occur for the control sample. It is possible that these were produced by a nuclear process. We assumed these signal corresponded to ^{28}Si and ^{39}K and investigated the abundance of their isotopes. Table I lists the abundances obtained from the signal intensities of corresponding mass numbers, compared with the natural abundances. Considering the statistical uncertainties, the measured abundances are not anomalous for the current data. Otherwise, an impurity background with mass number of 40, which can be seen in the mass spectrum for control sample, may cause the anomaly in the abundance. However we should continue observing the signals with these masses to clarify the possibility of these being nuclear products.

4. Conclusion

We performed deuterium permeation experiments using a multi-layered Pd/Ni

sample and investigated the occurrence of selected nuclear transmutation reactions. However, transmutation products from ^{133}Cs were not confirmed thus far. We proposed to improve the deuterium permeation efficiency by modifying sample conditions in a future study. In addition, we still need to understand the properties of Pd-Ni binary metal in deuterium permeation/diffusion in order to induce a nuclear reaction.

References

- [1] Y. Iwamura *et al.*, Jpn. J. Appl. Phys. 41 (2002) 4642.
- [2] Y. Iwamura *et al.*, Proc of JCF13 (2013) 196.
- [3] H. Sakoh *et al.*, Proc of JCF11 (2011) 16.
- [4] G. Hosokawa *et al.*, Proc of JCF13 (2013) 188.
- [5] H. Tamura (ed), “Suiso-kyuzou-goukin” (1998) (in Japanese)
- [6] S. Narita *et al.*, Proc of JCF9 (2009) 11.

Bound states of the nucleus-monopole system

Tetsuo SAWADA

Institute of Quantum Science, Nihon University, Tokyo, Japan

Abstract In order to understand the nuclear cold fusion strictly in the framework of the quantum theory, the Schrödinger equation of the system, where small number of the nucleons and a magnetic monopole coexist, is solved. By solving the equation, we can understand why the channels of $t+p$ and ${}^3\text{He}+n$ are closed when the reaction $d+d \rightarrow \alpha$ proceeds.

1. Introduction

We shall consider the systems of the magnetic monopole and the small nuclei ($A < 5$). The mass of the magnetic monopole is set equal to infinity for simplicity, therefore the Hamiltonian is the sum of the kinetic energies of the constituent nucleons in the magnetic Coulomb field and the nuclear potential between constituent nucleons. Since from the charge quantization condition of Dirac: $*QQ/\hbar c = n/2$ with integer n , the "fine structure constant" of the magnetic side is $*e^2/\hbar c = 137/4$, which should be compared with the value of the ordinary (electric) fine structure constant $e^2/\hbar c = 1/137$. Since the magnetic Coulomb field is super-strong, the interaction energy of the magnetic dipole moment of the nucleon $\mu = \kappa(e^2/2m)$, in which $\kappa = 2.793$ and -1.913 respectively for the proton and the neutron, has the order of magnitude of nuclear interaction.

It is important to know the change of the energy level structure of the system of the magnetic monopole and the nucleus ($*e-A$), because from the energy conservation we can determine which channels of the final state stay open. It is also important to calculate binding energy and the wave function of the ground state of the deuteron plus magnetic monopole system ($*e-d$), because when two deuterons are trapped by the same magnetic monopole ($d-*e-d$), deuterons must fuse to become more stable particle namely α -particle. If we remember that the spin of the α -particle is zero, it is not attracted by $*e$, but it must be simply emitted. The transition rate can be calculated if we know the wave functions of the $d-*e$ system and $\alpha-*e$, we can determine the transition rate by using the standard formula of the quantum mechanics namely the "Fermi's golden rule". As long as the magnetic monopole is available, which is believed to be

created abundantly in the process of the big bang, and is diluted as the space expands and may become the rare particle today, we can use the magnetic monopole as the catalyst of the nuclear fusion reaction at zero incident energy.

In Section 2, the monopole harmonics, which is the generalization of the well-known spherical harmonics, is introduced. As the simplest application, we shall determine the wave function of the spin-0 charged particle in the magnetic Coulomb field produced by magnetic monopole fixed at the origin. In Section 3, spin-1/2 particles in the magnetic Coulomb field are considered. Tables of the energy levels of the proton, neutron, triton and ${}^3\text{He}$ are given along with their orbital radius. Section 4 is used to do the variational calculation of the deuteron-monopole system (d-*e) and the energy level of the ground state is determined, which is $E = -4.45$ MeV. If the two deuterons are trapped by the same magnetic monopole (d-*e-d), it must decay to the more stable state (α -*e). So the α is simply emitted from the magnetic monopole, and so *e plays the role as the catalyst of the cold nuclear fusion reaction. It is also pointed out that the binding energy of d-*e-d, which is $-E = 8.9$ MeV, is large enough to close the channels t+p and ${}^3\text{He}$ -n.

2. Monopole harmonics and the motion of a spin zero particle

The Hamiltonian of the charged spin-zero particle in the external magnetic Coulomb field is obtained by the gauge substitution $\vec{p} \rightarrow (\vec{p} - (Q/c)\vec{A})$ where \vec{A} is the vector potential whose rotation is the magnetic Coulomb field $\vec{B} = *Q(\hat{r}/r^2)$. However since there is the gauge ambiguity that change of the vector potential by $\vec{A} \rightarrow \vec{A} + \vec{\nabla}\Lambda(\vec{r})$ does not affect to its rotation namely to the magnetic field $\vec{B}(\vec{r})$, we can divide whole space into two domains $R^{(n)}$ and $R^{(s)}$, namely into the northern hemisphere and the southern hemisphere, and assign the vector potentials of different gauges. In the assignment the vector potentials must be regular in the given domains. Our choice is

$$\vec{A}^{(n)} = *Q \frac{(1 - \cos \theta)}{r \sin \theta} \hat{e}_\phi \quad \text{in } R^{(n)}, \quad (1)$$

and

$$\vec{A}^{(s)} = *Q \frac{(-1 - \cos \theta)}{r \sin \theta} \hat{e}_\phi \quad \text{in } R^{(s)}. \quad (2)$$

The rotation of $\vec{A}^{(n)}$ is the Coulomb field plus a string running on the z-axis with $z < 0$, on the other hand the rotation of $\vec{A}^{(s)}$ is the Coulomb field plus a string running on the z-axis with $z > 0$. In this way, we can obtain the magnetic Coulomb field without the Dirac string. To see the magnetic Coulomb field, we use the formula for rotation in the

spherical coordinate system:

$$\begin{aligned}
 (\vec{\nabla} \times \vec{A})_r &= \frac{1}{r \sin \theta} \left\{ \frac{\partial}{\partial \theta} (\sin \theta A_\phi) - \frac{\partial A_\theta}{\partial \phi} \right\}, \\
 (\vec{\nabla} \times \vec{A})_\theta &= \frac{1}{r} \left\{ \frac{1}{\sin \theta} \frac{\partial A_r}{\partial \phi} - \frac{\partial}{\partial r} (r A_\phi) \right\}, \\
 (\vec{\nabla} \times \vec{A})_\phi &= \frac{1}{r} \left\{ \frac{\partial}{\partial r} (r A_\theta) - \frac{\partial A_r}{\partial \theta} \right\}.
 \end{aligned} \tag{3}$$

If we remember that in the spherical coordinate the gradient $\vec{\nabla}$ is

$$\vec{\nabla} = \hat{e}_r \frac{\partial}{\partial r} + \hat{e}_\theta \frac{1}{r} \frac{\partial}{\partial \theta} + \hat{e}_\phi \frac{1}{r \sin \theta} \frac{\partial}{\partial \phi}, \tag{4}$$

the gauge function is $\Lambda(\vec{r}) = -2 *Q\phi$, because

$$\vec{A}^{(s)} - \vec{A}^{(n)} = -2 *Q \frac{1}{r \sin \theta} \hat{e}_\phi \equiv \vec{\nabla} \Lambda. \tag{5}$$

The Hamiltonian of the spin-0 particle of mass M and the electric charge Ze in the Coulombic magnetic field produced by the magnetic monopole $*eD$ fixed at the origin is

$$H_0 = -\frac{\hbar^2}{2M} (\vec{\nabla} - i \frac{Ze}{\hbar c} \vec{A})^2, \tag{6}$$

in which \vec{A} is given in Eq.(1) and Eq.(2). We are going to solve the eigen-value equation $H_0\Psi = E\Psi$ in the separable form: $\Psi = R(r)Y(\theta, \phi)$. The angular part $Y(\theta, \phi)$ is the eigen-function of angular momentum \vec{L}^2 and L_z which are defined by

$$\vec{L} = \vec{r} \times (\vec{p} - i \frac{Ze}{c} \vec{A}) - \hbar q \hat{e}_r, \quad \text{where} \quad q = \frac{D *e Ze}{\hbar c} = \frac{DZ}{2}. \tag{7}$$

The first term of \vec{L} is the orbital angular momentum, whereas the second term is the extra angular momentum which arises when the magnetic charge ($D*e$) and the electric charge (Ze) coexists. When $q = 0$, the angular part $Y(\theta, \phi)$ reduces to the ordinary spherical harmonics $Y_{\ell, m}(\theta, \phi)$. However for $q \neq 0$, new functions must appear. Let us rewrite

$$\vec{L}^2 = -\hbar^2 \left[\frac{1}{\sin \theta} \frac{\partial}{\partial \theta} (\sin \theta \frac{\partial}{\partial \theta}) + \frac{1}{\sin^2 \theta} \frac{\partial^2}{\partial \phi^2} \mp 2iq \frac{1}{1 \pm \cos \theta} \frac{\partial}{\partial \phi} - 2q^2 \frac{1}{1 \pm \cos \theta} \right], \tag{8}$$

and

$$L_z = -i\hbar \frac{\partial}{\partial \phi} \mp q\hbar, \tag{9}$$

where \pm sign correspond to the domains of the north and the south hemispheres. The

eigen-function of L_z must have the form $Y = \Theta(z) \exp[i(m \pm q)\phi]$, where $z = \cos\theta$. When the eigen-value of \bar{L}^2 is $\ell(\ell+1)$, the equation $\Theta(z)$ must satisfy is

$$\left[(1-z^2) \frac{d^2}{dz^2} - 2z \frac{d}{dz} - \frac{1}{1-z^2} (m+qz)^2 + \ell(\ell+1) - q^2 \right] \Theta(z) = 0. \quad (10)$$

Its solutions can be written by using the Jacobi polynomials. However it is more convenient to write the result by using the Wigner's d-function of the rotation matrix, since most of the text book of the nuclear physics contains the tables of the d-functions.

The monopole harmonics Y becomes :

$$Y_{q,\ell,m}^{(n)}(\theta, \phi) = \sqrt{\frac{2\ell+1}{4\pi}} e^{+iq\phi} d_{-q,m}^{(\ell)}(\theta) e^{+im\phi} \quad \text{in} \quad 0 \leq \theta < \frac{\pi}{2} + \varepsilon, \quad (11)$$

and

$$Y_{q,\ell,m}^{(s)}(\theta, \phi) = \sqrt{\frac{2\ell+1}{4\pi}} e^{-iq\phi} d_{-q,m}^{(\ell)}(\theta) e^{+im\phi} \quad \text{in} \quad \frac{\pi}{2} - \varepsilon < \theta \leq \pi, \quad (12)$$

with $\ell = |q|, |q|+1, |q|+2, \dots$ and $m = -\ell, -\ell+1, \dots, \ell$, which is the generalization of the well-known spherical harmonics $Y_{\ell,m}$.

The Hamiltonian H_0 of Eq.(6) can be expressed by using the angular momentum operator \bar{L}^2 :

$$H_0 = -\frac{1}{2M} \left[\frac{\partial^2}{\partial r^2} + \frac{2}{r} \frac{\partial}{\partial r} - \frac{1}{\hbar^2 r^2} (\bar{L}^2 - \hbar^2 q^2) \right]. \quad (13)$$

If we write the wave function as $\Psi(\vec{r}) = R(r)Y_{q,\ell,m}(\theta, \phi)$, $R(r)$ must satisfy

$$\left[-\frac{1}{2Mr^2} \frac{d}{dr} \left(r^2 \frac{d}{dr} \right) + \frac{\ell(\ell+1) - q^2}{2Mr^2} \right] R(r) = ER(r), \quad (14)$$

the solution which does not blow up at $r=0$ is the J-Bessel:

$$R(r) = \frac{1}{\sqrt{kr}} J_\mu(kr), \quad (15)$$

where

$$k = \sqrt{2ME}, \quad \text{and} \quad \mu = \sqrt{\ell(\ell+1) - q^2 + 1/4} = \sqrt{(\ell+1/2)^2 - q^2} > 0. \quad (16)$$

For $E < 0$, there is no meaningful solution, and therefore no bound state. This wave function describe the motion of the spin-0 charged particle in the magnetic Coulomb field whose source is the magnetic monopole $*Q = *eD$ fixed at the origin. So it describes the motion of the charged pion, or the alpha particle whenever the deformation of the composite particle is negligible.

3. Spin 1/2 particle in the magnetic Coulomb field

In this Section we shall consider the motion of the spin 1/2 particle with the total magnetic dipole moment $\vec{\mu} = \kappa_{tot}(e^2/2m)\vec{\sigma}$ in the magnetic Coulomb field produced by a magnetic monopole $*eD$ fixed at the origin, in which D is the magnetic charge number and is the magnetic counterpart of the "electric" charge number Z . $D = 1$ is Dirac's monopole whereas $D = 2$ is Schwinger's monopole. We start to compose the eigen-states of \vec{J}^2 and J_z where $\vec{J} = \vec{L} + \vec{\sigma}/2$ in which the eigen-value of \vec{L}^2 is $\ell(\ell+1)$ with $\ell = |q|, |q|+1, |q|+2, \dots$. If we add the spin $\vec{\sigma}/2$ term to \vec{L} we get two states $j = \ell - 1/2$ and $j = \ell + 1/2$. It is the standard procedure to make the eigen-functions of \vec{J} by using the Clebsch-Gordan coefficients. However since j is what is conserved, it is more adequate to reverse the variables in classifying the states, namely for given j there are two states of $\ell: \ell = j - 1/2$ and $j + 1/2$, except for the smallest j state ($j = |q| - 1/2$). After Wu-Yang [1], it is convenient to call the doublet states type-A and the singlet state type-B.

For given j , there are two states:

$$\begin{aligned} \Phi_{j,m}^{(1)} &= \sqrt{\frac{j+m}{2j}} Y_{q,j-1/2,m-1/2} \begin{pmatrix} 1 \\ 0 \end{pmatrix} + \sqrt{\frac{j-m}{2j}} Y_{q,j-1/2,m+1/2} \begin{pmatrix} 0 \\ 1 \end{pmatrix} \\ &= \begin{bmatrix} \sqrt{\frac{j+m}{2j}} Y_{q,j-1/2,m-1/2} \\ \sqrt{\frac{j-m}{2j}} Y_{q,j-1/2,m+1/2} \end{bmatrix}, \end{aligned} \quad (17)$$

and

$$\begin{aligned} \Phi_{j,m}^{(2)} &= -\sqrt{\frac{j-m+1}{2j+2}} Y_{q,j+1/2,m-1/2} \begin{pmatrix} 1 \\ 0 \end{pmatrix} + \sqrt{\frac{j+m+1}{2j+2}} Y_{q,j+1/2,m+1/2} \begin{pmatrix} 0 \\ 1 \end{pmatrix} \\ &= \begin{bmatrix} -\sqrt{\frac{j-m+1}{2j+2}} Y_{q,j+1/2,m-1/2} \\ \sqrt{\frac{j+m+1}{2j+2}} Y_{q,j+1/2,m+1/2} \end{bmatrix}, \end{aligned} \quad (18)$$

for $j \geq |q| + 1/2$ (type-A). On the other hand for $j = |q| - 1/2$ (type-B), $\Phi_{j,m}^{(1)}$ of Eq. (17) vanishes, and there remains only one state $\Phi_{j,m}^{(2)}$ of Eq.(18). It is convenient to introduce a new notation to the type-B state:

$$\eta_m = \begin{bmatrix} -\sqrt{\frac{|q|-m+1/2}{2|q|+1}} Y_{q,|q|,m-1/2} \\ \sqrt{\frac{|q|+m+1/2}{2|q|+1}} Y_{q,|q|,m+1/2} \end{bmatrix}. \quad (19)$$

The importance of the type-B state comes from the fact that the ground state is always type-B state, and that is the eigen-state of the (pseudo-)scalar operator $(\vec{\sigma} \cdot \hat{r})$ with the eigen-value +1, and it is sometimes called "hedgehog state" since the spin direction is outward and spherical.

The Hamiltonian H of the proton in the magnetic Coulomb field is [2]:

$$H = \frac{1}{2m_p} (-i\vec{\nabla} - e\vec{A})^2 - \frac{1}{r^2} \frac{b(r)}{2m_p} (\vec{\sigma} \cdot \hat{r}), \quad (20)$$

where the form factor function is

$$b(r) = \bar{b} F(ar) \equiv \bar{b} \left\{ 1 - e^{-ar} \left(1 + ar + \frac{a^2 r^2}{2} \right) \right\}, \quad (21)$$

with

$$\bar{b} = \kappa_{tot} |q| = 2.7928 |q|, \quad q = D/2 \quad \text{and} \quad a = 6.04 \mu_\pi. \quad (22)$$

The parameter a relates to the proton radius, which is 0.811 fm, by $\langle r^2 \rangle = 12/a^2$.

For the type-B amplitude

$$\Psi = \frac{g(r)}{r} \eta_m, \quad (23)$$

the equation of the radial function $g(r)$ becomes

$$\left[\frac{d^2}{dr^2} - \kappa^2 - \frac{(|q|-b(r))}{r^2} \right] g(r) = 0 \quad \text{with} \quad \kappa^2 = -2m_p E. \quad (24)$$

For $ar \gg 1$, $b(r)$ becomes the constant \bar{b} and the equation (24) reduces to the Bessel equation, the solution, which damps for large ar , is

$$g(r) = \sqrt{\kappa r} K_{i\mu}(\kappa r) \quad \text{with} \quad i\mu = \sqrt{|q|(1-\kappa_{tot})+1/4}. \quad (25)$$

Since the behavior $g(r)$ at the origin $C_1 r^\alpha$ is determined by the index relation $\alpha = 1/2 + \sqrt{|q|+1/4}$, we integrate Eq. (24) to the matching point $ar = ar_m \gg 1$. The binding energies of the ground states turn out $-E = 0.1882$ MeV and 2.4065 MeV for $D = 1$ and $D = 2$ magnetic monopoles respectively, whereas the radii of the orbits of the ground states are $\bar{r} = 11.0$ fm and 3.67 fm, respectively. E of the first few excited states are given also in the Tables below for $D = 1$ and 2. In the same Tables the values

of the parameters μ and C_1 which appear in the infinitely many binding energy levels

$$-E = C_1 \exp\left[-\frac{2\pi}{\mu}(n-1)\right] \quad \text{with } n = 1, 2, 3 \dots, \quad (26)$$

where n is the principal quantum number, are also given. The level structure of Eq. (26) is the characteristic feature of $1/r^2$ potential (Efimov levels), which should be compared with the well-known Bohr levels $-E = c'/n^2$.

Although we considered the system of the proton and the magnetic monopole $*eD$, we can also apply the same technique to other small nuclei of spin 1/2 such as triton (t) and ^3He as long as the deformations of the nuclei in the magnetic Coulomb field are negligible, by simply changing the parameters such as the mass m , charge Z , magnetic moment κ_{tot} and a , which relates to the radius of the nucleus \bar{r} by $a^2 = 12/\bar{r}^2$. In the Table the binding energy and the orbital radius $\sqrt{\langle r^2 \rangle}$ of t and ^3He are also given. Among them n and t have the type-A bound states of the form $\psi = [f(r)\Phi_{j,m}^{(1)} + g(r)\Phi_{j,m}^{(2)}]/r$, whose radial functions satisfy:

$$\left[\frac{d^2}{dr^2} + 2ME - \frac{R}{r^2} \right] \begin{pmatrix} f \\ g \end{pmatrix} = 0, \quad (27)$$

where

$$R = \begin{pmatrix} (j + \frac{1}{2})(j + \frac{1}{2}) - q^2 + b(r) \frac{2q}{2j+1} & -b(r) \frac{\sqrt{(2j+1)^2 - 4q^2}}{2j+1} \\ -b(r) \frac{\sqrt{(2j+1)^2 - 4q^2}}{2j+1} & (j + \frac{1}{2})(j + \frac{3}{2}) - q^2 - b(r) \frac{2q}{2j+1} \end{pmatrix}. \quad (28)$$

Table 1. The first few binding energies $-E$ and the orbital radii $\langle r^2 \rangle^{1/2}$ of the n, p, t and ${}^3\text{He}$ in the Coulomb field produced by Dirac's magnetic monopole ($D = 1$). n is the principal quantum number.

$D = 1$	q	j (type)	n	$-E$	$\langle r^2 \rangle^{1/2}$
n	0	1/2 (A)	1	37.37 eV	647.7 fm
			2	1.375×10^{-6} eV	8.57×10^6 fm
			⋮		
			∞	($C_1 = 37.37$ eV)	($\mu = 0.3670$)
p	1/2	0 (B)	1	0.1882 MeV	11.00 fm
			2	70.046 eV	547.6 fm
			3	0.03069 eV	27257 fm
			⋮		
∞	($C_1 = 0.1884$ MeV)	($\mu = 0.8040$)			
t	1/2	0 (B)	1	1.516 MeV	3.820 fm
			2	58.085 keV	19.36 fm
			3	2.226 keV	98.89 fm
			⋮		
∞	($C_1 = 1.516$ MeV)	($\mu = 1.9263$)			
t	1/2	1 (A)	1	2.178 keV	79.19 fm
			2	24.366 eV	748.7 fm
			3	0.02725 eV	7079 fm
			⋮		
∞	($C_1 = 2.1783$ eV)	($\mu = 1.3984$)			
${}^3\text{He}$	1	1/2 (B)	1	0.2484 MeV	7.371 fm
			2	2.7413 keV	70.36 fm
			3	30.047 eV	672.15 fm
			⋮		
∞	($C_1 = 0.2502$ MeV)	($\mu = 1.3921$)			

Table 2. The first few binding energies $-E$ and the orbital radii $\langle r^2 \rangle^{1/2}$ of the n, p, t and ${}^3\text{He}$ in the magnetic Coulomb field produced by Schwinger's magnetic monopole ($D = 2$). n is the principal quantum number of the infinitely many energy levels which converge to $-E = 0$.

$D = 2$	q	j (type)	n	$-E$	$\langle r^2 \rangle^{1/2}$
n	0	1/2 (A)	1	0.8003 MeV	5.728 fm
			2	1.115 keV	158.97 fm
			3	1.542 eV	4139.3 fm
			⋮		
			∞	($C_1 = 0.8040$ MeV)	($\mu = 0.9545$)
p	1	1/2 (B)	1	2.4065 MeV	3.666 fm
			2	15.457 keV	47.70 fm
			3	98.231 eV	598.42 fm
			⋮		
			∞	($C_1 = 2.4322$ MeV)	($\mu = 1.2421$)
t	1	1/2 (B)	1	4.366 MeV	2.779 fm
			2	0.5479 MeV	8.464 fm
			3	57.766 keV	26.31 fm
			⋮		
			∞	($C_1 = 5.4085$ MeV)	($\mu = 2.7697$)
t	1	3/2 (A)	1	1.203 MeV	4.651 fm
			2	73.162 keV	19.20 fm
			3	4.2423 keV	79.88 fm
			⋮		
			∞	($C_1 = 1.2696$ MeV)	($\mu = 2.2042$)
t	1	5/2 (A)	1	0.5342 eV	3169.1 fm
			2	8.465×10^{-8} eV	7.961×10^6 fm
			⋮		
			∞	($C_1 = 0.53418$ eV)	($\mu = 0.4013$)
			${}^3\text{He}$	2	3/2 (B)
2	51.115 keV	21.50 fm			
3	2.3239 keV	100.9 fm			
⋮					
∞	($C_1 = 1.1259$ MeV)	($\mu = 2.0312$)			

4. Deuteron in the magnetic Coulomb field

In the previous sections, we considered the system A-*e where A is the small nucleus and in which the deformations of the nucleus in the magnetic Coulomb field are neglected. This approximation is correct when A is the tightly bound composite particles such as ${}^4\text{He}$, t and ${}^3\text{He}$. However deuteron is the exception, because its binding energy is too small (2.22 MeV) and its orbital is spread. Instead we apply the variational calculation of the two-body proton-neutron system in the external field produced by the

magnetic monopole *e. The Hamiltonian H of the system is:

$$H = H_0^{(p)} + H_0^{(n)} + V_N, \quad (29)$$

where

$$H_0^{(p)} = -\frac{1}{2m} \left(\hbar \vec{\nabla}_1 - i \frac{e}{c} \vec{A} \right)^2 - \frac{1}{r_1^2} \frac{\kappa_{tot}^{(p)} |q|}{2m} (\vec{\sigma}^{(p)} \cdot \hat{r}_1) F(r_1), \quad (29a)$$

and

$$H_0^{(n)} = -\frac{1}{2m} \hbar^2 \vec{\nabla}_2^2 - \frac{1}{r_2^2} \frac{\kappa_{tot}^{(n)} |q|}{2m} (\vec{\sigma}^{(n)} \cdot \hat{r}_2) F(r_2), \quad (29b)$$

in which $V_N(r)$ is the nuclear potential and $\vec{r} = \vec{r}_2 - \vec{r}_1$ is the relative coordinate of the two nucleons. It is interesting to regard $\kappa_{tot}^{(n)}$ as a free parameter of the system, and set equal to zero: ($\kappa_{tot}^{(n)} = 0$), rather than actual $\kappa_{tot}^{(n)} = -1.913$. The relative wave function of the neutron $\varphi(r)$ must be the same as the neutron wave function of the deuteron in vacuum. Therefore what we have to determine is the energy of the proton in the magnetic Coulomb fields. Our assumed form of the trial function of the radial part of the proton $g(r_1)\eta_m$ is the GEM (Gaussian Expansion Method) form:

$$g(r_1) = \sum_k \sum_{j=1}^n C_j^{(k)} \exp[-u_k y_k^{j-1} r_1^2]. \quad (30)$$

Namely the terms have the Gaussian form whose range parameters are the geometrical series. There are set of such terms specified by (k). We must determine the coefficients by minimizing the energy expectation value

$$E = \frac{\langle \Psi | H | \Psi \rangle}{\langle \Psi | \Psi \rangle}. \quad (31)$$

Our result of the search for $\kappa_n = 0$ case is $E = -4.760$ MeV. As we move κ_n to the actual value of the magnetic moment of the neutron namely to $\kappa_n = -1.91314$ the energy increases to $E = -4.450$ MeV., when the magnetic monopole is Dirac's type ($D = 1$).

It is interesting to consider the nuclear fusion process, which start to occur when two deuterons are trapped by the same magnetic monopole d-*e-d whose energy level is $E = -8.90$ MeV. There are four channels to transfer, they are d-d, t-p, ${}^3\text{He}-n$ and ${}^4\text{He}$ in addition to the magnetic monopole fixed at the origin. However if we start from the ground state of d-*e-d, the only open channel of the final state is ${}^4\text{He}$. Since the binding energies of the triton (t) and ${}^3\text{He}$ are 8.5 MeV and 7.7 MeV, respectively, it is energetically impossible to transit from the ground state of d-*e-d to the continuous states of the t-p and the ${}^3\text{He}-n$ channels whose threshold is $E = -8.5$ MeV and $E = -7.7$ MeV, respectively. On the other hand, the channel of ${}^4\text{He}$ stays open, since its

threshold occurs at $E = -28.2$ MeV. It is well-known that in the low energy d+d reactions in vacuum, $d+d \rightarrow t+p$ and $d+d \rightarrow {}^3\text{He}+n$ are the main channels with 50% each in the branching ratio. However in the nuclear cold fusion, the only open channel is ${}^4\text{He}$, and this is understood by the energy conservation law.

It is important to see another role of the external field produced by the magnetic monopole. In the nuclear reaction in vacuum, the process $d+d \rightarrow {}^4\text{He}$ is forbidden, or in general the exothermic (two body) \rightarrow (one body) reaction violates the law of the momentum conservation. This is evident if we see the process in the center of mass system, the momentum of the final state particle must be zero from the momentum conservation, whereas the energy conservation requires that the magnitude of the momentum of the final state particle is $|\vec{p}| = \sqrt{2M_f Q}$ when the incident energy is close to zero. In our case of $d+d \rightarrow \alpha$, the mass of the final state particle is $M_f = 3732$ MeV and the Q value of the process is $Q = 23.9$ MeV. Therefore in order to recover the momentum conservation, the momentum $-\vec{p}$ must be transferred to the external potential. In our case, numerical value of the momentum transfer is $|\vec{p}| = 422$ MeV/c whose de Broglie wave length is $\lambda = \hbar / |\vec{p}| = 0.56$ fm. So in order to absorb such a large momentum transfer, the size of the source of the external potential must be sharply localized, it must be the order of magnitude as λ . For example, the electron cloud of the atom whose size is order of magnitude of Å cannot do the job to absorb such a large momentum transfer.

5. Comments and discussions

It is interesting that the quantum theory can explain almost all the phenomena of the nuclear reaction in vacuum. So it is natural to try to understand the nuclear cold fusion also in the framework of the quantum theory. Even if we determine to use the quantum theory as the form, we have the freedom to choose the system to apply the theory. In applying the theory, the energy-momentum conservation is the easiest to apply. The most important change of the cold fusion from the ordinary nuclear reaction is that a new reaction $d+d \rightarrow \alpha$ appears, however which violates the momentum conservation, so we need the external potential to absorb the extra momentum of the nuclear system. Another important thing is the change of the open channels of the final state in the d+d reaction. Namely in the nuclear reaction in vacuum, final states of the low energy d+d reaction are t+p and ${}^3\text{He}+n$ with the branching ratio 0.5 and 0.5 respectively. However in the cold fusion, these two channels are closed and the channel ${}^4\text{He}$ opens instead. The simplest way to close the channels is the kinematic one, namely if the d+d reaction starts after they are deeply bounded to the external particle they cannot

energetically transfer to the continuous states of $t + p$ or ${}^3\text{He} + n$. If we remember the binding energy of t and ${}^3\text{He}$ is 8.5MeV. and 7.7MeV. respectively, the condition to close both channels is $2B < 8.5\text{MeV}$, where B is the binding energy of a deuteron. The nucleons can do the strong interaction with each other by exchanging mesons, however the nucleons have additional attributes; the electric charge (Ze) and the magnetic dipole moment ($\vec{\mu} = \kappa_{tot}(e/2m)\vec{\sigma}$), they can make the electromagnetic interaction with external field \vec{E} and \vec{B} respectively. If the sources of the external fields are particles, they are the electrically charged particle (e) and the magnetically charged particle ($*e$) namely the magnetic monopole. Since the fine structure constant is $e^2/\hbar c = 1/137$, the electric interaction is weak by two orders of magnitude compared to the strong interaction, so we can neglect the possibility that external source is the electric charge. However since the magnetic counterpart of the fine structure constant is $*e^2/\hbar c = 137/4$ due to the Dirac's charge quantization condition, the magnetic Coulomb field is super-strong. Therefore the strength of the interaction $-\vec{\mu} \cdot \vec{B}$ is the order of magnitude of the strong interaction because $*ee/\hbar c = 1/2$. In Section 4, using the variational calculation, the energy level of the ground state of the $d-*e$ system is $E = -B = -4.45$ MeV, in which zero point of E is the state where three particles p , n and $*e$ separate infinitely. Since value of B satisfies the condition $2B < 8.5$ MeV, the channels of $t+p$ and ${}^3\text{He}+n$ must be closed. If we remember that in general the variational calculation gives the upper bound of a level, the binding energy B can be a little larger than $B = 4.45$ MeV. However even in such a case, our conclusion that the channels of $t+p$ and ${}^3\text{He}+n$ must close does not change.

If the nuclear cold fusion is the process where two deuterons are trapped by the same magnetic monopoles $*e$ with the orbital size of several fm, the two deuterons come close and fuse to become more stable alpha particle. Because the monopole $*e$ does not have ability to attract the spin-0 particle as explained in Section 1, the α is simply emitted whose kinetic energy is 19.3 MeV, and there remains the fresh magnetic monopole $*e$, and it starts to attract the surrounding deuteron anew. In this way magnetic monopole plays the role as the catalyst of the nuclear cold fusion reaction in the deuteron rich environment. Therefore the magnetic monopole $*e$ is the most important candidate of the source particle of the required external field.

The magnetic monopole was introduced to symmetrize the Maxwell equations with respect to the interchange of the electricity and the magnetism. It is believed that in the process of the Big Bang, the magnetic monopole are created abundantly, however its density becomes dilute as the space expands. Since the magnetic monopole is the rare particle today, magnetic charge density and its current are close to zero: $*\rho \sim 0$ and

* $j \sim 0$, therefore the symmetrical Maxwell equations reduce to the ordinary Maxwell equations. So we can hope to trap the floating magnetic monopole to the place where deuteron density is high. In some model of the hadron, for example in the dyon model due to J. Schwinger [3], hadrons are the magnetically neutral composite state of the magnetic monopoles, namely the hadrons are regarded as the magnetic counterpart of the ordinary (electric) atoms. We can hope to obtain the magnetic monopole by the ionization of the hadrons. The necessary devices to trap, to identify and to slow down will be explained in a separate paper.

References

- [1] T. T. Wu and C. N. Yang, Nucl. Phys. **B107**, 365 (1973)
- [2] T. Sawada, Foundation of Physics, **23**, 291 (1993)
- [3] J. Schwinger, Science, **165**, 757 (1969)

Atomic Nucleus and Neutron — Nuclear Physics Revisited with the Viewpoint of the Cold Fusion Phenomenon

H. Kozima and K. Kaki*

Cold Fusion Research Laboratory,
597-16 Yatsu, Aoi, Shizuoka, 421-1202 Japan
*Shizuoka University, 836 Oya, Suruga, Shizuoka, 422-8529 Japan

Abstract

Nuclear reactions induced by thermal neutrons are reviewed in connection with the new interest caused by the cold fusion phenomenon (CFP) where observed emergence of new elements and new nuclides in solids composed of host elements and hydrogen isotopes (CF-materials) at near room temperature without specific acceleration mechanisms. Nuclear physics developed in the 20th century has mainly investigated isolated nuclei and nucleons with temporal interaction between them and incidentally a nuclear matter with high density neutrons (neutron star matter) in relation to the existence of the neutron star in the universe. On the other hand, the experimental data sets obtained in the CFP as a whole have suggested the realization of a specific state (cf-matter) in CF-materials where occur nuclear reactions similar to those occurring at high energy regions in free space considered in nuclear physics and in neutron star matter. Examining nuclear reactions investigated in nuclear physics, we have noticed several new features of the neutron-nuclear interaction not taken up by now for explanation of extraordinary results obtained in the CFP. One of the interesting features is the nature of the boundary layer between a nucleus and a surrounding neutron matter. Increase of the ratio (n_o/n_i) of neutron densities of the outside neutron matter n_o and that of the inside nucleus n_i makes the energy of the boundary layer lower resulting in the decrease of the barrier height for an alpha-decay and finally in the increase of the decay probability (or the shortening of decay time). Another feature is a possibility of fission of nuclei with medium proton number Z by simultaneous absorption of several neutrons which is applicable to explanation of nuclear transmutations with a large variation of the nucleon number A in the CFP. It is well known in nuclear physics that the fission reactions of nuclei with small Z (e.g. ${}^6_3\text{Li}$ and ${}^{10}_5\text{B}$) and large Z (e.g. ${}^{235}_{92}\text{U}$ and ${}^{239}_{94}\text{Pu}$) are induced or accelerated by absorption of a neutron even if the instability of a compound nucleus with a medium Z (e.g. ${}^{A+1}_{46}\text{Pd}$ ($A = 102 - 110$)) formed by absorption of a neutron is not enough to induce the fission of the nucleus. However, simultaneous absorption of several neutrons by a nucleus suggested in the CFP has given us a hint to investigate a possible fission of medium Z nuclei by this mechanism. These features of nuclei developed but not fully contemplated in nuclear physics are taken up in this paper in relation to the events found in the CFP.

1. Introduction

In the long history of the nuclear physics since the discovery of the nucleus by A. Rutherford in 1911, especially after the discovery of the neutron by Chadwick in 1932, there has been accumulated much knowledge about atomic nuclei of more than one hundred elements. However, the main knowledge is confined fundamentally to nuclei isolated in free space with some exceptions of a nucleus in temporal interaction with another one (and sometimes others). Some works, however, have been done on the nuclei immersed in a neutron sea (neutron star matter) in relation to the neutron star. Recently, there is a rapid progress of investigation of exotic nuclei which is giving an important key to connect the physics of isolated nuclei and that of neutron star matter.

The investigation of the cold fusion phenomenon (CFP), on the other hand, which has started at the end of 1980th revealed some characteristics of nuclei interacting each other in condensed matters containing hydrogen isotopes with high concentration (CF-materials). However, the CFP is now under investigation from various ways of approach without decisive explanation for its mechanism after its discovery about a quarter of a century ago. According to the successful approach to the problem by a phenomenological model [Kozima 1998, 2004, 2006, 2014a, 2014b], this unsolved problem seems to be related closely to the interaction of nuclei in solids (lattice nuclei) with neutrons trapped there. The interaction of a nucleus and neutrons has also been investigated in nuclear physics in relation to the exotic nuclei, synthesis of heavy elements in stars, and neutron star matter. Our knowledge obtained in the investigation of the CFP may give a hint to develop physics of isolated nucleus and the neutron star matter investigated in 20th century into physics of interacting nuclei in transition-metal hydrides and deuterides.

In this paper, we reconsider the nuclear physics developed in the 20th century mainly as the science of nuclei isolated at their initial and final states interacting in between for a short period of time and partially as a science of nuclei immersed in a neutron sea. Our investigation is concentrated in the interaction between nuclei and neutrons in relation to our knowledge obtained in the CFP. In the TNCF model proposed by us and successful to explain various experimental facts in the CFP, there are several premises related to the nature of neutrons in CF-materials and their interaction with nuclei. The interesting knowledge about properties of nuclei useful to understand the premises of the model is investigated in relation to the CFP. Especially, following particular topics among others are picked up here to emphasize the close relation of nuclear physics and the CFP; the two-neutron separation energy is taken up in relation to the possible fission of medium mass number nuclei by absorption of several neutrons to explain

experimental facts observed in the CFP [Kozima 2014b], the boundary layer between a nucleus and the surrounding neutron gas is in relation to the decay-time shortening of alpha-decaying nuclei [Kozima 2006, 2014a], and the extended distribution of neutrons in exotic nuclei is in relation to the neutron band formation in CF-materials by the super-nuclear interaction between neutrons in different lattice nuclei mediated by interstitial protons or deuterons [Kozima 2006, 2008].

2. Fundamental Knowledge of Nuclear Physics

In nuclear physics developed in 20th century, isolated nuclei interacting for a moment between their initial and final isolated states of them have been treated (e.g. [Blatt 1952]) except some exceptional cases such as the neutron star matter (e.g. [Negele 1973]). The nuclei have been assumed being in their isolated (ground) state in the initial and final stages even when they interact in between. Thus, the fundamental properties of nuclei have been disclosed as explained in text books (e.g. [Blatt 1952]). In recent years, however, there has been developed investigation of specific properties of neutrons in new fields showing existence of exotic nuclei with large excesses of neutrons over protons and also in syntheses of heavy elements in stars assisted by neutrons.

In addition to this general features of the nuclear physics developed in the 20th century, it should be emphasized that the statistical nature of nuclear processes is ubiquitous in nuclear physics. One of the most simple and well-known facts is the α -decay of radium nucleus ($^{226}_{88}\text{Ra}$); we can not predict when a specific radium nucleus $^{226}_{88}\text{Ra}$ under investigation will decay to a radon nucleus ($^{222}_{86}\text{Rn}$) by emission of an alpha particle (^4_2He) but we know the constant of the statistical decay process describing the temporal variation of the number of $^{226}_{88}\text{Ra}$ nuclei in a system. This statistical nature of the laws ubiquitous in the world of elementary particles has been put aside in discussions about the reproducibility of measurements of physical quantities where elementary particles participate.

Following regions of energy and categories of nuclei used in nuclear physics [Blatt 1952] are convenient to use in discussion henceforth:

The ranges of energy ε of the incident particle are divided in five regions:

- I. Low energies: $0 < \varepsilon < 1000 \text{ eV}$.
- II. Intermediate energies: $1 \text{ keV} < \varepsilon < 500 \text{ keV}$.
- III. High energies: $0.5 \text{ MeV} < \varepsilon < 10 \text{ MeV}$.
- IV. Very high energies: $10 \text{ MeV} < \varepsilon < 50 \text{ MeV}$.
- V. Ultrahigh energies: $50 \text{ MeV} < \varepsilon < \infty$.

The target nuclei are divided into three categories according to their nucleon (mass)

number A ;

- A. Light nuclei: $1 \leq A \leq 25$.
- B. Intermediate nuclei: $25 \leq A \leq 80$.
- C. Heavy nuclei: $80 \leq A \leq 240$.

In this section, we review the results related to the interaction between a nucleus and a thermal neutron developed in nuclear physics keeping our minds at the possible mechanisms of the CFP.

The light nuclei (group A) must be treated individually. It is almost impossible to apply any general rules describing nuclear reactions in that group. The reactions with intermediate or heavy nuclei are of different character in the five energy regions. The outstanding features of these regions can be characterized as follows: Regions I and II are almost exclusively confined to neutron reactions and the former (low energy) is characterized by the preponderance of resonance capture of neutrons in heavy nuclei.

Only few neutron reactions can take place with neutrons of low or intermediate energy. For intermediate nuclei the most important reactions are elastic scattering and radiative capture.

2.1. Number of stable isotopes of a nucleus ${}^A_Z\text{X}$ with a mass (nucleon) number A and a proton number Z

There are several stable isotopes ${}^A_Z\text{X}$ of an element ${}_Z\text{X}$ (or X) with different values of the nucleon number A (or of the neutron number $N (= A - Z)$) as shown in Fig. 2.1. The number of the stable isotopes, N_I , is a characteristic of the element ${}_Z\text{X}$ reflecting the state of nucleons in the nucleus.

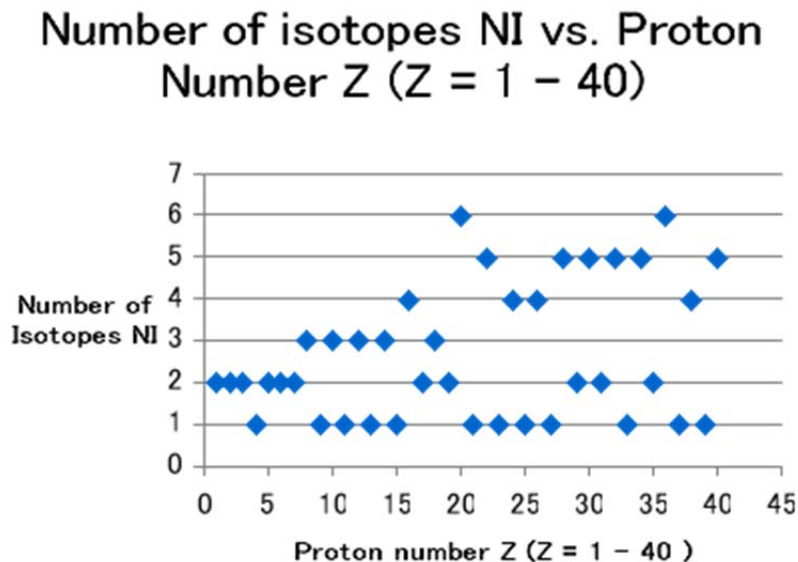
The first noticeable character of Fig. 2.1 is the low value of N_I for the elements with an odd proton number Z . Why? This question of the small number of isotopes for odd proton numbers Z is explained by the nuclear spectroscopy where the stability condition of a nucleus is explained as a function of the symmetry effect, the charge effect and the spin-dependence of nuclear forces [Blatt 1952]. The symmetry effect showing independence of the nuclear force from nucleon species (proton or neutron) plays an essential role in the investigation of fission of nuclei by absorption of neutrons.

The dependence of N_I on Z is a characteristic closely related to the fission of low proton number nuclei by absorption of a thermal neutron.

The nuclei with small Z and very large Z make fission when they absorbed a thermal neutron (or a neutron with zero energy). Examples of the former case are ${}^6_3\text{Li}$ and ${}^{10}_5\text{B}$ and the latter are ${}^{235}_{92}\text{U}$ and ${}^{239}_{94}\text{Pu}$. This fact may be related to the fact that there are a few stable isotopes for elements with small and with very large proton numbers Z as

seen in Figs. 2.1 (a) and (b) and will be discussed in Sec. 2.4.

(a)



(b)

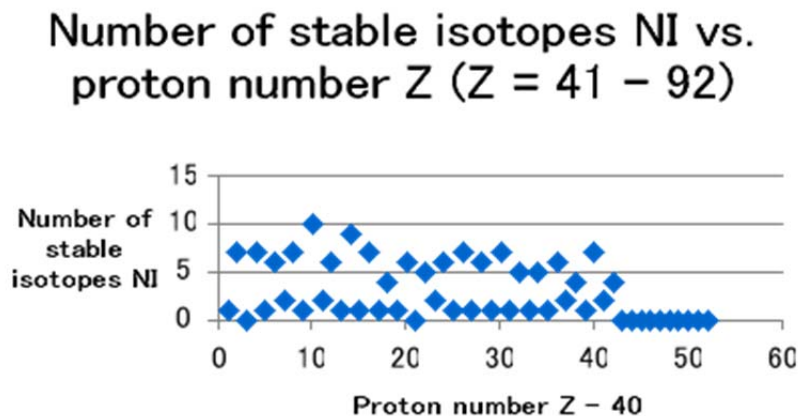


Fig. 2.1. Number of isotopes N_I vs. proton number Z of nucleus A_ZX (a) $Z = 1 - 40$ and (b) $Z = 41 - 92$.

2.2. Binding Energy and Binding Fraction

The total binding energy B of a nucleus A_ZX is defined by a following equation using the mass defect Δ ;

$$B = ZM_p c^2 + (A - Z) M_n c^2 - U \equiv c^2 \Delta, \tag{2.1}$$

$$\Delta \equiv ZM_p + (A - Z)M_n - M_{nucl}$$

where U is the total energy of the nucleus expressed as $U = M_{nucl}c^2$ with the mass of the nucleus M_{nucl} .

The binding fraction f is defined by B as follows:

$$f = B/A. \quad (2.2)$$

In Fig. 2.2, f is plotted as a function of the mass (nucleon) number A for stable nuclei.

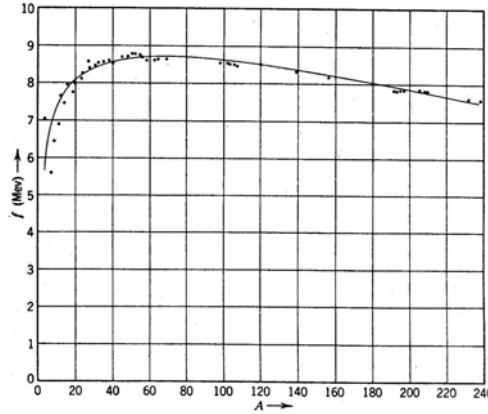


Fig. 2.2. Binding fraction f of stable nuclei as a function of mass number A [Blatt 1952].

The decrease of the binding fraction f at both ends of this figure, at small and large values of A , is another characteristic related to the above mentioned characteristic of the number of isotopes and is also related to the fission of nucleus by absorption of a thermal neutron as discussed in Sec. 2.5. The smooth variation of f in the medium region of A tells us stability of nuclei here against fission by absorption of a single neutron. The experimental evidence of nuclear transmutations suggesting nuclear fission of intermediate nuclei obtained in the CFP should be explained by the fission induced by multi-neutron absorption. Possibility of such reactions will be discussed also in Sec. 2.4 in relation to the two-neutron separation energy observed in exotic nuclei.

2.3. Mass Formula

Nuclear ground state energy E is the negative of the binding energy B and is given by the Weizsaecker semi-empirical formula [Blatt 1952, VI Sec.2];

$$E = -B = -u_v A + 4u_r T_c^2/A + 4u_c Z(Z-1)A^{-1/3} + u_s A^{2/3} \quad (2.3)$$

Here, u_v , u_r , u_c and u_s are the volume energy constant per unit volume of the nucleus, the symmetry energy constant, the Coulomb energy constant, and the surface energy constant per unit area of the surface. We notice here that the surface energy term in the Eq. (2.3) should have close relation with the separation energy discussed in the next

section. The boundary energy of the surface between a nucleus and a surrounding neutron sea, if it exists, gives influence on the alpha decay of the nucleus (cf. Sec. 2.9).

Separation Energy

The separation energy $S_a(X)$ of a particle a from a given nucleus X is defined as the energy necessary to remove to infinity the particle a from the nucleus X in its ground state, leaving the residual nucleus Y ($Y + a = X$) also in its ground state. The values of S for a nucleon separation are close to the value of the binding fraction $f \approx 8$ MeV, i.e. the energy necessary to remove one nucleon is approximately equal to the average binding energy per nucleon. However, there is a general tendency for the separation energy of a nucleon to deviate from the binding fraction in a region of A where the binding fraction varies appreciably with mass number, i.e. in regions of small and large A . This is another indication of instability of nuclide in these regions.

2.3.1. Neutron separation energy S_n .

The neutron separation energy S_n from the nucleus with Z protons and N neutrons is expressed as

$$S_n = B(Z, N) - B(Z, N - 1). \quad (2.4)$$

This expression can be rewritten in the form

$$S_n = f(Z, N) + (A - 1)[f(Z, N) - f(Z, N - 1)]. \quad (2.5)$$

Assuming that $f(Z, N)$ is a smooth function of A by a primary approximation, we obtain from (2.5)

$$S_n \approx f(A) + (A - 1) df/dA. \quad (2.6)$$

For heavy nuclei, the binding fraction decreases with increasing A so that the separation energies are systematically smaller than the binding fractions. For $A > 200$, the separation energies are of the order of 5.5 to 6 MeV, whereas f is of the order of 7.5 MeV.

The dependence of S_n on A in Eq. (2.6) is closely related to fission of heavy nuclei by the absorption of a neutron as discussed in Sec. 2.5.

2.3.2. Alpha separation energy S_α

The same approximation used in the calculation of the neutron separation energy (2.6) is applied to the calculation of the alpha separation energy S_α . The result is

$$S_\alpha \approx 4f(A) - B(\alpha) + 4(A - 4) df/dA \quad (2.7)$$

where $B(\alpha) = 28.23$ MeV is the binding energy of the alpha-particle. Comparing (2.6) with (2.7) we can deduce a conclusion that the alpha separation energies for heavy

nuclei may be expected to be much lower than the neutron or proton separation energies;

$$S_{\alpha} \ll S_n. \quad (\text{for heavy nuclei}) \quad (2.8)$$

Indeed, very many heavy nuclei are unstable against alpha-particle emission from their ground states, i.e., S_{α} is actually negative.

This is a cause of acceleration of alpha decay by thermal neutron absorption feeding about 8 MeV to the nucleus.

2.3.3. Two-neutron separation energy S_{2n}

It is interesting to notice that the two-neutron transfer is considered in exotic nuclei [Zdenek 2006]. The complex situation of the exotic nuclei in the region $Z = 8 - 13$ (O - Al) made researchers to make an attempt to clarify the behaviour of two-neutron separation energies S_{2n} in this region. They observed several stable nuclei in this region while their masses are not known yet. Nevertheless, their S_{2n} values must be positive and therefore the authors have included the "expected" S_{2n} values of the heaviest stable isotopes $^{22}_6\text{C}$, $^{23}_7\text{N}$, $^{29,31}_9\text{F}$ and $^{31,32}_{10}\text{Ne}$ with large circles in Fig. 2.3 [Zdenek 2006, Fig. 8]. The "expected" S_{2n} values for $^{29,31}_9\text{F}$ and $^{31,32}_{10}\text{Ne}$ point out the region where they probably have to be located due to their experimentally found particle stability (positive S_{2n} values). A behavior typical of the filling in shells can be seen from the characteristics corresponding to the ^{20}Ca , ^{19}K and ^{18}Ar isotopes. The two shell closures at $N = 20$ and $N = 28$ are evidenced by the corresponding sharp decrease of the S_{2n} value when two neutrons are added after crossing magic numbers ($N = 20$ and 28). After this sharp drop at the drop point N_{dp} (corresponding to $N_{shell} + 2$) the values of S_{2n} step-down only slowly as the filling of the next shell starts to influence S_{2n} .

The positive energy for the two-neutron separation says, conversely speaking, there occurs exothermic reactions when such an exotic nucleus as $^{50}_{20}\text{Ca}$ absorbs two-neutron from surrounding free neutron sea (cf-matter) becoming unstable for fission. This possibility may be related to the nuclear transmutation observed in the CFP as discussed in the next section and another paper presented at this Conference [Kozima 2014b].

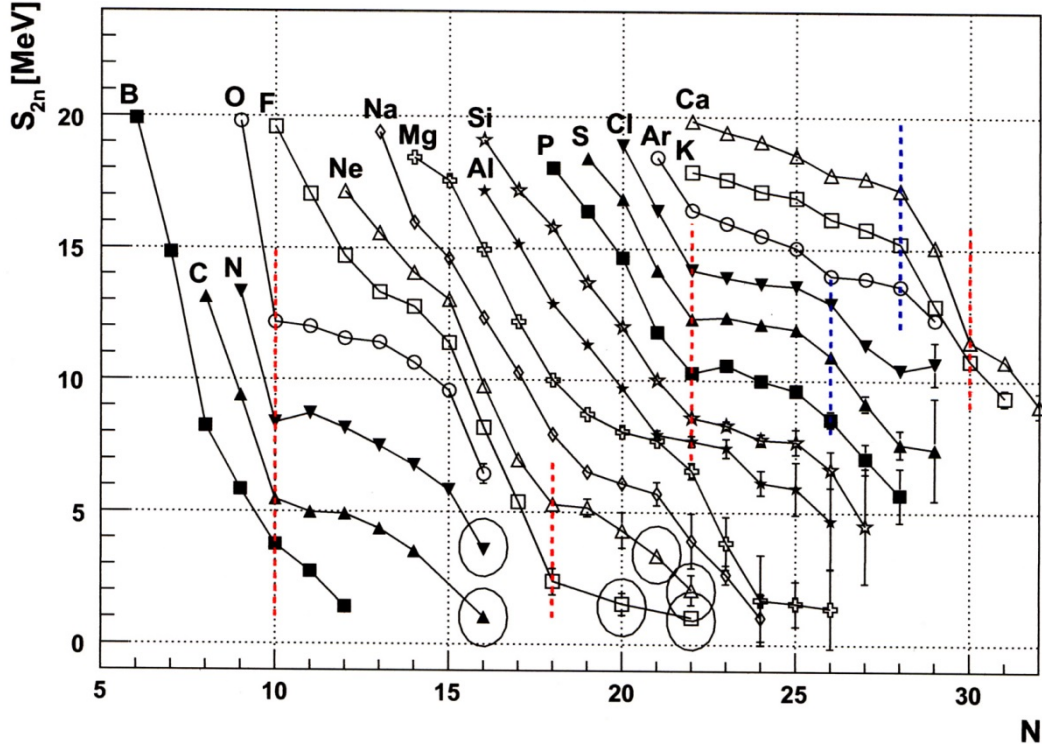


Fig. 2.3. Two-neutron separation energy S_{2n} vs. N – the drop points are visualized by vertical dotted red lines [Zdenek 2006, Fig. 8].

2.4. Fission

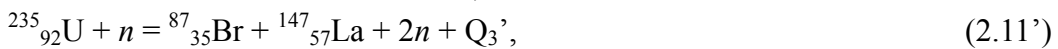
When a nucleus A_ZX absorbs a thermal neutron (or a neutron with zero energy), the resultant compound nucleus ${}^{A+1}_ZX$ makes a fission into several nuclei and nucleons. Experimentally, we know that the fission occurs for nuclei in both regions of a small Z (or nucleon number A), e.g. ${}^6_3\text{Li}$ and ${}^{10}_5\text{B}$, and of a large Z (or nucleon number A), e.g. ${}^{235}_{92}\text{U}$ and ${}^{239}_{94}\text{Pu}$.

Examples of the former are;



where $Q_1 = 4.8$ MeV, $Q_2 = 2.79$ MeV. It is interesting to notice that nuclide ${}^7_3\text{Li}$ and ${}^{11}_5\text{B}$ are stable and their natural abundances are higher than their sisters ${}^6_3\text{Li}$ and ${}^{10}_5\text{B}$ as discussed below.

Examples of the latter are;



where $Q_3 \approx Q_3' \approx Q_4 \approx 200$ MeV. It is known that the process of fission may occur in

about 30 different ways.

Extending our knowledge of fission reactions induced by single neutron absorption, it is possible to conclude that the fission of medium Z nuclei may be capable by simultaneous absorption of several neutrons in terms of a nucleon cluster ${}^A_Z\Delta$. The two-neutron separation of exotic nuclei discussed above in Sec. 2.4.3 may have close relation to this problem. Possibility of this process will be discussed further in Section 2.5.3.

Table 2.1. Natural abundance of lithium and boron [Firestone 1996].

Isotope	${}^6_3\text{Li}$	${}^7_3\text{Li}$	${}^{10}_5\text{B}$	${}^{11}_5\text{B}$
Natural abundance (%)	7.52	92.52	19.92	80.12

Interesting facts should be noticed about the existence of stable isotopes of ${}^7_3\text{Li}$ and ${}^{11}_5\text{B}$ despite the fact that reactions (2.9) and (2.10) occur respectively. The natural isotopic ratios of lithium and boron are listed up in Table 2.1. Furthermore, neutron absorption cross sections σ_γ ($\equiv \sigma(n, \gamma)$) and σ_α ($\equiv \sigma(n, \alpha)$) are shown in Figs. 2.4 and 2.5 for ${}^6_3\text{Li}$ and ${}^{10}_5\text{B}$, respectively.

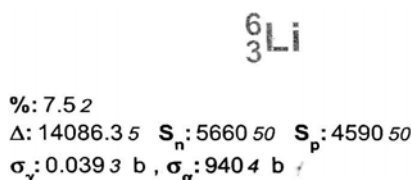


Fig. 2.4. Neutron absorption cross sections σ_γ and σ_α of ${}^6_3\text{Li}$ [Firestone 1996].

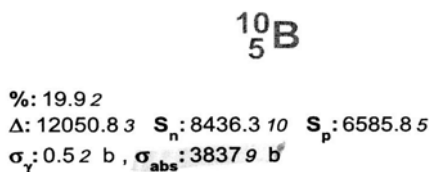


Fig. 2.5. Neutron absorption cross sections σ_γ and σ_α of ${}^{10}_5\text{B}$ [Firestone 1996].

2.4.1. Fission (or α -emission) of light nuclei induced by absorption of a thermal neutron

The fission of the low Z nucleus induced by a thermal neutron is known in nuclear physics for a long time but not taken up seriously due to its limited use in application. A few cases of the use of the reaction is the production of tritium by the reaction (2.7)

with a fairly large absorption cross section 940.3 b of ${}^6_3\text{Li}$ and the detection of neutrons by the reaction (2.8) with a very large absorption cross section (≈ 3837 b) of the ${}^{10}_5\text{B}$.

It is noticed that the reaction products of reactions (2.7) and (2.8) are measured in the CFP;

n - ${}^6_3\text{Li}$ while ${}^7_3\text{Li}$ is stable [Passell 2002].



$$Q = 4.8 \text{ MeV}$$

n - ${}^{10}_5\text{B}$ while ${}^{11}_5\text{B}$ is stable [Passell 1996, 1997].



$$Q = 2.79 \text{ MeV}$$

The energy of about 8 MeV fed to the nucleus by absorption of a thermal neutron makes the compound nucleus unstable resulting in the fission of the nucleus. This process will be explained by the liquid drop model of the nucleus. It is noticed again that the compound nuclei ${}^6_3\text{Li}$ and ${}^{10}_5\text{B}$ in their ground states are stable and do not decay.

Explanation of the reaction ${}^{10}_5\text{B} (n, \alpha) {}^7_3\text{Li}$ [Blatt 1952 (Chap. 9, Sec. 5A)]

When boron is exposed to slow neutrons, the (n, α) reaction on ${}^{10}_5\text{B}$ is the leading process. The Q value of this reaction is 2.78 MeV. This reaction is of special interest because (n, α) reactions with slow neutrons do not occur very frequently. In intermediate and heavy nuclei, neutrons in energy regions I and II introduced above produce elastic scattering or capture (and in some cases fission). The occurrence of (n, α) reactions is usually excluded because of the preventive effect of the Coulomb barrier. In the case of boron, however, the favorable Q value and the low Coulomb barrier (about 2.5 MeV) between ${}^7_3\text{Li}$ and an alpha-particle make it possible that an alpha-particle is emitted by the compound nucleus with considerable probability. Alpha-particle emission competes successfully against neutron capture; the radiative capture cross section is less than 10^{-5} of the (n, α) cross section. The (n, α) reaction on ${}^{10}_5\text{B}$ can be considered a neutron-induced fission of boron into ${}^7_3\text{Li}$ and ${}^4_2\text{He}^4$.

The alpha-particles are emitted into two channels, corresponding to the ground state of ${}^7_3\text{Li}$ ($Q = 2.78$ MeV) and to the first excited state of ${}^7_3\text{Li}$ ($Q = 2.30$ MeV). The emission probabilities for thermal neutron bombardment are in the ratio 93 to 7 in favor of the excited state.

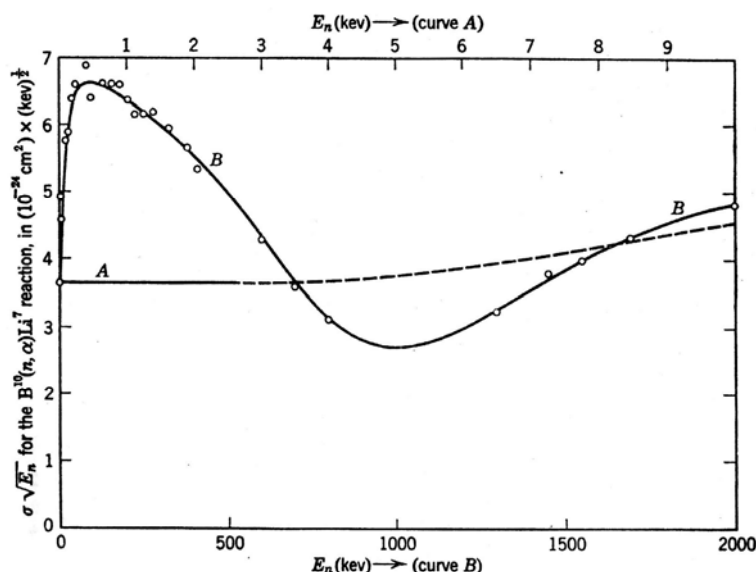


Fig. 2.6. $\sigma(n, \alpha)$ in boron. This plot shows the product $\sigma \sqrt{\epsilon}$ in order to remove the $1/\sqrt{\epsilon}$ factor. There are no reliable measurements between 1 keV and about 10 keV. The dashed part of curve A is a plausible interpolation. The horizontal part below 1 keV ($1/\sqrt{\epsilon}$ dependence) is very well established ([Blatt 1952]).

The observed energy dependence of the (n, α) cross section of $^{10}_5\text{B}$ is shown in Fig. 2.6 [Blatt 1952, IX Fig. 5.1]. For neutron energies up to 10 keV it is almost exactly proportional to $\epsilon^{-1/2}$. The qualitative features of this curve can be understood by the Breit-Wigner formula for the reaction cross section, with a reaction width (in this case the width for the emission of the alpha-particles) of the order of 250 keV and resonance energy of about 100 keV. Such a large width is not unexpected in view of the large level distances in $^{11}_5\text{B}$, and in view of the weakness of the Coulomb barrier for alpha-emission. The $\epsilon^{-1/2}$ dependence of the cross section at energies below 1 keV follows from the Breit-Wigner formula [Blatt 1952, VIII (7.25)]. It is remarkable and very characteristic of this reaction that the $\epsilon^{-1/2}$ dependence extends to energies up to 10^4 eV. This is due to the large reaction width Γ^s_α . Hence the resonance factor is very slowly varying and the main energy dependence comes from the proportionality to $\lambda/2n$.

Similar explanation will be given to the reaction of $^6_3\text{Li}(n, \alpha)^3_1\text{H}$.

2.4.2. Fission of heavy nuclei induced by absorption of a thermal neutron

The heavy nuclei possible to make spontaneous fission can be excited by an absorption-emission process of a thermal neutron to give the excess energy to the outgoing neutron without emitting residual particles which are observed in the reactions in free space.

The most important difference of the fission reactions at low and high values of the proton number is the generation of several (more than one) excess neutrons accompanied to the reaction at the latter case due to the surplus neutrons in the product nuclei. This characteristic has been used for the chain reaction of uranium and plutonium in atomic pile.

Illustrative fission reaction of a heavy nucleus A_ZX by absorption of a thermal neutron is written down as follows:



where $A = A' + A'' + 2$ and $Z = Z' + Z''$. Empirical distributions of A' and A'' in reactions of three nuclei ${}^{233}_{92}\text{U}$, ${}^{235}_{92}\text{U}$ and ${}^{239}_{94}\text{Pu}$ were shown in Fig. 2.7.

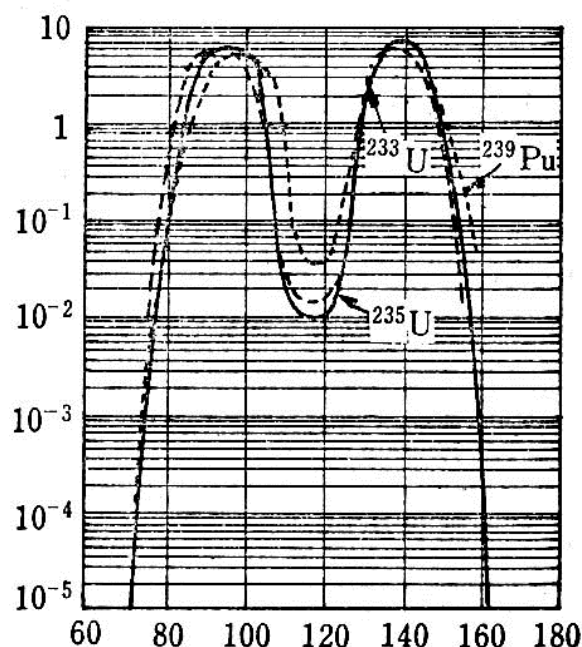


Fig. 2.7. Mass fission yield curves for ${}^{233}\text{U} + n$ (thermal), ${}^{235}\text{U} + n$ (thermal), ${}^{239}\text{Pu} + n$ (thermal). Yields (in log scale) for the three reactions were plotted as functions of mass number A of the product nuclei (e.g. X' and X'' in Eq. (2.5)) [Zukai 1974].

2.4.3. Fission of medium nuclei induced by absorption of a nucleon cluster

For the nuclei with medium numbers of proton numbers, there are few data of nuclear fission by absorption of a thermal neutron in nuclear physics. It is supposed that fission may be ignored in the r -process of heavy element production by absorption of a neutron for the nuclei with medium proton numbers ($Z < 80$) [Qian 2003].

However, the possibility of fission reaction for medium nuclei with proton numbers

between 10 and 80 ($10 < Z < 80$) is not absurd if we notice a situation realized in a CF-material where a nucleus is dipped in a kind of free neutron sea, cf-matter. There is an interesting example of multi-neutron transfer from a nucleus: the two-neutron separation of exotic nuclei discussed in Sec. 2.4.3 [Zdenek 2006, Lu 2013]. In these examples, especially ${}^6\text{He}$ and ${}^8\text{He}$, the single neutron absorption by ${}^4\text{He}$ and ${}^6\text{He}$ is not possible but two-neutron absorption is realistic. This is an interesting case of multi-neutron transfer between a nucleus and the surrounding neutron sea (cf-matter) considered in the CFP. We will discuss possibility of multi-neutron transfer using the knowledge of nuclear physics.

At first, as in the case of alpha decay, the boundary surface energy between the nucleus and the cf-matter decreases with the increase of the density ratio (n_o/n_i). Then the fission barrier will become lower than that in the case of isolated nucleus. This effect is similar to the case of alpha decay. Secondly, we can feed a nucleon cluster ${}^A_Z\Delta$ with Z protons and $N (= A - Z)$ neutrons to a nucleus causing stability of the nucleus lower. As in the case of induced fission of light nuclei, ${}^6_3\text{Li}$ and ${}^{10}_5\text{B}$ by absorption of a neutron, we may have fission reactions of medium nuclei by absorption of a nucleon cluster ${}^A_Z\Delta$ from surrounding free neutron sea of neutron star matter or cf-matter in the CFP. It is easily conceivable that the more the number of neutrons ($A - Z$) in the cluster becomes, the easier the compound nucleus thus formed do fission. The various nuclei generated in the CFP have suggested the nuclear transmutation by fission of medium nuclei which may be explained by the mechanism explained above. Application of this idea to the CFP is given in a paper presented at this Conference [Kozima 2014b].

As in the cases of alpha and beta decays, interest of nuclear physicists has not been in the problems such as decay time shortening and fission barrier lowering caused by a free neutron sea treated in neutron star matter. It is a realistic problem to consider a possibility of absorption of a nucleon cluster in CF-materials where lattice nuclei (nuclei at lattice points) are dipped in a free neutron sea (cf-matter).

2.5. Alpha-Decay and Effect of Neutron Absorption on It

The nuclides with large number of proton are unstable against emission of a part of its components, especially a group of two neutrons and two protons, alpha particle. When the alpha particle formed temporarily in the nucleus pass through the potential barrier (as shown in Fig. 2.8) at the boundary, the nucleus ${}^A_Z\text{X}$ separates into two parts, one the alpha particle ${}^4_2\text{He}$ and another remaining nucleus ${}^{A-4}_{Z-2}\text{X}'$. This reaction is the alpha decay of the nucleus ${}^A_Z\text{X}$.

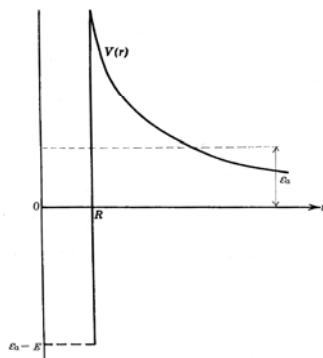


Fig. 2.8. Potential energy of two nuclei as a function of their distance (schematic) (After [Blatt 1952]).

In our qualitative picture, we assume that the alpha-particle starts out from the interior of the compound nucleus with a certain kinetic energy E (measured from the bottom of the interior well). It approaches the barrier at $r = R$ (nuclear radius) from the inside and may or may not pass through the barrier. If it does pass through the barrier, it has the kinetic energy ϵ_α far away (for $r \rightarrow \infty$). In this schematic picture, we can replace the conditions inside the compound nucleus by a constant potential $V(r) = \epsilon_\alpha - E$ for $r \leq R$ (Fig. 2.8).

The decay probability $2n\Gamma_\alpha / h$ of a compound state into the alpha-channel can be written

$$2n\Gamma_\alpha / h = \omega_0 4s_\ell KR / [(KR)^2 + \Delta_\ell^2] \quad (2.14)$$

where ω_0 is the number of attempts per second of the alpha-particle to penetrate through the barrier (surface of the nucleus) into the outside expressed as

$$\omega_0 \approx D/h \quad (2.15)$$

with D the level distance between levels of the same type (angular momentum and parity). The wave number K corresponds to the kinetic energy inside: $K^2 = 2(2\pi)^2 M_\alpha E / h^2$. The magnitudes s_ℓ and Δ_ℓ are defined in terms of the behavior of the wave function in the outside region. For the magnitude of order estimation, we can take only the particle with $\ell = 0$ and then we can put $s_0 = kR$ and $\Delta_0 = 0$ where k is the wave number at infinity ($k^2 = 2(2\pi)^2 M_\alpha \epsilon_\alpha / h^2$).

Then, the expression (2.14) is rewritten as

$$2n\Gamma_\alpha / h = (\omega_0 h / nE) (2\epsilon_\alpha / M_\alpha)^{1/2} \quad (2.16)$$

This formula shows two dependences of the emission probability on the interior quantities ω_0 and E . The largest influence of thermal neutron absorption on the alpha decay of a nucleus may be through the change of E : The increase of internal energy of a nucleus by about 8 MeV makes the nucleus more unstable and the E is decreased. This effect makes the probability (2.16) larger. Another effect of the neutron absorption is

through the change of the level distance D . It seems the level distance becomes larger for the shallower potential well contributing for the increase of emission probability.

It is interesting to notice the relation between the potential barrier for the alpha emission and the surface energy contributing to the equation of mass formula as $u_s A^{2/3}$ in Eq. (2.3) [Blatt 1952, Sec. VI-2]. The value of the coefficient u_s is estimated as $u_s \approx 13.1$ MeV. The total potential energy is lowered in absolute value compared to what we would get if we just considered a sphere of the size of the nucleus inside a very large volume of condensed nuclear matter.

From its origin of the surface energy, the value of u_s surely decreases with increase of the ratio of neutron densities n_o/n_i where n_o is density outside and n_i is that inside the surface of the nucleus when it is immersed in a neutron sea. Though the concept of the surface energy u_s is directly related to single particle behavior of nucleons in the nucleus, it is closely related to the alpha particle behavior in the nucleus and should have positive correlation with the potential barrier for the alpha decay (c.f. Sec. 2.9).

This concept of the potential barrier for the alpha decay is applied to explain the decay time shortening in actinoid hydrides and deuterides and given in a paper presented at this Conference [Kozima 2014a].

2.6. Beta-Decay and Effect of Neutron Absorption by the Parent Nucleus on It

When a nucleus A_ZX contains an excess number of neutrons over that in stable states, neutrons in the nucleus are unstable to be remained there and one of the neutrons experiences nuclear transmutation into a proton emitting an electron and a neutrino. This is the beta decay of the nucleus A_ZX with a mass number A and a proton number Z into another nucleus with the same mass number but with a proton number $Z+1$, ${}^A_{Z+1}X'$.

Half-lives of beta-emitter

The probability of decay into a given momentum interval dp of the electrons is given by a formula [Blatt 1952, VIII (2.13)];

$$P(p) dp = C F(Z,E) p^2 (E_0 - E)^2 dp, \quad (2.17)$$

where C is a constant which in general depends on the specific nuclei involved in the decay, E_0 is the energy available from the nuclear transition, and $F(Z,E)$ is given approximately by

$$F(Z,E) = |\psi_e(0)|^2 / |\psi_e(0)|^2_{\text{free}} = 2n\eta / [1 - \exp(-2n\eta)], \quad (2.18)$$

where $\eta = 2\pi Ze^2/hv$ for electrons, $\eta = -2\pi Ze^2/hv$ for positrons, v being the speed of the particle far away, Z the atomic number of the product (daughter) nucleus.

The half-life t_{-} of the beta-decay is defined by the total probability per unit time that a beta-active nucleus will decay given by integration of $P(p)dp$ over all electron momenta in the beta-spectrum [Blatt 1952 XIII 4 (4.1)]:

$$\beta^{-} \text{ decay probability} = \ln 2 / t_{-} = C f_{-}(Z, E_0), \quad (2.19)$$

where $f_{-}(Z, E_0)$ is the integral

$$f_{-}(Z, E_0) = \int_0^{p_0} F(Z, E) p^2 (E_0 - E)^2 dp. \quad (2.20)$$

The upper limit of integration, $p_0 = (E_0^2 - 1)^{1/2}$, is the maximum momentum in the electron spectrum, expressed by the unit mc .

The integral of (2.20) can be evaluated explicitly for $Z = 0$, i.e., for the case where the Coulomb effect on the spectrum is neglected. The result is

$$f_{-}(0, E_0) = (1/60)(E_0^2 - 1)^{1/2} (2E_0^4 - 9E_0^2 - 8) + (1/4)E_0 \ln[E_0 + (E_0^2 - 1)^{1/2}] \quad (2.21)$$

For very large E_0 , this function is proportional to E_0^5 . However, in the energy region of interest, $1.1 \leq E_0 \leq 10$, f_{-} does not follow an E_0^5 law but is more nearly proportional to $(E_0 - 1)^4$.

For the proton number Z not equal to 0, the integral (2.20) must be evaluated numerically.

Anyway, the beta-decay probability depends strongly on the total energy liberated by the nuclear transition of the beta decay. The absorption of a thermal neutron gives energy of about 8 MeV to the nucleus that may increase E_0 by an amount about this value resulting in the half-life shortening such as that observed in the CFP.

The beta-decays of nuclei after absorption of a neutron have been used to explain synthesis of heavy elements in stars where interaction between a nucleus and a neutron occurs frequently [Burbidge 1957, Qian 2003].

Interesting facts should be noticed about the existence of stable isotopes of ${}^7_3\text{Li}$ and ${}^{11}_5\text{B}$ in the cases (2.9) and (2.10). In relation to this fact, we may have a possibility of the decay time shortening of beta nuclei, e.g. compound nuclei ${}^{40}_{19}\text{K}^*$ generated by reaction $n + {}^{39}_{19}\text{K}$ and ${}^{107}_{46}\text{Pd}^*$ by $n + {}^{106}_{46}\text{Pd}$ [Kozima 2014b, Sec. 6.4.3] while we have no data about it in nuclear data tables. The decay constants of ${}^{40}_{19}\text{K}$ and ${}^{107}_{46}\text{Pd}$ are written as 1.27×10^9 y and 1.3×10^9 y, respectively. These values may be measured at some time later after the reaction without regard to the amounts of the product nuclei ${}^{40}_{20}\text{Ca}$ and ${}^{107}_{47}\text{Ag}$.

2.7. Exotic Nuclei and Neutron Levels at Zero Energy

Existence of exotic nuclei with large imbalance of the proton number Z and the neutron number N ($= A - Z$) in isolated states of a nucleus ${}^A_Z\text{X}$ has attracted strong

attention and has been extensively investigated in recent years. Several interesting features of the nucleus have been revealed by the investigation of the exotic nucleus [Wiedenhover 2007]: 1) Very neutron-rich nuclei are expected to exhibit diffuse surfaces which lead to a reduced spin-orbit coupling and “melting” of the shell structure. 2) Many examples for modification of shell structure in neutron-rich nuclei are known ($N, Z < 50$). 3) What may be the more interesting question: What are the collective excitations of neutron matter? 4) What is the neutron-wavefunction? Pair transfer $^{16}\text{C}(p,t)^{14}\text{C}$ (+ ?). 5) Neutron-rich nuclei have shell structure different from their “ stable ” siblings and their proton-rich mirrors! 6) New collective excitations have to be expected: Neutron-only collectivity?

New information about the behavior of neutrons in exotic nucleus is obtained by a laser probing technique in ^6_2He and ^8_2He isotopes exhibiting an exotic nuclear structure that consists of a tightly bound ^4He -like core with additional neutrons orbiting at a relatively large distance, forming a halo [Lu 2013]. The charge radii of these light halo nuclei have now been determined for the first time independent of nuclear structure models.

Extended distribution of neutrons over that of proton and fairly good coincidence of theory and experiment are shown in Fig. 2.9 for ^6_2He and ^8_2He [Lu 2013].

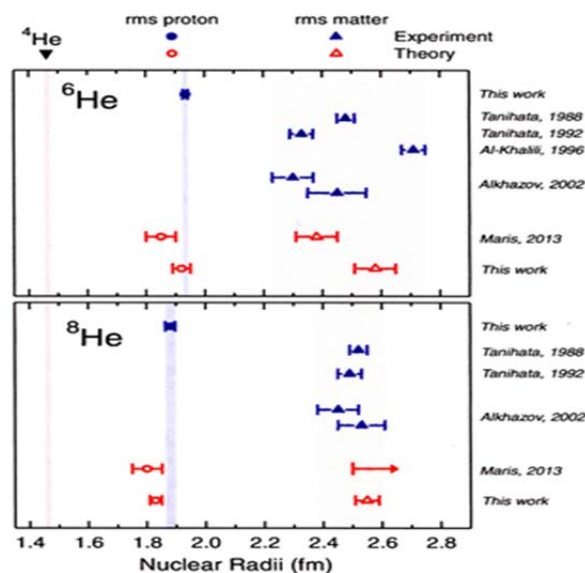


Fig. 2.9. Comparison between experimental and theoretical values of point-proton and matter radii for ^6_2He (top panel) and ^8_2He (bottom panel) [Lu 2013, Fig. 8]

Another data of extended distribution of neutrons are shown in Fig. 2.10 by the theoretical density distributions by the Green’s function Monte Carlo (GFMC) calculation for ^4_2He , ^6_2He and ^8_2He .

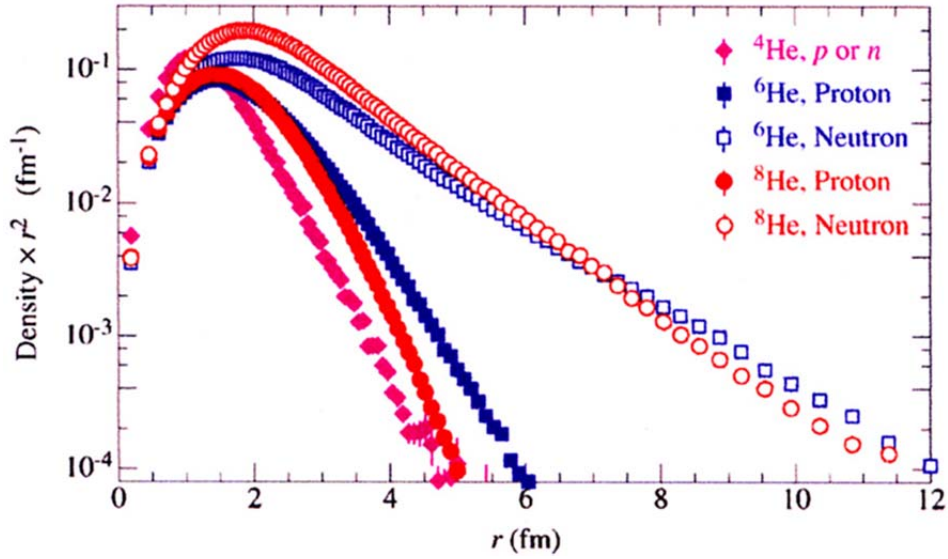


Fig. 2.10. Point-proton and point-neutron densities of the even helium isotopes as extracted from GFMC calculations [Lu 2013, Fig. 10]

Table 2.2. Half-lives, charge and point-proton radii in Li and Be isotopes [Lu 2013, Table VIII].

TABLE VIII. Half-lives, spin parities, experimental charge radii, and experimental and GFMC point-proton radii in the Li and Be isotope chains. Charge radii are based on isotope shift measurements in Li atoms (Nörtershäuser *et al.*, 2011a) and Be⁺ ions (Krieger *et al.*, 2012) and are referenced to the values of the stable ⁶Li and ⁹Be, respectively, which are independently determined from electron scattering experiments. The first uncertainty of the charge radii has been determined from the quoted error of the isotope shift, whereas the second one includes the uncertainty of the reference radius. Radii are in fm. The GFMC values (Pastore *et al.*, 2013) are for the AV18 + IL7 Hamiltonian.

Isotope	$t_{1/2}$	J^π	r_c	Expt	r_p GFMC
⁶ Li	Stable	1 ⁺	2.589(0)(39)	2.45(4)	2.39(1)
⁷ Li	Stable	3/2 ⁻	2.444(4)(43)	2.31(5)	2.28(1)
⁸ Li	840 ms	2 ⁺	2.339(7)(45)	2.20(5)	2.10(1)
⁹ Li	180 ms	3/2 ⁻	2.245(7)(47)	2.11(5)	1.97(1)
¹¹ Li	8.5 ms	3/2 ⁻	2.482(14)(44)	2.38(5)	
⁷ Be	53 d	3/2 ⁻	2.646(10)(16)	2.507(17)	2.47(1)
⁹ Be	Stable	3/2 ⁻	2.519(0)(12)	2.385(13)	2.37(1)
¹⁰ Be	1.5 Myr	0 ⁺	2.361(9)(17)	2.224(18)	2.19(1)
¹¹ Be	14 s	1/2 ⁺	2.466(8)(15)	2.341(16)	
¹² Be	24 ms	0 ⁺	2.503(9)(15)	2.386(16)	

Some numerical data on the characteristics of exotic nuclei with small proton number Z are listed in Table 2.2 [Lu 2013].

The study of neutron-rich nuclei provides an important insight into the nuclear forces that hold these loosely bound systems together. Investigation of the nuclear forces in the

extremely neutron-rich environment different from that in ordinary nuclear matter is in progress with use of this technique.

The experimental data showing the exotic nuclei, however, is limited to nuclei with proton numbers less than 50 at present. It is considered that there are no exotic nuclei for elements with Z larger than 50. One of the recent data is given in Fig. 2.11 and Table 2.3 for $^{32-35}_{12}\text{Mg}$ [Kanungo 2011].

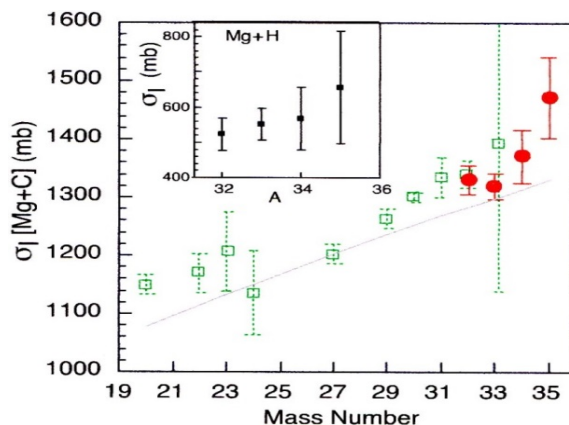


Fig. 2.11. (Color online) The measured interaction cross section for $^{32}_{12}\text{Mg} - ^{35}\text{Mg}$ (circle) on a C target and (inset) on H [derived from a $(\text{CH}_2)_n$ target and C target data]. The open squares show data from Ref. [14] of [Kanungo 2011]. The line (normalized close to stability) shows the monotonic increase expected from an $A^{1/3}$ dependence on radii [Kanungo 2011].

Table 2.3. Measured interaction cross sections and the rms [$R_{\text{rms}}^m(\text{ex})$] matter radii for $^{32-35}_{12}\text{Mg}$ extracted from them are compared with the HF and RMF predictions . [Kanungo 2011]

Isotope	σ_I^C (mb)	σ_I^H (mb)	$R_{\text{rms}}^m(\text{ex})$ (fm)	HF [6] ^a (fm)	RMF [20] (fm)
^{32}Mg	1331(24)	523(47)	3.17 ± 0.11	3.20	3.21
^{33}Mg	1320(23)	552(45)	3.19 ± 0.03	3.23	3.26
^{34}Mg	1372(46)	568(90)	3.23 ± 0.13	3.26	3.33
^{35}Mg	1472(70)	657(160)	3.40 ± 0.24	3.30	3.38

^aThe values are read from [6].

The situation will change largely if the nuclei are dipped in a free neutron sea, or cf-matter in the case of the CFP. It has not been tried theoretically to investigate possible existence of the exotic nuclei at medium mass numbers which we do usually encounter with in the CFP. We can imagine that the interaction of a nucleus and the free neutron sea stabilizes the nucleus in an extremely neutron rich state as a simulation done 40 years ago had shown [Negele 1973].

In a theoretical approach to solve riddles revealed in the CFP, the extended distribution of neutrons in hypothetical exotic nuclei with large excess of neutrons $N \gg Z$ was used to realize a situation in the CF-materials where neutron bands are formed by neutron-neutron interaction mediated by occluded hydrogen isotopes [Kozima 2006 Sec. 3.5.3.1]. The nuclear forces that hold these loosely bound systems together revealed by the investigation of exotic nuclei introduced above may have close relation to the super-nuclear interaction assumed in the TNCF model for the CFP. The CFP is most frequently observed in transition-metal deuterides and hydrides, especially in TiD_x (H_x), NiH_x (D_x), and PdD_x (H_x). Furthermore, these transition-metal nuclei have a common characteristic; existence of excited neutron levels near zero (evaporation levels) in an isolated nucleus, $3s_{1/2}$ in $^{A}_{22}\text{Ti}$ ($A = 46 \sim 50$), $3s_{1/2}$ in $^{A}_{28}\text{Ni}$ ($A = 58 \sim 64$), and $3p_{3/2}$ and $3p_{1/2}$ in $^{A}_{46}\text{Pd}$ ($A = 102 \sim 110$) as shown in Fig. 2.12 [Bohr 1969].

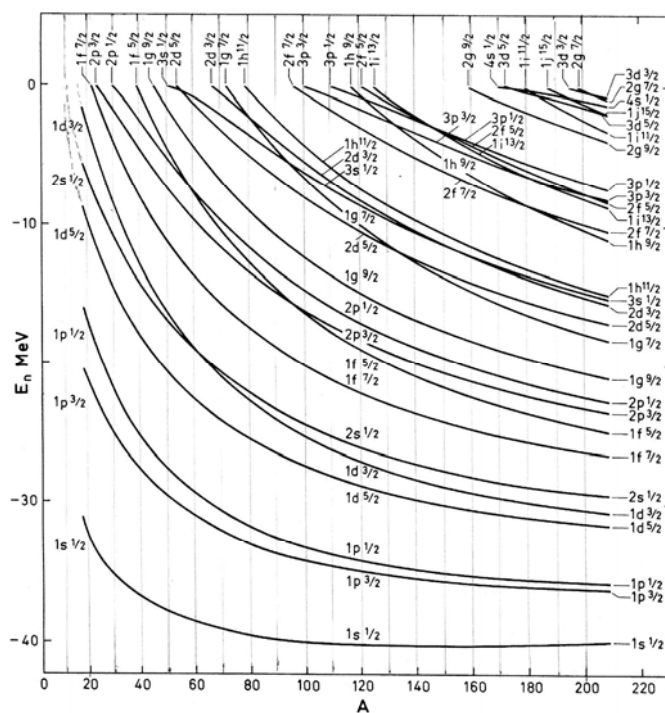


Fig. 2.12. Energies of neutron orbits calculated by C.J. Veje [Bohr 1969].

It is not known the relation of these excited neutron levels and the neutron halo in exotic nuclei at present even if we know that “Neutron-rich nuclei have shell structure different from their “stable” siblings and their proton-rich mirrors!” [Wiedenhover 2007]. From the viewpoint of the CFP, the relation should be very close and these neutron levels are contributing to the stabilization of the exotic nuclei of the corresponding nuclides. Therefore, the investigations on the CFP in PdH_x (D_x), TiD_x (H_x)

and NiH_x (D_x) systems will give information about the neutron halo of exotic nuclei at lattice points, about the wavefunction of protons or deuterons at interstices, and about interaction of lattice nuclei and interstitial protons/deuterons.

2.8. Nuclear Cross Sections near Threshold for Neutrons

A nuclear (α, β) reaction shows certain characteristic properties when the channel energy of one of the partners, ε_α or ε_β , is very near zero [Blatt 1952 (Chap. 8)]. This is the situation we meet in the CFP and we cite the conclusions in this section.

Zero incident energy

Obviously, the reaction cross section $\sigma(\alpha, \beta)$ at $\varepsilon_\alpha \rightarrow 0$ is zero unless the reaction is exoergic: $Q_{\alpha\beta} > 0$. The cross section $\sigma(\alpha, \beta)$ for neutron-induced reactions for neutrons with $\ell = 0$ is given as

$$\sigma(\alpha, \beta) = \text{const. } \varepsilon_\alpha^{-1/2}, \text{ (for } \varepsilon_\alpha \rightarrow 0 \text{ in neutron induced reactions)} \quad (2.13)$$

which is the well-known $1/v$ law.

Zero outgoing energy

The asymptotic properties of $\sigma(\alpha, \beta)$ for $\varepsilon_\beta \rightarrow 0$ can also be stated in a similar form. This case occurs only if the reaction is endoergic: $Q_{\alpha\beta} < 0$. We get the cross section for neutrons with $\ell = 0$ (because most of the neutrons emerging at threshold have $\ell = 0$)

$$\sigma(\alpha, \beta) = \text{const. } \varepsilon_\beta^{1/2} \text{ (for } \varepsilon_\beta \rightarrow 0, \text{ outgoing neutrons)} \quad (2.14)$$

Elastic scattering

The asymptotic property of the elastic scattering for neutrons is given as follows in the same situation for the above cases;

$$\sigma(\alpha, \alpha) = \text{const. (for } \varepsilon_\alpha \rightarrow 0, \text{ elastic scattering of neutrons)} \quad (2.15)$$

The neutron scattering cross section approaches a constant value as the energy approaches zero.

2.9. Neutron Star Matter and Interaction of Nuclei with Neutron

An approach to nuclear phenomena somewhat different from those given above is the treatment of the neutron star matter (e.g. [Baym 1971, Negele 1973]). In this approach, nucleus is considered in its ground state at equilibrium with a free neutron gas outside. This is another valuable investigation to consider the situation appearing in the CFP from our point of view. Details of the relation between the CFP and the neutron

star matter will be given in another paper [Kozima 2014b] presented in this Conference. We give here only interesting results obtained in nuclear physics in close relevance with the CFP. There are two features of the neutron star matter (NSM) related to the CFP; one is the interaction of a free neutron with an alien nucleus and another is the interaction of a nucleon cluster in the neutron star matter and an alien nucleus.

Baym et al. [Baym 1971] investigated the constitution of the ground state of neutron star matter and its equation of state in a regime from a density of $4.3 \times 10^{11} \text{ g/cm}^3$ ($2.8 \times 10^{35} \text{ nucleons/cm}^3$), where free neutrons begin to "drip" out of the nuclei, up to densities $\approx 5 \times 10^{14} \text{ g/cm}^3$ ($3.4 \times 10^{38} \text{ nucleons/cm}^3$), where standard nuclear-matter theory is still reliable in the free neutron regime by a compressible liquid-drop model. They estimated the energy of nuclei in the regime.

The main concern of their investigation is on the transition between the phase with nuclei and the liquid phase at higher densities. They found that nuclei survive in the matter up to a density $\approx 2.4 \times 10^{14} \text{ g/cm}^3$ ($1.6 \times 10^{38} \text{ nucleons/cm}^3$). The transition between the phase with nuclei and the liquid phase at higher densities occurs as follows: The nuclei grow in size until they begin to touch; the remaining inhomogeneity of the density smooths out with increase of the density until it disappears at about $3 \times 10^{14} \text{ g/cm}^3$ ($2 \times 10^{38} \text{ nucleons/cm}^3$) in the first-order transition. It is shown that the uniform liquid is unstable against density fluctuations below this density; the wavelength of the most unstable density fluctuation is close to the limiting lattice constant in the nuclear phase.

On the other hand, Negele et al. [Negele 1973] investigated the same problem using a simple form for the energy density of a nuclear many-body system. They constructed a reliable theory of a nucleon many-body system derived from the two-body nucleon-nucleon interaction. The relevant two-body correlations are incorporated in a two-body effective interaction, and the energy density is expressed as an extremely simple functional of the density and kinetic energy density via the density matrix expansion. Using the self-consistent Hartree-Fock calculation for the nuclear wave functions in a unit cell, they have determined the ground state configuration of matter at sub-nuclear density from lower densities of about 10^7 g/cm^3 ($10^{31} \text{ nucleons/cm}^3$) up to 10^{14} g/cm^3 ($10^{38} \text{ nucleons/cm}^3$) and also have shown the change of nucleus (nuclear cluster) surrounded by a dilute neutron gas: As the baryon density is increased, nucleus become progressively more neutron rich until neutrons eventually escape, yielding a Coulomb lattice of bound neutron and proton clusters (nucleon clusters) surrounded by a dilute neutron gas. The clusters enlarge and the lattice constant decreases with the increasing density.

One of the most striking features of their results is the degree to which the nuclei (nuclear clusters) in the free neutron regime resemble ordinary nuclei; the usual shell model level sequence is maintained throughout the free neutron regime and the interior nuclear density does not deviate significantly from the density of ordinary nuclei.

It should be noticed that the neutron density fluctuations at the low density region diminishes as the number of neutrons becomes sufficiently large and one approaches a statistical regime. In the application of their results to the situation in the CFP, we have a freedom to relax the condition to meet the actuality in the experimental data. The variety of the nuclear products in the CFP may have close relation to this fluctuation in the neutron density.

We may extrapolate the result to the rather lower densities of about 10^{10} nucleons/cm³ in the CFP to obtain the Fig. 2.13.

From this oversimplified figure, we can guess the Z/A ratio is about 0.48 at $\log n_b = 10$ which will be used in the discussion of the CFP in the next papers [Kozima 2014a, 2014b].

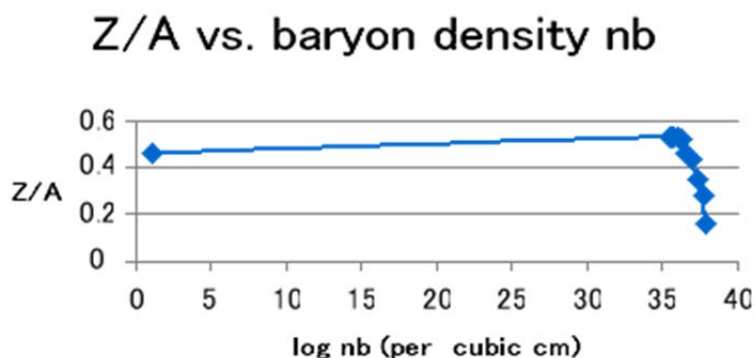


Fig. 2.13. Z/A vs. baryon density n_b (cm⁻³) after Negele et al. [Negele 1973 Table 3]. The data of normal nuclei is taken as $\langle Z/A \rangle = 0.46$ at $\log n_b = 1$.

The investigation of the neutron star matter introduced above [Baym 1971, Negele 1973] has been done assuming a thin free neutron gas in homogeneous space increasing the density of the gas up to about 1.6×10^{38} nucleons/cm³ where the system becomes homogeneous neutron star. There is a serious problem to ask what occurs in the above system when there is a solid lattice of nuclei in addition to the thin free neutron gas. This problem will be a key to investigate the events observed in the CFP and be taken up in our following paper [Kozima 2014b].

In the CFP, the neutron density estimated with various experimental data sets ranges from 10^6 to 10^{13} nucleons/cm³ if we use usually used cross sections for neutron-nuclear interaction in nuclear physics [Kozima 2006]. These values of the neutron density are

rather small compared to the minimum value (10^{31} nucleons/cm³) used by Negele et al. [Negele 1973] in their investigation of the neutron star matter. This point will be discussed in detail in another paper presented at this Conference [Kozima 2014b].

Nuclear Boundary Surface between a Nucleus and the Free Neutron Gas

The boundary surface between a nucleus with a neutron density n_i and the surrounding neutron gas with a neutron density n_o is schematically depicted in Fig. 2.14 after Baym et al. [Baym 1971].

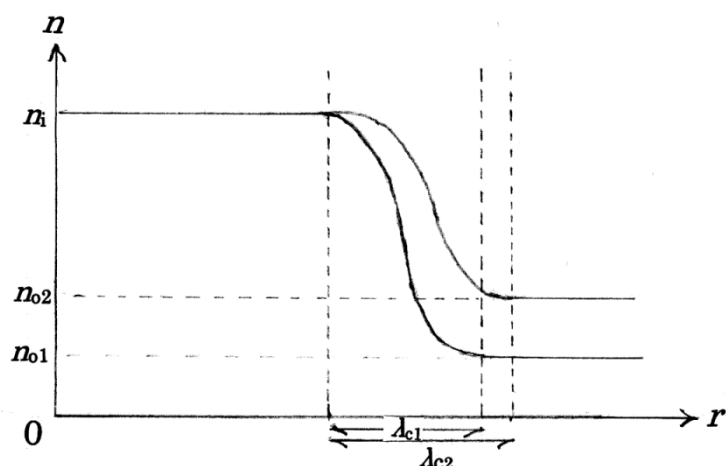


Fig. 2.14. Schematic distribution of neutron density n along an outward straight line r from the center of the nucleus. Two cases for different values of neutron density of the neutron sea n_o are plotted to illustrate the dependence of boundary surface on the density ratio n_o/n_i (cf. Eq. (2.18)).

The total surface energy per unit area of the boundary layer, E_{surf} , is calculated by Thomas-Fermi approximation and is proportional to $(n_i - n_o)^{3/2}$;

$$E_{\text{surf}} = C(n_i - n_o)^{3/2} = Cn_i^{3/2}(1 - n_o/n_i)^{3/2} \quad (2.16)$$

with a constant C [Baym 1971]. The dependence of E_{surf} ($= y$) on the density ratio n_o/n_i ($= x$) is plotted in Fig. 2.15.

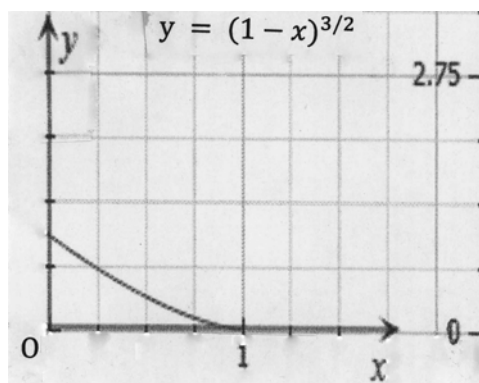


Fig. 2.15. Dependence of the surface energy E_{surf} ($= y$) on the density ratio n_o/n_i ($= x$).

The surface thickness λ_c is directly proportional to k_c^{-1} , with k_c the momentum of the nucleons just at the top of the square-well potential used for the order of magnitude estimation, which is given by the density of neutrons in the nucleus, n_i , and that of the free neutron gas outside the nucleus, n_o [Baym 1971, Eq. (4.27)]

$$k_c^3/1.5 n_i^2 = n_i - n_o. \quad (2.17)$$

Using the ratio $\eta \equiv n_o/n_i$ of neutron densities at outside to that at inside the nucleus, the thickness of the surface λ_c is written as

$$\lambda_c = C (n_i)^{-1/3} (1 - \eta)^{-1/3}, \quad (2.18)$$

where C is a constant of an order of magnitude 1. Dependence of λ_c on η ($\equiv n_o/n_i$) is plotted in Fig. 2.16 as a dependence of y (λ_c) on x ($\eta \equiv x(n_o/n_i)$).

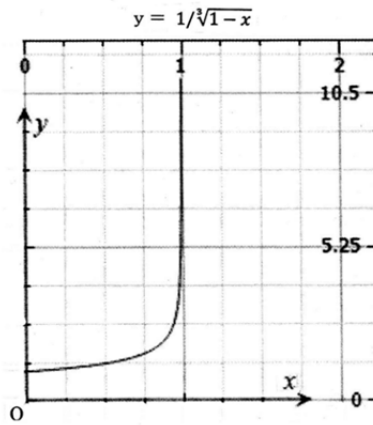


Fig. 2.16. Graph of $y = (1 - x)^{-1/3}$, where $y \equiv \lambda_c$ and $x \equiv n_o/n_i$. The graph of this figure between $x = 0$ and 1 corresponds the thickness λ_c (2.18) of the surface boundary showing a weak dependence of λ_c on the density ratio $\eta \equiv n_o/n_i$ at small η and drastic decrease at $\eta \leq 1$.

The weak dependence of the thickness λ_c on the density ratio $\eta \equiv n_o/n_i$ at small η ($\equiv n_o/n_i$) depicted in Fig. 2.14 suggests that the treatments in the phenomenological approach used in the TNCF model are meaningful if the extrapolation of the method used by Baym et al. [Baym 1971] is applicable to the case of the CFP ($n_o \sim 10^8 - 10^{12} \text{ cm}^{-3}$) where the density ratio η is supposed to be about $10^{10}/10^{38} = 10^{-28}$.

A possible result of the existence of surface boundary with a surface energy E_{surf} and a thickness λ_c between nuclear matter in the nucleus and outside neutron sea may be related to the acceleration of alpha decay (or the decay-time shortening) of a quasi-stable radioactive nuclei by formation of neutron star matter (or the cf-matter in the case of the CFP) surrounding them [Kozima 2014a, 2014b]. The nucleon cluster ${}^4_2\Delta$ formed in the nucleus transmits through the boundary, the probability of which depends

on $\eta \equiv n_o/n_i$, resulting in alpha-decay of the nucleus.

The penetration factor P through a barrier is given by a formula [Schiff 1968];

$$P = \exp[-2 \int_{r_1}^{r_2} \kappa(r) dr], \quad (2.19)$$

$$\kappa(r) = (2m/h) \{2m[V(r) - E]\}^{1/2} \quad (2.20)$$

The integrand of the equation (2.19) or the function (2.20) is proportional to the square root of potential energy looked up by the incident energy. The total energy of the boundary surface between a nucleus and the free neutron gas (2.16) serves to this probability for the penetration of a nucleon cluster ${}^4_2\Delta$ through the boundary.

Existence of the cf-matter outside the nucleus in the CF-material means $n_o \neq 0$. Then, the equation (2.19) suggests us that the decay-time shortenings of uranium [Dash 2003] and thorium [Monti 2005] are explicable in accordance with other events observed in the CFP with the formation of cf-matter in the CF-materials [Kozima 2014a, 2014b].

3. Conclusions

Since the discovery of the neutron by Chadwick in 1932, the neutron played the leading character together with the proton, which was found in 1918, in the physics of the atomic nucleus. Due to the characteristics of the neutron without electric charge and instability in free space with the lifetime of 887 s [Caso 1998], the neutron has been a riddle for 80 years revealing its entity little by little until now. At first, the nuclear force, describing the interaction of a neutron with a proton and another neutron, was the central problem and solved by introduction of a new particle, pion. It was considered the nuclear force is charge independent, i.e. the same between two nucleons, proton or neutron.

Progress in the nuclear physics has revealed a new phase of the neutron; characteristic of neutron-neutron interaction in exotic nuclei [Kanungo 2011, Lu 2013]. There are raised such questions on the properties of the neutron and their effects on the nucleus [Wiedenhöver 2007].

- 1) Very neutron-rich nuclei are expected to exhibit diffuse surfaces which lead to a reduced spin-orbit coupling and “melting” of the shell structure.
- 2) Many examples for modification of shell structure in neutron-rich nuclei are known ($N, Z < 50$).
- 3) What may be the more interesting question: What are the collective excitations of neutron matter?
- 4) What is the neutron-wavefunction? Pair transfer ${}^{16}\text{C}(p,t){}^{14}\text{C} (+\gamma?)$.
- 5) Neutron-rich nuclei have shell structure different from their “stable” siblings and their proton-rich mirrors!

6) New collective excitations have to be expected: Neutron-only collectivity?

In conclusion, we have to say that physics of the neutron is not completed yet but on its way of progress. In addition to these new developments around the neutron in the nuclear physics, we can add another feature of the neutron revealed in the solid-state nuclear physics. The cold fusion phenomenon (CFP), or phenomenon based on solid-state nuclear reactions, asked explanation of curious events solved only by nuclear reactions in room-temperature solid hydrides and deuterides (CF-materials). Due to absence of any acceleration mechanism to excite relevant particles over 1 keV, we have to make a supposition that there is the participation of neutrons in the events observed in the cold fusion phenomenon (CFP). Evidence of the participation of neutrons have been obtained in experiments [Kozima 2006, Sec. 2.2.1.4] and the problem is proposed as how it is possible neutrons to exist and react with other nuclei in the system (CF-materials we named) resulting in various events in the CFP.

A phenomenological model was proposed where existence of neutrons with a density of around 10^{10} cm^{-3} (cf-matter) was assumed a priori in the CF-materials. The existence of such a neutron in CF-materials (mainly transition-metal hydrides and deuterides) has been investigated quantum mechanically using knowledge of metal hydrides obtained in solid state physics and of neutron halos obtained in nuclear physics [Kozima 2006, Sec. 3.7.5].

As has been discussed in our books and papers [Kozima 2004, 2006, 2008, 2013], the CFP is explained qualitatively and sometimes semi-quantitatively by our phenomenological model (the TNCF model). The model has been investigated quantum mechanically and the premises of the TNCF model have principally been explained by the formation of neutron bands due to the super-nuclear interaction, interaction between lattice nuclei mediated by interstitial hydrogen isotopes. The novel knowledge of exotic nuclei gives a strong support for the realization of the super-nuclear interaction due to the extended distribution of neutron wavefunctions in them. If the cf-matter is realized by the formation of neutron bands, then the elaborate works on the neutron star matter give us a tool to explain various nuclear reactions necessary to explain experimental facts such as the decay-time shortening and nuclear fission of medium mass-number nuclei in CF-materials at near room temperature.

If the scenario depicted in the investigation of the cf-matter in the CF-materials be realistic, we may have a new development of neutron physics in solids with a high density of hydrogen isotopes (CF-materials). By the way, the existence of the cf-matter should be related with new phenomena, a part of which may be the CFP, in physics of metal hydrides. The physics of metal hydrides has been investigated for more than 100

years and is a central theme in relation to the hydrogen storage for applications. The CFP is a phenomenon closely related to the developing fields of nuclear physics and also solid state physics and gives us a perspective interesting enough to explore new physics of neutrons in solids not known until now.

Acknowledgement

The authors would like to express their thanks to Professor T. Miyakawa of National Defense Academy of Japan for his valuable discussions throughout this work.

References

- [Baym 1971] G. Baym, H.A. Bethe and C.J. Pethick, "Neutron Star Matter," *Nuclear Phys.* **A175**, 225 – 271 (1971).
- [Blatt 1952] J.M. Blatt and V.F. Weisskopf, *Theoretical Nuclear Physics*, John Wiley and sons, New York, 1952. ISBN-10: 0-471-08019-5
- [Bohr 1969] A. Bohr and B.R. Mottelson, *Nuclear Structure I*, Benjamin, New York, 1969.
- [Burbidge 1957] E.M. Burbidge, G.R. Burbidge, W.A. Fowler and F. Hoyle, "Synthesis of the Elements in Stars," *Rev. Mod. Phys.*, **29**, pp. 547 – 656 (1957).
- [Caso 1998] C. Caso et al., "Review of Particle Physics," *Eur. Phys. J.*, **C3**, 1 (1998).
- [Firestone 1996] R.B. Firestone, *Table of Isotopes*, CD-ROM 8th edition, v. 1.0, Wiley-Interscience, 1996.
- [Kanungo 2011] R. Kanungo, A. Prochazka, W. Horiuchi et al., "Matter Radii of $^{32-35}\text{Mg}$," *Phys. Rev.* **C83**, 021302-1 – 4 (2011).
- [Kozima 1998] H. Kozima, *Discovery of the Cold Fusion Phenomenon*, Ohtake Shuppan, Tokyo, Japan, 1998. ISBN 4-87186-044-2.
- [Kozima 2004] H. Kozima, "Quantum Physics of Cold Fusion Phenomenon," *Developments in Quantum Physics Researches – 2004*, pp. 167 – 196, Ed. V. Krasnoholovets, Nova Science Publishers, Inc., New York, 2004. ISBN 1-59454-003-9
- [Kozima 2006] H. Kozima, *The Science of the Cold Fusion Phenomenon*, Elsevier Science, 2006. ISBN-10: 0-08-045110-1.
- [Kozima 2008] H. Kozima, "Physics of the Cold Fusion Phenomenon," *Proc. ICCF13* (June 25 – July 1, 2007, Dagomys, Sochi, Russia) pp. 690 – 703 (2008).
- [Kozima 2013] H. Kozima, "Cold Fusion Phenomenon in Open, Nonequilibrium, Multi-component Systems – Self-organization of Optimum Structure," *Proc. JCF13* **13-19**, pp. 134 - 157 (2013).

- [Kozima 2014a] H. Kozima, “Nuclear Transmutation in Actinoid Hydrides and Deuterides,” *Proc. JCF14*, **14-15**, pp. xx - yy (2014) (to be published) and posted at JCF website: <http://jcfirs.org/file/jcf14-proceedings.pdf>.
And also *Reports of CFRL* 14-2, 1 – 10 (March, 2014) that is posted at CFRL website:; <http://www.geocities.jp/hjrfq930/Papers/paperr/paperr.html>
- [Kozima 2014b] H. Kozima, “Nuclear Transmutations (NTs) in Cold Fusion Phenomenon (CFP) and Nuclear Physics,” *Proc. JCF14* **14-15**, pp. xx – yy (2014) which is posted at JCF website: <http://jcfirs.org/file/jcf14-proceedings.pdf>.
This paper is also published as *Reports of CFRL* **14-3**, pp. 1 – 28 (2014) which is posted at CFRL website: <http://www.geocities.jp/hjrfq930/Papers/paperr/paperr.html>
- [Lu 2013] Z.-T. Lu, P. Mueller, G.W. F. Drake, W. Nörtershäuser, S.C. Pieper and Z.-C. Yan, “Colloquium: Laser probing of neutron-rich nuclei in light atoms,” *Rev. Mod. Phys.*, **85**, 1383 – 1400 (2013).
- [Negele 1973] J.W. Negele and D. Vautherin, “Neutron Star Matter at Sub-nuclear Densities,” *Nuclear Physics*, **A207**, 298 - 320 (1973).
- [Passell 1996] T.O. Passell, “Search for Nuclear Reaction Products in Heat-Producing Palladium,” *Proc. ICCF6*, pp. 282 – 290 (1996).
- [Passell 1997] T.O. Passell, “Search for Nuclear Reaction Products in Heat-Producing Pd,” *Proc. ICCF7*, pp. 309 – 313 (1998).
- [Passell 2002] T.O. Passell, “Evidence for Lithium-6 Depletion in Pd Exposed to Gaseous Deuterium and Hydrogen,” *Proc. ICCF9*, pp. 299 – 304 (2002). ISBN 7-302-06489-X/O·292.
- [Qian 2003] Y.-Z. Qian, “The Origin of the Heavy Elements: Recent Progress in the Understanding of the *r*-Process,” *Prog. Part. Nucl. Phys.*, **50**, 153 – 199 (2003).
- [Schiff 1968] L.I. Schiff, *Quantum Mechanics*, McGraw-Hill Kogakusha, 1968. ISBN 0-07-085643-5
- [Wiedenhöver 2007] Ingo Wiedenhöver, “Exotic Nuclei” Lecture note given at National Nuclear Physics Summer School, 7/16/2007 Tallahassee, Florida.
- [Zdenek 2006] Zdenek Dlouhy, “Structure and Properties of Exotic Nuclei using Radioactive Nuclear Beams,” (doctoral theses) Praha, Listopad, 2006.
- [Zukai 1974] Zukai Genshiryoku Yogo Ziten (1974). (Illustrated Dictionary of Atomic Power Terms, in Japanese) Nikkan Kogyo Shinbunsha, Tokyo, 1974. NDC 429.03

Nuclear Transmutation in Actinoid Hydrides and Deuterides

Hideo Kozima

Cold Fusion Research Laboratory
597-16, Yatsu, Aoi, Shizuoka, 421-1202 Japan

Abstract

Nuclear transmutations observed in the cold fusion phenomenon (CFP) have attracted attention from various points of view. Our sense of wonder at events in the CFP is based on the common sense that phenomena occurring in a nucleus are isolated from the drama played in the world of atoms outside of the nucleus without few exceptional cases such as the Knight shift in NMR, the change of K-capture probability by environment and the Moessbauer effect where they show weak connections between two world.

As have been revealed by many experimental data sets observed in the CFP, there are various events showing occurrence of nuclear reactions in materials composed of host elements and hydrogen isotopes (protium or/and deuterium) with a comparable ratio to the host (cf-materials) even when there is no specific acceleration mechanism. In the events of nuclear reactions observed in the CFP, one of the most interesting is the nuclear transmutations of nuclei with several decay channels (including radioactive nuclei such as $^{235}_{92}\text{U}$ and $^{231}_{90}\text{Th}$) in free space. To explain these transmutations it was necessary to assume a gigantic shortening of the decay time in cf-materials compared to that observed in free space.

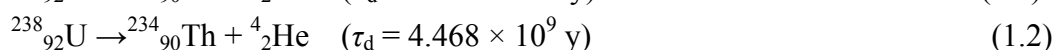
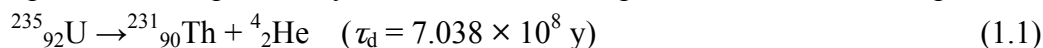
We have proposed a model (TNCF model) to give a successful unified explanation for various events in the CFP from excess energy generation, emissions of charged particles and neutron, and to nuclear transmutations. The experimental data sets on the nuclear transmutation of radioactive nuclei obtained in the CFP include many details of the measurements and give us materials for their analysis if we can use them properly. In this paper, we used the knowledge of nuclear physics on the interaction of a nucleus and neutron sea (corresponding to the cf-matter in our model) to give a unified and consistent explanation of the decay-time shortening observed in uranium (and thorium) hydrides and deuterides prepared by the implantation in a glow discharge or by the absorption in electrolyses.

1. Introduction – Spontaneous and Induced Decay of Actinoids

In the history of nuclear physics, we have noticed the existence of nuclei which decay spontaneously. The actinoids are the typical nuclides which show this characteristic. They also show induced decays absorbing a neutron. These characteristics are written down as reaction formulae as follows;

1.1 Spontaneous disintegrations

(1) Spontaneous Alpha Decay of Actinoids – Examples with half-lives τ_d in parentheses.

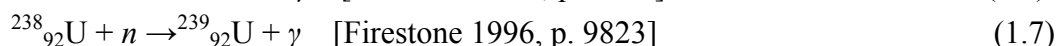


(2) Spontaneous fission – Examples



1.2 Nuclear transmutations induced by neutron absorption

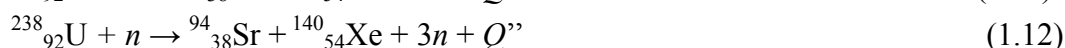
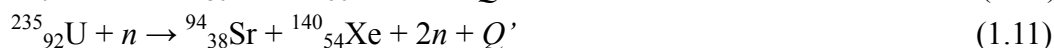
(1) Gamma emission after absorption of a neutron – Examples



(2) Alpha decay induced by neutron absorption – Examples



(3) Fission induced by neutron absorption - Examples



We have proposed a model (TNCF model) to give a successful unified explanation for various events in the cold fusion phenomenon (CFP) from excess energy generation, emissions of charged particles and neutron, and to nuclear transmutations investigated after 1989. It is a characteristic of the CFP that it has been observed only in specific solids (cf-materials) composed of lattice nuclei and hydrogen isotopes with comparable number densities to each other.

The original assumption of the existence of the “trapped neutron” in the TNCF model proposed in 1993 [Kozima 1994] has been replaced by formation of a new state (cf-matter) composed of quasi-free neutrons and a little protons and electrons to neutralize it as a whole in the recent quantal investigation of premises of the TNCF model [Kozima 2006 (Sec. 3.7.5), 2008c].

In the investigation of the nuclear reactions of actinoids in cf-materials, we have to

consider nuclear reactions induced by spontaneous mechanisms as listed above in 1.1 and also those induced by absorption of neutrons as listed in 1.2. Furthermore, as we have discussed several times (cf. [Kozima 2006, 2014b]), it is necessary to consider not only reactions induced by absorption of a neutron (as in 1.2) but also those induced by absorption of a nucleon cluster ${}^A_Z\Delta$ composed of Z protons and $(A - Z)$ neutrons. In this paper, however, we confine our investigation only assuming the cases induced by the absorption of a single neutron for simplicity.

Then, we have to investigate the disintegrations of actinoid nuclei in their hydrides and deuterides as observed in the experiments as shown in Section 2 taking possible reactions (1.1) – (1.12) into our consideration as discussed in Section 3.

2. Experimental Data Sets of CFP in Actinoids Hydrides and Deuterides

There are several works on the emission of neutrons and charged particles in actinoid hydrides and deuterides. In this section, we introduce several data sets from the works performed in the history of the CF research to investigate them from our point of view in the next section.

2.1. Neutron Emission in UD_3 and TiD_x

Neutron emissions in uranium deuteride (UD_3) and deuterium-loaded titanium (TiD_x) samples were measured with a detector of high detection efficiency [Jiang 2012]. The efficiency of detection was calibrated by ${}^{252}Cf$ neutron source to be greater than 50%.

The “cascade bursts” of neutrons were measured several times only for UD_3 and TiD_x ($x = 1$ and 1.4) samples but not for control samples of uranium oxide and deuterium-unloaded Ti foils. The authors suggested that the cascade neutron bursts might originate in the nuclear reactions occurring in the surface region of samples with widths of a micro-nanometer size.

This result suggests that the neutron emission in both UD_3 and TiD_x may be induced by the same cause. We have proposed a mechanism where the cf-matter is responsible for nuclear reactions in the CFP based on the TNCF model [Kozima 2011a]. The suggestion of surface nature of the emission of neutrons by Jiang et al. is consistent with our explanation of neutron-nuclear interactions in localized regions at surface where the cf-matter is apt to be formed [Kozima 2011b].

Uranium nucleus fissions spontaneously into two nuclei and a neutron (or neutrons). The observation of neutrons emitted from UD_3 and TiD_x by Jiang et al. suggests that the emission of neutrons in uranium deuteride is fundamentally governed by the CFP in

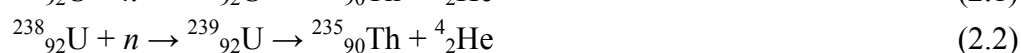
cf-materials. So, we may be able to investigate the emission of charged particles in actinoid hydrides and deuterides using our model which has been successfully applied to various events in the CFP.

2.2. Radiations of Actinoid Hydrides and Deuterides

J. Dash and his collaborators in Portland State University, Oregon, USA have extensively studied characteristic changes of the decay patterns of uranium and thorium in their compounds with protium (hydrogen) and deuterium [Goddard 2000, Dash 2003a, 2003b, 2005]. The compounds were prepared by the methods using electrolysis and glow discharge.

In the case of glow discharge [Dash 2003a, 2003b], they confirmed using gamma ray spectroscopy that there are thorium isotopes identified as $^{231}_{90}\text{Th}$ and $^{234}_{90}\text{Th}$ which are expected to be generated from $^{235}_{92}\text{U}$ and $^{238}_{92}\text{U}$ by alpha decays (1.1) and (1.2), respectively. This is a typical example of the “decay-time shortening” for the reactions by the formation of cf-matter as discussed in other papers presented at this Conference [Kozima 2014a (Sec. 2.10), 2014b (Sec. 6.5.3)]. The decay-time shortening, i.e. a drastic decrease of the decay constant of an unstable nucleus in cf-materials from that in free space, of alpha disintegration is expected when there is formed the neutron star matter (or cf-matter in the case of the CFP) surrounding the quasi-stable nuclei which disintegrates by alpha emission.

However, there remains some ambiguity if the gamma spectra used to determine the thorium isotopes are not identified as due to $^{231}_{90}\text{Th}$ and $^{234}_{90}\text{Th}$. If they are due to $^{232}_{90}\text{Th}$ and $^{235}_{90}\text{Th}$, the observed spectra are consistent with the mechanism of alpha decay after single neutron absorption of $^{238}_{92}\text{U}$ and $^{235}_{92}\text{U}$, respectively.



Therefore, we have to be cautious to investigate changes of the decay characteristic of actinoids in cf-materials which depend various variables in the sample.

2.2.1. Co-deposition of U_3O_8 and H on Ni Cathode with Acidic Electrolyte and Pt Anode

Co-deposition of U_3O_8 and H on Ni cathodes with an acidic electrolyte and a Pt anode was performed [Goddard 2000]. In this case, they measured increase of the radiation from 2900 (control) to 3700 counts (co-deposited sample) measured by a G-M counter for the same amount of U_3O_8 . There are observed existence of Cs, Fe and Ni on the nickel cathode and also topography change of the surface in the form of donut-like

eruptions as shown in Fig. 2.1.

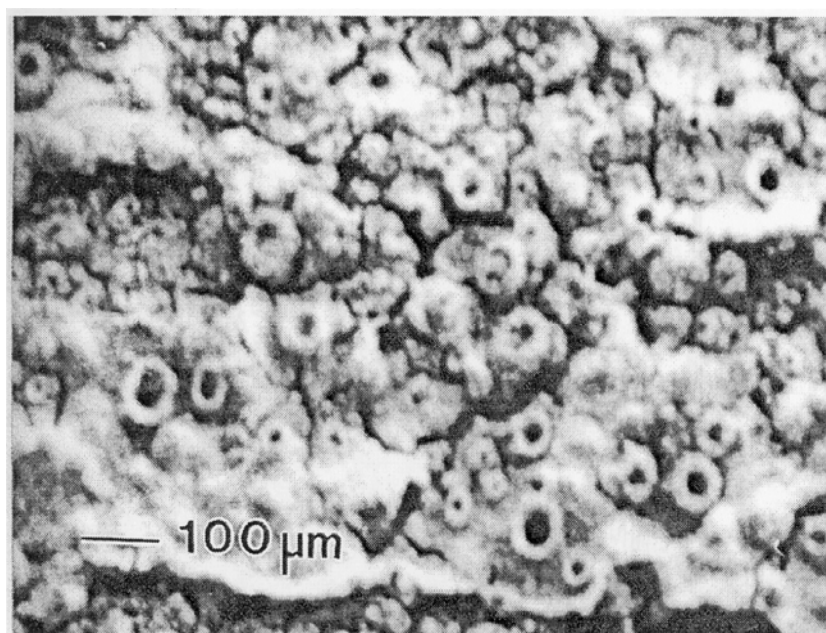


Fig. 2.1. Typical micrograph of U_3O_8 electroplated on a nickel cathode after experiment.

Radiation

The radiation emitted by the electroplated U_3O_8 (A) was compared with radiation emitted by unelectrolyzed U_3O_8 (B).

(A) Initially produced about 2900 counts/3 minutes (4-17-00). This increased spodically in steps to ~ 3700 counts/(3 minutes) (5-11-00) and stayed there until 6-8-00 when ended the measurements.

(B) Emitted ~ 1250 counts/(3 minutes) remaining almost constant over the entire period of measurements.

Gamma spectroscopy

The net integral of 86 peaks of measured γ -radiation from a 10 mg sample in 25 hours gave 53,000 counts (A) and 31,000 counts (B).

Surface topography

Observation by a SEM (scanning electron microscope) showed that Donut-like features appeared showing voids surrounded by raised circular rims (Fig. 2.1).

New elements

Cesium (Cs), iron (Fe) and nickel (Ni) (and possibly fermium (Fm)) are detected by EDS (energy dispersive spectrometer).

2.2.2. Implantation of Hydrogen Isotopes into Uranium Cathode by

Glow Discharge

Uranium foils were attached to the cathode made of stainless steel in a glow discharge apparatus. Either hydrogen or deuterium ions was implanted to uranium by the glow discharge at a voltage of about 500 V [Dash 2003a].

There are four samples exposed to plasmas; 1) H1 (to H₂ plasma for 43 hours), 2) H2 (to H₂ plasma for 18 hours), 3) D1 (D₂ plasma for 100 hours), 4) D2 (D₂ plasma for 500 hours).

Alpha, beta and gamma measurements were made on samples exposed to the plasmas and compared with the results on a control uranium foil without exposure. An example of measurements is shown in Fig. 2.2 for the gamma radiation measured on August and November of 2001 and April of 2002 [Dash 2003a (Fig. 4)]. Here, we notice a positive correlation between the implantation time and the intensity of the gamma radiation of uranium.

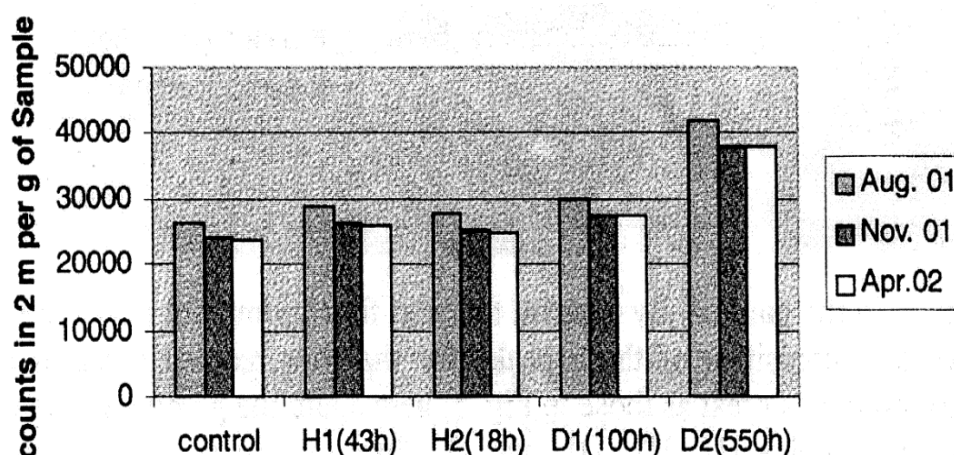


Fig. 2.2. Gamma radiation from uranium samples after exposure to hydrogen isotope plasmas [Dash 2003a].

Samples were examined with a SEM and analyzed with an EDS.

- 1) **Approximate counts of alpha-, beta- and gamma-radiations per gram of uranium** (after [Dash 2003a, Figs. 2, 3 and 4]).

Table 2.1. Counts of alpha-, beta- and gamma radiations per gram of uranium after exposure to hydrogen isotope plasmas.

	Control	H1	H2	D1	D2
α (in 2 hours $\times 10^{-4}$)	2.3	6.0	5.9	6.0	11.4
β (in 2 min. $\times 10^{-5}$)	1.70	1.85	1.80	1.95	2.75
(in 2 min. $\times 10^{-4}$)	2.50	2.67	2.55	2.72	3.92

In this table, we notice the strong correlation of the increases of the α -, β - and γ -radiations and the implantation times of deuterium D₂ in D1 and D2 samples.

2) Approximate net counts of 98.5 keV characteristic X-ray of $^{238}_{92}\text{U}$ per gram of sample (after [Dash 2003a, Fig. 6])

Table 2.2. Counts of 98.5 keV characteristic X-ray of $^{238}_{92}\text{U}$ per gram of sample after exposure to hydrogen isotope plasmas.

	Control	H1	H2	D1	D2
X (in 24 hours $\times 10^{-4}$)	3.1	2.9	3.1	2.75	2.2

3) Approximate net counts of 92.4 keV characteristic gamma ray of $^{234}_{90}\text{Th}$ per gram of sample (after [Dash 2003a, Fig. 5])

Table 2.3. Counts of 92.4 keV characteristic X-ray of $^{234}_{90}\text{Th}$ per gram of sample after exposure to hydrogen isotope plasmas.

	Control	H1	H2	D1	D2
γ (in 2 min. $\times 10^{-4}$)	1.90	2.30	2.35	2.60	2.75

Decrease of $^{238}_{92}\text{U}$ in Table 2.2 and increase of $^{234}_{90}\text{Th}$ in Table 2.3 corresponding to the implantation time may be explained by the reaction (1.2).

4) Approximate net counts of 186 keV characteristic gamma ray of $^{235}_{92}\text{U}$ per gram of sample (after [Dash 2003a, Fig. 7])

Table 2.4. Counts of 186 keV characteristic gamma ray of $^{235}_{92}\text{U}$ per gram of sample after exposure to hydrogen isotope plasmas.

	Control	H1	H2	D1	D2
γ (in 24 hours $\times 10^{-4}$)	3.74	3.86	3.86	3.86	4.14

Increase of $^{235}_{92}\text{U}$ corresponding to the implantation time in D1 and D2 samples will be discussed in Sec. 3.3.1.

The confirmation of $^{234}_{90}\text{Th}$ [Dash 2003a] seems credible and the reaction (1.2) is reliable for the case of glow discharge experiment and the decay-time shortening is induced by the mechanism in terms of the cf-matter as discussed in our papers [Kozima 2014a, 2014b].

The surface topography observed by SEM showed pit structure after the electrolysis as shown in Fig. 2.3.

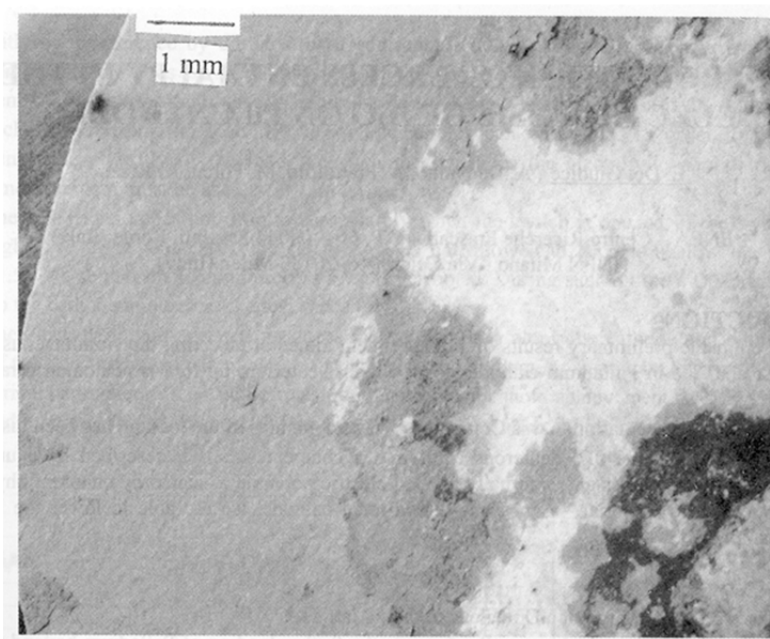


Fig. 2.3. SEM photograph of uranium sample D2 after exposure to deuterium plasma for about 550 hours. The relatively smooth rim on the left was protected from exposure to the plasma by a molybdenum nut which fastened the sample against the cathode.

2.2.3. Hydrogen Loading of Uranium by Electrolysis

Natural uranium foil of 0.18 mm thick and purity 99.98% was used as a cathode in electrolysis with 0.83 M and 0.74 M H_2SO_4 electrolyte in H_2O [Dash 2005]. Anode was platinum plate. The alpha, beta and gamma specific radioactivity were measured after the hydrogen loading and compared with the control. Gamma ray spectroscopy was also performed by EDS on the samples.

For two series of experiments, they obtained similar results to that obtained in discharge experiments (cf. Sec. 2.2.2): increases of $^{234}_{90}\text{Th}$ and $^{235}_{92}\text{U}$ characteristic gamma spectra and decrease of $K_{\alpha 1}$ characteristic X-ray peak of $^{238}_{92}\text{U}$.

The surface concentration (within a depth of about 1 μm) was determined by EDS. Increase of thorium and decrease of carbon was observed. The former is consistent with the spectroscopic measurement given above. The decrease of carbon in the surface

region is not explained at present.

3. Analysis of Experimental Data Sets

The cold fusion phenomenon (CFP) has been observed in solids composed of host elements and hydrogen isotopes with almost equal number densities of both components (cf-materials). Typical examples of the cf-materials are PdD_x ($x = 0.75 \sim 1.0$), NiH_x ($x \sim 1.0$), TiD_x ($x \sim 2.0$), (CH_x)_n (XLPE, $x \sim 2.0$ and $n = \infty$). Using a model (TNCF model) based on the experimental data, we have been able to explain semi-quantitatively various features of the CFP from production of excess energy to nuclear transmutations through emissions of charged particles and neutron [Kozima 2006, 2008a, 2010a, 2010b]. The investigation of the basis of the TNCF model has shown possible formation of a specific state of neutrons (cf-matter) in cf-materials having a characteristic super-lattice made of interlaced sublattices of host elements and hydrogen isotopes [Kozima 2006 (Sec. 3.7.3), 2008c].

The experimental data of Jiang et al. [Jiang 2012] introduced above has given us a fact that the neutron emission of uranium deuteride has a common characteristic of the CFP. Therefore, we may investigate the CFP in the actinoid hydrides and deuterides from our point of view which have been used successfully for the analyses of the CFP in other cf-materials.

3.1. Mechanism of the Cold Fusion Phenomenon (CFP) suggested by the TNCF Model

The nuclear reactions generating various events in the CFP occur in solids composed of host elements and hydrogen isotopes with comparable number densities of both components (cf-materials) at near room temperature (at most several hundred degrees Kelvin). To answer the natural question how to overcome the Coulomb barrier between charged particles against nuclear reactions, we have assumed existence of “trapped neutrons” in cf-materials. The model based on this fundamental premise (TNCF model) has given unified explanation of whole events in the CFP suggesting the existence of a hidden clue in the premises of the model.

The investigation of the premise of the trapped neutron has been elaborated using knowledge of transition metal hydrides in solid state physics and of exotic nuclei in nuclear physics [Kozima 2006]. The fundamental idea to show possible existence of “trapped neutrons” in cf-materials is the neutron bands generated by neutrons in lattice nuclei of host elements mediated by interstitial protons (or deuterons) in the cf-materials. The neutrons in a band formed by this mechanism constitute a “quasi-free neutron gas”

(cf-matter) and interact with foreign nuclei in the lattice or with dislocated nuclei of the host element especially in surface region and also in volume [Kozima 2012]. This situation is schematically depicted in Fig. 3.1.

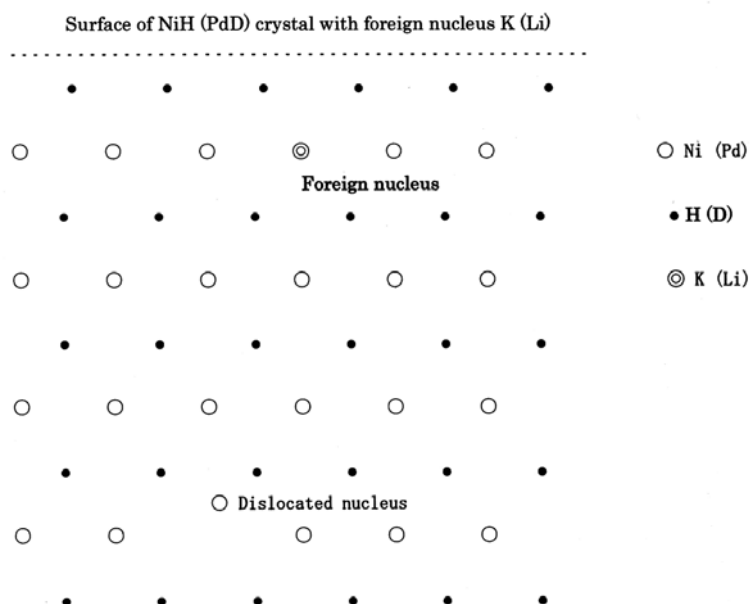


Fig. 3.1. Schematic 2-dimensional picture of the host lattice nuclei Ni (Pd), the interstitial hydrogen isotope H (D) and the foreign nucleus K (Li) in a NiH (PdD) crystal.

The experimental data obtained by Jiang et al. [Jiang 2012] has shown that the neutron emissions in UD_3 and in TiD_x have similarity. This fact suggests us that the cf-matters responsible to the CFP have been formed similarly in both cf-materials. A regular super-lattice is formed at least locally which is made of a sublattice of uranium (U) and another sublattice of deuteron (D) interlacing each other. The lattice structures of uranium deuterides UD_3 are given in the next subsection.

3.2. Structure of Uranium Hydride

Uranium hydrides and deuterides have been investigated as a neutron moderator, a nuclear fuel for the nuclear pile, and a bank of hydrogen storage.

The lattice of uranium hydride expands considerably during formation and UH_3 is therefore not an interstitial compound. In its lattice, each uranium atom is surrounded by 6 other uranium atoms and 12 atoms of hydrogen; each hydrogen atom occupies a large tetrahedral hole in the lattice. The density of hydrogen in uranium hydride is approximately the same as that in liquid water or in liquid hydrogen. The U-H-U

linkage through a hydrogen atom is present in the structure [Rundle 1947]. This linkage reminds us the super-nuclear interaction of lattice nuclei (e.g. Pd) mediated by the interstitial hydrogen isotopes (e.g. D) in transition-metal hydrides and deuterides (e.g. PdD) depicted similarly as Pd-D-Pd linkage [Kozima 2006, Fig. 3.3].

There exist two crystal modifications of uranium hydride. They are both cubic: an α form that is obtained at low temperatures and a β form that is grown when the formation temperature is above 250 °C. After growth, both forms are metastable at room temperature and below, but the α form slowly converts to the β form upon heating to 100 °C. Both α - and β -UH₃ are ferromagnetic at temperatures below ~180 K. Above 180 degrees K, they are paramagnetic [Wikipedia, *Uranium hydrides*].

The lattice structures of the α and the β forms of UH₃ compounds are shown in Figs. 3.2 and 3.3, respectively [Katz 1986].

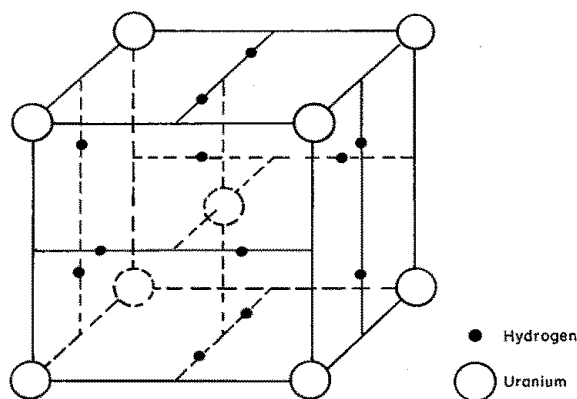


Fig. 3.2. Lattice structure of α -UH₃ [Katz 1986].

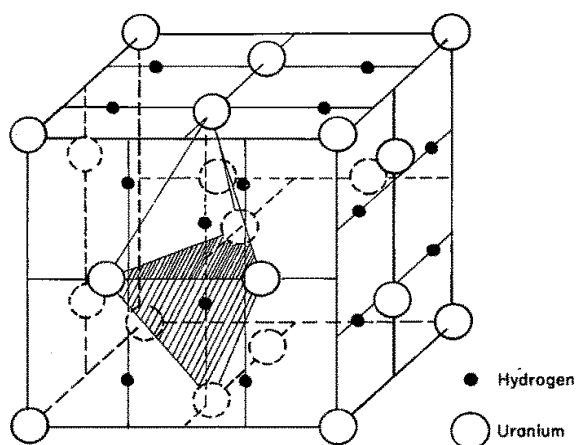


Fig. 3.3. Lattice structure of β -UH₃ [Katz 1986].

The structures of UH₃ shown in Figs. 3.2 and 3.3 demonstrate the complex feature of the UH₃ structure compared with other cf-materials such as PdD_x, NiH_x and XLPE.

However, how the structure of the UH_3 is complex, the regularity of the arrays of uranium and hydrogen in each sublattices suffices the condition for formation of neutron bands speculated in our papers to legitimate the existence of cf-matter [Kozima 2006, 2008c].

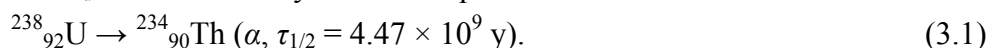
Therefore, we may be able to apply our model to the experimental data sets of nuclear transmutations in actinoid hydrides and deuterides introduced in Section 2.

3.3. Explanation of Experimental Data Sets introduced in Section 2 and Decay-Time Shortening by TNCF Model

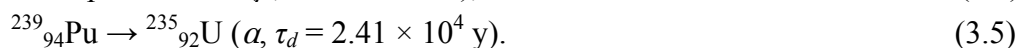
The experimental data sets obtained by Goddard et al. [Goddard 2000] and Dash et al. [Dash 2003, 2005] revealed a common characteristic of decay-time shortening of actinoid hydrides and deuterides irrelevant to their methods of formation. The positive correlation between implantation time of hydrogen isotopes into uranium and amounts of radiation (by the decay-time shortening) (cf. Fig. 2.2) is interpreted as an indication that the formation of cf-matter in the sample is provided by the formation of the superlattice of uranium and hydrogen isotopes from our point of view (cf. Sec. 3.3.2).

3.3.1. Explanation of Nuclear Transmutation observed in Experiments

The decrease of $^{238}_{92}\text{U}$ and increase of $^{235}_{92}\text{U}$ and $^{234}_{90}\text{Th}$ observed by Dash et al. (cf. Sec. 2.2.3) is explained by following reactions. The increase of $^{234}_{90}\text{Th}$ is due to the decay-time shortening of the following spontaneous decay process (Eq. (1.2)) with a decay time τ_d of 4.468×10^9 year in free space:



The increase of $^{235}_{92}\text{U}$ may be the successive reactions (decay type, half-life in free space) started from the reaction (1.7) followed by β -decays and an α -decay of resultant nuclides written down as follows:



Again, the decay reaction (3.5) may be accelerated by the decay-time shortening in the cf-material.

The rise of radiation observed in the experiment by Goddard et al. (cf. Sec. 2.2.1) is explained by the increase of the decay reaction (3.1) by the decay-time shortening. The appearance of Fe and Cs on the cathode and the morphology change of the cathode surface have shown the occurrence of nuclear transmutations accompanying excess heat

in this system but without data on its mechanism.

The increases of $^{234}_{90}\text{Th}$ and $^{235}_{92}\text{U}$ determined by characteristic gamma rays in the experiment by Dash et al. (cf. Sec. 2.2.2) are also indication of the nuclear reactions written down in Eqs. (3.1) – (3.5). The morphology change of the surface shown in Fig. 2.3 clearly shows the occurrence of nuclear reactions accompanying a huge excess heat generation resulting in the nuclear transmutation described by these equations even if there is no observation of the transmuted nuclei $^{239}_{92}\text{U}$, $^{239}_{93}\text{Np}$ and $^{239}_{94}\text{Pu}$.

3.3.2. Explanation of the Decay-time Shortening

As has been shown in our papers presented at this conference [Kozima 2014a, 2014b], the height of the surface layer of radioactive nucleus preventing emission of nucleons in free space becomes lower according to the increase of the density n_o of neutrons in the cf-matter surrounding the nucleus with a neutron density n_i , or the increase of the density ratio n_o/n_i of neutrons outside and inside the nucleus. This feature is depicted in Fig. 3.4 where the surface energy of the boundary $E_{\text{surf}} (\equiv y)$ decreases with the increase of the density ratio $n_o/n_i (\equiv x)$ [Negele 1973].

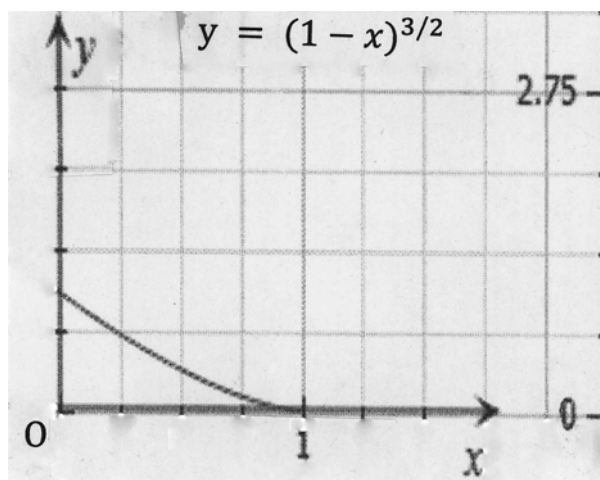


Fig. 3.4. Dependence of the surface energy $E_{\text{surf}} (\equiv y)$ on the density ratio $n_o/n_i (\equiv x)$.

It is clear that the lower the surface energy of the boundary, the easier a nucleon escapes from the nucleus. The same logic will be applicable to the emission of an alpha particle from a nucleus to explain the decay-time shortening observed by Dash et al. [Goddard 2000, Dash 2003, 2005] by the formation of a high-density neutron medium (cf-matter) in the cf-material, especially at its surface or boundary region [Kozima 2006, 2014a].

Instability of the metastable states of UD_3 (transition from α - to β -phase explained in Sec. 3.2) shows that it is difficult to realize a stable superlattice of UD_3 (UH_3) composed of a uranium sublattice and a deuteron (proton) sublattice. This may be the reason that there is a temporal change of radiation for samples irradiated by plasmas (e.g. Fig. 2.2)

It is reasonable that the amount of increase in α -radiation has positive correlation to the average density of hydrogen isotopes which is surely proportional to the time of plasma discharge and electrolysis (e.g. Table 2.1).

Thus, the data sets of the decay-time shortening of uranium and thorium introduced above are consistently explained by the TNCF model using the concept of cf-matter suggested by the neutron star matter elaborated in 1970's in relation to the explanation of the neutron star [Baym 1971, Negele 1973].

4. Conclusions

Experimental data sets on actinoid hydrides and deuterides have been analyzed and explained using the TNCF model. The experimental data have shown that these hydrides and deuterides are classified as the cf-materials where occurs the cold fusion phenomenon (CFP) and the observed events are understood by nuclear reactions common to other reactions observed in cf-materials, mainly transition-metal hydrides and deuterides.

The changes of radiation properties of actinoids occluding hydrogen isotopes are explained by formation of the cf-matter similar to the free neutron sea in neutron star matter and then by the interaction of actinoid nucleus and the cf-matter. Acceleration of the alpha decay of $^{238}_{92}\text{U}$ into $^{234}_{90}\text{Th}$, the so-called the decay-time shortening, is explained by the change of the boundary layer between the nucleus $^{238}_{92}\text{U}$ and the cf-matter induced by the increase of the density ratio n_0/n_i of neutrons due to the formation of the cf-matter.

A possible application of this phenomenon to $^A_{94}\text{Pu}$ ($A = 238 - 244$) is hopeful.

If we can handle plutonium isotopes which are produced in atomic plants as hazardous waste properly to accelerate their decay, it is the savior of our age from the dangerous nuclear waste waiting its resolution. As shown in Table 4.1, plutonium isotopes have very long decay times and therefore the decay-time shortening as shown in the CFP will be applicable to transmute them into other nuclides easy to treat with.

Table 4.1 Decay characteristics of plutonium isotopes

Isotope	Decay mode	Half-life	Decay heat	Spon. fission neutrons
$^{238}_{94}\text{Pu}$	alpha to $^{234}_{92}\text{U}$	87.74 (y)	560 (W/kg)	2600 (1/g•sec)
$^{239}_{94}\text{Pu}$	alpha to $^{235}_{92}\text{U}$	24100	1.9	0.022
$^{240}_{94}\text{Pu}$	alpha to $^{236}_{92}\text{U}$ + Spont. Fission	6560	6.8	910
$^{241}_{94}\text{Pu}$	e^- to $^{241}_{95}\text{Am}$	14.4	4.2	0.049
$^{242}_{94}\text{Pu}$	alpha to $^{238}_{92}\text{U}$	376000	0.1	1700

Instead of neutron bombardment in free space, we can use the cf-materials to give an effect of neutrons on target nuclei. This fact may be interesting in science and technology of the neutron-nuclear interaction in low energy region.

Acknowledgement

The author would like to express his thanks to Prof. John Dash of Portland State University for valuable discussions during this work and also to Dr. S.-S. Jiang of China Institute of Atomic Energy for his kindness to send him the paper published in *Chin. Phys. Lett.* He is also indebted to Prof. H. Suganuma of Shizuoka University for his help in obtaining information about structures of UH_3 and valuable discussions with him.

References

- [Baym 1971] G. Baym, H.A. Bethe and C.J. Pethick, "Neutron Star Matter," *Nuclear Physics*, **A175**, 225 – 271 (1971).
- [Dash 1993] J. Dash, G. Noble and D. Diman, "Surface Morphology and Microcomposition of Palladium Cathodes after Electrolysis in Acidified Light and Heavy Water: Correlation with Excess Heat," *Trans. Fusion Technol.*, **26**, 299 – 306 (1993).
- [Dash 1994a] J. Dash, G. Noble and D. Diman, "Changes in Surface Topography and Microcomposition of a Palladium Cathode caused by Electrolysis in Acidified Light Water," *Proc. Int. Sym. Cold Fusion and Advanced Energy Sources* (Minsk, Belarus, May 25 – 26, 1994), pp. 172 – 183 (1994).
- [Dash 1994b] J. Dash, G. Noble and D. Diman, "Surface Morphology and Microcomposition of Palladium Cathodes after Electrolysis in Acidified Light and Heavy Water: Correlation with Excess Heat," *Proc. ICCF4*, **2**, pp. 25-1 – 25-11 (1994).
- [Dash 1996] J. Dash, "Chemical Changes and Excess Heat caused by Electrolysis with

- H₂SO₄ – D₂O Electrolyte,” *Proc. ICCF6*, pp. 477 – 481 (1996).
- [Dash 1997] J. Dash, R. Kopecek and S. Miguet, “Excess Heat and Unexpected Elements from Aqueous Electrolysis with Titanium and Palladium Cathodes,” *Proc. 32th Intersociety Energy Conversion Engineering Conference*, 2, pp. 1350 – 1355 (1997).
- [Dash 2003a] J. Dash, I. Savvatimova, S. Frantz, E. Weis and H. Kozima, “Effects of Glow Discharge with Hydrogen Isotope Plasmas on Radioactivity of Uranium,” *Proc. ICCF9*, pp.77 – 81 (2003). ISBN 7-302-06489-X/O·292
- [Dash 2003b] J. Dash, H. Kozima, I. Savvatimova, S. Frantz and E. Weis, “Effects of Glow Discharge with Hydrogen Isotope Plasmas on Radioactivity of Uranium,” *Proc. 11th Intern. Conf. Emerging Nuclear Energy Systems*, p.122 – 126 (2003).
- [Dash 2005] J. Dash and D. Chicea, “Changes in the Radioactivity, Topography, and Surface Composition of Uranium after Hydrogen Loading by Aqueous Electrolysis,” *Proc. ICCF10*, pp. 463 – 474 (2005). ISBN 981-256-564-7
- [Firestone 1996] R.B. Firestone, *Table of Isotopes*, CD-ROM 8th edition, v. 1.0, Wiley-Interscience, 1996.
- [Fleischmann 1989] M, Fleischmann, S. Pons and M. Hawkins, "Electrochemically induced Nuclear Fusion of Deuterium," *J. Electroanal. Chem.*, 261, 301 – 308 (1989).
- [Goddard 2000] G. Goddard, J. Dash and S. Frantz, “Characterization of Uranium Codeposited with Hydrogen on Nickel Cathodes,” *Transactions of American Nuclear Soc.* **83**, 376 – 378 (2000).
- [Jiang 2012] S. Jiang, X. Xu et al., “Anomalous Neutron Burst Emissions in Deuterium-Loaded Metals: Nuclear Reaction at Normal Temperature,” *Chinese Physics Lett.*, **29**, pp. 112501-1 – 4 (2012). And also S. Jiang, X. Xu et al., “Neutron Burst Emission from Uranium Deuteride and Deuterium-Loaded Titanium,” *Proc. ICCF17* (preprint version).
- [Katz 1986] J.J. Katz, G.T. Seaborg and L.R. Morss, *The Chemistry of the Actinide Elements*, Vol.1 (Second Edition), Chapman and Hall, 1986.
- [Kozima 1994] H. Kozima, “Trapped Neutron Catalyzed Fusion of deuterons and Protons in Inhomogeneous Solids,” *Trans. Fusion Technol.*, **26**, 508 – 515 (1994).
- [Kozima 1998] H. Kozima, *Discovery of the Cold Fusion Phenomenon* (Ohtake Shuppan Inc., 1998). ISBN 4-87186-044-2.
- [Kozima 2002] H. Kozima, “An Explanation of Data Sets obtained by McKubre et al. (Excess Heat), Clarke (Null Results of ⁴He and ³He) and Clarke et al. (Tritium) with ‘Arata Cell,’” *Proc. ICCF9*, pp. 182 – 185 (2002). ISBN 7-302-06489-X/O ·292

- [Kozima 2006] H. Kozima, *The Science of the Cold Fusion Phenomenon*, Elsevier Science, 2006. ISBN-10: 0-08-045110-1.
- [Kozima 2008a] H. Kozima, “Phenomenology of the Cold Fusion Phenomenon,” *Reports of CFRL (Cold Fusion Research Laboratory)*, **8-3**, pp. 1 – 23 (September, 2008). <http://www.geocities.jp/hjrfq930/Papers/paperr/paperr.html>
- [Kozima 2008b] H. Kozima, W.W. Zhang and J. Dash, “Precision Measurement of Excess Energy in Electrolytic System Pd/D/H₂SO₄ and Inverse-Power Distribution of Energy Pulses vs. Excess Energy,” *Proc. ICCF13*, pp. 348 – 358 (2008). ISBN 978-5-93271-428-7. And also *Reports of CFRL* **11-5**, pp. 1 – 14 (January, 2008); <http://www.geocities.jp/hjrfq930/Papers/paperr/paperr.html>
- [Kozima 2008c] H. Kozima, “Physics of the Cold Fusion Phenomenon,” *Proc. ICCF13*, pp. 690 – 703 (2008). ISBN 978-5-93271-428-7. And also *Reports of CFRL* **11-4**, pp. 1 – 21 (January, 2011); <http://www.geocities.jp/hjrfq930/Papers/paperr/paperr.html>
- [Kozima 2010a] H. Kozima, “Neutron Emission in the Cold Fusion Phenomenon,” *Proc. JCF11*, pp. 76 – 82 (2010). <http://jcfrs.org/file/jcf11-proceedings.pdf>
And also *Reports of CFRL (Cold Fusion Research Laboratory)* **11-3**, 1 – 12 (January, 2011); <http://www.geocities.jp/hjrfq930/Papers/paperr/paperr.html>
- [Kozima 2010b] H. Kozima, “Localization of Nuclear Reactions in the Cold Fusion Phenomenon,” *Proc. JCF11*, pp. 59 – 69 (2010). <http://jcfrs.org/file/jcf11-proceedings.pdf>
And also *Reports of CFRL (Cold Fusion Research Laboratory)* **11-2**, 1 – 20 (January, 2011); <http://www.geocities.jp/hjrfq930/Papers/paperr/paperr.html>
- [Kozima 2013] H. Kozima, “Cold Fusion Phenomenon in Open, Nonequilibrium, Multi-component Systems – Self-organization of Optimum Structure,” *Proc. JCF13*, 13-19, pp. 134 – 157 (2013) and is posted at JCF website: <http://jcfrs.org/file/jcf13-proceedings.pdf>
The paper is also published as *Reports of CFRL* **13-3**, pp. 1 – 24 (2013) and posted at CFRL website: <http://www.geocities.jp/hjrfq930/Papers/paperr/paperr.html>
- [Kozima 2014a] H. Kozima and K. Kaki, “Atomic Nucleus and Neutron — Nuclear Physics Revisited with the Viewpoint of the Cold Fusion Phenomenon,” *Proc. JCF14*, **14-6**, pp. xx – xx+31 (2014). <http://jcfrs.org/file/jcf14-proceedings.pdf>
And also *Reports of CFRL (Cold Fusion Research Laboratory)* **14-1**, 1 – 31 (March, 2014); <http://www.geocities.jp/hjrfq930/Papers/paperr/paperr.html>
- [Kozima 2014b] H. Kozima, “Nuclear Transmutations (NTs) in Cold Fusion Phenomenon (CFP) and Nuclear Physics,” *Proc. JCF14*, **14-15**, pp. xx – xx+37

(2014). <http://jcfrs.org/file/jcf14-proceedings.pdf>

And also *Reports of CFRL* (Cold Fusion Research Laboratory) **14-3**, 1 – 37 (March, 2014); <http://www.geocities.jp/hjrfq930/Papers/paperr/paperr.html>

[Negele 1973] J.W. Negele and D. Vautherin, “Neutron Star Matter at Sub-nuclear Densities,” *Nuclear Physics*, **A207**, 298 - 320 (1973).

[Rundle 1947] R.E. Rundle, “The Structure of Uranium Hydride and Deuteride,” United State Atomic Commission MDDC-865, pp. 1 - 9 (1947).

Synthesis of nano-Pd particles in Y-zeolite pores by ultrasonic irradiation

X.F. Wang^{*1,2}, T. Mizuno², Y. Arata¹

¹ Arata Research & Development Center, 2-1 Yamadaoka, Suita, Osaka 5650871, Japan

² Hydrogen Engineering Application & Development Company, Three System Building 6 floor,
Kita-ku, North 12, West-4, 1-15, Sapporo 001-0012, Japan

*xfwang77@gmail.com

Abstract

In Solid Fusion research, metal nanoparticles have been attracting attention as a reaction medium. This paper provides the methodology for the synthesis of nano-Pd particles which is to irradiate the 35kHz ultrasonic waves on PdCl₂-zeolite solution. Nano Pd particles are synthesized in the Y-zeolite(SiO₂/Al₂O₃, Na₂O (wt%): 4) pores with pores size 0.8nm. Scanning electron microscope (SEM), Energy Dispersive X-ray Spectroscopy (EDS / EDX), transmission Electron Microscope (TEM) are applied to confirm the size and components of the particles. The size of nano Pd particles produced in the zeolite pores (by SEM, EDS analysis) is suppressed to below 0.8nm i.e. the pores size of Y-zeolite (to be confirmed by TEM analysis).

1. Introduction

It is well known that nanometer-sized particles display intrinsic different characteristics from those of the corresponding bulk materials due to their unique nanometer-scale structure. Metal nanoparticles, such as Pd particles, are attracting more and more researchers to this study due to its unique properties in Low Energy Nuclear Reactions (LENR, "Solid Fusion")[1, 2]. As shown in Fig.1, it has been investigated in gas loading system by several teams that nanoscale particles embedded in a matrix such as ZrO₂, zeolite, γ -Al₂O₃, etc[2]. We have confirmed the existence of "Solid Fusion" by applying nano-Pd powder (ZrO₂ · Pd, as shown in Fig.2) in D₂ gas loading system[3]. In Fig.2, nano-Pd particles of 50Å in size are embedded inside of matrix ZrO₂ (ZrO₂ · Pd: oxidized amorphous alloy of Zr₆₅Pd₃₅). This nano sized ZrO₂ · Pd powder works more effectively to absorb large amounts of deuterium (which in turn created solid fusion due to the relatively large specific surface area.) or and then cause solid fusion attributing to the relative large specific surface area.

In recent years, the reaction in Solid Fusion applying nano-Pd particles embedded in zeolite has been investigated by several groups[4~8]. However, because of the multiformity and sizes of the pores of zeolite, it is necessary to do further studies on the reaction of fusion applying nano-Pd particles embedded in zeolite. Under the laboratory conditions, it has been reported that the nano-Pd particles can be easily synthesized by ultrasonic irradiation[9]. In this paper, we report our recent results of the synthesis of nano-Pd particles in Y-zeolite pores by ultrasonic irradiation. This method of the synthesis of nano-Pd particles in Y-zeolite pores is simple and the Pd can be recycled. The sizes of the Pd particles can be easily controlled by the diameter of the pores of zeolite. The synthesis of nano-Pd particles produced in the laboratory is anticipated to further advance the research of Solid Fusion.

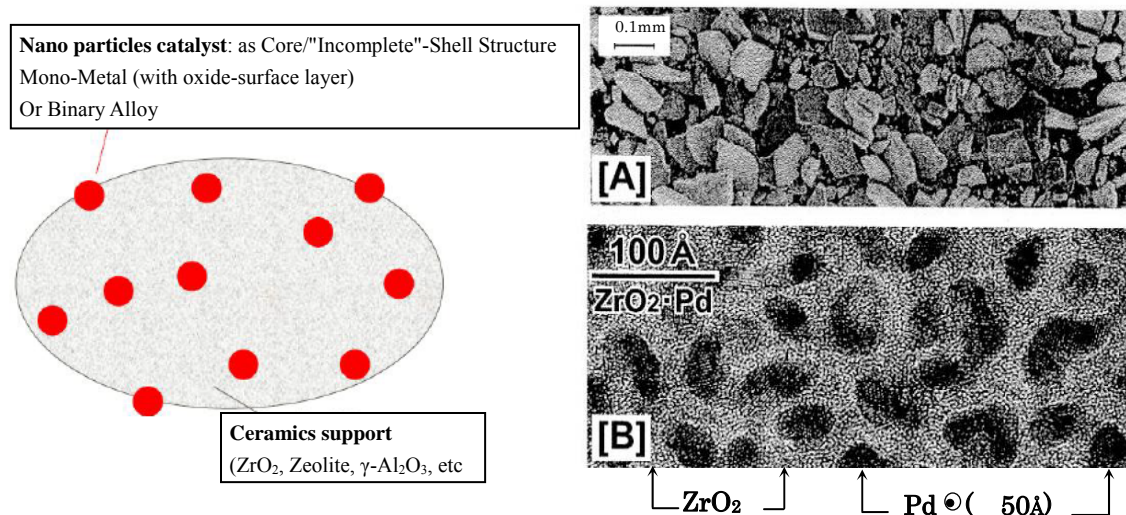


Fig.1. Nanoscale particles embedded in matrix

Fig.2. Pd embedded in ZrO₂

2. Experiments and results

Firstly, the solid PdCl₂ powder was dissolved into HCl solution to compound 1m-mol l⁻¹ PdCl₂ solution. Then the Y-zeolite with pores diameter of 0.8nm was immersed into 1m-mol l⁻¹ PdCl₂ solution (containing 0.2 mol l⁻¹ isopropanol) in a conical flask. The argon gas was purged into the flask to eliminated oxygen, and then the flask was covered with the lid. This solution with the solid zeolite powder was laid up for one week, to make the concentrations of Pd²⁺ ions and isopropanol in the pores of mesoporous zeolite the same as those in bulk solution [9]. After this sufficient immersion, 50ml solution of the mixed solution was transferred to a conical flask with volume of 100ml. Then the flask with cover, was put in the sonication bath (SHARP UT-105, 35kHz, 100W output power), and was irradiated for 8hours. This process is

shown in Fig.3.

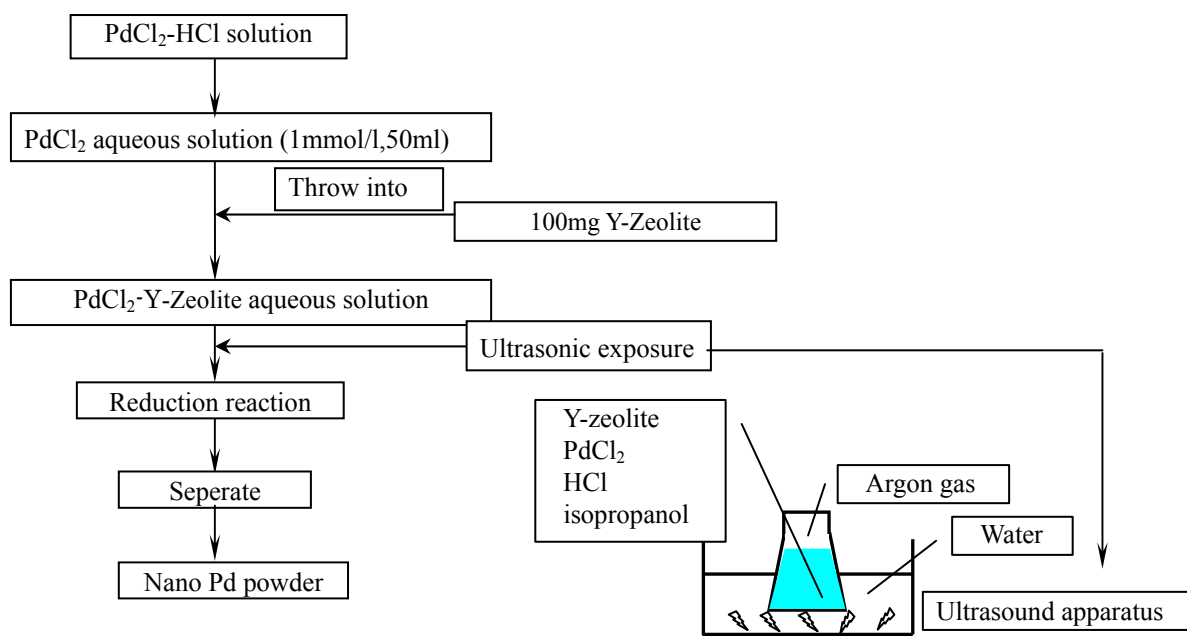


Fig.3. Schematic diagram of the process of synthesis

The sample of ultra sound irradiated solution was evaporated. The remained powder after the evaporation was analyzed by SEM and EDS analysis. As shown in Fig.4a, the size of the remained powder is under 10 μ m. Fig.4b is the EDS component analysis data of the particles as shown in Fig.4a. The results show that Pd element is obviously detected on the surface of the particles. To further confirm whether the Pd was synthesized within the porous of zeolite or not, a transmission Electron Microscope (TEM) analysis is needed. The TEM analysis is in progress now.

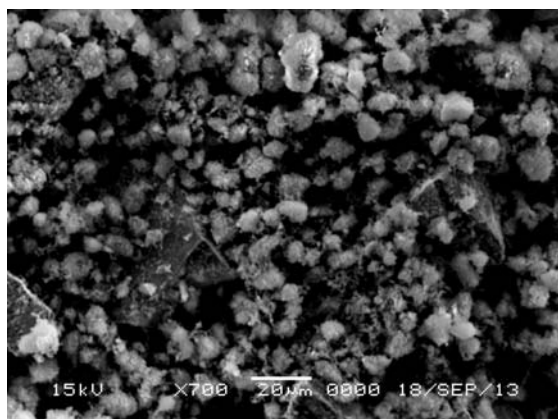


Fig.4a. Pd- Y zeolite SEM analysis X 700

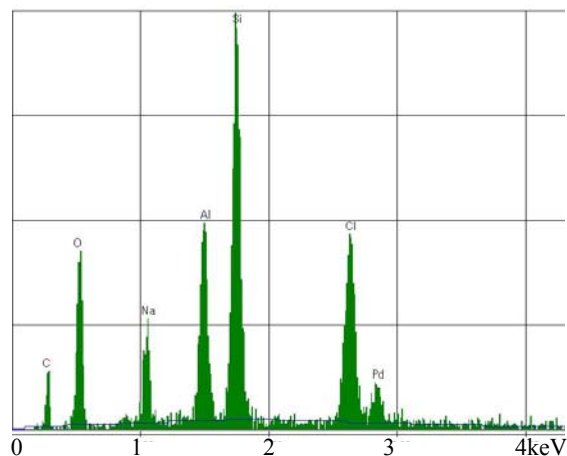


Fig.4b. Pd- Y zeolite EDS analysis

The framework type of the Y-zeolite applied in this paper was shown in Fig.5a. And the diameter of the pores is 0.8nm. That is to say that if the Pd was synthesized within the pores, the diameter of Pd will not be over 0.8nm (was controlled by the size of the pores of zeolite, as shown in Fig.5b).

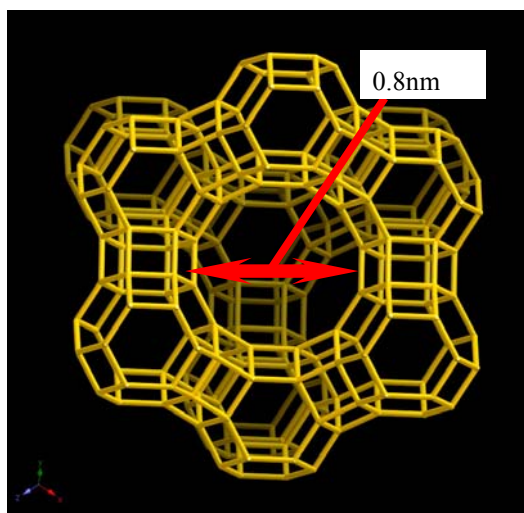


Fig.5a. Framework of Y-zeolite

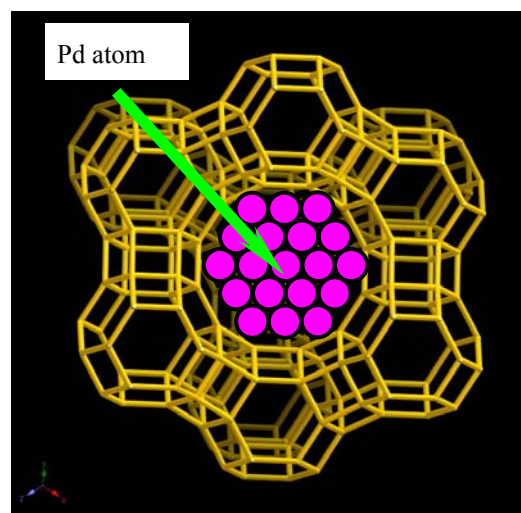
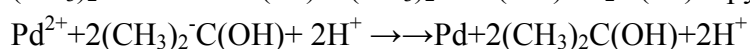
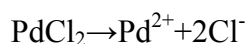


Fig.5b. Predicted structure of Pd- Y-zeolite

The proposed mechanism of sonochemical reduction of Pd^{2+} ions and formation of Pd particles in water by using ultrasonic irradiation is shown as follows [9,10]:



The Pd size confirmation by TEM and the process of large amount synthesis of Pd particles is now in progress. Upon confirmation of this process, the gas loading experiments of solid fusion applying nano Pd particles within pores of mesoporous zeolite will be investigated. As shown in table1, it should be pointed out that, Y-zeolite has certain Hydrogen storage capacity with the loading conditions: temperature--573K; pressure--10.0MPa; time--15min [11]. This capacity should not be ignored as to when to analyze the results of the gas loading experiments of solid fusion applying nano Pd particles within pores of mesoporous zeolite.

Table 1. Hydrogen storage capacity of zeolites containing different cage types (loading conditions: temperature 573K; pressure--10.0 Mpa; time--15min)

Zeolite	$V_{H_2,N}/m_Z$ (cm^3/g)	Cage type	k/m_Z (cages/g)	n_{H_2}/k (molecules/cage)
NaA	3.3	s	3.58×10^{20}	0.25
SAPO-42	1.6	s	4.20×10^{20}	0.10
Sodalite	9.2	s	1.41×10^{21}	0.17
NaX	2.6	s	3.58×10^{20}	0.20
NaY	2.6	s	3.79×10^{20}	0.18
Rho	0.5	α	n.a.	n.a.
ZK-5	0.5	α	n.a.	n.a.
Sigma-1	2.0	p	n.a.	n.a.

$V_{H_2,N}$ —hydrogen volume calculated for 273.15 K and 101.3 kPa; m_Z —mass of dry zeolite; k —number of sodalite cages; n_{H_2} —number of hydrogen molecules; s—sodalite cage; p—pentagondodecahedron; α — α -cage; n.a.—not applicable.

3. Conclusions

A simple method to synthesis nano Pd particles within the mesoporous zeolite host by soaking and subsequently irradiation by ultrasound in laboratory was introduced in this paper. Though, more work is needed, this method can be expected to produce a large amount of synthesis of Pd particles with controlled nano size, which are located within the pores of mesoporous zeolite, under laboratory condition.

References

- [1] F. Celani, P. Marini, et al., “Towards a High Temperature CMNS Reactor: Nano-Coated Pd Wires with D₂ at High Pressures”, Proc. ICCF15, Rome, Italy, pp.82-87, 2009.
- [2] A. Takahashi, 『Frontier of Cold Fusion 2011』, special issue of JCFRS, December 2011.
- [3] Y. Arata, Y.C. Zhang and X.F. Wang, “Production of Helium and Energy in the “Solid Fusion”, Proc. ICCF15, Rome, Italy, pp.72-81, 2009.
- [4] D. Kidwell, et al., Yes, “Virginia there is Heat, but It is Likely of Chemical Origin”, Proc. ICCF15, Rome, Italy, pp.100-109, 2009.
- [5] A. Sendis, “Desktop fusion of D₂ in palladium nanoparticles loaded in zeolites”, Senior Thesis of University of LaVerne, 2011.

- [6] O. Dmitriyeva, R. Cantwell, M. McConnell, and G. Moddel, “Deuterium & hydrogen loading into nano-Pd on zeolite and alumina matrices at low pressures”, 9th International Workshop on Anomalies in Hydrogen/Deuterium Loaded Metals, Sienna, Italy (2010).
- [7] H. Sakoh, Y. Miyoshi, A. Taniike, A. Kitamura, A. Takahashi, et al., “Silica-included Pd nano-powders repeatedly available for heat production by hydrogen isotope absorption”, Proc. JCF12, 2011.
- [8] T. Hioki, N. Sugimoto, et al., “Hydrogen Absorption Property of Pd-Doped Porous Materials”, Proc. ICCF18, 2013
- [9] W. Chen, W. Cai, et al., “A sonochemical approach to the confined synthesis of palladium nanoparticles in mesoporous silica”, Materials Letters, pp. 53-56, 50(2001).
- [10] K. Okitsu, H. Bandow, Y. Maeda, Y. Nagata, “Sonochemical Preparation of Ultrafine Palladium Particles”, Chem. Mater. , pp. 315-317, 8(1996).
- [11] J. Weitkamp, M. Fritz, S. Ernst, “Zeolites as media for hydrogen storage”, International Journal of Hydrogen Energy. Volume 20, Issue 12, December 1995, pp. 967–970.

Impressive Increase in Number of Etch Pit occasionally Produced on CR-39 in Light and Heavy Water Electrolysis Using Ni Film Cathode

H. Yamada, K. Mita, H. Aizawa and Y. Shida

Department of Electrical and Electronic Engineering, Iwate University, Ueda 4-3-5, Morioka, 020-8551 Japan yamadahi@iwate-u.ac.jp

Abstract

The primary purpose of this study is to establish a simple technique producing new convincing evidence that a nuclear reaction as low energy nuclear reaction (LENR) could accompany both heavy and light water electrolysis. Electrolysis of D₂O and H₂O solutions is carried out using a Ni film cathode under 20 DC current patterns. A small chip of the plastic track detector CR-39 is positioned just under the thin Ni film cathode to limit energy decrease of an energetic charged particle from the cathode. The present technique is simple but capable of detecting energetic charged particles produced on the cathode during electrolysis with higher efficiency. An impressive increase in number of etch pit is occasionally observed for both D₂O and H₂O solutions.

1. INTRODUCTION

The plastic track detector has become a popular method to detect energetic charged particles in low energy nuclear reaction (LENR) studies especially in electrolysis experiments. In these studies, the evidence of the reaction is in the form of nuclear damage trails made visible by etching of the plastic chips. Oriani et al. [1, 2], Lipson et al.[3, 4] and Roussetski[5] have performed light and heavy water electrolysis using the plastic track detector and have reported the generation of charged particle emission during the electrolysis.

However, there still exist technical complexities in using plastic detector in electrolysis experiment. In the previous studies, there have been a thin layer of electrolyte and/or a solid film between the cathode electrode and the plastic detector. Such construction could cause a considerable decrease in the energy of the charged particle emitted from the cathode.

In this present study, a chip of the plastic track detector CR-39 is positioned just under the thin Ni film cathode to limit energy decrease; a CR-39 chip of 30×30 mm in size is set in close contact with the rear surface of the cathode film. This construction avoids chemical attack on the chip by ions generated by the electrochemical reactions on the Ni film cathode. The present technique is simple but capable of detecting energetic charged particles produced on the cathode during electrolysis with higher efficiency. Using the present technique, we have studied energetic charged particle emission from the metal film cathodes for light and heavy water electrolysis [6-8].

The primary purpose of this study is to establish a simple technique producing new convincing evidence that a nuclear reaction as LENR could accompany both

heavy and light water electrolysis. Anomalous increase in number of etch pit has been observed in one out of 9 and 3 out of 15 electrolysis conditions for D₂O and H₂O solutions, respectively.

2. EXPERIMENTAL

2.1. Test cell and track detector

Electrolysis is carried out in a small plastic (polyoxymethylene) cell shown schematically in Fig. 1(a). It consists of a vertical plastic cylinder of 105 mm long and 10 mm inside diameter, a plastic stopper holding a wire anode, a lower portion of plastic base and a Ni film cathode. The left side and right side of Fig. 1(b) display the components of the cell and the cell assembled, respectively. The top of cylindrical portion of the cell is covered by the plastic stopper with loose contact, which permits the escape of the gas produced by electrolysis. A 5 μm thick Ni film is used as the metal cathode for both heavy and light water electrolysis. The 10 mm center area of the film with 30×40 mm in size forms the inner bottom of the test cell and serves as cathode. The anode is a 0.5 mm Pt wire. The upper portion of it is sheathed by an heat-shrinkable FEP tube surrounded with TFE and the lower part (~60 mm long) is formed a crude spiral with the diameter and the length of ~5 mm and ~30 mm, respectively. The lower end of the spiral plane is parallel to the cathode surface with a gap distance of ~10 mm.

Nine sheets of the track detector CR-39, produced by Fukuvi Chemical Industry Co., Ltd, are used in the study. The time interval from the production to the supplying of the sheet is in the range 15-127 days. A 30×30×0.9 mm chip, as shown in Fig. 2, is cut from a sheet of 300×300×0.9 mm in size and is stored in a refrigerator at 5 °C immediately after the supplying. The chip is carefully manipulated with tweezers. The center area of the front surface, which contacts to the metal film, is scratched to form a 10×10 mm square line, before removing the manufacture-supplied blue protective film. There exists a shallow pit of 30.2×30.2×0.5 mm in size at the center of the upper surface of the plastic base for a stable fixing the CR-39 chip. The CR-39 chip is mounted on the plastic base immediately after removing the protective film just before the experiment. The scratched surface of the chip is referred to as the front surface upon which the metal film cathode is overlaid. Then, the rear surface of the Ni film cathode area is set in close contact with the surface of the inside area bounded by the scratched 10×10 mm square line on the front surface of the CR-39 chip. Finally, both the Ni film and the CR-39 chip are clamped together with an O-ring seal, between the lower disc part of the cylinder and the upper disc part of the base, forming the bottom cap of the cell.

The arrangement of the cathode and the CR-39 chip is shown in the small circle of Fig. 1 (a). This construction is able to avoid chemical attack on the CR-39 chip by ions generated in the electrolyte and keep an ideal distance between the cathode and the detector chip. Thus, the construction could minimize the energy loss of charged particle, which could be produced on the surface of the thin Ni film and

penetrate through it in the electrolysis process, and would maximize the efficiency of the detecting particle.

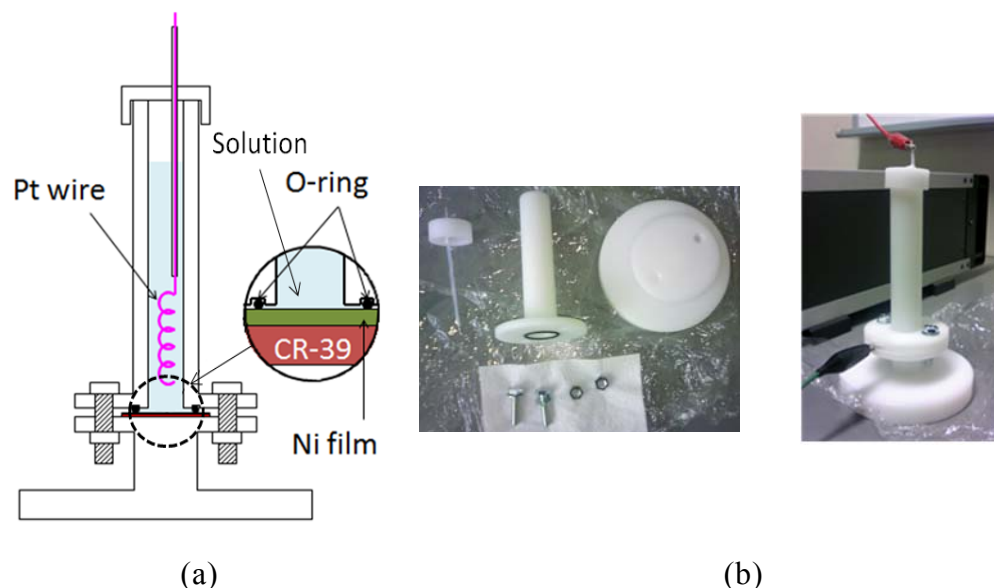


Fig. 1. Test cell for the electrolysis, (a) vertical cross section, (b) the view of the components of the cell (left) and its assembled (right).

2.2. Experiment procedure

After the lower portion of the cell is assembled to form a small vessel, the ~6 ml electrolyte solution is poured into the cell. Then, the stopper cap holding the anode is put on the upper opening.

The electrolysis is conducted for time range 20m-7d under DC current range 3-160 mA at voltage range 3-30 V. The current for the electrolysis is supplied by a constant-current power supply and no water is added during the electrolysis.

The CR-39 chip used for control experiments is always cut from the same sheet, and is carefully handled in exactly the same way as that used in the electrolysis experiment. In the control experiment, which is designated “Control” in the following figures, the CR-39 chip is mounted in the same designed test cell as that for the electrolysis with an unused Ni film and a solution and is positioned in the near the ongoing electrolysis cell during the electrolysis. The exposure time of CR-39 for the control experiments in the absence of electrolysis is same length as that for the electrolysis experiment. However, two electrolysis experiments are sometimes performed simultaneously using one control experiment. Besides, some electrolysis experiments are conducted without control experiment, mainly at the late period of the study. Thus the total number of chip obtained from the control experiment is less than that from the electrolysis one. After the electrolysis and control experiments, the cell assemblies are immediately disassembled to remove the CR-39 chips and the Ni films used.

The CR-39 chip is etched in 6N NaOH solution for 7 h at 70 °C immediately after each experiment. The measurement of etch pit is carried out using a digital microscope system (KEYENCE VHX-200), consisting of an optical microscope

with a camera and a PC. The 10×10 mm measurement area is the center of the chip surface shown in Fig. 2. The measurement of the diameter is conducted manually

Table 1. Electrolysis conditions. The 4 electrolysis conditions, in which the impressive increase in number of etch pit has been observed, are given with colored letters.

Solvent	Electrolyte	Current Pattern	Impressive	
H ₂ O	D ₂ O	0.1M-Li ₂ SO ₄	20mA·20m	
H ₂ O		1.0M-Li ₂ SO ₄	20mA·20m	
	D ₂ O	0.1M-Li ₂ SO ₄	20mA·7d	
H ₂ O		0.1M-Li ₂ SO ₄	160mA·1d	
H ₂ O		0.1M-Li ₂ SO ₄	160mA·3d	1/2
H ₂ O	D ₂ O	0.1M-Li ₂ SO ₄	3-160mA·7d	2/5
H ₂ O		1.0M-Li ₂ SO ₄	3-160mA·7d	
	D ₂ O	0.1M-Li ₂ SO ₄	20-10mA·1d·alter	
	D ₂ O	0.1M-Li ₂ SO ₄	(-20mA·20m,+20mA·5m)x8	
	D ₂ O	0.1M-Li ₂ SO ₄	(-20mA·23h55m,+20mA·5m)x7	3/6
H ₂ O		0.1M-Na ₂ SO ₄	160mA·3d	
H ₂ O		0.1M-Na ₂ SO ₄	3-160mA·7d	
H ₂ O		0.1M-Na ₂ SO ₄	(-20mA·23h55m,+20mA·5m)x7	
H ₂ O	D ₂ O	0.1M-LiOH	20mA·7d	
H ₂ O	D ₂ O	0.1M-LiOH	3-160mA·7d	1/5
	D ₂ O	0.1M-LiOH	(-20mA·23h55m,+20mA·5m)x7	
H ₂ O		0.1M-LiCl	20mA·7d	
H ₂ O		0.1M-LiCl	100mA·7d	
H ₂ O		0.1M-LiCl	3-160mA·7d	
H ₂ O		0.1M-LiCl	50-80mA·1d·alter	

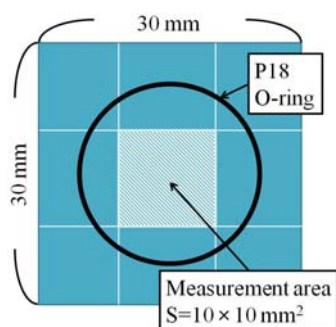


Fig. 2. CR-39 chip.

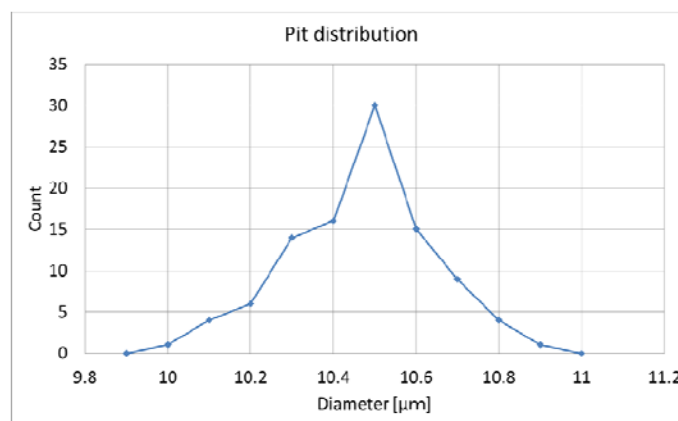


Fig. 3. Distribution of the diameter of a randomly selected pit by the manual measurement.

and minor axis is adopted as the diameter for the pit with oval rim. The distribution of the diameter by the manual 100 measurements for a randomly selected pit is presented in Fig. 3. The figure gives the measurement error of ± 0.4μm.

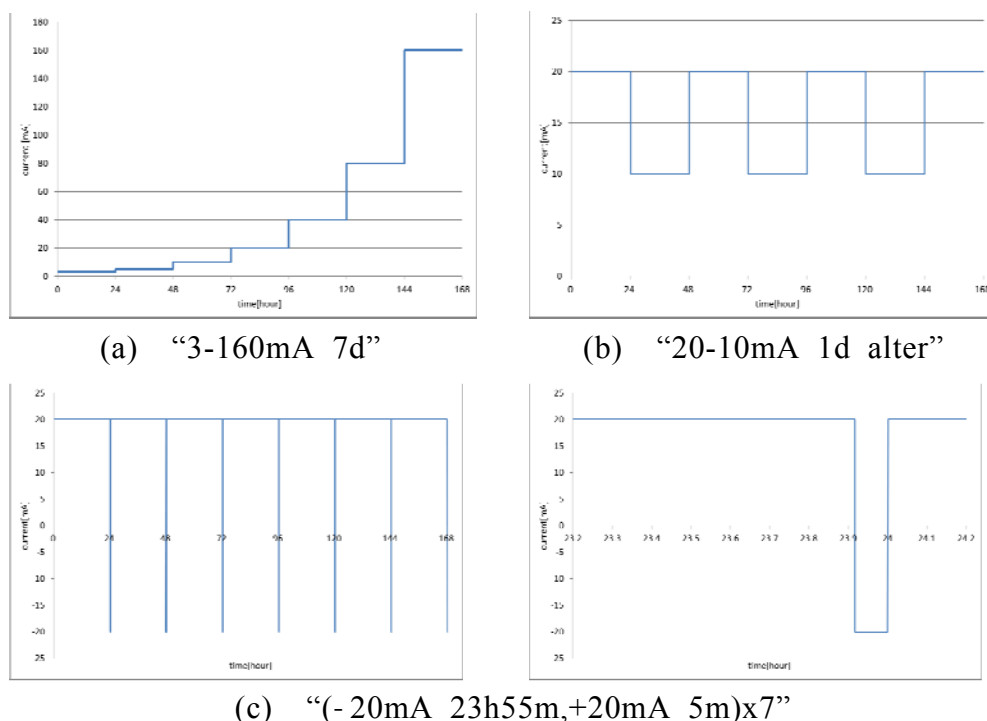


Fig. 4. Periodical change in the supplied current.

2.3. Electrolysis condition

The electrolyte solutions for the heavy water electrolysis are $\text{Li}_2\text{SO}_4/\text{D}_2\text{O}$ and $\text{LiOH}/\text{D}_2\text{O}$. Those for the light water electrolysis are $\text{Li}_2\text{SO}_4/\text{H}_2\text{O}$, $\text{LiOH}/\text{H}_2\text{O}$, $\text{Na}_2\text{SO}_4/\text{H}_2\text{O}$ and $\text{LiCl}/\text{H}_2\text{O}$. Most of the experiments are performed using 0.1-M solutions, as shown in the second column of Table 1.

The electrolysis experiment is performed under total 20 electrolysis conditions for H_2O and/or D_2O solutions, which are compiled into Table 1. There are 10 DC current patterns in the 20 electrolysis conditions. The patterns are designated “20mA · 20m”, “20mA · 7d”, “100mA · 7d”, “160mA · 1d”, “160mA · 3d”, “3-160mA · 7d”, “20-10mA · 1d · alter”, “50-80mA · 1d · alter”, “(-20mA · 20m, +20mA · 5m) x 8” and “(-20mA · 23h55m, +20mA · 5m) x 7”, as given in the third column of Table 1. The “20mA · 20m” and “20mA · 7d” mean that the application current is constant DC 20 mA for 20 m and one week, respectively. The “100mA · 7d” means that the application current is constant DC 100 mA for one week. The “160mA · 1d” and “160mA · 3d” mean that the application current is constant DC 160 mA for 24 h and 72 h, respectively. The “3-160mA · 7d” means that DC is changed from 3 to 160 mA in stepwise every 24 h for one week, as illustrated in Fig. 4(a). The “20-10mA · 1d · alter” means that the application current alternates between 20 and 10 mA every day with negative cathode, and ends with 20 mA, as illustrated in Fig. 4(b); the total electrolysis time is 168 h. The “50-80mA · 1d ·

alter” means that the current alternates between 50 and 80 mA every day with negative cathode, and ends with 50 mA; the total electrolysis time

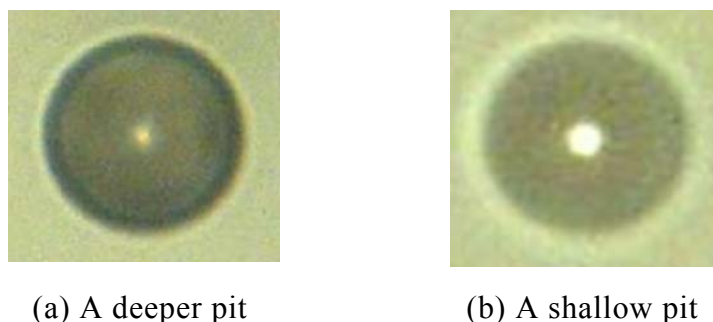


Fig. 5. Photomicrograph of the etch pit.

is 168 h. The “(-20mA·20m,+20mA·5m)x8” consisted of 8 cycles; the application current is DC 20 mA with negative cathode for 20 min, followed by DC 20 mA with positive cathode for 5 min in each cycle. Thus, the total electrolysis time is 200 min. The “(-20mA·23h55m,+20mA·5m)x7” consisted of 7 cycles; the application current is DC 20 mA with negative cathode for 23 h and 55 min, followed by DC 20 mA with positive cathode for 5 min in each cycle, as illustrated in Fig. 4(c). The total electrolysis time is 168 h.

3. RESULT AND DISCUSSION

3.1. General aspect

The experiment is usually performed ~5 runs for each electrolysis condition. The pits are counted only within the inside area bounded by the scratched 10×10 mm square line on the front surface of the CR-39 chip, as mentioned above. The number of pit in the inside area is compared with that found in the control chip. It may generally be necessary to distinguish nuclear pits produced during electrolysis from artifacts caused by manufacturing defects in the detector plastic. The appearance of the nuclear pits has generally been thought to have much darker wide rim in the microscope. Because the pit has a relatively deeper bottom and the diameter of the bottom is rather small compared with that of the rim; Fig. 5(a) shows a typical photomicrograph of such pit. In addition, there still exist many ambiguous pits whose origin, nuclear or artifactual, is hardly determined. Accordingly, the etch pits with narrow darker rim, as typically shown in Fig. 5(b), are not excluded in counting in this study; all the etch pits observed are counted. Namely, the pits with shallow form having narrow darker rim in the microscope are distinguished from those with deeper bottom having much darker wide in this study. They are classified into two types; one with shallow form and the other with deeper bottom are designated as “U” and “V”, respectively in the following figures. About one out of 20 pits is difficult to distinguish between “U” and “V”.

The control experiment is expected to give some nuclear tracks already present in the CR-39 sheet as received from the supplier, as well as those produced during the entire experimental process by radioisotopes such as radon in the

environment. Further, some of the pits originating from manufacturing defects will unavoidably have a similar form to that of nuclear pits. For instance, one of the lot

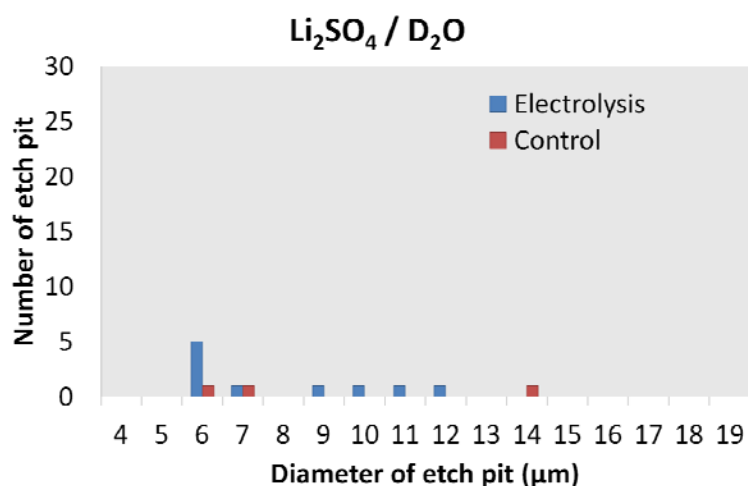


Fig. 6. Distribution of etch pit diameter, indicating no difference in number of etch pit between electrolysis and control experiment.

of CR-39 sheets has provided higher density of etch pit in almost all the control CR-39 chips from the beginning [8].

The result for all the 20 electrolysis conditions is compiled into the last column of Table 1 as the blank and the ratio of number of the impressive runs to that of total runs. The blank indicates that all the runs have given negative result. Most of the experiments under 20 electrolysis conditions using both solutions have presented no apparent increase in number of etch pit as well as no apparent difference in the distribution of etch pit diameter between the electrolysis and control experiments. Fig. 6 shows such typical relation between total number and the diameter of the etch pit for an electrolysis and the corresponding control experiment. The electrolysis has been carried out by constant DC 20 mA application for 168 h with Li₂SO₄/D₂O solution, in this case. In general, there are many ambiguous runs hard to be excluded from positive result at any electrolysis condition. These results describe that a summing up the number of etch pit, over a series of experiment for a fixed electrolysis condition, would suppress an appearance of the characteristics of the LENR.

Consequently, we have focused our interest on only the impressive positive result. Figures 7 and 8 show the relation between the numbers of etch pit and the time interval from the supplying of the track detector sheet to the beginning of the experiment for the control and electrolysis experiment, respectively. The total number of chip obtained for control and experiment is 155 and 203, respectively. The maximum number of etch pit for the control chip is 29, as seen in Fig. 7. Therefore, the impressive positive number of etch pit is designated as more than 87, which is 3 times larger than 29.

The maximum time interval for the control chip is 200 days, as seen in Fig. 7. The corresponding chips show no considerable increase in number of etch pit. The

sheet, from which those chips are cut, has been supplied 104 days after the production. This implies that the chips keep generally a stable condition for 304 days from the production to the beginning of the experiment.

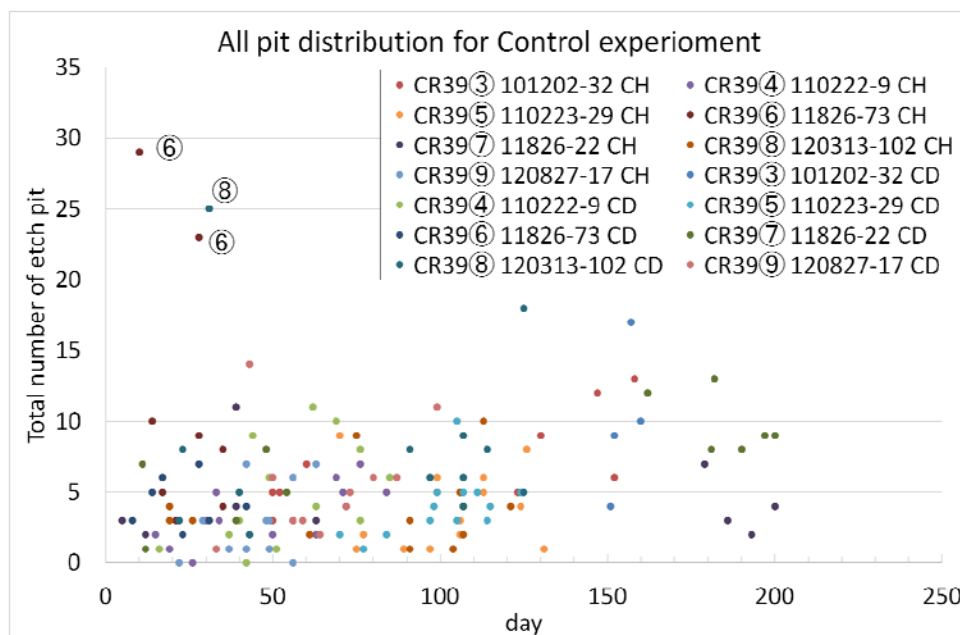


Fig. 7. The relation between the numbers of etch pit and the time interval from the supplying to the beginning of the experiment for the control chip.

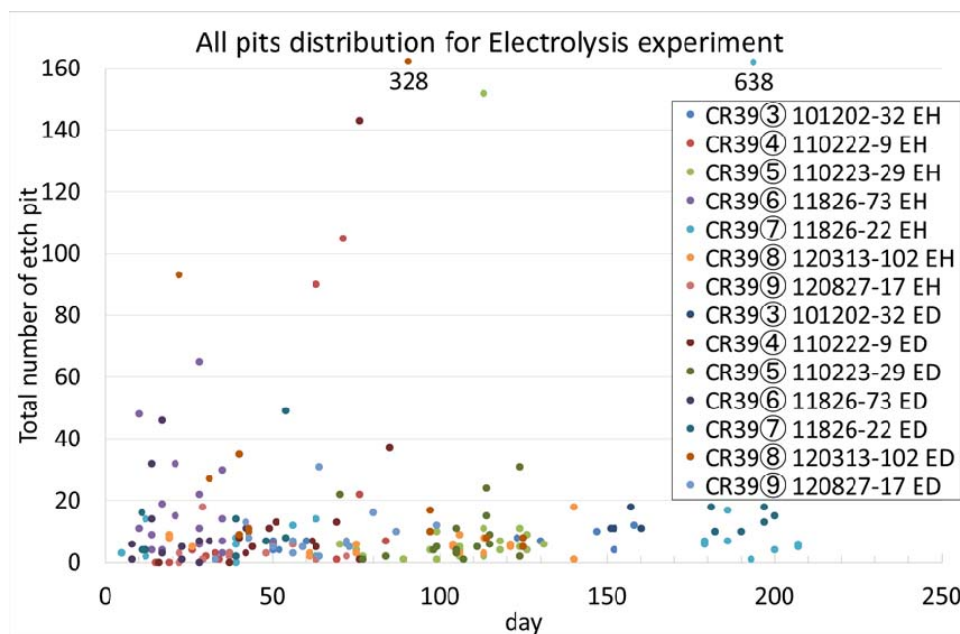


Fig. 8. The relation between the numbers of etch pit and the time interval from the supplying to beginning of the experiment for the electrolysis chip.

3.2. Anomalous result

The marked difference in number of etch pit between electrolysis and control experiment has been observed in one out of 9 electrolysis conditions for D₂O

solution. The only significant difference is obtained from the current pattern “(-20mA·23h55m,+20mA·5m)x7” by the Li₂SO₄/D₂O electrolysis, as presented in

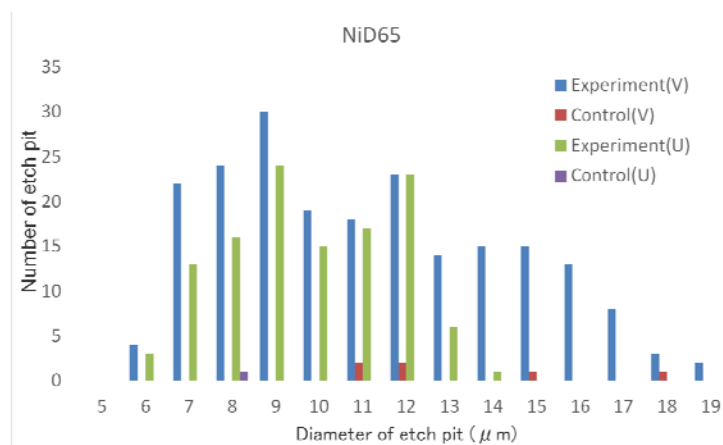


Fig. 9. Distribution of etch pit diameter for Li₂SO₄/D₂O electrolysis by the current pattern “(-20mA·23h55m,+20mA·5m)x7”, indicating an impressive increase in number of etch pit between electrolysis and control experiment.

Table 1. Fig. 9 provides the distribution as the relation between total number and the diameter of the etch pit for one of the electrolysis and the corresponding control experiments under the current pattern. It is seen in the figure that the number of etch pit for electrolysis is quite different from that for control experiment. Besides, there exists no peak in the distribution for the control chip, similar to that in Fig. 6. While a semi-Gaussian distribution of etch pit diameter rang 6-19 μm is seen for the electrolysis chip. Such impressive increase and similar distribution of etch pit are observed in 3 out of 6 runs under the same electrolysis condition, as given in last column of the table. It should be pointed out that the etch pit with diameter range 5-20 μm has been commonly observed both on the electrolysis and control chips. This indicates that the origin relating to the etch pit with diameter range 5-20 μm could easily be produced in the chip by several causes regardless of control or electrolysis experiments.

The impressive increase in number of etch pit has been occasionally observed in 3 out of 15 electrolysis conditions for H₂O solution. Such increase has been obtained commonly using the current amplitude of 160mA. The distributions of all the 4 anomalous results for the H₂O solution are shown in Fig. 10-13. As the number of the pit on the control chip is commonly small compared with that for the electrolysis one, the date of the control is excluded from these figures. A significantly large number of etch pit with the diameter range 4-15 μm has been observed for LiOH/H₂O electrolysis, as shown in Fig. 13, even though the impressive increase has taken place in one out of 5 runs. Only 2 etch pits have been observed in the corresponding control chip. Contrary, considerable large number of 638 has been observed on single CR-39 chip for electrolysis experiment; it presents rare but possible feature. Similar semi-Gaussian distribution to that in Fig.

9 is seen in the Fig. 13. The number density of etch pit in the area out of P-18 O-ring, shown in Fig. 2, is almost same as that on the control chip. It is interesting

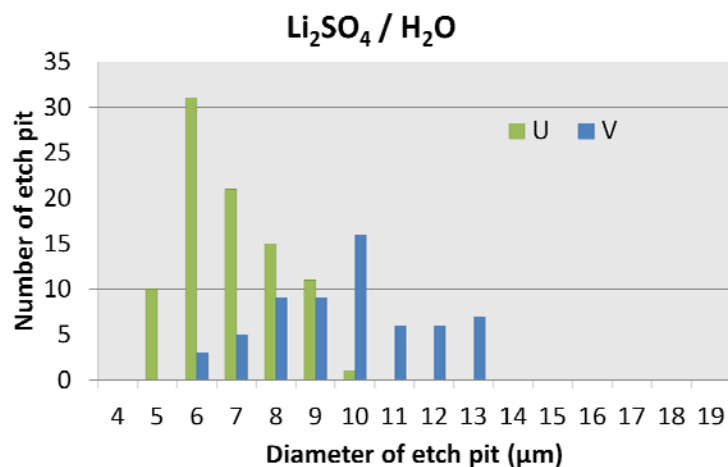


Fig. 10. Distribution of etch pit diameter with an impressive increase in number of etch pit for $\text{Li}_2\text{SO}_4/\text{H}_2\text{O}$ electrolysis by the current pattern “160mA·3d”.

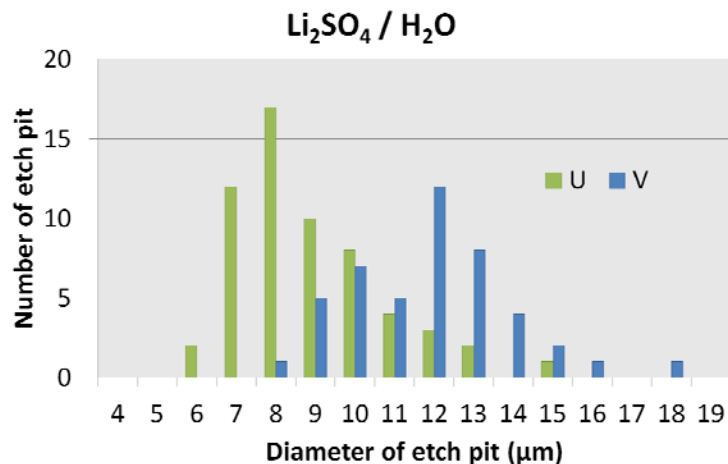


Fig. 11. Distribution of etch pit diameter with an impressive increase in number of etch pit for $\text{Li}_2\text{SO}_4/\text{H}_2\text{O}$ electrolysis by “3-160mA·7d”.

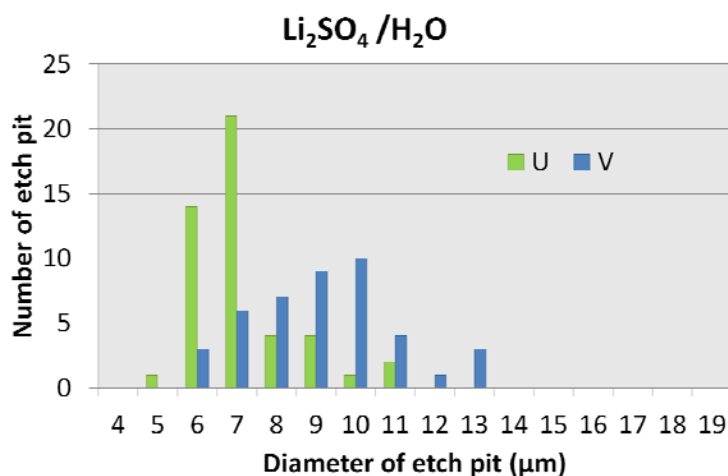


Fig. 12. Distribution of etch pit diameter with an impressive increase in number of etch pit for $\text{Li}_2\text{SO}_4/\text{H}_2\text{O}$ electrolysis by “3-160mA·7d”.

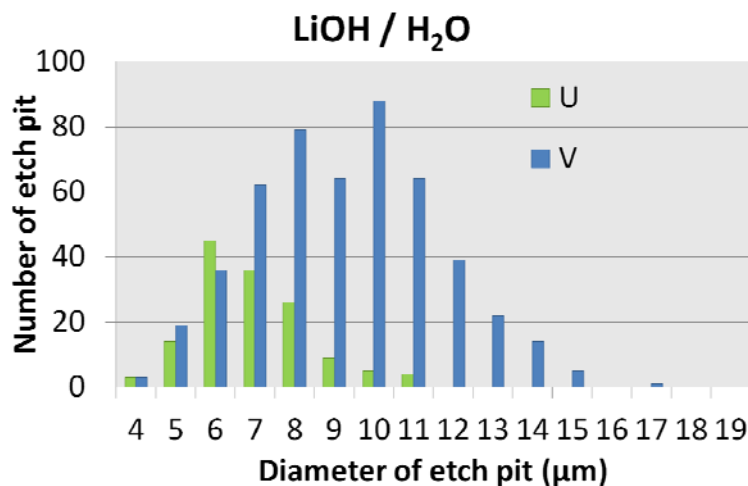


Fig. 13. Distribution of etch pit diameter with an impressive increase in number of etch pit for $\text{LiOH}/\text{H}_2\text{O}$ electrolysis by “3-160mA·7d”.

to note that the distribution of “U” looks different from that of “V”. There exists a possibility that the two distributions correspond to two particles with different energies of the order of MeV.

It is demonstrated that the impressive increase in number of the etch pit on the CR-39 chips could be attributed to a nuclear process occurring at the Ni film electrode in the operating electrolysis cell. The common key factors to increase the number of the anomalous etch pit for both D_2O and H_2O solutions might be Ni film cathode, the electrolysis time more than the order of 10 h and Li in the electrolyte solution. The diffusion constant of D/H in Ni is so small that the density of D/H in near the surface of Ni film cathode could be saturated in relatively short time. Therefore, the density of D/H in the uppermost surface region of Ni film might become large enough to trigger the LENR after the time of the order of 10 h from the beginning of electrolysis.

It has already been confirmed that the current flowing through the metal cathode, mechanical stirring of solution and the solution temperature have no effect on producing tracks [6]. The DC 160 mA application increases the temperature of the solution from room one to 43 . To the contrary, the 20 mA application does not change the solution temperature. Thus, the anomalous positive result for D_2O electrolysis at the condition “(-20mA-23h55m,+20mA-5m)x7” has revealed again that the change in the temperature does not account for the anomalous increase of the number of the etch pit.

4. CONCLUSION

A simple experimental technique using a thin Ni film in conjunction with the track detector CR-39 is presented to detect energetic charged particles produced by

a nuclear reaction in heavy and light water electrolysis. Impressive increase in number of etch pit has been observed in one out of 9 and 3 out of 15 electrolysis conditions for D₂O and H₂O solutions, respectively.

The result suggests a LENR occurring on the Ni film cathode during the light water electrolysis as well as the heavy water one. The common factors to increase number of the anomalous etch pit on the CR-39 chip might be Ni film cathode, the long electrolysis time and Li in the electrolyte solution. All the results indicate a characteristic of LENR in the electrolysis that the reaction does not always takes place in every electrolysis experiment but occasionally does under the same experimental condition.

ACKNOWLEDGMENT

This work is financially supported by a Grant-in-Aid for a Challenging Exploratory Research (23656205) in the Scientific Research Foundation from MEXT in Japan.

REFERENCES

- [1] R. A. Oriani et al., Jpn. J. Appl. Phys., Vol. 41, p. 6180 (2002)
- [2] R. A. Oriani, Proc. 14th Int. Conf. Cold Fusion, p. 250 (2008)
- [3] A. G. Lipson et al., Proc. 10th Int. Conf. Cold Fusion, p.539 (2003)
- [4] A. G. Lipson et al., Proc. 11th Int. Conf. Cold Fusion, p. 324 (2004)
- [5] A. S. Roussetski, Proc. 11th Int. Conf. Cold Fusion, p. 274 (2004)
- [6] H. Yamada et al., Proc. 10th Meeting of Japan CF Research Society, p. 41 (2010)
- [7] H. Yamada et al., Proc. 11th Meeting of Japan CF Research Society, p. 41 (2011)
- [8] K. Mita et al., Proc. 12th Meeting of Japan CF Research Society, p. 43 (2012)

D(H)-Cluster Langevin Code and Some Calculated Results

Akito Takahashi^{1*} and Daniel Rocha²

¹Technova Inc., Tokyo Japan, ²Rio de Janeiro, Brazil

*akito@sutv.zaq.ne.jp [Technova-6201-NT-21]

[Abstract]

A PC code based on the quantum mechanical Langevin equation to simulate dynamic motion of deuterium (or hydrogen) cluster with three dimensional symmetry has been developed for studying very fast condensation or oscillation behavior in time-step of 0.001 as (1.0E-21 second) for overall time interval of several fs to 500 fs. Some numerical results are typically shown for two cases of condensation behavior; 1) reaching to ground state oscillations as for $D(H)_2^+$ ion molecule, $d\mu d$ muonic molecule, $3D^+$ ionic molecule, $6D/OSC$ and others, and 2) making fast collapse to get in the strong/weak nuclear interaction range of d-d (or p-p) inter-nuclear distance as for $4D(H)/TSC$, $6D(H)/Rhombic-dodecahedron$, $8D(H)/Rhombic-dodecahedron$ and $20D(H)/Rhombic-triacontahedron$.

Keywords: PC code, D(H)-cluster dynamics, ground state oscillation, fast collapse, $4D(H)/TSC$, $6D(H)-Rhombic-dodecahedron$, larger clusters, nuclear interaction, simulation of cold fusion

1. Introduction

Time dependent motion of deuterium (or protium) cluster is calculable by a computer code based on the quantum-mechanical Langevin equation [1, 2]. Especially the dynamics analyses of a three body d-e-d or p-e-p, a 5-body d-e-d-e-d or p-e-p-e-p (namely D_3^+ or H_3^+ ionic molecule) and a 8-body d-e-d-e-d-e-d-e (4D) or p-e-p-e-p-e-p-e (4H) cluster under the Platonic symmetry (TSC: tetrahedral symmetric condensate) are important to understand the underlying mechanisms of condensed matter nuclear reactions aka cold fusion [3]. The dynamic analysis is quite applicable to investigate time-dependent behavior of the three body system of d-muon-d after sticking of muon onto a d-e-d molecule. The QM Langevin method is also applicable for much larger clusters under the Platonic symmetry, such as $6D(H)$, $8D(H)$, $12D(H)$ and $20D(H)$ clusters.

We have made a generalized D(H)-Cluster Langevin Code revised from the original crude one [1, 2]. We show some typical calculations of 1) dynamic motion going to the

ground state, for systems having ground state eigen-values (namely steady molecules), 2) collapsing motion going to several-tens or smaller fm size transitory condensates which may cause very enhanced multi-body nuclear interactions by strong (for D) or weak (for H) boson exchange (namely multi-body fusion), and 3) oscillation motion of EQPET clusters with electron Cooper pair and quadruplet [1, 2].

A muonic d- μ -d system converged in 8.3 fs to its ground state with the inter-nuclear d-d distance of 790 fm (0.79 pm) after approximately 80 oscillations from the time when a muon stuck onto a d-e-d state with 138 pm d-d distance of the electronic D₂⁺ molecule ground state. A 4D(H)/TSC cluster collapses to the “nuclear interaction size” (20 fm to 4 fm) in 1-4 fs depending on the adoption of different type of trapping potential functions (Vs2 or Vs1 potential, for instance), always. The Rhombic dodecahedron of 6D(2-) and the Rhombic triacontahedron 20D(8+) may collapse into the nuclear interaction size. Some other examples are also shown. A list of BASIC program of the Cluster Langevin code is given in Appendix.

2. Basic Methodology for QM-Langevin Calculation

The idea is based on the known QM electron wave-functions for d-e-d and d-e-e-d systems to form 3 dimensional volumetric symmetry to attain stable force-balance structure. These 3 dimensional symmetry systems are an elongated di-cone and ‘regular’ di-cone, respectively for 2D⁺ and D₂ molecule [2]. The ground state QM electron wave function for a d-e-d (or p-e-p) three body system is a linearly combined two 1S wave functions [2, 4], where each 1S wave function is for each D(H)-atom ground state of the d-e-d (or p-e-p) system. In [Fig.1](#), the feature of treatment for a d-e-d system is illustrated to apply to a QM Langevin equation for calculating its dynamic motion. The ground state orbit of electron QM center is a circular rotating one with $R_e = \text{Bohr radius}$ (52.9 pm) around the mid-point of inter-nuclear d-d distance. The electron kinetic energy of d-e-d (or p-e-p) ground state is 13.6 eV that is the same value with 13.6 eV of electron kinetic energy of a D(H)-atom ground state. The inter-nuclear distance R_{dd} (or R_{pp}) of d-e-d (or p-e-p) ground state is 138 pm. The Coulombic trapping potential Vs1(1,1) of the d-e-d (or p-e-p) three body system is given in Appendix of Reference-[3] and also in Reference [5] and graphic view is shown in [Fig.2](#). In the previous calculations [1, 2] for 4D/TSC, we have used the Vs2(1,1) potential for D₂ molecule or its approximate function Vs1(2,2) for a bosonized electron pair. In this paper, we will use Vs1(1,1) potential for every surface (regular triangle of d-d-d or p-p-p geometry) of various kind

of polyhedrons, as a unified potential component of polyhedral D(H)-cluster as 3D(H), 4D(H), 6D(H), 8D(H), 12D(H) and 20D(H) systems.

D₂⁺ (dde) Langevin Equation

$$m_d \frac{d^2 R_{dd}}{dt^2} = -2 \frac{e^2}{R_{de}^2} + \frac{e^2}{R_{dd}^2} + \frac{m_e v_e^2}{R_e} - \frac{\partial V_s(R_{dd}, 1, 1)}{\partial R_{dd}} + f(t)$$

$$-e^2 \left\langle \frac{2}{R_{de}^2} - \frac{1}{R_{dd}^2} \right\rangle + \left\langle \frac{m_e v_e^2}{R_e} \right\rangle = 0$$

$$m_d \frac{d^2 \langle R_{dd} \rangle}{dt^2} = - \frac{\partial V_s(R_{dd}, 1, 1)}{\partial \langle R_{dd} \rangle}$$

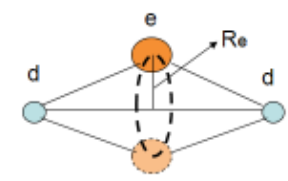
$\langle R_{dd} \rangle (\infty) = R_{gs} = 138 \text{ pm}$

Electron KE = 13.6 eV

$\langle R_{dd} \rangle = 138 \text{ pm}$
 $\langle R_e \rangle = 52.9 \text{ pm}$

Elongated Di-Cone

Electron Wave Function:
 Linear combination of 1S wave function



Technova Inc. テクノバ 6201-NT-20

Fig.1: Treatment of dynamic motion of a d-e-d three body system by a QM Langevin equation.

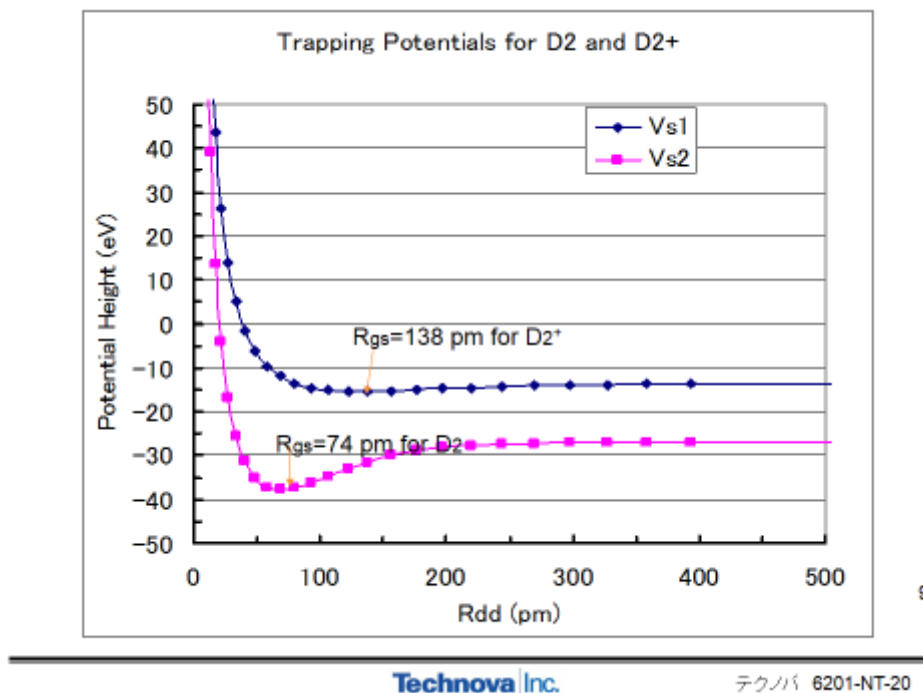


Fig.2: Coulombic trapping potential of a d-e-d system (D₂⁺), compared with D₂ one.

In this paper, all mathematical equations are only described in slide-figures. Derivations of equations for the QM Langevin method are fully given in References [2, 3]. This style of paper is chosen for aiming at easier explanation of physical processes employed for making program and computations, without getting into detail of mathematics derivations.

The case of TSC is special because of double octahedral symmetry for electron wave-function and deuteron wave-function of the TS (tetrahedral symmetry) configuration. This condition makes the usage of V_{s2} potential (derived from a combined 1S product-wave-functions [4, 5]) possible for the confinement force by electrons which have much larger de Broglie wave-length than deuteron wave length. In this paper, we employ a new rule for evaluating the friction term by electron QM-clouds in the QM-Langevin equation, that is the adoption of $V_{s1}(1,1)$ potential always for a unit of d-d-d or p-p-p regular triangle surface configuration. We think, we have obtained similar results between the old rule (ACSLENR Vol.1 paper for 4D/TSC) and the new rule ($N_f=4$, $N_e=6$, V_{s1} for 4D/TSC): the condensation time to collapse was 1.4fs and 3.6fs from 74pm to 20fm, respectively for the old and the new rule: So we may apply both rules for 4D/TSC.

When a 4D/TSC gets into the collapse region with less than about 20 fm d-d distance, strong nuclear interaction between 4 deuterons work significantly to form ${}^8\text{Be}^*$ intermediate compound nucleus by the 4D simultaneous fusion [2, 3] and time-dependent fusion rates have been calculated using the Fermi's golden rule with estimated Coulomb barrier penetration factors (time-dependent) by the HMEQPET method [2, 3]. In the case of 4H/TSC dynamic condensation, it can get into extremely collapsed state of TSC with very small inter-nuclear p-p distances as small as $R_{pp}=2\text{fm}$, and electron capture with a proton would induce weak-strong fusion reaction to form ${}^4\text{Li}^*$ intermediate compound state [1, 6, 7]. Nucleon halo models have been developed to study the final state interactions and ashes (nuclear products) [6, 7]. Major nuclear ashes are ${}^4\text{He}$ ($2.0\text{E}+11$ per joule) by the 4D/TSC fusion and ${}^3\text{He}$ and D (ca. $1.0\text{E}+12$ per joule) by the 4H/TSC WS fusion, without significant hard radiations but low energy photons (BOLEP) and very weak secondary gamma-rays, respectively.

For other combinations for 3D, 6D, 8D, 12D, 20D and so forth, we do not have the double symmetry as that of 4D/TSC. (The situation is same for any H-cluster.) So AT's idea (ACSLENRSB Vol.2 [3]) was to learn the QM electron behavior of 3D+ stable ionic molecule, for which we have experimental confirmation on 3D+ stable ion in plasma and some solutions of Schroedinger QM calculations were given [2]. The idea is to apply the confinement force of $V_{s1}(1,1)$ potential for a d-e-d (or p-e-p) three body

QM system, for a basic component per a regular triangle face of total confining potential of combined D(H) polyhedral system having many faces and edges.

It is an approximate way of QM for such complicated systems as 3D+, 6D(2-), 8D(2+), 12D(8-), 20D(8+), and so on. We need careful study by cross-checking so far if the approximate approach is rational.

Because of much larger QM wave length of electrons than d(p)'s, we need a free 'rotation space' of electron QM-orbit (to satisfy HUP: Heisenberg Uncertainty Principle) for 'expectation position' for every d-d (or p-p) dipole edge. The d-e-d (2D+) system makes stable (ground state) force-balanced system as a di-cone in 3-dimensional way: the force balance holds between the central attraction force (centripetal force to the center-of-mass point) and the centrifugal force by electron rotation (circular orbit) of expectation position around the center-of-mass point (mid-point of d-d "dipole" edge). Because of 2 electrons in 3D+ system, the circular rotation orbit can be shared for 3 d-d edges in 3-dimensional symmetric way to take balance within HUP (or electron de Broglie wave-length domain). It means, the balance is not possible in the view of classical mechanics, because only two d-d edges can share electron rotation simultaneously and the third deuteron will be kicked outside. **The HUP helps the balance for simultaneous electron sharing for 3 d-d edges and thus 3D+ can be stable quantum-mechanically.**

If we consider a 3D++ case, the regular triangle of 3d's cannot be sustained while electron is rotating around a d-d edge and therefore the third deuteron shall apart (by d-d repulsion force) from the system. Consequently, 3D++ breaks up to 2D+ (d-e-d) and deuteron. The helping force by HUP will not be enough. (We need more study here.)

Then, what will happen for 6D(2-) 3-dimensional symmetric system by 'orthogonal' combination of deuteron-octahedron and electron-cube (Rhombic Dodecahedron)?

This is our challenging problem. We think the solution by our new rule (8Nf and 12Ne) may be right. A triangle surface of deuteron-octahedron has no 'back-side' surface for an 'paired electrons' but has for an electron, so that 8 Nf will be OK as every d-d edge has sharing d-e-d type rotation orbit simultaneously to avoid break-up.

However, we are assuming that the same partial QM electron wave-function as that of the d-e-d system, namely Vs1(1,1) confining potential for a d-d pair, holds for every electron 'QM-center' on the triangle surface. The validity of this assumption shall be further studied.

For more complicated systems as 8D(2+), 12D(8-), 20D(8+), and their relative states as 'neutral' like 6D, 8D, 12D, 20D having 'fractional' net-charge of electron QM-center at a face, we do not know exactly whether the analogy of partial Vs1(1,1) friction may

hold or not.

The formulation of QM-Langevin equation for many-body polyhedral system has been derived in Reference [2]. The original form for 4D/TSC as used in Reference [3] is shown in Fig.3 with physical meaning of balance of forces between the Coulombic centripetal force, the friction by QM electron cloud and the deviation force from pure Platonic symmetry. The form of cluster trapping potential is shown accordingly.

ACS2007

TSC Langevin Equation:

$$6m_d \frac{d^2 \langle R_{dd} \rangle}{dt^2} = - \frac{11.85}{\langle R_{dd} \rangle^2} - 6 \frac{\partial V_s(\langle R_{dd} \rangle; m, Z)}{\partial \langle R_{dd} \rangle} + 6.6 \left\langle \frac{(R' - R_{dd})^2}{R_{dd}^4} \right\rangle$$

Coulombic
Centripetal
Force

Friction
By electron
Cloud

Deviation
From
Platonic symmetry

TSC Trapping Potential:

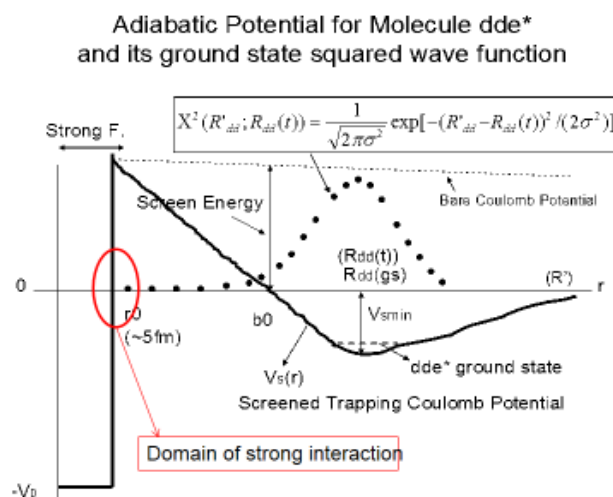
$$V_{tsc}(R'; R_{dd}(t)) = - \frac{11.85}{R_{dd}(t)} + 6V_s(R_{dd}(t); m, Z) + 2.2 \frac{|R' - R_{dd}(t)|^3}{[R_{dd}(t)]^4}$$

15

Technova Inc.

テクノバ 6201-NT-20

Fig.3: The QM-Langevin equation and trapping potential, originally used for Ref.[3] for 4D/TSC condensation motion.



Time dependent d-d pair (for nearest d and d of polyhedron) wave function is approximated with a Gaussian wave function, adiabatically which pseudo-eigenvalue can be estimated by the HMEQPET method [2, 3]. The QM weight (barrier factor) of d-d wave function to getting into the range of strong interaction (See Fig.4) is also estimated by the WKB approximation in the HMEQPET method.

Now, our general formulas of new QM-Langevin code is shown in Fig.5 for many body polyhedral system.

QM Average of Langevin Equation for D(H) Cluster

$$N_e m_d \frac{d^2 R}{dt^2} = -\frac{k}{R^2} - N_f \frac{\partial V_s}{\partial R} + f(t) \quad \text{Ne: Number of d-d edges}$$

$$N_e m_d \left\langle \Psi(R, R') \left| \frac{d^2 R}{dt^2} \right| \Psi(R, R') \right\rangle = - \left\langle \Psi(R, R') \left| \frac{k}{R^2} \right| \Psi(R, R') \right\rangle$$

$$- N_f \left\langle \Psi(R, R') \left| \frac{\partial V_s}{\partial R} \right| \Psi(R, R') \right\rangle + \left\langle \Psi(R, R') \left| f(t) \right| \Psi(R, R') \right\rangle$$

$$\Psi(R, R') = \frac{1}{\sqrt{2\pi\sigma^2}} \exp(-(R'-R)^2 / (2\sigma^2)) \quad \text{Gaussian Wave Function}$$

$$N_e m_d \frac{d^2 \langle R \rangle}{dt^2} = -\frac{k}{R^2} - N_f \frac{\partial V_s}{\partial R} + \langle f(t) \rangle \quad \text{Equation for Expectation Value} \quad 37$$

Technova Inc. テクノバ 6201-NT-20

Fig.5: general formulas of QM-Langevin method for Platonic polyhedral

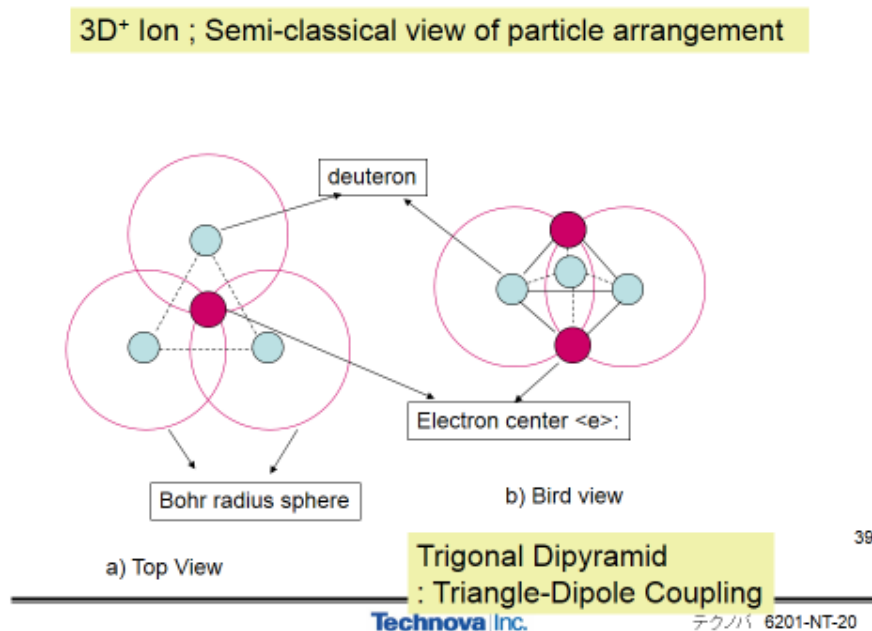
3. Some Calculated Results

A PC code as given in Appendix has been developed using Basic programming. We show some typical results and discussions in the following for 1) D(H)-clusters getting to stable ground state oscillations, 2) D(H)-clusters getting to collapses in nuclear strong/weak interaction ranges, and 3) virtual EQPET molecules with bosonized electrons.

3.1. Results for Stable D(H)-Clusters

The 3D(H)+ ionic molecule exists stably in solar plasma and accelerator ion-source plasma. The solution of the 5-body Schroedinger equation [8] has been given and

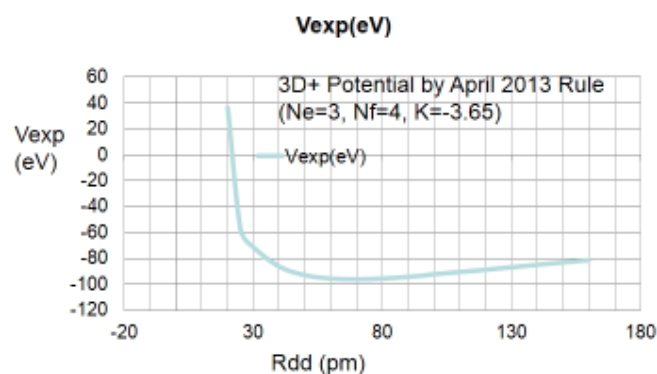
discussed in our previous paper comparing with our QM-Langevin solution, in good agreement [3]. The polyhedral structure of the 5-body d-e-d-e-d system is illustrated in Fig.6.



39

Fig.6: The polyhedral composition of 3D(H)⁺ ionic molecule

New Nf Rule by April 2013
Nf =4: (3-faces of a triangle-pyramid for e per 3 d-d edges)x2e x
2 faces of 3d-triangle for 3D+
Nf=4 :(3-faces of a triangle-pyramid for e per 3 d-d edges)x4-
faces of 4d tetrahedron for 4D/TSC



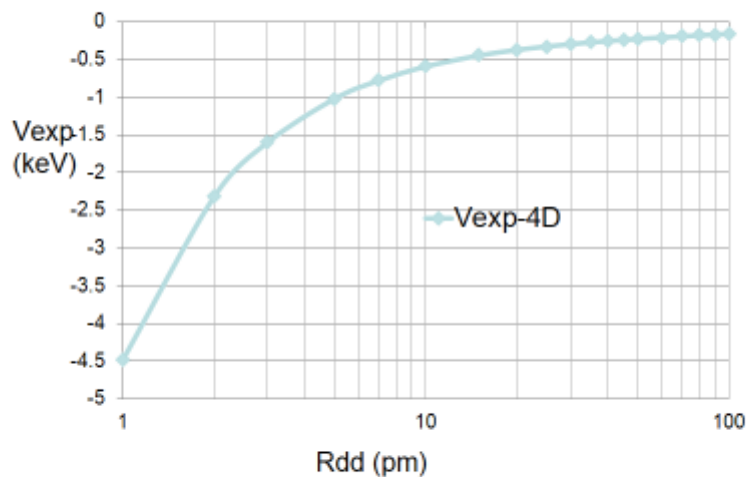
41

Technova Inc.

テクノバ 6201-NT-20

Fig.7: Trapping potential of 3D(H)⁺ ionic molecule, given by our new rule for QM-Langevin equation

4D/TS Cluster Trapping Potentials (expectation values) by April-2013 Rule



43

Fig.8: Trapping potential of 4D(H)/TSC by our new rule with Vs1(1,1)

Table-1: Three key parameters for QM-Langevin calculations for D(H)-clusters

Parameters for Langevin Cal.: for Electron Friction of Vs1(1,1)

Cluster	k value (keVpm)	Ne	Nf
2D+: d-e-d	0	1	1
3D+	3.65	3	4
4D/TS	11.85	6	4
6D/RD	18.45	12	8
8D/RD	18.45	12	6
12D/RT	15.51	30	20
20D/RT	19.11	30	12

101

Using our new rule based on components of triangle faces with $V_{s1}(1,1)$ trapping potential, the number of faces $N_f = 4$: (3-faces of a triangle-pyramid for e per 3 d-d edges) $\times 2$ faces of 3d-triangle for $3D^+$: is concluded. Its trapping potential is shown in Fig.7. The $3D(H)^+$ polyhedron has three d-d edges ($N_e = 3$). Interestingly, the $4D(H)/TSC$ has $N_f = 4$ (and $N_e = 6$) with its regular triangle surfaces, but the trapping potential shape is quite different, namely having no well-type minimum as shown in Fig.8. In Table-1, three key parameters, namely k-value of centripetal force, number of edges N_e and number of faces N_f are given for various polyhedrons. D. Rocha has calculated k-values for various configuration of polyhedral, using an excel sheet calculation by summing up all components of attractive and repulsive Coulombic potentials for possible d-d, d-e and e-e distances between QM charge centers.

The initial two oscillations of $3D^+$ cluster by the present D(H)-cluster Langevin code is shown in Fig.9.

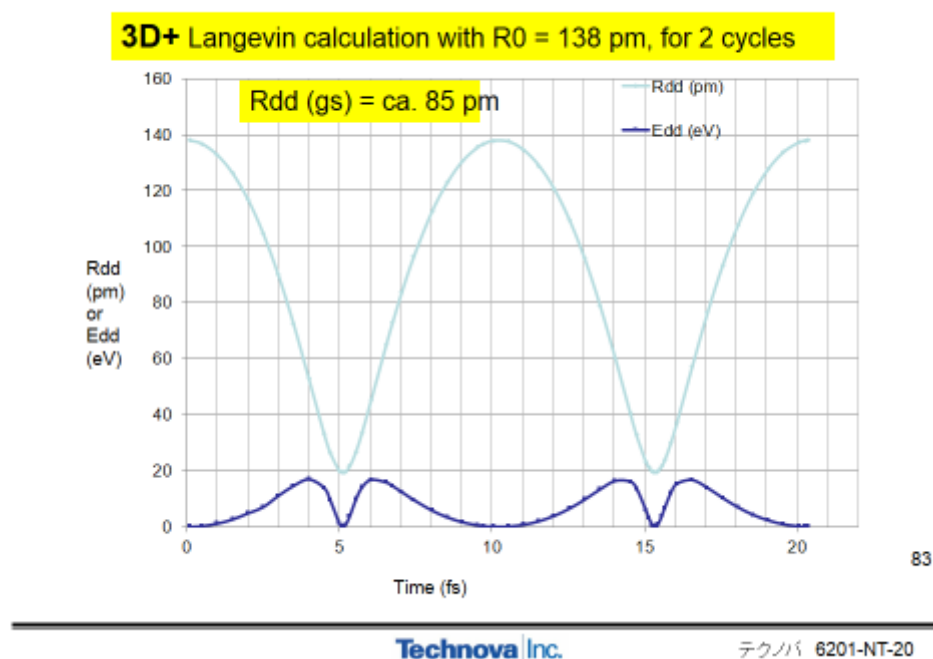
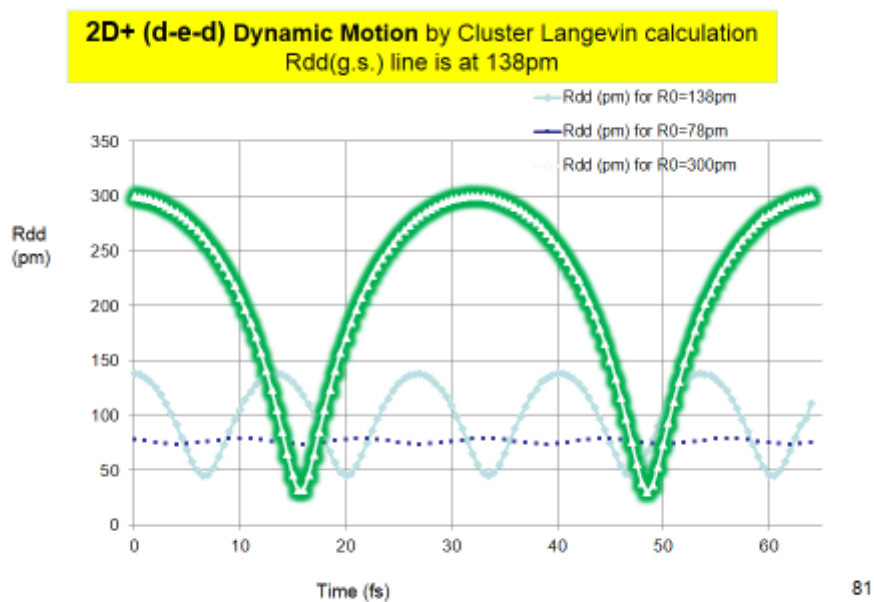


Fig.9: Initial two cycles of oscillation for $3D^+$ ionic molecule

Initial two cycles of simulated oscillation for $3D^+$ cluster is shown in Fig.9. It has the ground state with $R_{dd}(gs) = 85$ pm which is in good agreement with the result of Schrodinger equation analysis [8]. When starting calculation with $R_0 = 138$ pm, complete steady oscillation with same amplitude was attained after about 500 oscillations. Changing R_0 value around 138 pm, we have found almost the same

converging oscillation mode that is regarded as ground state.

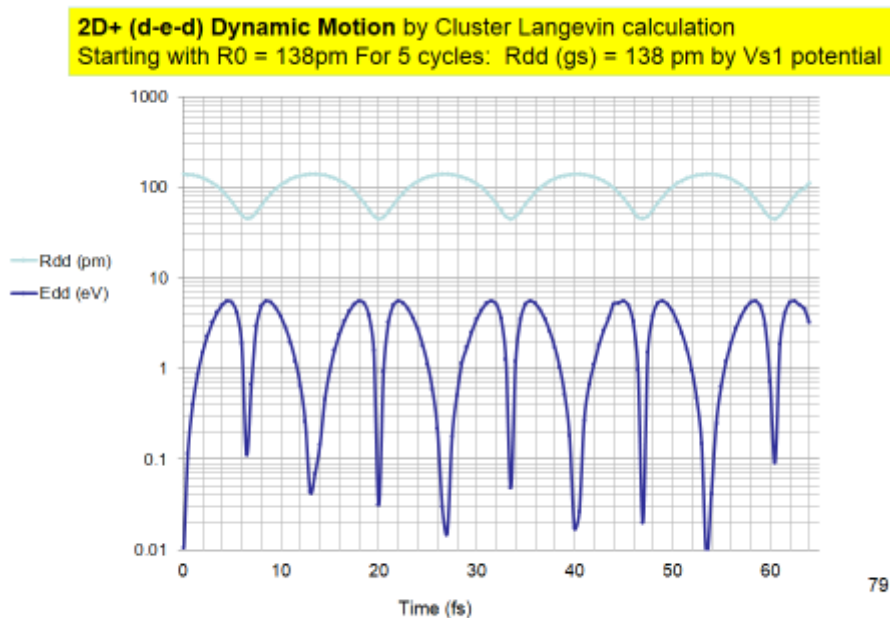


81

Technova Inc.

テクノバ 6201-NT-20

Fig.10: Initial two cycles of oscillation for 3D+ cluster started with R = 300 pm



79

Technova Inc.

テクノバ 6201-NT-20

Fig.11: Initial 5 cycles of oscillation motion for 2D+(d-e-d) ionic molecule, started with R0 = 138 pm

The simplest cluster in the present paper is a d-e-d three body system. The first two cycles by starting with $R_0 = 300$ pm is shown in Fig.10. Comparison is made with starting conditions of $R_0 = 138$ pm and 78 pm. By random sampling of starting conditions we obtain corresponding oscillation curves. The ensemble average of curves will give the ground state solution. We know the ground state $R_{dd}(gs) = 138$ pm, as already discussed in Fig.1. Initial 5 cycles of oscillating motion of $2D^+$ (d-e-d) are plotted in Fig.11 for variation of $R_{dd}(t)$ and relative kinetic energy of d-d pair.

The next interesting three body system is a muonic d-d molecule. When a muon sticks to a D_2 molecule, how does the time-dependent motion of $d\mu d$ system look like? We used trapping potential of $V_{s1}(50,2)$ that is known to be almost equivalent to $V_{s1}(207,1)$ [3]. Using the starting value $R_0 = 74$ pm, simulation by the present code has given an interesting first oscillation cycle curves as shown in Fig.12. After about 2.7 fs, there happens very sharp valley of $R_{dd}(t)$ curve and local maximum of relative d-d kinetic energy curve, the extended figure of which is drawn in Fig.13. The local minimum d-d distance there is $R_{dd} = 0.2$ pm and the local maximum relative d-d kinetic energy is ca. 3.0 keV. Next local maximum d-d distance after the first oscillation cycle is $R_{dd} =$ ca. 52 pm which is smaller than the starting value of 74 pm; namely the system is condensing.

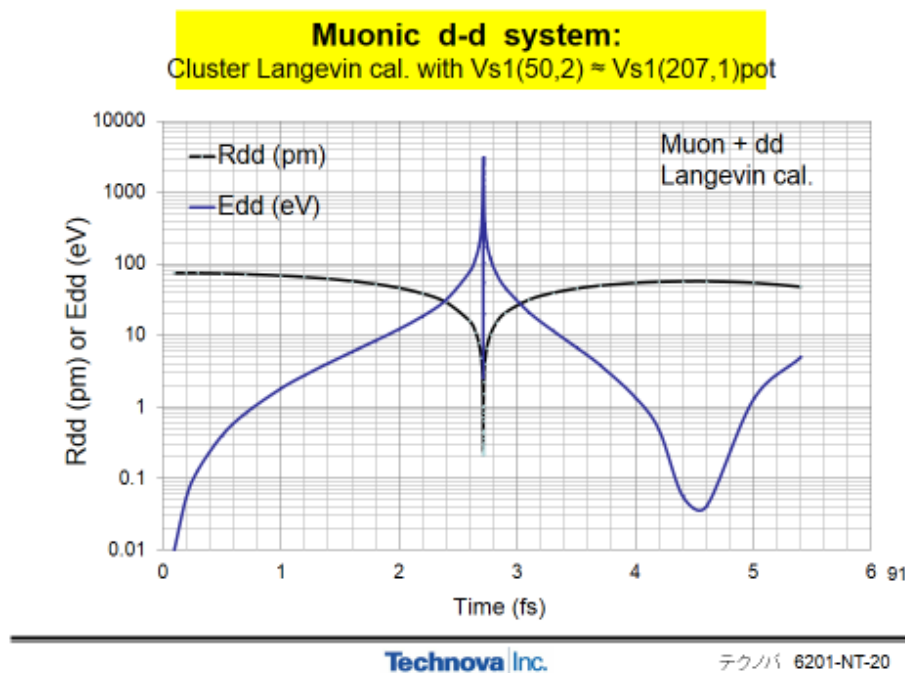


Fig.12: The initial one cycle of oscillation motion of muonic d-d molecule after sticking of muon onto a D_2 molecule.

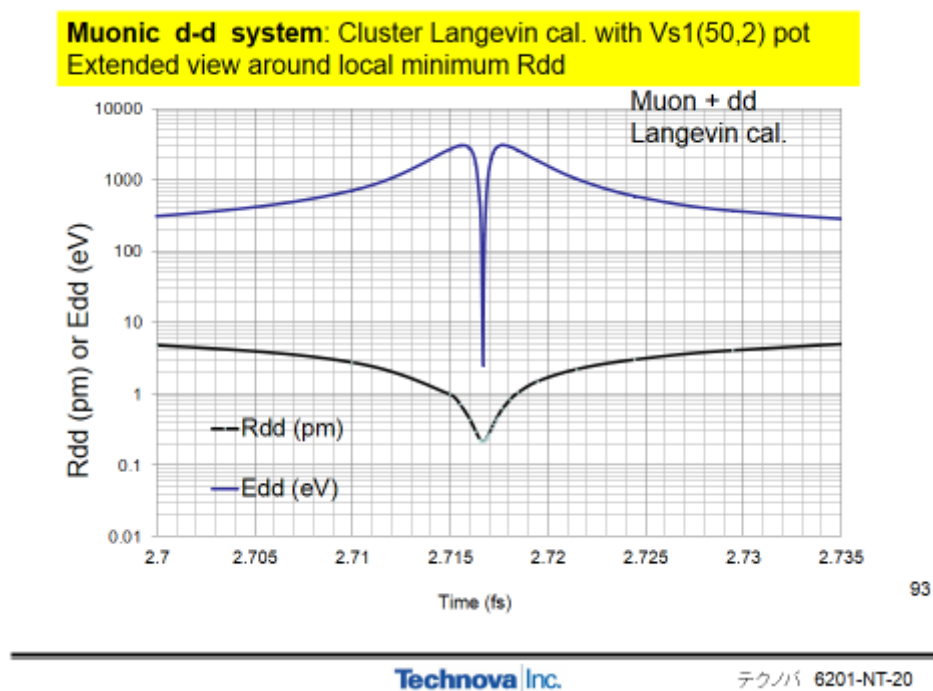


Fig. 13: Extended graph of Fig.12, for time interval around 2.7 fs

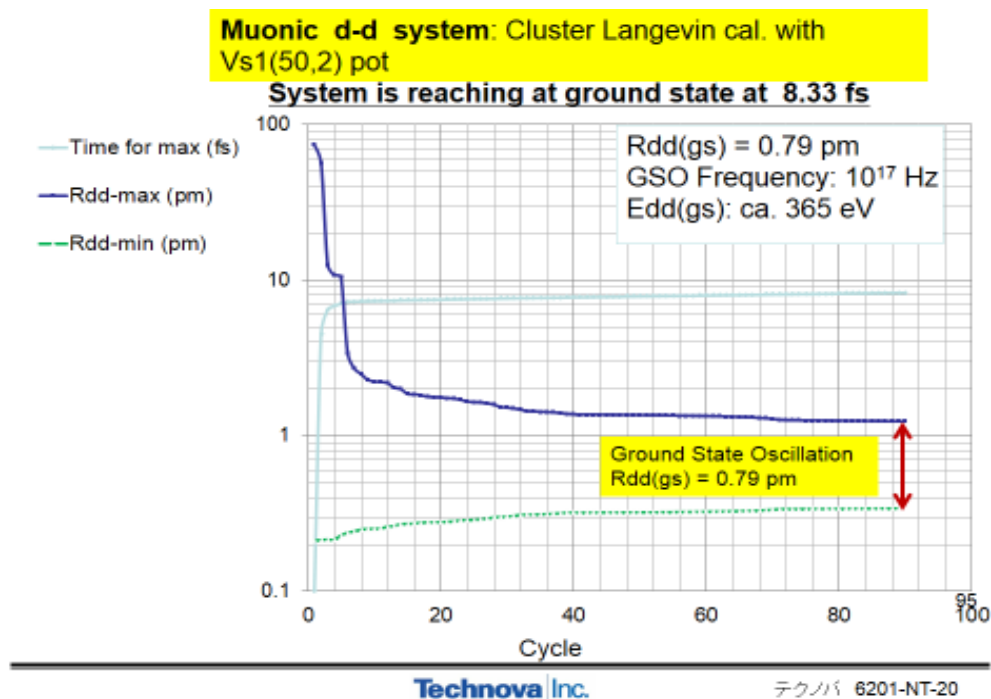


Fig.14: Condensing behavior of muonic d-d molecule after sticking of muon onto D_2 molecule. Changing starting R0 values around 100-50 pm does not effect on the converging 'ground' state.

For succeeding cycles of simulation, local maximum values of $R_{dd}(t)$ decrease and local minimum values of $R_{dd}(t)$ slowly increases as shown in Fig.14. After about 80 cycles of oscillation, it looks converging to an asymptotic oscillation that is regarded as the ground state of muonic d-d molecule with $R_{dd}(gs) = 0.79\text{pm}$. The ground state oscillation frequency is ca. $1.0\text{E}+17$ Hz and the ground state relative d-d kinetic energy is estimated as ca. 365 eV which is a double score of the previously estimated value 180 eV by the QM variational calculation with Gaussian wave function ($R_{dd}(gs)$ was 0.805 pm in that case) [9]. In the QM variational calculation [3, 9], we used a reduced mass for a d-d pair to be 1.0, while the mass of d in the present QM Langevin code is 2.0. Therefore the double score is understandable as the difference in conversion from the center-of-mass system to the laboratory system.

Now we come back to a known standard case of D_2 molecule. We know the mathematical functions [4, 5] in $V_{s2}(1,1)$ potential for trapping D_2 molecule have difficulty in numerical calculation of its derivative (field-force form) to apply to QM Langevin calculation. However, we find that $V_{s1}(1,1.41)$ potential has very close curve to that of $V_{s2}(1,1)$ as compared in Fig.15. Therefore, we can simulate an approximate dynamic motion of D_2 molecule by the present code with use of $V_{s1}(1, 1.41)$ potential. The initial two cycles of oscillation motion are drawn in Fig.16.

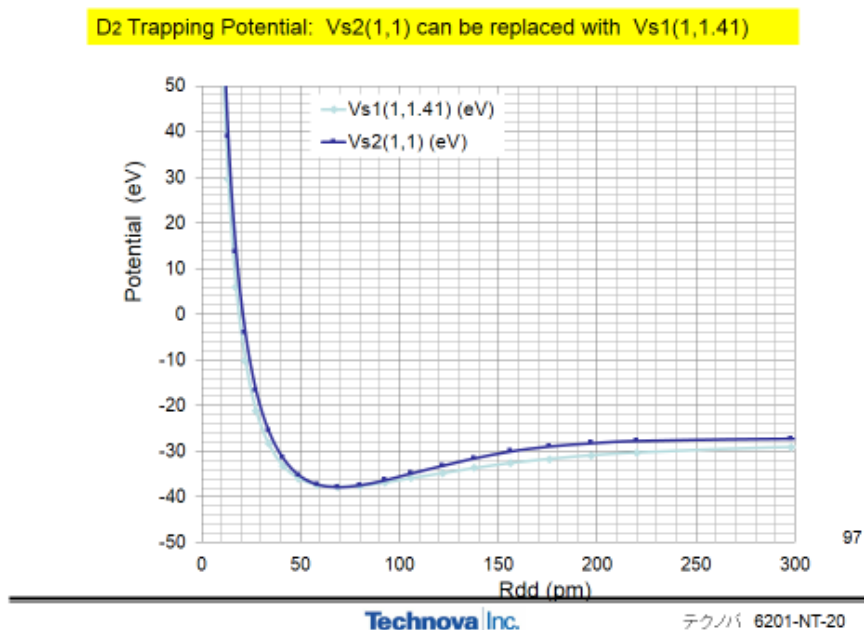


Fig.15: $V_{s1}(1, 1.41)$ potential behaves closely to that of $V_{s2}(1,1)$ potential of D_2 molecule

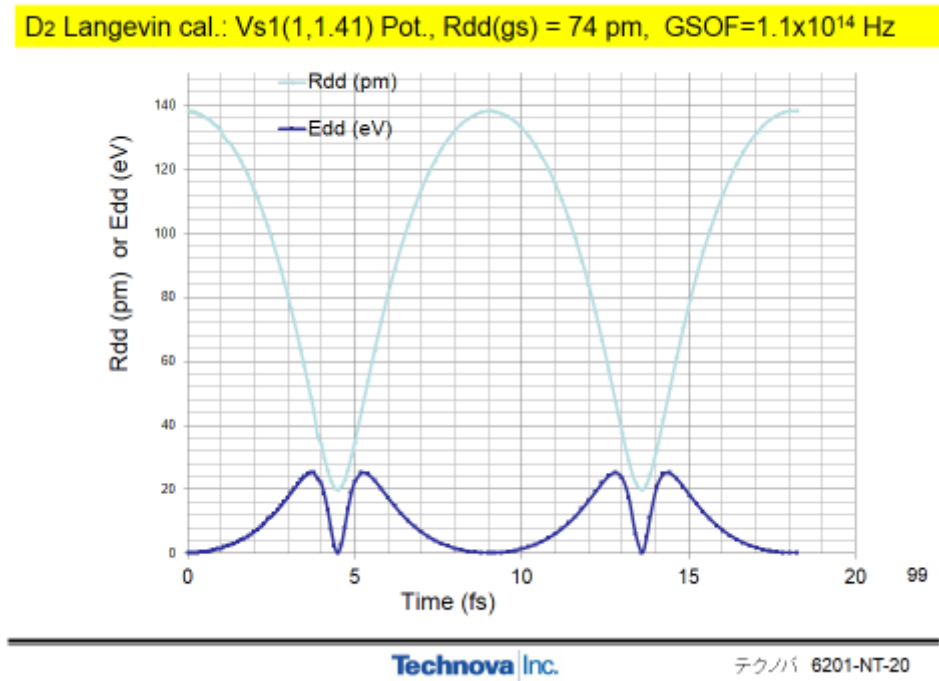


Fig.16: Initial two cycles of oscillation motion for D₂ molecule

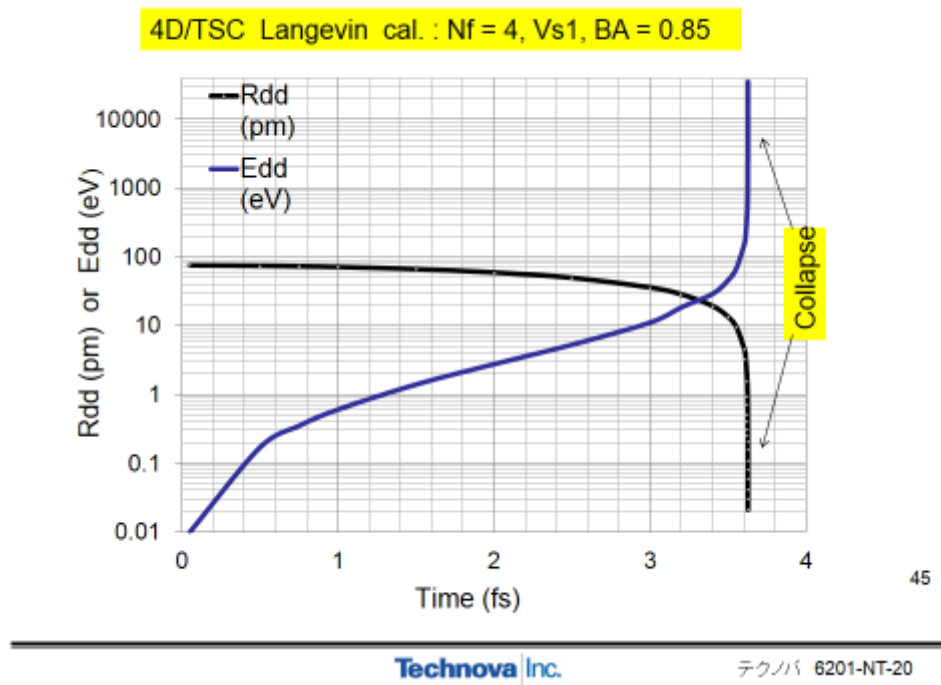


Fig.17: Condensation and collapse of 4D/TSC as simulated by the present code with the new rule for face trapping potential component

3.2. Condensation Collapse of D(H)-Cluster Polyhedron

Now we argue on the results for larger D(H)-clusters than 3D under 3 dimensional symmetry (Platonic symmetry). We have already given three key parameters for various D(H)-clusters in [Table-1](#). The result for 4D/TSC by the new rule of usage of Vs1(1,1) potential for its unit face of triangle d-d-d is shown in [Fig. 17](#). The 4D-cluster collapses at around 3.6 fs after the TS formation, while it was after 1.4 fs by using the old rule in References [2, 3] which used Vs1(2,2) potential of ‘bosonized electron pair’ on d-e-e-d surface of cubic TSC configuration.

[Fig.18](#) illustrates the feature of 6D(2-) Rhombic dodecahedron. It has 12 d-d edges (Ne = 12) and 8 triangle d-d-d faces (Nf = 8). The value of k is estimated by D. Rocha to be 18.45 keVpm. The results of simulation by the present code are shown in [Figs. 19 and 20](#). It has given collapse after ca. 4.1 fs. Near collapsing time-interval, we had to use very fine time meshes as 0.000001 fs (1.0E-21 s) as shown in [Fig.20](#). Such very small time meshes would have not been tried in the past molecular dynamics codes conventionally available: usually as (1.0E-18 s) would have been the smallest time mesh as far as tried. Therefore, usual molecular dynamics codes (or static Schrodinger equation analyses) should have missed the collapsing states of D(H)-clusters which have no static ground state eigen-values but transient condensing and collapse evolution.

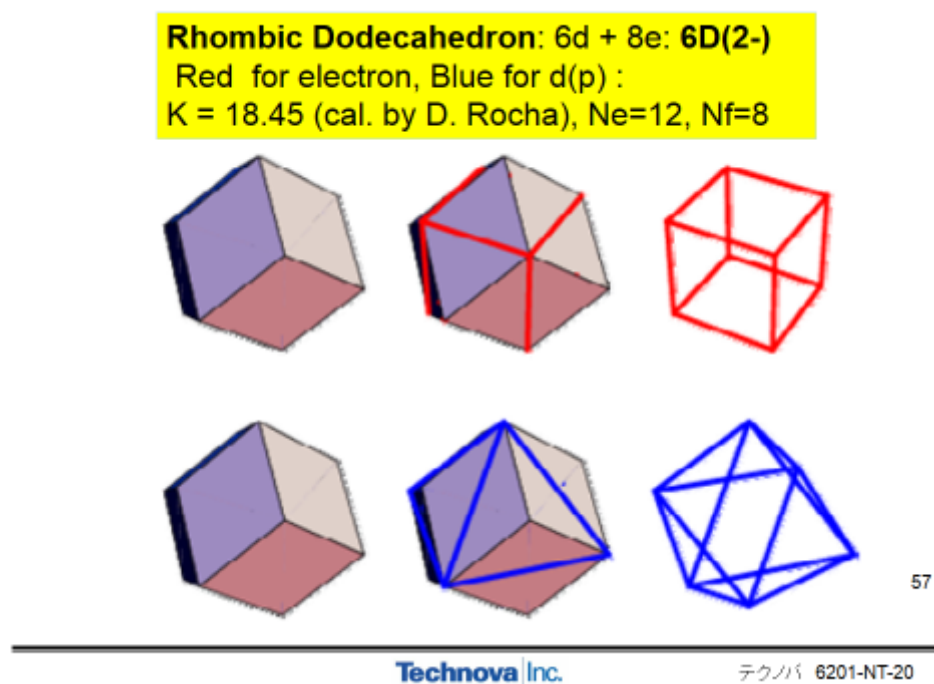


Fig.18: Rhombic dodecahedron is the polyhedron of 6D(2-)-cluster

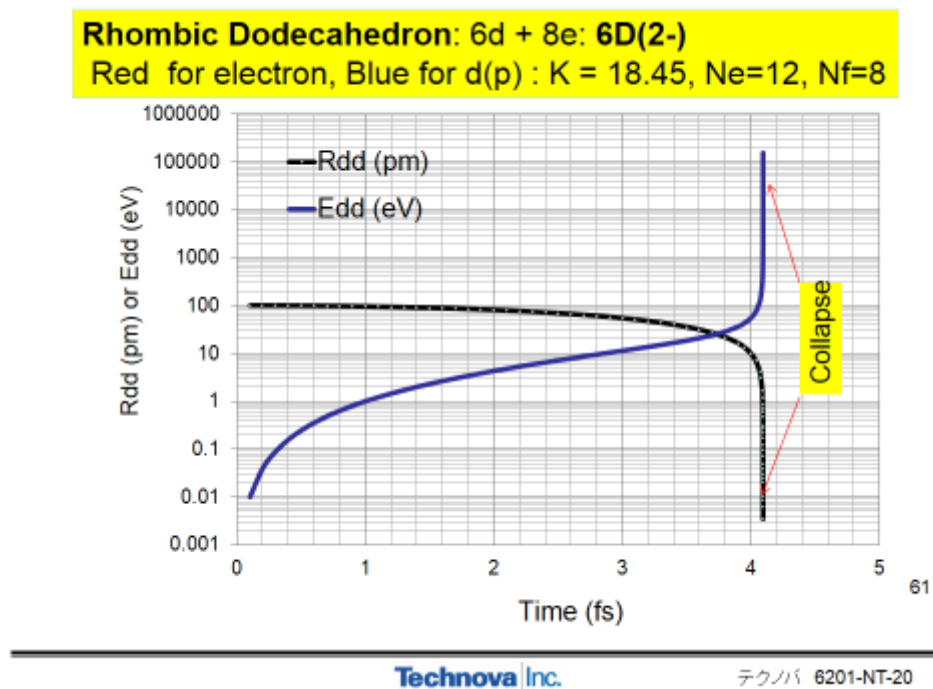


Fig.19: Simulated results of condensation motion of 6D(2-) Rhombic dodecahedron, getting to collapse after ca. 4.1 fs and maybe inducing 6D multi-body fusion

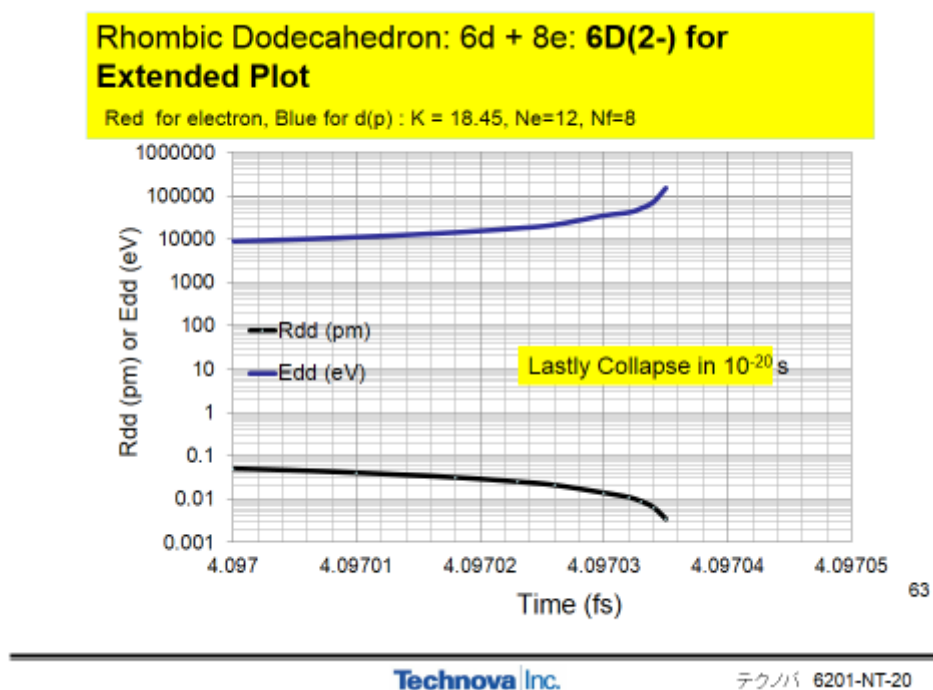


Fig.20: Extended graph of condensing evolution before collapse at around 4.097035 fs

When we exchange QM centers between electrons (red) and deuterons (blue) in Fig.18, we get 8D(2+) cluster of Rhombic dodecahedron. The result of simulation by the present code is shown in Fig.21. This 8D(2+) cluster may also collapse at ca. 3 fs after the cluster polyhedron formation.

Example for more larger D(H)-cluster is for the case of 20D(8+) cluster of Rhombic triacontahedron as its geometrical feature is illustrated in Fig.22. This 20D(8+) cluster may also collapse at around 6.5 fs after the cluster formation. What kind of strong interactions (so many body fusion?) will happen is the remained problem of nuclear physics consideration.

When we exchange QM centers between electrons (red) and deuterons (blue) of Fig.22, we get 12D(8-) cluster of Rhombic triacontahedron. The simulation calculation for the system, as shown in Fig.24, does not make collapse but converges to steady oscillation of ground state, interestingly. We tried to find that some other polyhedral cluster as 6D(2-)/OSC does not collapse either.

To summarize the results of simulation for various clusters, in the view of collapse and possible multi-body nuclear interactions, Table-2 is conclusively obtained.

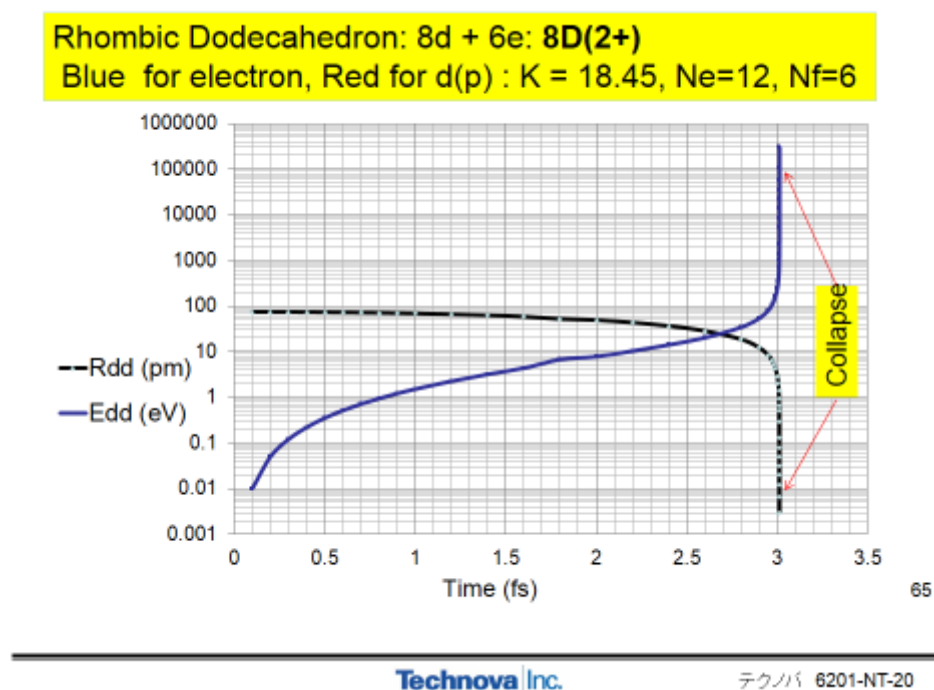


Fig.21: Results of simulation for condensation motion of 8D(2+) cluster

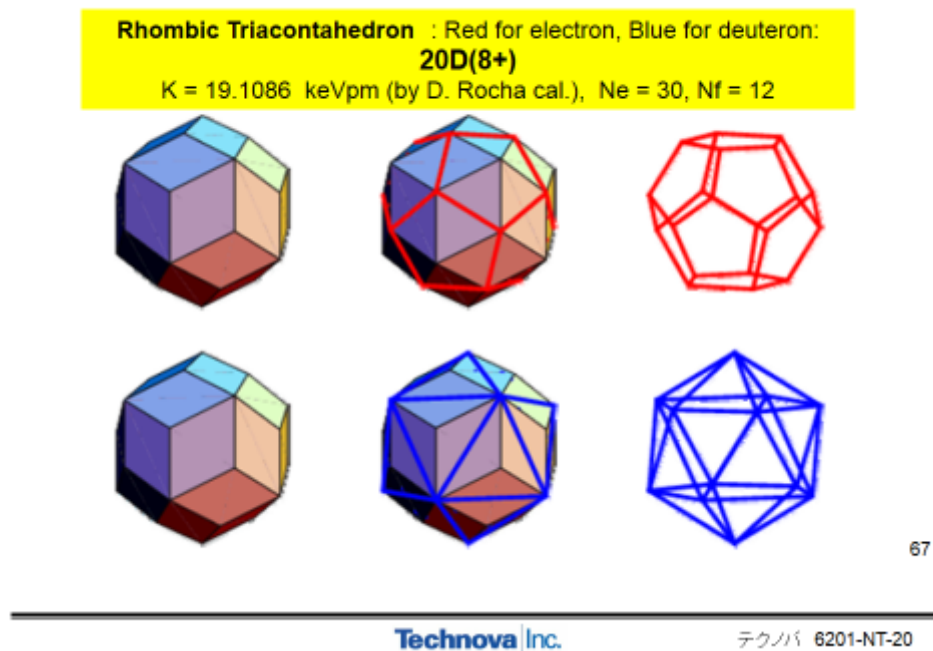


Fig.22: Geometrical feature of 20D(8+) cluster of Rhombic triacontahedron

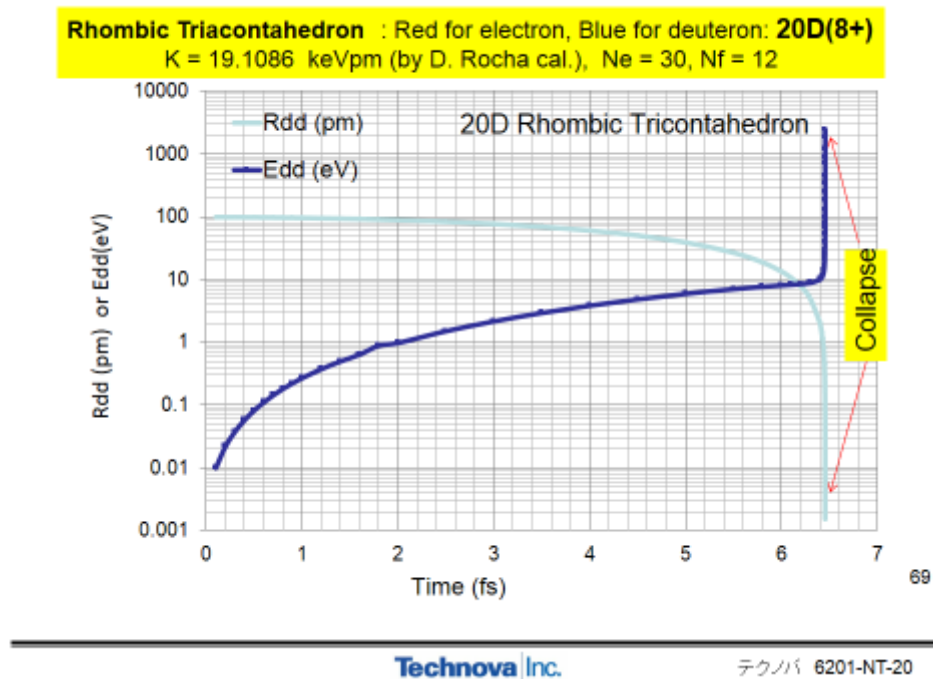
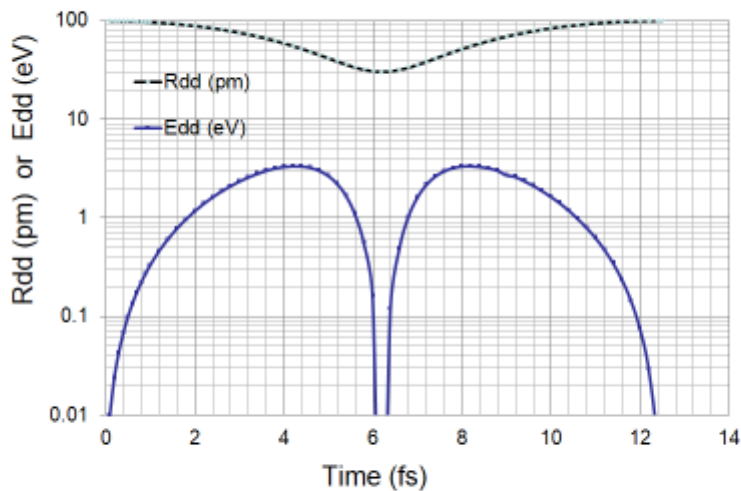


Fig.23: Results of simulation for 20D(8+) cluster of Rhombic triacontahedron

Rhombic Triacontahedron : Red for deuteron, Blue for electron: 12D(8-)
 K = 15.51 keVpm (by D. Rocha cal.), Ne = 30, Nf = 20: For one cycle



71

Fig.24: Results of simulation for 12D(8-) cluster of Rhombic triacontahedron

Table-2: Summary of condensation and collapse states for D-clusters;

Here RD denotes Rhombic dodecahedron and RT does Rhombic triacontahedron.

Summary of Results

Cluster Type	Collapse? (Rdd-min ≤ 10 fm)	Rdd (gs)	Remarks
d-e-d (2D+)	N	138 pm	
d- μ -d	N	0.79 pm	DD fusion in 0.1ns
3D+	N	85 pm	
4D/TS	Y		100% 4D fusion
6D/RD	Y		100% 6D fusion
8D/RD	Y		100% 8D fusion or 4D fusion?
12D/RT	N	ca. 80 pm	
20D/RT	Y		What kind of fusion?

103

3.3. Simulation of EQPET D(H)-Clusters

Because of the spin arrangement of electrons in D(H)-clusters of polyhedra, condensation motion may be somewhat different from above results for which the spin effect was not treated.

The anti-parallel arrangement of spins for counter-part electrons in polyhedron of D(H)-cluster, bosonized pseudo-particle state of coupled electrons were assumed in our previous study on D(H)-cluster condensation [5]. The typical bosonized pseudo-particle states of oriented electrons as assumed in reference [5] are illustrated in [Fig.25](#).

Results of simulation calculations for EQPET clusters by the present code are shown in [Figs. 26 through 29](#). In many cases, EQPET clusters have very diminished size ground states as summarized in [Table-3](#). Since these diminished size states as ground states have infinite life time and very close d-d (or p-p) inter-nuclear distances, reaction rates by strong (even weak) interactions may become significantly large to be able to argue on the possibility of condensed matter nuclear reactions aka cold fusion.

In this paper, example figures for H-systems are not specifically shown. However condensation speed is inversely proportional to mass and all figures may be rescaled for the case of H-clusters.

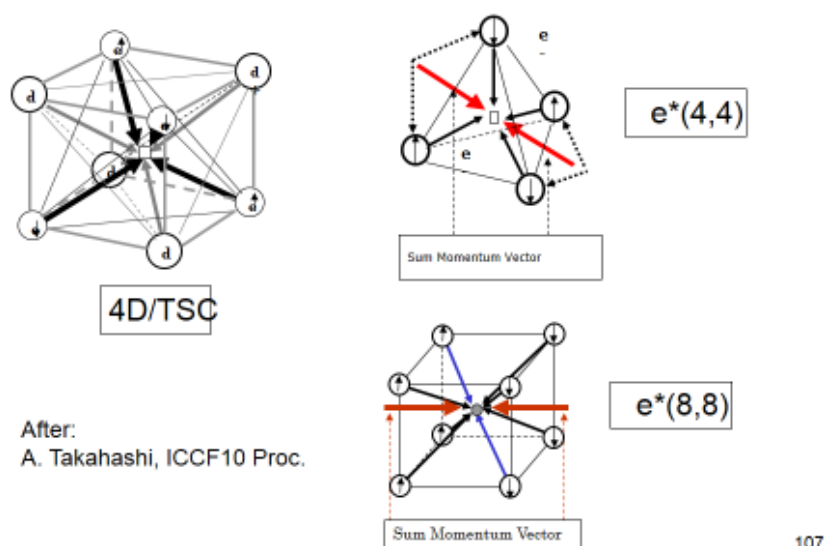


Fig.25: Assumed bosonized quasi-particles of oriented electrons

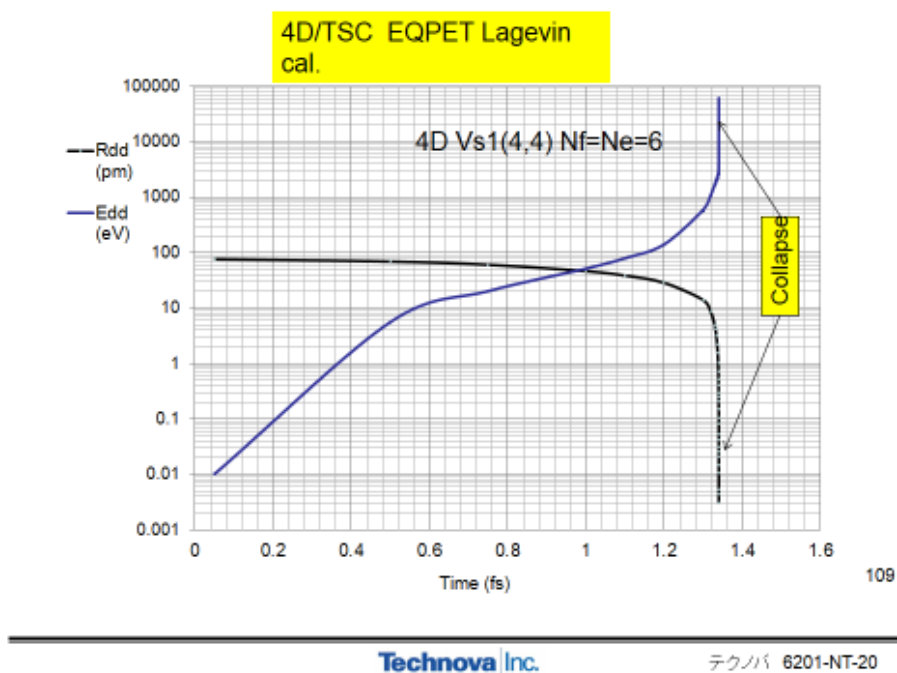


Fig.26: Results of simulation for 4D/TSC cluster with Vs1(4,4) EQPET potential

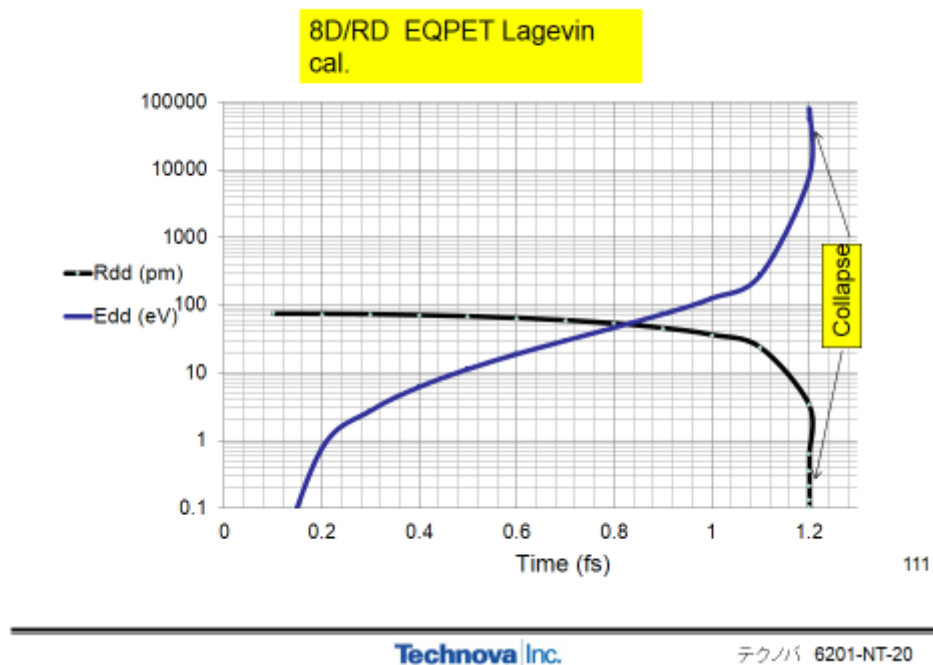
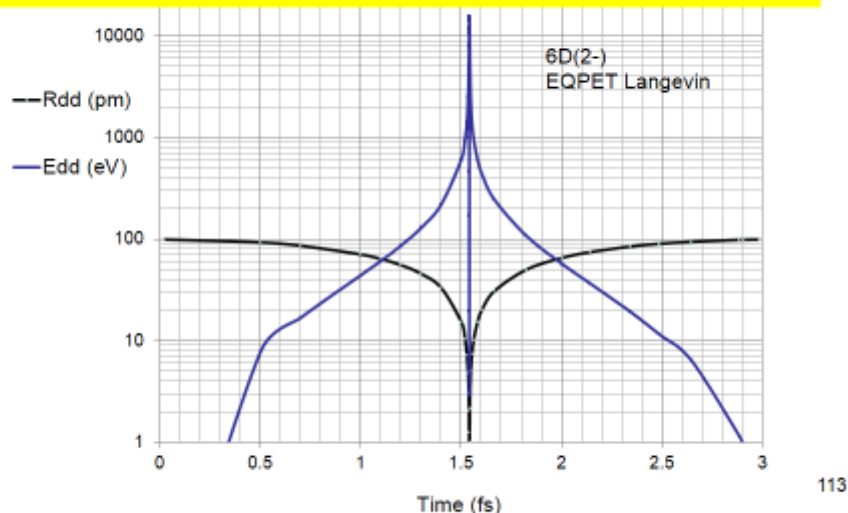


Fig.27: Results of simulation for EQPET 8D/RD cluster

6D (2-) EQPET Langevin cal.: Vs1(8,8) Potential for friction
 After ca. 300fs, it converges to the femto-molecule with Rdd(gs)
 =360fm



Technova Inc.

テクノバ 6201-NT-20

Fig.28: Results of simulation for EQPET 6D(2-) cluster with Vs1(8,8) potential, having no collapse but converged ground state of diminished size cluster (Rdd(gs) = 125 fm)

Table-3: Summary of converged ‘ground’ sates for EQPET clusters

Calculated convergence-to-Femto-Molecule
 by EQPET Langevin mode (Use dim 200000): by
 D.R.

Cluster Type	e* (m, Z)	Rdd (gs) (fm)
4D/TSC	(4,4)	None (collapse)
6D(2-)/OSC	(8,8)	360
6D(2-)/RD	(8,8)	125
6D(n)/RD	(6,6)	300 (Nf=12)
12D(8-)/RT	(20,20)	42
20D(8+)/RT	(12,12)	150

117

Technova Inc.

テクノバ 6201-NT-20

A typical example of simulation for such EQPET clusters is the cases of 4D/TSC with $V_{s1}(4,4)$ trapping potential and 8D/RD neutral-cluster with $V_{s1}(8,8)$ trapping potential. Results of simulation on condensation/collapse motion by the present code are shown in Figs. 26 and 27.

4. Concluding Remarks

A generalized PC computer code written by Basic language has been developed for making simulation calculations on very time-sensitive dynamics behavior of polyhedral D(H) clusters which transient behavior is recognized very important according to the physical mechanisms of condensed matter nuclear reactions aka cold fusion.

For realizing the frictional/constraint force components caused by the quantum mechanical motion of electrons in D(H)-cluster, the well-studied Coulombic trapping potential $V_{s1}(1,1)$ of three body system (d-e-d or p-e-p) was used as a unit of particle trapping force per a regular triangle d-d-d (or p-p-p) surface of D(H)-cluster polyhedron assuming the 3 dimensional symmetry (Platonic symmetry). Evaluating three key parameters as k-value of centripetal Coulombic force of cluster, number of d-d (or p-p) edges N_e and number of regular triangle surfaces for individual D(H)-cluster, the programmed D(H)-cluster Langevin code can be run for simulation of very precise time-dependent behavior of condensation and sometimes collapsing states.

Time steps of numerical Verlet run must be very fine as $1.0E-21$ s to find very rapidly collapsing states. Such extremely small time mesh dynamics may be new in molecular/cluster-forming dynamics codes as given conventionally. Usual time mesh calculations with a few fs or even few as time mesh should miss easily the collapse states due to the time-averaging or error accumulation in time-step sequences of numerical calculation. Of course, the eigenvalue approach by the static Schroedinger equations cannot resolve such very fast transient behavior. The developed QM-Langevin method is a unique tool that should be very usable in studying underlying dynamic mechanisms of condensed matter nuclear reactions aka cold fusion.

Summary of most important consequences in this respect of cold fusion is given in Table-2. We may conclude the polyhedral D(H) cluster such as 4D(H)/TS, 6D/RD, 8D/RD, 20D/RT have something to do with inducing dreamy cold fusion events.

Acknowledgment: Kind support to this work by Technova colleagues (A. Kitamura, R. Seto and Y. Fujita) is appreciated.

References:

- [1] Akito Takahashi: The basics of deuteron cluster dynamics as shown by Langevin equation, American Chemical Society *LENRSB (Low Energy Nuclear Reaction Source Book)* 2 (2009) 193-217
- [2] Akito Takahashi and Norio Yabuuchi: Study on 4D/TSC condensation motion by non-linear Langevin equation, American Chemical Society *LENRSB* 1 (2008) 57-83
- [3] Akito Takahashi: Physics of Cold Fusion by TSC Theory, *J. Physical Science and Application*, 3(3) (2013) 191-198
- [4] L. C. Pauling, A. Wilson: Introduction to Quantum Mechanics with Applications to Chemistry, McGraw-Hill, New York, 1935
- [5] Akito Takahashi: JCMNS, Vol.1, 62-85 (2007)
- [6] A. Takahashi, D. Rocha: Proc. JCF-13, pp.10-31 (2013), <http://jcfrs.org/file/jcf13-proceedings.pdf>
- [7] Akito Takahashi: Nuclear Products of Cold Fusion by TSC Theory, Proc. ICCF18, to be published in JCMNS (see <http://vixra.org/abs/1309.0072> also)
- [8] I. D. Petsarakis, et al.: J. Chem. Phys., 87 (1983) 3806
- [9] Akito Takahashi: Kinetic Reaction Energy of Cold Fusion, JCF-12-7, Proc. JCF-12, pp. 67-76 (2013), <http://jcfrs.org/file/jcf13-proceedings.pdf>

Appendix: D(H)-Cluster Langevin Program

- 1 ! Cluster Langevin Code (written by Akito Takahashi, revised on April 11 2013)
- 2 ! Instruction: Time-dependent motion of d-d (or p-p) distance for a polyhedral deuteron(d) or proton(p) cluster is calculated.
- 3 ! Source Literature: Akito Takahashi: The Basics of Deuteron-Cluster Dynamics as Shown by a Langevin Equation, ACSLENRSB Vol.2, Chapter 11, pp.193-217, 2009
- 4 ! the second literature: A. Takahashi, N. Yabuuchi, Study on 4D/TSC Condensation Motion by Non-Linear Langevin Equation, ACSLENRSB Vol.1, pp.57-83, 2008
- 5 ! Correction in the second literature: In Appendix, (A-4) minus is missing for K, (A-9) minus should be removed for K'
- 11 ! ms: mass number (cf. electron) of electronic quasi-particle, Z: relative charge (cf. electron)

of EQ

12 ! BA: bias factor by $\langle f(t) \rangle$ for the main centripetal Coulombic force: BA=0.91 is recommended for most cases.

16 input BA

17 print using "BA=%.#" :BA

20 input ms

30 print using "ms=%.#" :ms

40 input Z

50 print using "Z=%.#" :Z

55 ! EK is k-value (keVpm) for centripetal force, EK=3.65 for 3D+, EK=11.85 for 4D/TSC, EK=10.97 for 6D(2-)

56 ! FNf is the number of effective faces of d(or p)-polyhedron: FNf=4 for 3D+, FNf=4(for Vs1(1,1)) or 6(for Vs1(2,2) or Vs1(4,4)) for 4D, Nf=8 (for Vs1(1,1)) for 6D

57 ! FNe is the number of nearest d-d edges: FNe=3 for 3D+, FNe=6 for 4D, FNe=12 for 6D

58 ! fmrev is the inverse of d (or p)-mass: 4.77E4 for deuteron, 2*4.77E4 for proton (See the second literature).

59 ! R0 is the starting d-d distance in pm unit.

60 ! Please write-in the following parameters in line 62-66

62 LET EK=11.85

63 LET FNf=6

64 LET FNe=6

65 LET fmrev = 4.77E4

66 LET R0=74.0

69 input TDT

70 print using "DT=%.#" :TDT

100 DIM RDD(2000), R(2000), T(2000), V(2000), VS1(2000), FCOND(2000), BALANCE(2000), G(2000), ED(2000), DT(2000)

110 ! T is in (fs), R and RDD are in (pm), V is in (pm/fs), VS1 and ED are in (keV), FCOND and BALANCE are in (pm/fs/fs)

210 LET V(1)=1.0

215 LET T(1)=0.0

218 LET R(1)=V(1)*TDT

220 LET IMAX=2000

230 LET I=1

300 do while I<IMAX

305 LET DT(I)=TDT

```

320 LET RDD(I)=R0-R(I)
321 if RDD(I)<=20 then LET DT(I)=0.1*TDT
322 if RDD(I)<=5 then LET DT(I)=0.01*TDT
323 if RDD(I)<=1 then LET DT(I)=0.001*TDT
324 if RDD(I)<=0.5 then LET DT(I)=0.0001*TDT
325 if RDD(I)<=0.05 then LET DT(I)=0.00001*TDT
315 if RDD(I)<=0.001 then LET RDD(I)=0.001
330 LET y=ms*Z*RDD(I)/52.9
340 LET FJ=0.0272*Z^2*ms*(-1/y+(1+1/y)*exp(-2*y))
350 LET FK=-0.0272*Z^2*ms*(1+y)*exp(-y)
360 LET FD=(1+y+y^2/3)*exp(-y)
365 LET VS1(I)=-0.0136*Z^2*ms+1.44/RDD(I)+(FJ+FK)/(1+FD)
370 LET FJD=(5.14E-4)*Z^3*ms^2*((1.0-exp(-2*y))/y^2-2*(1.0+1/y)*exp(-2*y))
380 LET FKD=(5.14E-4)*Z^3*ms^2*y*exp(-y)
390 LET FDD=-0.0063*(y+y^3)*exp(-y)
400 LET DVS=-1.44/RDD(I)^2+((FJD+FKD)*(1+FD)+(FJ+FK)*FDD)/(1+FD)^2
410 LET BALANCE(I)=(FNf*fmrev/FNe)*DVS
420 LET FCOND(I)=(EK*fmrev/FNe)/RDD(I)^2
430 LET G(I)=BA*FCOND(I)+BALANCE(I)
500 ! Verlet Solution
510 LET R(I+1)=R(I)+V(I)*DT(I)+0.5*G(I)*DT(I)^2
512 LET RDD(I+1)=R0-R(I+1)
513 if RDD(I+1)<=0.001 then LET RDD(I+1)=0.001
515 LET y=ms*Z*RDD(I+1)/52.9
516 LET FJ=0.0272*Z^2*ms*(-1/y+(1+1/y)*exp(-2*y))
517 LET FK=-0.0272*Z^2*ms*(1+y)*exp(-y)
518 LET FD=(1+y+y^2/3)*exp(-y)
519 LET FJD=(5.14E-4)*Z^3*ms^2*((1.0-exp(-2*y))/y^2-2*(1.0+1/y)*exp(-2*y))
520 LET FKD=(5.14E-4)*Z^3*ms^2*y*exp(-y)
521 LET FDD=-0.0063*(y+y^3)*exp(-y)
522 LET DVS=-1.44/RDD(I+1)^2+((FJD+FKD)*(1+FD)+(FJ+FK)*FDD)/(1+FD)^2
523 LET G(I+1)=BA*(fmrev*EK/FNe)/RDD(I+1)^2+(fmrev*FNf/FNe)*DVS
530 LET V(I+1)=V(I)+(DT(I)/2)*(G(I+1)+G(I))
540 LET ED(I)=(0.5/fmrev)*V(I)^2
590 if RDD(I)<=0.001 then LET IMAX=I
595 if RDD(I)<=0.001 then LET RDD(I)=0.001

```


Computer Simulation of Hydrogen States around T-site in Ni, Pd and Cu Metals

Hidemi Miura
Izumi-ku, Sendai. Japan

Abstract: We simulated the hydrogen (H) states in nickel (Ni) and copper (Cu) metals using a quantum molecular dynamics on personal computers to compare with our previous simulation in palladium (Pd) metal. We calculated the total energy, charge density and electronic structure of the host bulk metal by a computer simulation program within Density Functional Theory based on the local density approximation using pseudo-potentials and a plane-wave basis. We observed similarly to the previous simulation the impurity atoms could move from O sites to T sites under the small lattice deformation such as atomic vibration at room temperature, and they could hop out from the T site pushed with increased energy of the contracted tetrahedron surrounding it.

Keywords: computer simulation, quantum molecular dynamics, tetrahedron, Ni, Pd, Cu, H states

1. Introduction

A lot of nuclear fusion and nuclear transmutation phenomena have been reported in experiments of deuterium (D) and hydrogen (H) with condensed matter. Then we have simulated the hydrogen states in palladium (Pd) metal of face centered cubic lattice using a quantum molecular dynamics on a personal computer¹⁾ in order to examine what kind of conditions cause two and more H/D atoms to gather in condensed matter such as metals and to squeeze into condensations and nuclear reactions.

This time, we simulated H states in nickel (Ni) and copper (Cu) metals using a quantum molecular dynamics on personal computers to compare with our previous simulation in Pd metal. The same kinds of simulations were done again in Pd metal using other pseudo-potentials. We calculated the total energy, charge density and electronic structure of the host bulk metal by a computer simulation program within Density Functional Theory based on the local density approximation using pseudo-potentials and a plane-wave basis in the same method with the previous simulation. We carried out simulations of H states including four of 32 occluded H atoms surrounding a tetrahedron composed of four Ni, Pd or Cu metal atoms or twelve H atoms surrounding an octahedron composed of six Ni, Pd or Cu metal atoms in the 2x2x2 super cell deforming the tetrahedron or the octahedron respectively, and

imposing the periodic boundary conditions on the super cell at temperature 0 K.

We investigated the energy differences between the total energy with an impurity atom of H or alkali/alkaline-earth metal such as lithium (Li), sodium (Na), potassium (K), magnesium (Mg), calcium (Ca) which entered into the T site of Ni, Pd or Cu metal lattice and the total energy without it. Although Pd metal can occlude more H/D atoms than others, simulations were done in the same full occlusion of H in all O sites of three host metals. We observed the impurity atoms could move from O sites to T sites under the small lattice deformation such as atomic vibration at room temperature, and could hop out from the T site pushed with increased energy of the contracted tetrahedron surrounding it. Four H atoms adjacent to the tetrahedron seemed to be squeezed into it as a trigger reaction of hopping out impurity atom and could cause condensation to nuclear fusion and/or nuclear transmutation. Because of dominant energy of H atom in the T site H atom would stay in the O site at even large expanding deformation, the tetrahedral symmetry of four H atoms would be kept to cause and continue the nuclear reaction within Takahashi's TSC (Tetrahedral Symmetric Condensation) Theory which supports H/D-cluster condensation of nuclear reaction in condensed matter^{2,3)}.

2. Calculations

We made the quantum electronic state calculations under the lattice deformation changing the interatomic distances of the tetrahedron or octahedron composed of four or six Ni, Pd or Cu atoms around a T site or O site near the center of 2x2x2 super cell. And we obtained the total energy, charge density and electronic structure of the simulation system of 28 Ni, Pd or Cu atoms with four vacancies and occluded 32 H atoms in all O sites at temperature 0 K, that is, we took no motion of the atoms in the simulation system into account.

(1) Hardware and Software Used for Calculation

We used personal computers which had 6 cores / 12 ways CPU and 32 GB main memory, and 4 cores / 8 ways CPU and 16 GB main memory. And we used the first principles electronic state simulation program ABINIT which was using plane waves for the basis function and norm preservation type pseudo-potentials with semi core^{4,5)}, and we used VESTA for visualization of the charge density of calculation results⁶⁾.

(2) Restrictions of the Arrangement of Ni, Pd or Cu Atoms and H Atoms

We applied the following restrictions for the arrangement of Ni, Pd or Cu atoms and four or twelve H atoms because of computational complexity and calculation time.

Four vacancies are located at four of 32 Ni, Pd or Cu atoms, which are on the four edges of the large tetrahedron circumscribed around the concerned small regular

tetrahedron or on the four edges of the large cube circumscribed around the concerned small regular octahedron in the 2x2x2 super cell.

The locations of Ni, Pd or Cu atoms outside the concerned small tetrahedron or small octahedron are not altered even when the interatomic distances of the tetrahedron or octahedron are changed.

The four or twelve H atoms adjacent to the concerned small tetrahedron or small octahedron are located at the four or twelve centers of octahedrons (original O sites) slightly moved by lattice deformation respectively.

(3) Impurity atom

Each calculation was done when the impurity atom of H or alkali/alkaline-earth metal such as Li, Na, K, Mg, Ca entered or not entered into the T site in the tetrahedron or the O site in the octahedron.

(4) Deformation of Tetrahedron or Octahedron

The deformation of tetrahedron or octahedron d/a was defined as the ratio of the edge length change of unit cell (d) to the lattice constant (a), and varied from -0.04 to 0.04 in 5 steps changing the interatomic lattice distances.

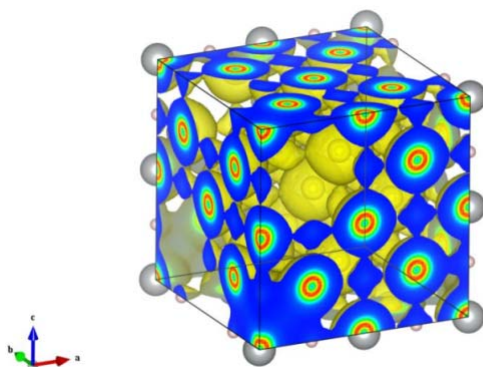


Figure 1 Charge density distribution in Ni lattice of 2x2x2 super cell with four vacancies.

(Red indicates high electron density and blue indicates low.)

For example, Fig. 1 shows the charge density distribution when an impurity Ca atom enters into the T site (hidden by blue electron cloud at lower left front corner) of 2x2x2 super cell of 28 Ni atoms with the four vacancies and 32 H atoms occlude in all O sites (small light purple balls) at the deformation $d/a = 0.00$.

3. Results and Discussion

(1) Energy Differences of the Total Energy with and without an Impurity Atom

We calculated the total energy of 28 Ni, Pd or Cu bulk metal with the four

Vacancies and 32 occluded H atoms in the O sites, deforming the tetrahedron or octahedron with or without an impurity atom of H, Li, Na, K, Mg or Ca. Fig. 2 shows the energy differences between the total energy with each impurity atom in the T site and the total energy without it respectively by solid lines in Ni metal for example, and shows those with and without the impurity atom in the O site which contract or expand in the anti-phase to the tetrahedron by broken lines all together.

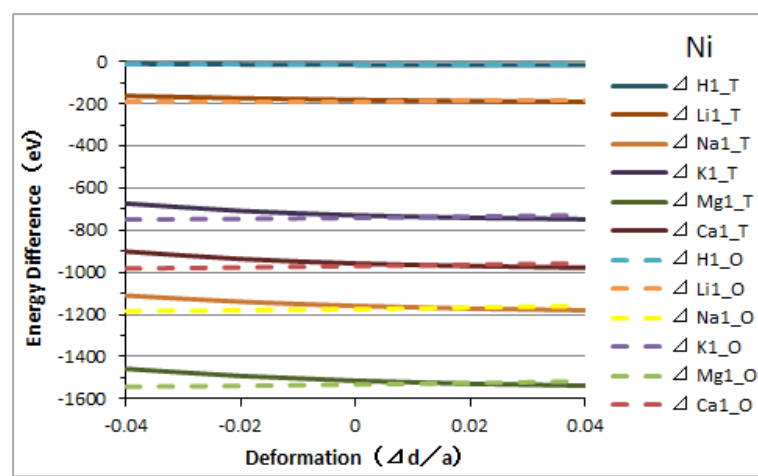


Figure 2 Energy differences between the total energy with and without an impurity atom in Ni metal.

(Those of tetrahedron are denoted by solid lines and those of octahedron in anti-phase by broken lines.)

Generally total energies calculated by computer programs within Density Functional Theory are depend on using pseudo-potentials, then we cannot compare directly the total energies of different element simulation systems. The energy differences in the above Fig. 2 using pseudo-potentials with semi core spread widely about 1,500 eV on each impurity atom. But the graphs of solid lines and broken lines for each impurity atom cross at near $d/a = 0.02$ respectively.

(2) Deducted Effects of Impurity Atoms on Total Energy

It would be thought that impurity atoms in the bulk metal move from vacancies to other ones shaken by lattice atomic vibrations or other impulses passing through O sites and T sites in a while. Although the energy of atomic vibration at room temperature is not large enough to move more than one H/D atoms simultaneously, the impurity atom could gain the enough energy from the same lattice atomic vibration and give a part of it to cause for H/D atoms to move together.

Then we considered how the impurity atom entered into the T site and hopped out

from it. In order to investigate the possibility for impurity atoms to move between T sites and O sites, we calculated the remainder between energy differences of the tetrahedron and those of the octahedron in the anti-phase contraction or expansion mentioned above (1) as the effect of impurity atoms on total energy. If the value is positive, the total energy of impurity atom entered into the tetrahedron is larger than that of the octahedron, and then the impurity atom could not move from the O site to the T site easily. It would be conceivable that impurity atoms move more easily in atomic vibration when their effects of impurity atoms on total energy are near 0 eV at smaller deformation. The possible mechanism of impurity atom hopping is speculated in the following.

By deducting the energy differences of the octahedron from that of the tetrahedron, we also could erase the inherence of energy differences which depended on the pseudo-potential of each impurity atom, and could consequently get to compare directly the changes of energy gained from surrounding lattice atoms and occluded H atoms when the impurity atom entered into the T site or the O site. Although the tetrahedron and the octahedron next to each other cannot contract and expand symmetrically in the same time, we can briefly estimate the possible movement of impurity atom between the T site and the O site by this way.

Similar Change of Deducted Effects of Impurity Atoms on the Whole

The deducted effects of impurity atoms on total energy of Ni, Pd and Cu metals are shown as Fig. 3. Those of Pd metal using new kind of pseudo-potentials with semi core were consistent with previous results using other pseudo-potentials without semi core.

The deducted effects of impurity atoms on total energy change almost similarly on the whole. In the deformation range of expanding tetrahedron and contracting octahedron of all host metals shown in the right side of upper graphs, the deducted effects of impurity atoms on total energy become 0 eV near $d/a = 0.02$ which is the rough deformation of atomic vibration 0.1 \AA . In the opposite deformation of contracting tetrahedron and expanding octahedron near $d/a = -0.02$ of atomic vibration, in all host metals the deducted effects of H atom on total energy increase only about 5 eV, those of Li atom increase $15 \sim 20 \text{ eV}$, and those of other impurity atoms increase $30 \sim 50 \text{ eV}$. Because the increase of total energy has been estimated about 8 eV when four H atoms in the O sites adjacent to the tetrahedron move on the four centers of triangular lattices which compose the boundary planes between four octahedrons and the tetrahedron in previous simulation of Pd metal¹⁾, the impurity atom entered into the T site could hop out from it giving a part of the increased energy to cause for surrounding H atoms to move together.

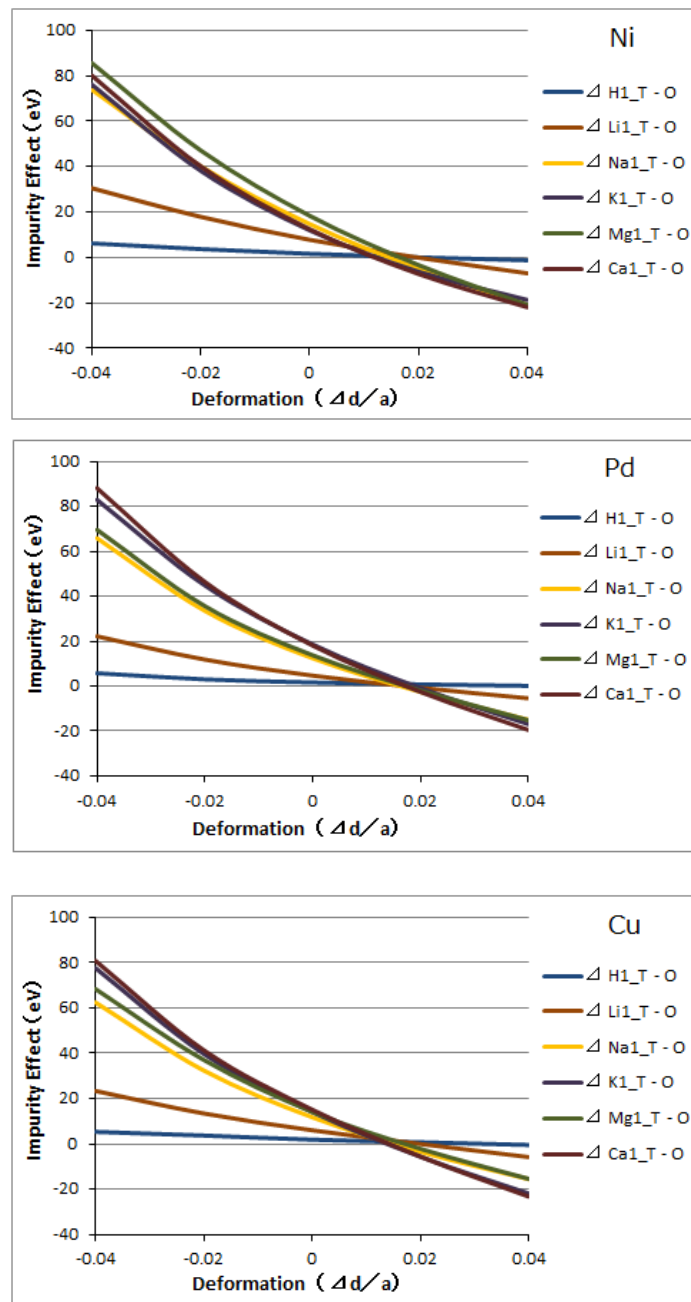


Figure 3 Deducted Effects of impurity atoms on total energy of Ni, Pd and Cu metals.

Different Change of Deducted Effects of Impurity Atoms near Null Value

The deducted effects of impurity atoms on total energy change in different ways for every host metals at near $d/a = 0.02$ where they are near null of deducted effects of impurity atoms. Fig. 4 shows the deformation range of expanding tetrahedron and contracting octahedron around $d/a = 0.02$ enlarged the right side of Fig. 3.

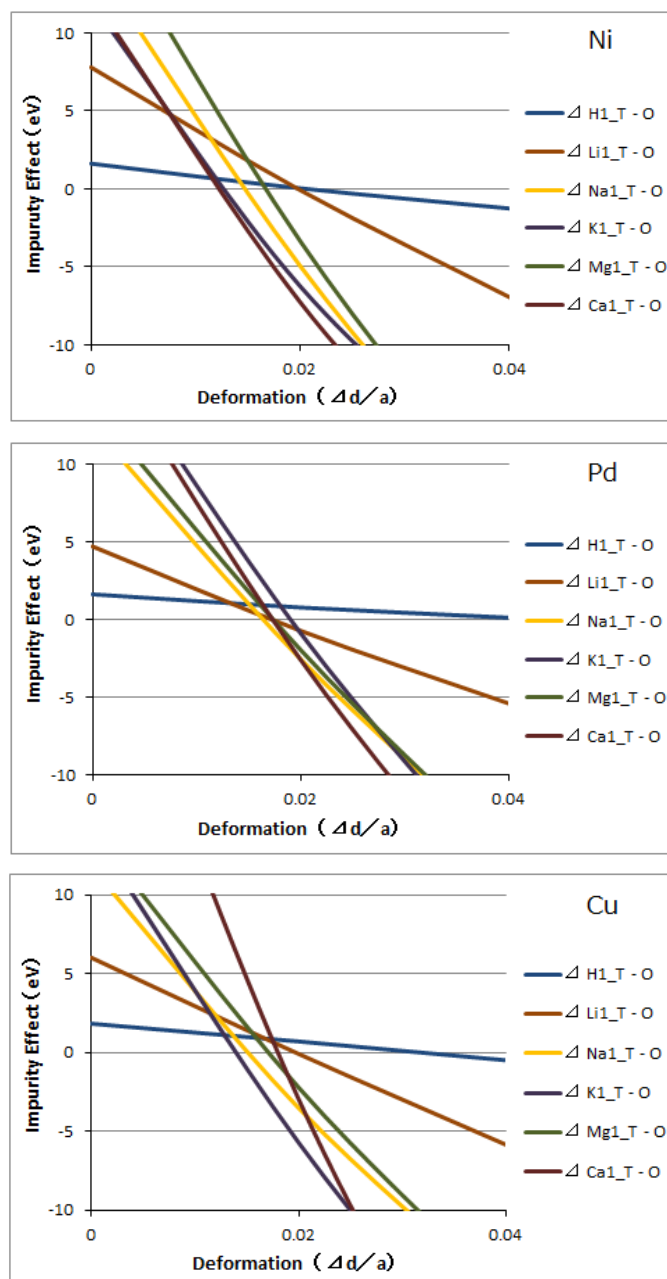


Figure 4 Deducted Effects of impurity atoms on total energy of Ni, Pd and Cu metals.

(Graphs show deformation range of expansion of tetrahedron and contraction of octahedron.)

Calculations were done by fixing the rapidly oscillating H atoms and impurity atoms to the equilibrium points of O sites or T site respectively while by deforming the slowly oscillating lattice structure of heavy metal atoms. The whole of atoms are considered to be equilibrium energy states by interacting each other and the movement of surrounding electrons. However, when the impurity atom enters into the O site or T

site and then the local energy of states change too quickly for surrounding atoms of the impurity atom to keep the energy balances before the sufficient lattice relaxations, the local state would probably transfer with such as the movement of impurity atom.

Then when the lattice deformation of negative deductive effect is smaller, the impurity atom would move from the O site to the T site in the expansion of tetrahedron and contraction of octahedron. And when the deductive effect increases quickly, the impurity atom would move from the T site to the O site in the opposite contraction of tetrahedron and expansion of octahedron.

In all host metals, the deducted effects of H atom on total energy at $d/a = 0.00$ are about 1.5 eV, namely the total energy of H atom in the T site are about 1.5 eV larger than those in the O site. Those of Li atom 5 ~ 8 eV larger, and those of other impurity atoms more than 10 eV larger. And the effect of Ca atom on total energy changes most quickly. Although the deducted effect of H atom on total energy is small, in Pd metal, it becomes barely 0 eV when the tetrahedron expands and the octahedron contracts largely $d/a = \sim 0.04$ about twice times of the deformation of atomic vibration.

In Ni metal, the deducted effects of K and Ca atoms on total energy are 0 eV at smaller deformation than other impurity atoms where the deducted effect of H atom on total energy is about 0.5 eV. In Pd metal, those of impurity atoms except H and K atoms are 0 eV at almost same deformation smaller than $d/a = 0.02$ where the effect of H atom on total energy is about 1.0 eV. Especially the deducted effect of Li atom on total energy is 0 eV at smaller deformation than in other host metals. In Cu metal, those of Na and K atoms become 0 eV at small deformation where that of H atom is about 1.0 eV.

Thus when there are some kinds of impurity atoms in the host metal, the impurity atom which has null deductive effect at smaller lattice deformation could enter into the tetrahedron in preference to others and hop out it. When the tetrahedral symmetrical arrangement of lattice atoms is broken slightly by non-breathing mode atomic vibrations or other causes, the impurity atom of the T site would receive unsymmetrical forces from surroundings and hop out from the T site. After that time, we are investigating, it might be occurred the tetrahedral symmetrical four H/D atoms (applying the results to D atoms) surrounding the tetrahedron would be drawn inside it and condense based on TSC Theory if the Coulomb repulsive forces were shielded appropriately by some way.

4. Summaries

We carried out the simulation of H states in Ni, Pd and Cu metal using the first principles electronic state simulation program on personal computers. And we

investigated the energy differences between the total energy with the impurity H, Li, Na, K, Mg or Ca atom in the T site or the O site and the total energy without it. It seemed to be improved in the deformation range of atomic vibration that the impurity atoms would draw four H atoms toward the T site. In the Pd metal, it seemed that the Li atom could draw four H/D atoms (applying the results to D atoms) surrounding the tetrahedron to cause mostly nuclear transmutation/fusion, and the Ca atom could draw four H/D atoms to cause nuclear reaction include fission or nuclear transmutation. In Ni and Cu metals, impurity K and Ca atoms seemed. Although Ni and Cu metals occlude H atoms less than Pd metal, we dared to carry out the simulation of H atoms in these metals same as Pd metal filled with H atoms occluded in all O sites. However, because platinum, silver and gold metals hardly occlude H/D atoms, it would be meaningless to simulate and discuss similarly to Ni, Pd and Cu metals as mentioned above.

Until now, we have used the simulation program available even to personal computers to investigate H states the T site or the O site in the symmetrically deformed tetrahedron or octahedron at 0 K in fragment calculation like a snap shot of the situation because of computational complexity and calculation time. Hereafter, we will have to improve the precision of simulation considering how this tetrahedral or octahedral symmetrical deformation will take place in the bulk metal and even in the nano-particle metal based on the lattice vibration and impulse propagation theory at proper temperatures using such as phonon response simulations more precisely and consistently.

References

- 1) H. Miura, Computer Simulation of Hydrogen States near T site in Pd Metal, Proc. of 13th Meeting of Japan CF Research Society, p. 108 (2012)
- 2) A. Takahashi, Deuteron cluster fusion and related nuclear reaction in metal-deuterium/hydrogen systems, Recent Res. Devel. Phys. 6, 1-28 (2005).
- 3) A. Takahashi, Chronicle of Condensed Cluster Fusion Models, Proc. of 8th Meeting of Japan CF Research Society, p. 51 (2007).
- 4) X. Gonze, B. Amadon, P.-M. Anglade, J.-M. Beuken, F. Bottin, P. Boulanger, F. Bruneval, D. Caliste, R. Caracas, M. Cote, T. Deutsch, L. Genovese, Ph. Ghosez, M. Giantomassi, S. Goedecker, D.R. Hamann, P. Hermet, F. Jollet, G. Jomard, S. Leroux, M. Mancini, S. Mazevet, M.J.T. Oliveira, G. Onida, Y. Pouillon, T. Rangel, G.-M. Rignanese, D. Sangalli, R. Shaltaf, M. Torrent, M.J. Verstraete, G. Zerah, J.W. Zwanziger, Computer Phys. Commun. 180, 2582-2615 (2009).
"ABINIT : First-principles approach of materials and nanosystem properties."

- 5) X. Gonze, G.-M. Rignanese, M. Verstraete, J.-M. Beuken, Y. Pouillon, R. Caracas, F. Jollet, M. Torrent, G. Zerah, M. Mikami, Ph. Ghosez, M. Veithen, J.-Y. Raty, V. Olevano, F. Bruneval, L. Reining, R. Godby, G. Onida, D.R. Hamann, and D.C. Allan. *Zeit. Kristallogr.* 220, 558-562 (2005).
"A brief introduction to the ABINIT software package."
- 6) K. Momma and F. Izumi, "VESTA: a three-dimensional visualization system for electronic and structural analysis," *J. Appl. Crystallogr.*, 41:653-658, 2008.

Numerical simulation of vortex appeared on electrode surface under long-term evolution of deuterium in 0.1 M LiOD –Vortex formation triggered by pillar current initiation

H. NUMATA

Tokyo Institute of Technology, Retired; Present address: 60 Higasidai
Kaneyama machi, Iwaki city, Fukushima prefecture, Japan 974-8211

Abstract: During long-term electrolysis on well annealed thick Pd rod (9.0 mm Φ) in 0.1 M LiOD, vortex pattern was observed. To understand the peculiar phenomenon, we proposed N-cycle model, which composed of four sequential processes including CF reaction; 1. In-take and compression, 2. Trigger, 3. CF reaction, 4. Scavenger. In Scavenger these vortex and vortex-thread were formed in the sub-surface layer, where the formation mechanism was explained by the motion of hypothetical particles mass (HPM) possessing high explosive energy (plausibly attributable to CF reaction). We have conducted computational simulations for analyzing the motion of HPM, however there have been unsolved problem that the size of vortex was larger than those obtained by the numerical simulations.

In this study, taking the appearance of vortex and the related solid-state properties: e.g., long-term deuterium absorption/desorption, as a complex phenomenon, CF reaction was neatly discussed and an appropriate model with the motion of HPM was presented. Through N-reaction cycle model there have been introduced two mechanisms; one: contribute to evolution of vortex and two: to momentum transfer in Scavenger. Furthermore, we went back to the original N-cycle model and proposed new Trigger as External trigger. It is expected that this modification of Trigger helps us establish more relevant model on our numerical simulation.

Key words: Vortex, Cold fusion, Nuclear reaction cycle model, Trigger, Pd, Numerical simulation

1 Introduction

During long-term electrolysis on well annealed thick Pd rod (9.0 mm ϕ) in 0.1 M LiOD, vortex pattern was observed on the postelectrolysis electrode surface¹⁻²⁾. The electrode microstructure showed two long faults without any cracks on the surface. Since the formation of this peculiar morphology of vortices can be highly plausible to the result of Cold Fusion (CF) reaction, the precise mechanism of vortices formation must be elucidated in relation with the solid-state phenomenon accompanied with long-term evolution of deuterium in 0.1 M LiOD. From more basic point of view, in-situ measurements of the solid-state properties of dilation, resistance and electrode potential were conducted and it revealed that the thick Pd electrode was composed of the core structure enveloped by the sub-surface layer. The latter exhibited the characteristics of non-equilibrium deuterium absorption/desorption reaction³⁻⁴⁾.

To understand a complex phenomenon during long-term electrolysis, N-reaction cycle model proposed⁵⁻⁶⁾ is composed of four sequential processes: In-take and compression — Trigger — (CF reaction) — Scavenger. By accounting for these multiple processes it is conjectured that the last process: Scavenger shows traces of vortex on the electrode surface as a consequence of the cyclic process continuation. Since then, our research purpose has been to simulate these processes using numerical simulation and finally to obtain vortex pattern in 3D space analyzing the motion of HPM.

So far, the previous works published as references 1-6 were concerned with well-known cold fusion experiment (the measurements of neutron count rate, electrode potential and bath temperature, and postelectrolysis microscopic observation) and the solid-state properties of Pd under electrochemical deuterium (hydrogen) charging.

Following these studies, a conceptual model, which was expected to help us understand cold fusion reaction as a complex phenomenon was proposed⁵⁻⁶⁾. The works published as references 7-14), which we called the present work in this paper, are concerned with an application of numerical simulation to the interfacial electrochemical phenomenon. Because of a pioneerwork and a lack of scientific data with the interface, the present work has been slowly developed, although the vortex pattern was successfully obtained in 2D space by a numerical simulation method: Lattice gas cellular automata (LGCA) numerical simulation⁷⁻¹¹⁾.

In the framework of the present work we have tried several numerical simulations: structure of interface (sub-surface layer and obstacle), magnetic field, introduction of voids or lattice defects, etc. As a result, it is shown that the motion of HPM was expressed in terms of helicity¹³⁾. Even though LGCA numerical simulation evolved a single vortex pattern and a cascade of vortices⁷⁻¹¹⁾, it is essentially difficult to include an influence of an electromagnetic field in the calculation. Then we have challenged the other numerical simulation: Discretization method for the motion of HPM under an influence of the magnetic field in the sub-surface layer. The temporal HPM trajectory in 3D sub-surface layer showed helical streamlines presenting vortex pattern on the electrode surface¹²⁾. Noting that the motion of HPM is mainly determined by an electromagnetic field, the macroscopic electromagnetic field of the interface occurring hydrogen evolution was evaluated in the last paper¹⁴⁾. At present, our research interests is focused on the evaluation of relevant model in terms of the magnetic field in the sub-surface layer. We have also found the difficulty in utilization of the former N-reaction cycle model and then some modification is tried in this study.

In this study, a modified Trigger: pillar current initiation is evaluated using discretization method, and old and conceptual N-reaction cycle model is discussed in relation with Trigger and CF reaction resulting in vortex obtained by numerical simulation.

2 Experimental

2.1 Long-term evolution of deuterium on thick rod Pd electrode in 0.1 M LiOD

Usually cold fusion experiments at ambient temperatures have been conducted by electrolysis of heavy water on a Pd electrode. In the previous work two series of long-term electrolysis in 0.1 M LiOD were conducted where the experimental conditions were different; Pd rod with a diameter of 9 mm for two months run¹⁻²⁾ and with a diameter of 21 mm for ca. six months run⁵⁾ referred to Exp.1 and Exp.2, respectively. The other experimental details were similar to both the runs^{1-3, 5-6)}. The surface pretreatment and electrolysis conditions are shown in Table 1 and the results of neutron measurement are described elsewhere^{1-2, 5)}.

Table1 Experimental conditions of Exp.1.

Run No.	Current, mAcm ⁻²	Pretreatment
1st	0.05-40 40-500	Cast, 800°C anneal(10 ⁻⁶ Torr) Acid treatment
2nd	40	Polishing, Acid treatment, Evacuation, D ₂ gas charge
3rd	40	Evacuation, Polishing, Acid treatment
4th	40	Evacuation, Polishing, Acid treatment

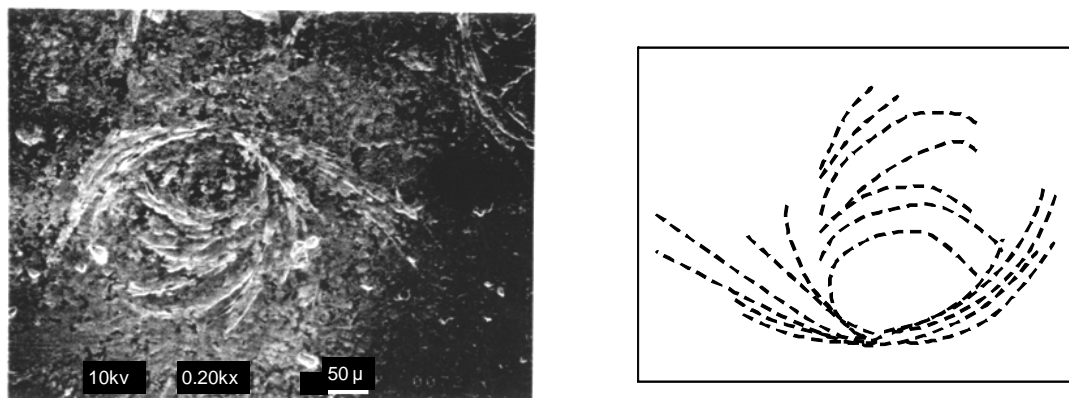


Fig. 1 Vortex appeared on Pd electrode surface after long-term electrolysis in 0.1 M LiOD (a), Duplicate of SEM picture (b).

2.2 Vortex obtained by Exp. 1 for N-reaction cycle model

As shown in Table 1 the electrolysis for deuterium absorption was conducted as follows; the electrode was removed from the cell and carefully re-installed four times during which the diameter of the electrode was measured at three positions (top, middle and bottom). During 1st run the dilation at the bottom end showed 7 % while in those of 2nd-4th runs the values at these positions approached asymptotically to 7.8-8.3 %.

Figure 1 shows a significant morphology of a thick rod Pd electrode observed on the surface after long-term electrolysis in 0.1 M LiOD¹⁻³⁾. This peculiar morphology was named as vortex. It is not a substance adhered on the surface, but is a material on which the morphology is deeply impressed in a shape of a ditch. This is the morphology which formation mechanism will be elucidated in the present work.

3 Results and Discussion

3.1 N-reaction cycle model

Alternatively, our research endeavors have been devoted to a fundamental study of deuterium absorption behavior: e.g., microscopic structural changes of Pd during prolonged deuterium/hydrogen absorption/desorption by electrolysis^{4, 15)}. Though a precise description is not shown in this paper, prior to model construction, ideas relevant in computational simulation and consistent with experimental results are evolved:

- Significance of modeling: For consistency relevant linkage between experimental results and numerical simulation
- Elemental analysis regarding complicated phenomenon as a whole
- The following two key points are realized: (1) improved reproducibility of the experiments resides in continuation of the cycle (2) on systematic consideration the hindered factors might come to the surface

- On this model application there have been remained unsolved problem that the vortex size of several tens of micrometers, where deuterium evolution really took place, might be consistent with a pattern obtained by computational simulation
- Above results with respect to the structural change of Pd: discrimination of the sub-surface and the bulk developed by the deformation

Considering such structural changes on the electrode surface and the bulk it is possible to think these unusual treatments are related with CF reaction. That is, the electrolysis performance makes the special microstructure (shown below in the simulation model), where that process is named as the Intake of reactant (absorption) followed by compression. Next, CF reaction could be initiated by some Trigger after an incubation period. At this moment, in the matrixes around reaction sites the explosive energy of CF reaction is transferred to the kinetic energy of mobile hypothetical particles mass. In order to make the explosive energy spread over from the reaction site, hypothetical particles mass (HPM: a group of small charged particles is considered as particles mass in this study) was assumed to be a working medium in the following simulation. Instantaneously, flow with high energy evolves and inevitably interacts with the matrix of the sub-surface layer leaving in vortices on the sample's surface (these sequential reactions are schematically shown as a single vortex formation in Fig.3).

Under such an idea, by considering the phenomena as an analogy with an energy engine (4 reciprocating cycle), N-reaction cycle model⁵⁻⁶⁾ was proposed. As schematically shown in Fig.2, it consists of 4 sequential processes: Intake and compression — Trigger — CF reaction — Scavenger where instead of CF reaction and Trigger, microstructure formation is incorporated into the successive chain and followed by Scavenger. In Scavenger of Fig.2, the HPM works in two ways; it moves towards the surface of reaction vessel leaving the traces, vortex or vortices (indicated as ①), and in another way it moves to neighboring vessels without any traces on the surface (indicated as ②). This process is further discussed in Chapter 3.3.

In Fig.2 the reaction vessel (indicated by double solid lines) is composed of the tough

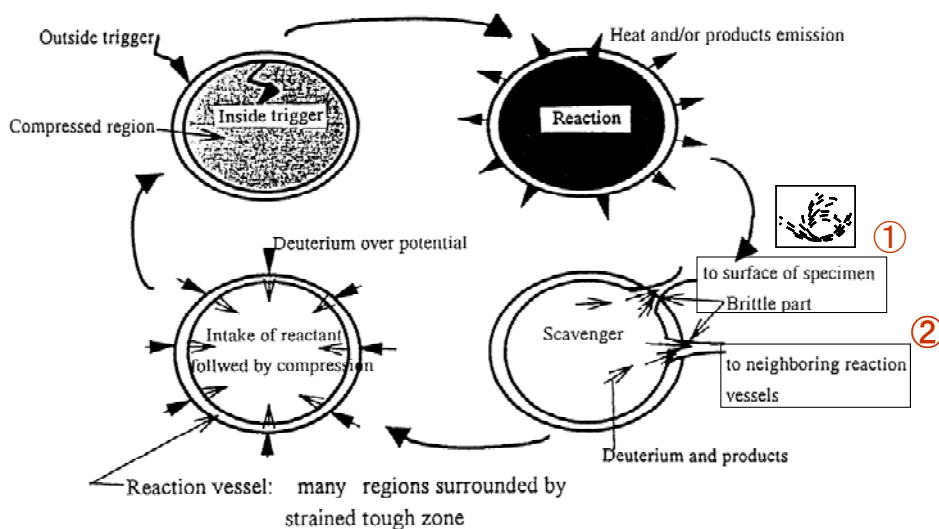


Fig.2 Schematic of a nuclear reaction cycle model.

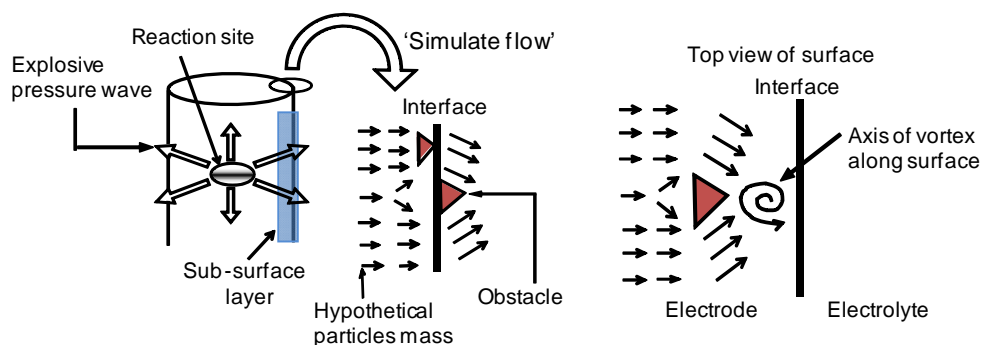


Fig.3 Illustrative drawing of a single vortex showing the motion of the HPM possessing explosive energy transferred from a reaction site. It is also shown perspective view of an out flow of the HPM at the interface.

wall, which might be formed after long-term electrolysis or under repeated deuterium absorption/desorption performances. It is noted that the wall functions facile desorptive contraction/sluggish absorptive expansion^{4, 15}). Furthermore, for Scavenger the followings are demonstrated; in-situ measurements of the physicochemical properties of Pd-H(D) system elucidated the formation of fine nano-precipitates: Pd-D_{2-x} in β - phase matrix³). These precipitates assume the characteristics of non-equilibrium, hence superplasticity is often observed during their transient state¹⁶). Therefore, it is envisaged that the above mentioned flow could trail through such softened matrix: sub-surface layer resulting in the experimentally observed vortices.

3.2 Deduction of single vortex from N-cycle model for simulating the motion of HPM

In the following chapters, it is noted that our discussion are concerned with “microscopic point of view” togetherwith “macroscopic descriptions with e.g., vortex pattern, vortices, surface morphology, etc.”, which could lead us confused consideration. It is also noted that there have been two numerical simulation methods: Lattice gas cellular automata (LGCA) (in Chapters 3.3-3.4 of reference 12) and discretization method (in Chapter 3.5 of reference 12) have been utilized in our work, whereas the goal of both methods is expected to approach toward the same conclusion (characteristics see Appendix 2 of reference 12). Hereafter, details of the numerical simulation results are given in the references.

First of all, it is acceptable that the application of numerical simulation helps us to understand microscopic mechanism of the vortices formation in relation with N-cycle model. Before conducting the calculation, the computational domain (2D/3D and its form), working medium, initial and boundary conditions, and physical rule determining the motion should be carefully determined so as to be consistent with the real phenomenon.

Let's focus our attention to the Scavenger process after CF reaction (corresponding to in Fig.2) from a microscopic view point. In other words, Scavenger process means macroscopically an evolution of vortex on the electrode surface. The key issues are the evolution of HPM with high energy, the interaction of HPM with obstacles, and the motion with the magnetic field interaction through the sub-surface layer (the last item is discussed in Chapter 3.4). Figure 3 schematically shows a single vortex evolution due to an out flow of HPM to the electrode surface where a vortex is formed behind the corresponding obstacle. Instead of the influence of the magnetic field, clearly seen there, the axis of the vortex is along that of the cylindrical electrode. In the left of Fig.3,

the HPM with high energy moves through the sub-surface layer where two types of obstacles are indicated. First, at a predicted reaction site, HPM spreads radially in 360° direction, and subsequently some parts reach the sub-surface layer. The condition for the radial motion will be established using a long prism crystal^{1, 5)}. View from upper shows aligned vectors coincidentally rushes towards the interface as ‘Simulated flow’. There have been appeared simulated flow vectors normal to the electrode interface. In the right of Fig.3, it shows how evolves a vortex behind an obstacle as a result of flow disturbance. It is easily understood for such flows to be disturbed due to the obstacles.

Previous papers¹⁰⁻¹¹⁾ mainly concerned with morphological identification of the vortex (single vortex) comparing with the experimental and 2D LGCA computational patterns. The results of the simulation qualitatively well agree with the experimental patterns. In the LGCA the individual particle possesses its own momentum and all the flows should synchronize with the occurrence of the reaction. Further details of the numerical simulation have been discussed elsewhere^{10, 12)}: e.g., the nature of obstacles as actual structural inhomogeneity. In the future work more advanced LGCA simulations should be directed toward complicated cases to simulate the motion of HPM.

3.3 Structure and properties of the sub-surface layer deduced from N-cycle model: large vortex and vortex-thread

Until this the subject has been limited in Scavenger, especially of Fig.2, which means a single vortex appearing on the electrode surface. In fact, the behavior of Scavenger might be complicated such that a few reactions proceed concurrently during long-term electrolysis treatment¹⁷⁾. Here, some experimental observation is disclosed; when long-term and non-intermittent deuterium evolution was conducted on the electrode/electrolysis cell, the dynamic gaseous babble evolution occurred on the electrode surface, even if the electrolysis had stopped. As shown in Fig.4, the phenomenon is called “Breathing mode” where the babble evolution/cessation spontaneously starts and periodically continues in a quasi steady state. The cycle period is in the range of about a minute. Thus, this conceives us for having such complicated electrode structures and functions, a part of which does not appear appreciably.

Based on the experimental observations and considerations explained above, we conceived that an electrode subjected to deuterium absorption/desorption, essentially behaved in two regimes; one is that it played a role in transferring energy (momentum) towards a surface, and subsequently appeared vortex or vortices patterns thereon; and another is played a role in transferring energy, however, the phenomenon was caused by the motion of HPM underneath the surface resulting no trace on the electrode surface¹⁸⁾. Two characteristic morphologies of the surface and underneath

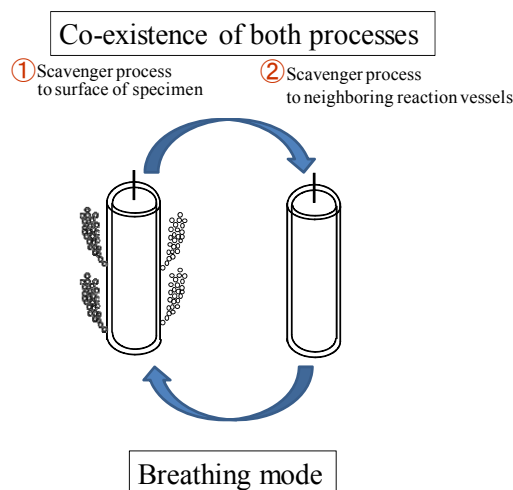


Fig.4 Schematic of spontaneous evolution/cessation of babbles, which conceives us dynamic HPM transportation and an evolution of vortex during the Scavenger process.

microstructures are discussed *vide infra*, in relation with the macroscopic appearances of the scavenger process. In Fig.5 it shows the locus of the occasional particle flow on the Pd surface (correspond to Fig.2), which was identical to the experimentally observed large vortex pattern. By comparing the vortex pattern with the experimentally obtained one, the axis of the motion leaned due to the interface's magnetic field⁷⁾. On the other hand, Fig.5 shows the continuous flow of HPM from a vessel to a neighboring one (corresponds to Fig.2). In Fig.5 many vortices are evolved behind obstacles and a cascade of vortices is seen. In this case, the large vortex was taken as being composed of cascade vortices like thread. Hence, a reasonable inference leads conclude us that the vortex occasionally occurred on the surface, while the cascade vortices, vortex-thread, moves underneath the electrode surface. This view might not be inconsistent with the irregularity of sub-surface layer under an annealing at 1100¹⁹⁾. Therefore, it is claimed that the appearances of the vortices are strongly concerned with the kinetics of the mass transfer phenomenon underneath the surface.

Here, new idea evolves from the above discussion, involving equilibrium and non-equilibrium states, which explain how the explosive energy (flow of HPM) can be transferred, resulting in an evolution of vortex on a surface of hexahedron: sub-surface layer as reaction space. In Fig.6 the structure of sub-surface layer is schematically shown in 3D, where the explosive energy is transferred from the reaction site. There is shown moving HPM from the inner surface to the electrode surface through the thick piping distributed in the sub-surface layer. Thus, the thick piping works as a channel for smooth transportation. By the way, the variation of a working medium is useful because the results of present computational simulation exhibits rather simple patterns with smaller dimension. Considering the case of Fig.5 , vortex-threads themselves or single vortex may be enable to move instead of HPM assuming that such motion of HPM through thick piping is taken as similar to that of vortex threads. However, there still exists the question how large scale of vortices evolved (actually those diameters range to c.a. 80 μ m).

Then it necessitates a quantitative equation with respect to energy and mass transfer in the sub-surface layer. Momentum and mass transportation in the sub-surface layer might be accomplished in the following ways; it

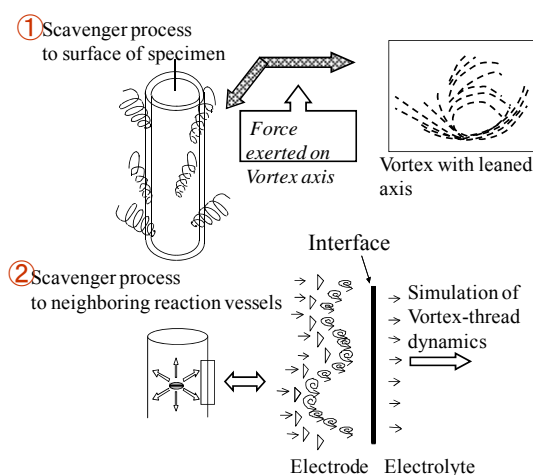


Fig.5 Schematics of vortex with leaned axis and vortex thread during the Scavenger process: motion of HPM from a vessel to a surface and from a vessel to a neighboring one¹¹⁾.

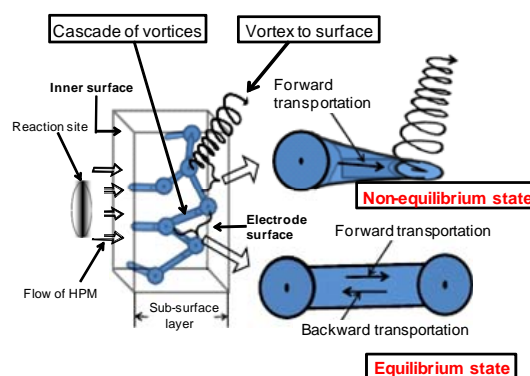


Fig.6 Transportation phenomenon in sub-surface layer and evolution of vortex associated with the motion of HPM.

holds forward transportation rate and backward one equal implying an equilibrium state, and otherwise net transportation rate with either direction continues implying a non-equilibrium state (see right of Fig.6). In the latter case, as shown in Fig.6 the net flow encounters by Rayleigh–Taylor’s instability resulting in an evolution of vortices.

3.4 Motion of HPM under the influence of a magnetic field: significance of Trigger with respect to the influence of a magnetic field on numerical simulation

As shown above, it has become apparent that the motion of HPM was significantly influenced by the electromagnetic field and barriers (e.g., wall and obstacle) in the sub-surface layer. We analyzed the motion of HPM through the sub-surface layer using discretization method (refer Appendix 1 of reference 12) under the influence of a magnetic field. It was shown that the time evolution of HPM traces was mainly influenced by the evaluated magnetic flux density¹²⁾. The calculation was performed adopting the cylindrical magnetic field distribution accompanied by ejected particles (v_0 : initial velocity) from the cylinder bottom to top.

So far, we have examined several experimental conditions including the above case, however the trajectories of HPM were totally different or inconsistent with some evaluation points between experiments and calculation. Here, the magnetic flux density and the other experimental conditions, irrespective of valid or not in the calculation, are shown in Table 2 of Appendix 1. Then we re-examine more appropriate model concerning the magnetic configuration underneath the electrode surface. As shown in Fig.2, intervening CF reaction, Trigger and Scavenger are present, both of which mean not CF reaction itself but its cause and result. It is insisted that these two processes are strongly linked each other. Therefore, if we change the type of Trigger, an appropriate magnetic flux density might be highly expected.

On the forgoing calculation, an appropriate magnetic flux density was first given and the motion of HPM calculated; thus, as the preceding step of the calculation, there had been done the evaluation of magnetic flux density based on the Internal Trigger. The term of “Internal” means that any kinds of phenomena within the experimental system could be Trigger, which subsequently initiates the occurrence of CF reaction, that is, Rayleigh–Taylor’s instability. On the other hand, “External” means that some action from outside stimulates the surface of the electrode resulting CF reaction.

In this study, it necessitates changing the magnetic flux density, and then we go back to N-cycle model as shown in Fig.2, where Trigger is indicated as inner and outer Trigger. For consistency the terms: “inner/outer” are replaced by “Internal/External” this time. Essentially, there might be existed important differences between two types of Trigger. In this study, we first adopt the External Trigger: abrupt discharge like thunder, which had been previously presumed to be cosmic ray. It might work to stimulate the formation of well conditioned reaction vessel in N-cycle model.

3.5 Preliminary results of the motion of HPM: local pillar current initiation as External Trigger

Although precise defining of Trigger is skipped here, local pillar current initiation makes a thorough understanding of Trigger associated with the resulting surface appearances in Scavenger. As shown in Table 2 of Appendix 1, Model (3) seemed one of the most promising model for this simulation.

4 Conclusion

In this study, the hitherto numerical simulations to analyze the motion of HPM in the sub-surface layer were re-examined for consistency. As a result, more advanced simulation was necessitated to analyze N-cycle reaction model. For simulation External trigger was evaluated as one of most promising model.

Here, we have reviewed our experimental results and could draw a scheme for numerical simulation accompanied with an application of a feedback (see Fig.7). Figure 8 also shows the schematic of our computational experiments as an application of numerical simulation for analyzing the CF reaction related phenomenon.

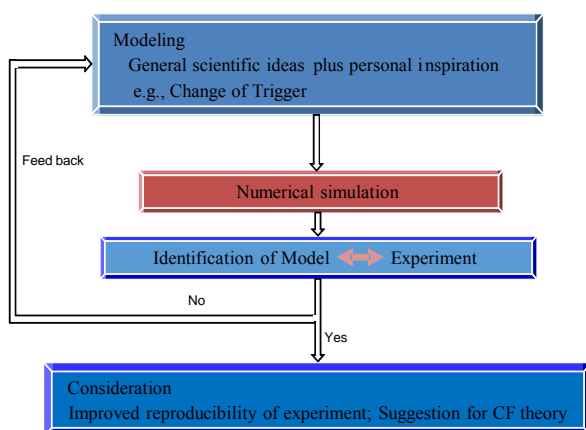


Fig.7 Scheme of our computational experiment and prospect.

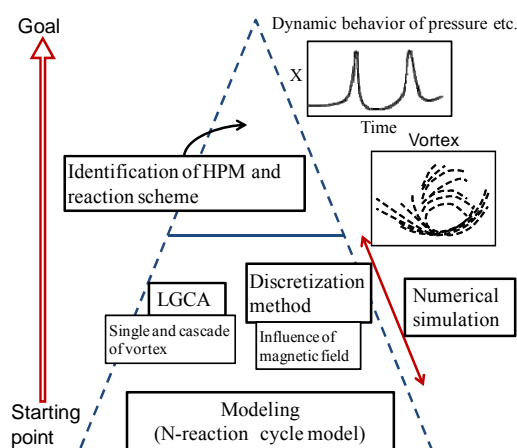


Fig.8 Schematic of application of N-cycle model to CF phenomenon.

Acknowledgements

We thank Mr. T. Suzuki of Concentration Heat and Momentum-Japan Ltd. for technical advices. We thank Mr. M. Ban for hitherto valuable discussions and cooperation, and S. Numata for the preparation of conference fee. We also thank the editor and reviewer for patient and kind work.

References

1. H. Numata et al.: Proc. Mini. Symp. Cold Fusion, Tokyo Metropolitan Univ., p.129 (1990)
2. R. Takagi et al.: Fusion Technol., **19** (1991)2135
3. H. Numata and I. Ohno: Fusion Technol., **38** (2000)206
4. H. Numata and I. Ohno: **ICCF6**, Toya Japan, vol.1, p.213(1997)
5. H. Numata et al.: Proc. Conf. Science of Cold Fusion, Vol.33, p.71, T.BRESSANI et al. eds., SIF, Bologna, Italy (1991)
6. H. Numata: Proc. Conf. 3rd New Hydrogen Energy Basic Research, (1996)55
7. H. Numata and M. Ban: **ICCF12**, Yokohama, p.411(2005)
8. H. Numata and M. Ban: Proc. JCF6, p.32 (2005)
9. H. Numata and M. Ban: Proc. JCF8, p.67 (2008)
10. H. Numata and M. Ban: Proc. JCF9, p.74 (2009)
11. H. Numata and M. Ban: Proc. JCF10, p.68 (2010)
12. H. Numata and M. Ban: Proc. JCF11, p.70 (2011)
13. H. Numata: Proc. JCF12, p.52 (20012)
14. H. Numata: Proc. JCF13, p.158 (2013)
15. H. Numata and M. Ban: Proc. JCF7, p.6 (2006)
16. Fine nano-precipitates in β -phase matrix in this case may be attributable to softening within the limited areas, and difficult to investigate due to their transient state.

17. During long-term evolution of deuterium (hydrogen) the gas evolution reaction proceeds steadily in the early stage; thus the electrode potential (nearly correspond to the hydrogen pressure in the Pd matrix) assumes an equilibrium obeying the Nernst equation. When the concentration of hydrogen exceeds ca. 0.8 the potential and the other properties change abruptly and decay progressively to unusual values. This phenomenon suggests unstable precipitation or voids/crack formation. Hence, the gas evolution reaction might proceed by an electrochemical reaction via diffusion and recombination, concurrently an occurrence of gas evolution through cracks even if under charging or uncharging. Thus, on modelling the reaction might be defined as multiple processes. Actually, different two reactions could occur concurrently, both of which play a similar role but appear as totally different phenomena.
18. In Scavenger of Fig.2, incorporating the above issue, there were naturally assumed alternative two mechanisms of HPM motion as a result of N-cycle model examination. One is of Fig.2: to an electrode surface and another of Fig.2: to a neighboring reaction vessel.
19. K. Kandasamy et al.: Surface and Coating Technol., **35**(1988)93

Appendix 1

Table 2 shows three models, which are incorporated in the evaluation of magnetic flux density. Model (1) was applied to the analysis of the vortex and a helical trajectory of HPM was calculated in the sub-surface layer. As a result, vortex patterns of ejected particles were obtained on the top of the cylinder. The other condition: Model (2) was employed in the magnetic flux density calculation and the result was inconvenient for our simulation. At present, Model (3) seemed one of most promising model.

Table 2 Characteristic values for evaluation of magnetic flux density in the sub-surface layer.

Model Item	(1)	(2)	(3)
Primary given boundary condition	Magnetic flux density; Cylinder: High value along centerline; and direction: tangential on the circumference	Electric potential: Each surface of Hexahedron was given	Magnetic flux density of pillar current: Coaxial circles of equal magnetic flux density distribution
Initial condition of ejected particles mass	Ejection site: 4 particles set at the inner surface of the Cylinder bottom	Ejection site: 1 particle set at the center of the inner surface of Hexahedron	Ejection site: Same as Model(1)

The Quantum States of the System Including Two Species of Charged Bosons in Ion Traps III

Ken-ichi TSUCHIYA[†], Aska OKUZUMI and Aiko WATANABE

*Department of Chemical Science and Engineering, Tokyo National College of Technology,
1220-2 Kunugida, Hachioji, Tokyo 193-0997, Japan*

[†] e-mail: tsuchiya@tokyo-ct.ac.jp

Abstract

Bose-Einstein condensation is one of the candidates for the trigger of nuclear reaction in solid. In this study, we have proposed a new method how to calculate the quantum states of the two species of charged bosons trapped in ion traps with harmonic potential, which is similar with the potential of O or T sites of the crystalline solids.

(**keywords**; Bose-Einstein condensation, nuclear reaction in solids, trapped quantum states, two charged bosons)

1. Introduction

It is well known that the mechanism of superconductivity is regarded as a Bose-Einstein Condensation (BEC) of electron pairs [1]. Many workers in condensed matter nuclear science also tried to explain the mechanism of cold fusion by using BEC. For example, groups of R.T.Bush et al. [2], Y.E.Kim et al. [3] and A.Takahashi et al. [4] have tried it and obtained interesting results. We also have tried it and obtained D-D reaction rates in Pd [5].

Our final target here is to obtain the nuclear reaction rates between two species of charged bosons trapped in ion traps with harmonic potential by using theories of Y.E.Kim et al. [6,7]. In this study, we have tried to calculate the quantum states of them as the first step. After that, the cross section of the nuclear reaction will be given from the quantum states of the particles by using the optical theorem [8]. Of course, we will be able to calculate the reaction rate from the cross section.

2. Mathematical Method

In our previous work [9], we showed a new method how to perform the numerical calculations for the problem on the mixtures of the two species of positively charged bosons in ion traps, which was proposed by Kim et al. [6,7]. Our formulas for species $i = 1$ and 2 were defined as the iterative process to determine the electro-static potential W_i and the probability density n_i based on the Poisson's and Schrodinger's equations, respectively. For example, the electro-static potential for species 1 are

written as

$$W_1(\mathbf{r}) = \int d\mathbf{r}' G_k(\mathbf{r} - \mathbf{r}') \left[\frac{e^2}{\epsilon_0} Z_1 \{Z_1 n_1(\mathbf{r}') + Z_2 n_2(\mathbf{r}')\} + k^2 W_1(\mathbf{r}') \right], \quad (1)$$

where function G_k and constant Z_i mean well-known Green's function of Helmholtz equation¹ and effective charge for species i , respectively. In Eq.(1), the probability density is given by

$$n_i(\mathbf{r}) = |\psi_i(\mathbf{r})|^2, \quad (2)$$

where $\psi_i(\mathbf{r})$ is a normalized solution of

$$\left\{ -\frac{\hbar^2}{2m_i} \nabla^2 + V_i(\mathbf{r}) + W_i(\mathbf{r}) \right\} \psi_i(\mathbf{r}) = \mu_i \psi_i(\mathbf{r}). \quad (3)$$

In Eq.(3), V_i and μ_i mean harmonic and chemical potentials for species i , respectively.

In the integral representation of the Poisson's equation in Eq.(1), the functions $n_1(\mathbf{r}')$, $n_2(\mathbf{r}')$ and $W_1(\mathbf{r}')$ in the integrand of the right hand side are regarded as old quantities in the recursive calculations, while the other functions are new quantities. Therefore, the electro-static potential and probability density are linked together, and furthermore, the equations for two species are connected. The flow chart for these calculations are shown in Fig.1

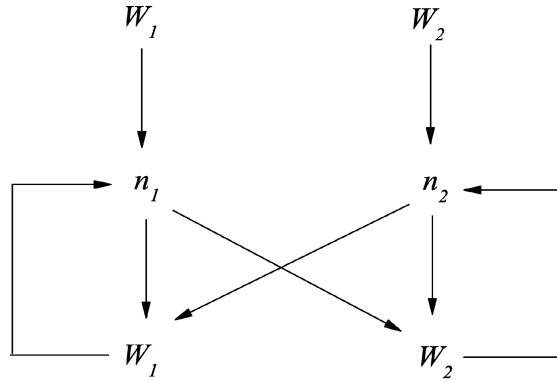


Fig. 1. The flow chart for the self-consistent calculation.

These doubly connected situations might be a cause of bad convergences, because small errors will rapidly expand in these equations.

¹ The Green's function for Helmholtz equation $(\nabla^2 + k^2)F(\mathbf{r}) = 0$ is defined as

$$G_k(\mathbf{r} - \mathbf{r}') = \frac{e^{-k|\mathbf{r}-\mathbf{r}'|}}{4\pi|\mathbf{r} - \mathbf{r}'|}.$$

We can regard Eq.(1) as an exact formula even if k is arbitrary.

The chemical potential in Eq.(3) should be selected to give damped solution at large $|\mathbf{r}|$. In our previous work [9], it was done by finding a node at large $|\mathbf{r}|$. In this work, it has done by finding a solution whose damping aspect at large $|\mathbf{r}|$ is similar in style to that of an asymptotic solution for the pure harmonic problem. This improved the convergence in the recursion method.

3. Calculation

In this study, we try to find a ground state solution. Therefore, all functions in Eq.(1) and Eq.(3) are spherical. Then, if we define a new function as

$$F_1(r) = \frac{e^2}{\varepsilon_0} Z_1 \{Z_1 n_1(r) + Z_2 n_2(r)\} + k^2 W_1(r), \quad (4)$$

Eq.(1) is rewritten as

$$W_1(r) = \int d\mathbf{r}' G_k(\mathbf{r} - \mathbf{r}') F_1(r'), \quad (5)$$

where $r = |\mathbf{r}|$ and the volume integration is performed over the all space. The angular parts of this volume integration are easily performed, and it is reduced to

$$W_1(r) = \frac{e^{-kr}}{kr} \int_0^r dr' \sinh(kr') F_1(r') + \frac{\sinh(kr)}{kr} \int_r^\infty dr' r' e^{-kr'} F_1(r'), \quad (6)$$

where a positive real constant k causes a rapid damping at large r . This damping means that Eq.(3) for the ground state at large r becomes the equation for the pure harmonic problem in one dimension which is written as

$$\left\{ -\frac{\hbar^2}{2m_i} \frac{1}{r^2} \frac{d}{dr} \left(r^2 \frac{d}{dr} \right) + \frac{1}{2} m_i \omega_i^2 r^2 \right\} \psi_i(r) = \mu_i \psi_i(r), \quad (7)$$

where ω_i is a frequency factor. For the case of ion traps, this factor is determined by the shape of the trap and electro-magnetic conditions. For the case of hydrogen-metal systems, it is determined by the potential around the stable sites.

Transforming Eq.(7) by using $\xi_i = \alpha_i r$, $\alpha_i = \sqrt{m_i \omega_i / \hbar}$, $\varepsilon_i = 2\mu_i / \hbar \omega_i$, $w_i = 2W_i / \hbar \omega_i$ and $u_i(\xi_i) = \xi_i \psi_i(\xi_i)$, we obtain dimensionless equation as

$$\left\{ -\frac{d^2}{d\xi_i^2} + \xi_i^2 + w_i(\xi_i) \right\} u_i(\xi_i) = \varepsilon_i u_i(\xi_i). \quad (8)$$

In this equation, w_i is regarded as the perturbation to the harmonic potential problem, since the harmonic potential is extremely larger than the electro-static potential at large ξ_i . For the case of the unperturbed system, we can write down the ground state solution corresponding to $\varepsilon_i^0 = 3$ and it's logarithmic derivative as

$$u_i^0(\xi_i) = \xi_i e^{-\xi_i^2/2} \quad (9)$$

and

$$\frac{d}{d\xi_i} \log u_i^o(\xi_i) = \frac{1 - \xi_i^2}{\xi_i}, \quad (10)$$

respectively. On the other hand, the perturbed ground state is unknown. In particular, the perturbed eigenvalue ε_i is unknown.

In our previous work [9], we found ε_i which gave $u_i(\xi_i) = 0$ at $\xi_i = \xi_i^{max}$. This means that ε_i which gave a node at particular ξ_i^{max} with a large value was found. The result given by this method strongly depends on the choice of ξ_i^{max} . This causes the bad convergence in the recursive calculation. In this study, we found ε_i numerically using Newton method which gave $\frac{d}{d\xi_i} \log u_i(\xi_i) = \frac{d}{d\xi_i} \log u_i^o(\xi_i)$ at ξ_i^{max} . This is done by defining a new function as

$$f(\varepsilon_i) = \left\{ \frac{d}{d\xi_i} \log u_i(\xi_i) - \frac{d}{d\xi_i} \log u_i^o(\xi_i) \right\}_{\xi_i = \xi_i^{max}} \quad (11)$$

and finding the solution for $f(\varepsilon_i) = 0$. In this equation, function u_i depends on the chemical potential. Therefore, we can draw f as a function of the chemical potential and find the perturbed solution whose damping aspect is similar with the asymptotic solution using Newton method.

In this study, we have performed the numerical calculations based on Kim's theory for the mixture of positively charged two bosons in ion traps by choosing D^+ , ${}^6\text{Li}^+$ as the positively charged bosons. As a result, we have obtained self-consistent quantum states of the mixture of one D^+ and one ${}^6\text{Li}^+$ in an ion trap.

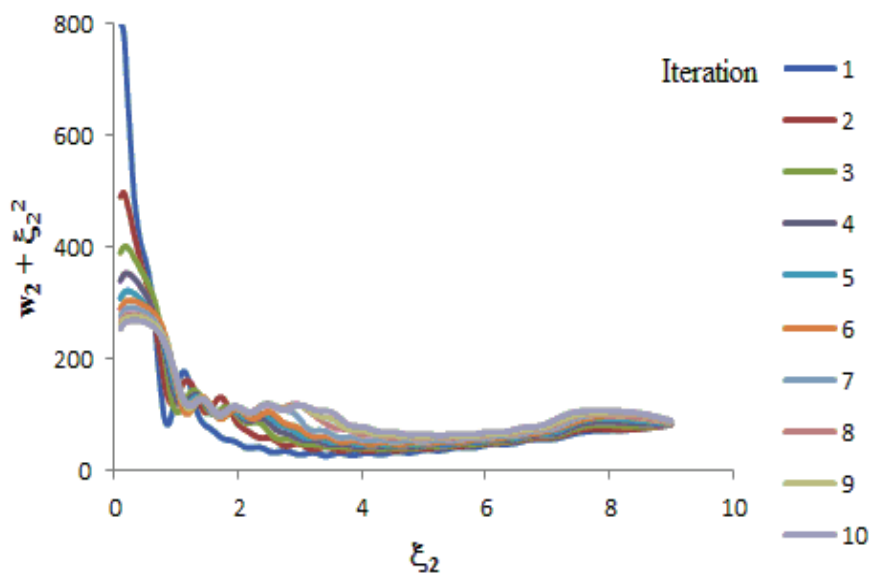
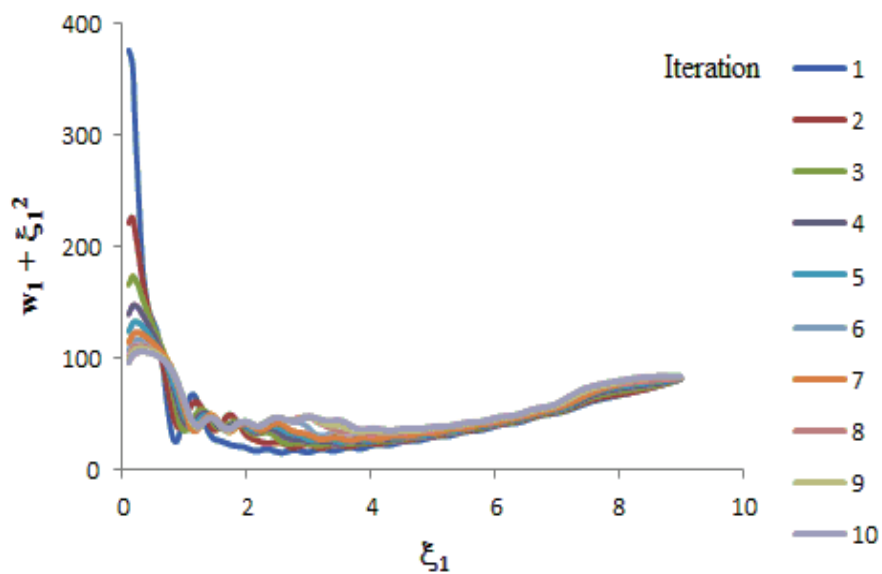
4. Results and Discussions

The results of total potentials for D^+ and ${}^6\text{Li}^+$ are plotted in Figs. 2 and 3. The probability densities for D^+ and ${}^6\text{Li}^+$ are also plotted in Figs. 4 and 5.

Seeing the results for D^+ in Figs 2 and 4, convergent solutions are obtained within the ten times iteration. However, convergences of the solution for ${}^6\text{Li}^+$ are not always good. The chemical potentials are used as the index parameters for convergences because they are not functions but single values. In this calculation, the convergences of the chemical potentials for D^+ and ${}^6\text{Li}^+$ are 2% and 6%, respectively. The mass difference between D^+ and ${}^6\text{Li}^+$ causes this unbalance. In Figs. 4 and 5, main peak of probability density exists at $\xi_i \approx 8$. Here, we should notice that $\alpha_1 \neq \alpha_2$. This means that main peaks of D^+ and ${}^6\text{Li}^+$ do not overlap completely.

In this study, positive charges of the ion cores are regarded as the point charges. The Coulomb repulsions between these point charges reflect the divergences of the potentials at the origins in Figs. 2 and 3. In order to describe the interactions between

ions which exist in the extremely narrow space, we should consider the interaction between the 1s electron of ${}^6\text{Li}^+$ and other particles. In this study, we neglect those interactions as an elementally approximation.



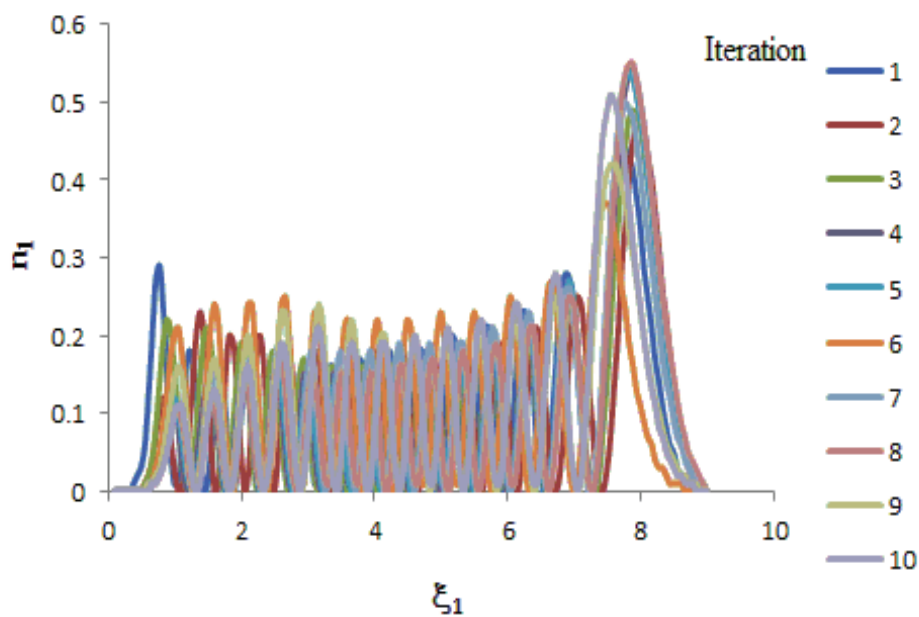


Fig. 4. Probability density of D^+ .

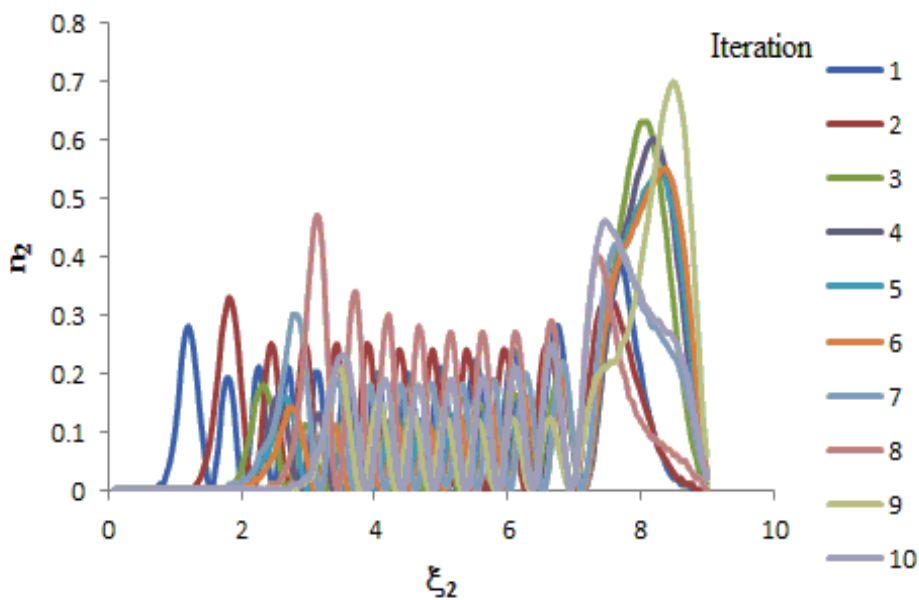


Fig. 5. Probability density of ${}^6\text{Li}^+$.

5. Conclusions

In our previous work [9], we showed the method how to perform the calculations proposed by Kim et al. [6,7]. In this study, we improved our previous work and

proposed a method how to find a ground state chemical potential. We can apply this method to the other calculations. For example, they are general mixed ratio of two species of charged bosons, arbitrary pair of two species, \dots . In near future, we will calculate the nuclear reaction rate between two charged bosons by using the optical theorem [8].

Acknowledgements

The authors wish to thank Prof. Y.E.Kim of Purdue Univ. for his advices about BEC. The authors also wish to thank Mr.K.Yasuda and Mr.T.Yamazaki for their daily helps.

References

- [1] J.Bardeen, L.N.Cooper and J.R.Schrieffer, "Theory of Superconductivity", Phys.Rev. **108**(1957)1175
- [2] R.T.Bush and R.D.Eagleton, "A Hypothetical Model to Probe an Elusive Phenomenon", J.Fusion Energy, **9**(1990)397
- [3] Y.E.Kim and A.L.Zubarev, "Equivalent Linear Two-Body Method for Many-Body Problems", J.Phys, **33**(2000)151
- [4] A.Takahashi and N.Yabuuchi, "Fusion Rates of Bosonised Condensates", J.Codensed Matter Nuc. Sci., **1**(2007)106
- [5] K.Tsuchiya, "Quantum States of Deuterons in Pd", International Journal of Hydrogen Energy, 29(2004)1513
- [6] Y.E.Kim and A.L.Zubarev, "Mixtures of Charged Bosons Confined in Harmonic Traps and Bose-Einstein Condensation Mechanism for Low Energy Nuclear Reactions and Transmutation Process in Condensed Matter", Condensed matter Nuclear Science, Proc. of ICCF11, France, p.711-717
- [7] Y.E.Kim, "Generalized Theory of Bose-Einstein Condensation Nuclear Fusion for Hydrogen-Metal System", Purdue Nuclear and Many Body Theory Group (PNMBTG) Preprint PNMBTG-6-2011 (June 2011).
- [8] Y.E.Kim and A.L.Zubarev, "Optical Theorem and Finite-Range Effect for Nuclear Reactions in Astrophysics", Few-Body Systems Suppl., **8**(1995)329
- [9] K.Tsuchiya et al. , Proc. of the 13th Meeting of Japan CF Research Society, pp.1-9

Nuclear Transmutations (NTs) in Cold Fusion Phenomenon (CFP) and Nuclear Physics

H. Kozima

Cold Fusion Research Laboratory,
597-16 Yatsu, Aoi, Shizuoka, 421-1202 Japan

Abstract

Vast experimental data sets of nuclear transmutation in the cold fusion phenomenon (CFP) in solids with deuterium and protium (cf-materials) are investigated from the phenomenological point of view, in terms of our model with a single adjustable parameter (TNCF model) applied successfully to various events in the CFP, using the recent knowledge of nuclear physics on the interaction of a nucleus and neutrons. The nuclear transmutations (NTs) in the CFP are classified into four groups; 1) Nuclear transmutation by absorption (NT_A), 2) Nuclear transmutation by decay (NT_D), 3) Nuclear transmutation by fission (NT_F), and 4) Nuclear transmutation by transformation (NT_T). In our explanation, the mechanisms of these NTs have a common factor, absorption of a neutron or a nucleon cluster from a surrounding cf-matter (corresponding to neutron sea considered in nuclear physics), which has been figured out in our investigation of the fundamental premises of the TNCF model. In addition to this common factor in their mechanisms of the NTs, there had been used additional assumptions in the case of NT_D and NT_F ; a) In the case of NT_D , it was necessary to assume the decay-time shortening of compound nuclei formed by absorption of neutrons, and b) In the case of NT_F , it was necessary to assume the fission of the compound nuclei with medium atomic numbers. In this paper, these assumptions explained by nuclear physics in another paper presented at this Conference are successfully applied to the consistent analyses of experimental data sets on the NTs obtained in these more than 20 years in the CFP.

In the former investigation of the CFP, we have given successful explanations of several features of the NTs in the CFP; i) The relation of frequency of occurrence N_{NT} to that of other events such as excess energy generation N_Q , ii) Local nature of nuclear reactions in the CFP, and iii) quantitative explanations of nuclear transmutations in Pd and Ni alloys. In addition to these investigations, we have given the theoretical explanation of the decay-time shortening using the knowledge obtained in nuclear physics.

Thus, the unified explanation of almost all events in the CFP based on the TNCF model, including the nuclear transmutations given in this paper and other events such as emissions of charged particles and neutrons given in former works, suggests that the “trapped neutrons” or the cf-matter in cf-materials assumed in our model has substantial meaning in the solid-state nuclear physics and will serve as a cornerstone of the science of the cold fusion phenomenon.

1. Introduction

The cold fusion phenomenon (CFP) is the name used at first by Chinese scientists (e.g. [Li 1991]) in their presentations at ICCF2 held in Como, Italy on June 29 – July 4, 1991 to call the new research field emerging from the discovery made by Fleischmann et al. in 1989 [Fleischmann 1989].

We would like to use this name to express “nuclear reactions and accompanying events occurring in open (with particle and energy supplies), non-equilibrium systems composed of solids with high densities of hydrogen isotopes (H and/or D) in ambient radiation” belong to Solid-State Nuclear Physics (SSNP) or Condensed Matter Nuclear Science (CMNS) [Kozima 1998, 2006, 2014c]. It should be noticed that the names such as solid-state nuclear physics (SSNP), condensed matter nuclear science (CMNS), low energy nuclear reactions (LENR) are too wide to express the proper content of the CFP as explained above.

Generally speaking, nuclear phenomena occurring in solids or condensed matters include various events from the Moessbauer effect, the neutron diffraction, neutron traps in thin film resonator, neutron guides, *d-d* reactions in crystals PdD_x bombarded by energetic deuterons, and so forth. The CFP belongs certainly also in this field because it includes nuclear reactions resulting in nuclear transmutations and excess energy production in solids.

Therefore, it is desirable to use an appropriate name to specify the research field including nuclear events in systems composed of host elements and hydrogen isotopes without artificial excitations above about 1 keV to distinguish it from events in different energy regions and also from other phenomena such as the Moessbauer effect, the Knight shift in NMR, change of K-capture probability by environment, and the neutron diffraction by solids. This is the reason we recommend the name “the cold fusion phenomenon (CFP)” for the phenomenon accompanying nuclear reactions in several complex compounds composed of specific host elements and hydrogen isotopes in ambient radiation without artificial excitations, after the use of “cold fusion” at “the First Annual Cold Fusion Conference” held at Salt Lake City in 1990.

One of wonderful events in the CFP is the generation of new nuclides at localized regions in surface layers with a width of about 1 μm [Kozima 2011a]. The nuclear transmutation (NT) is surely an important evidence of the nuclear character of the CFP even if there remains a question what is the mechanism of nuclear reactions resulting in the new nuclides. We will ascribe the appearance of the new nuclides to the nuclear transmutation of nuclei preexisted at the site where occurred the transmutation [Kozima 2006 (Sec. 2.2.1.3), 2011a]. It should be remembered that there are several

confirmations of the localization profile of transmuted nuclei at surface layers of about a few micrometers [Okamoto 1994, Bockris 1996, Mizuno 1996, Iwamura 2006, Celani 2010]

The science of the cold fusion phenomenon (CFP) is in its process of development at present even if we have proposed a powerful model in 2006 [Kozima 2006] based on the experimental facts where we assumed existence of quasi-stable neutrons in solids (the trapped neutron catalyzed fusion (TNCF) model) with a single adjustable parameter. The model has been successful to give a unified and consistent overview on the whole experimental facts in both protium and deuterium systems with full of a variety of events from the excess energy generation to nuclear transmutations with changes of the nucleon number A and the proton number Z from 1 to more than 10 [Kozima 2006, 2013b]. The success of the phenomenological model to explain the CFP as a whole has been shown in our books [Kozima 1998, 2004, and 2006] and recent papers [Kozima 2007 – 2013a, 2013b].

The numerical relation between numbers of reactions N_x and N_y generating observables x and y , respectively, determined by an experimental result has been reproduced by the model within a factor 3 [Kozima 1998, 2006]. Localization of nuclear reactions generating nuclear transmutation products has been explained by the TNCF model [Kozima 2004, 2006, 2011a]. Three empirical laws have been found in experimental data obtained in the CFP [Kozima 2012a] and their meaning has been investigated in relation to the complexity of the cf-materials expected from premises of the model [Kozima 2010a, 2012b, 2013b].

Based on the success of the phenomenological approach, we have started investigation of the basis of the TNCF model quantum mechanically [Kozima 2004, 2006, 2011c]. The existence of the “trapped neutron” assumed in the model is explained by the formation of valence bands of neutrons in lattice nuclei mediated by the occluded hydrogen isotope (protium or deuterium). Neutrons in the bands form the cf-matter which supplies a neutron n or a nucleon cluster ${}^A_Z\Delta$ to a nuclide for nuclear reactions resulting in nuclear transmutations discussed in this paper as a whole.

There is another face of the nuclear transmutation in the CFP related to nuclear physics. We would like to investigate this face using knowledge of nuclear physics summarized in another paper [Kozima 2014a] presented at this Conference. The main points of the investigation in this paper are put on the nuclear transmutation observed in the CFP and the neutron-nuclear interaction investigated in nuclear physics developed in the 20th century.

It should be emphasized that the nuclear products observed in the CFP range very

widely from tritium to lead (Pb) as shown in our book [Kozima 2006 Fig. 2.11] in relation to the “stability law in nuclear transmutation” and localize their position at surface regions of CF samples (cf-materials) [Kozima 2011a].

2. Summary of the Nuclear Physics

We have given a summary of knowledge of nuclear physics relevant to nuclear reactions supposed to occur in the CFP [Kozima 2014a]. In the huge quantity of knowledge piled up in nuclear physics in its history of about a century, there is much knowledge distributed in different branches of research fields which we can combine to use in the investigation of nuclear reactions occurring in cf-materials at near room temperature without any specific acceleration mechanism.

The knowledge we can use is in the low energy region $0 < \varepsilon < 1000$ eV according to the classification used in nuclear physics. To specify the nuclei in cf-materials, we can use the division of three categories according to their mass number (or nucleon number) A ;

- A. Light nuclei: $1 \leq A \leq 25$.
- B. Intermediate nuclei: $25 \leq A \leq 80$.
- C. Heavy nuclei: $80 \leq A \leq 240$.

According to our interest in the neutron-nucleus interaction, we have noticed the problem investigated in astrophysics to explain the synthesis of heavy elements in stars [Burbidge 1957, Qian 2003]. The interaction between a nucleus A_ZX and neutrons with a temperature about 10^7 K is used to generate another nucleus ${}^{A+1}_{Z+1}Y$ by absorption of a neutron followed by a beta-decay [Burbidge 1957]. We have used this reaction for the explanation of a kind of product nuclei in the CFP designated as the nuclear transmutation by decay NT_D [Kozima 2006].

In the second genre B, there is another type of approach to nuclear reactions in the neutron star matter assuming an equilibrium state composed of nuclei and a free neutron gas [Baym 1971, Negele 1973]. In this approach, the composition of nuclear cluster (or nucleon cluster) forming a lattice and the density of the surrounding free neutron gas are determined by a computer simulation. There are two features of the neutron star matter related to the CFP; the interaction of the free neutrons with an alien nucleus and that of a nucleon cluster with an alien nucleus. The former may result mainly in the nuclear transmutations by absorption (NT_A) and decay (NT_D) in the CFP by single neutron absorption. The latter, on the other hand, may result in the NT_A and the nuclear transmutation by fission (NT_F) by a nucleon cluster absorption as discussed in our recent paper [Kozima 2009b].

Exotic nuclei has extensively been investigated recently in nuclear physics [Zdenek 2006, Wiedenhover 2007, Kanungo 2011, Lu 2013] and is another interesting theme closely related to the cf-matter formation in the CFP. We have noticed this problem already and took up its essentials in our investigation of the cf-matter formation [Kozima 2006 Sec. 3.5.3.1].

We will review experimental data obtained in the CFP in the next section in relation to the ordinary nuclear physics and give a trial to understand the data using the knowledge obtained in the nuclear physics.

3. Interaction of a Thermal Neutron with a Foreign Nucleus in CF Materials

In ordinary nuclear physics, the nuclear reactions are treated as processes occurring between a particle a and an isolated nucleus X resulting in a particle b and a nucleus Y , symbolically written as $X(a, b)Y$, in a short time duration in which the interaction between them occurs as discussed in another paper presented in this Conference [Kozima 2014a].

Interaction of nucleons in a nucleus occurs through the so-called strong interaction by the nuclear force with a range of about 1 fm ($= 10^{-15}$ m) and almost independent of surrounding electrons and nuclei except the weak effect of the electromagnetic force between charged particles in the nucleus and surrounding charged particles. Therefore, it is considered usually that the nuclear events such as decays of radioactive nuclei are not influenced by the environment around the nuclei.

However, there is an example of an effect of surrounding electrons on the nuclear processes in a nucleus; Decay by orbital electron capture like ${}^7\text{Be}$ [Segre 1949, Ohtsuki 2004]. Thus, the nuclear process in a nucleus in isolated nuclei suffers a little from environmental particles when they can touch with nucleons in the nucleus.

One example of the interaction of a nucleus and surrounding neutrons is investigated in relation to the formation of neutron stars at baryon densities from 2.8×10^{35} nucleons/cm³, where free neutrons begin to "drip" out of the nuclei, up to densities $\approx 3.4 \times 10^{38}$ nucleons/cm³, where standard nuclear-matter theory is still reliable in the free neutron regime by a compressible liquid-drop model [Baym 1971, Negele 1973]. The formation of a Coulomb lattice of nucleon clusters (bound neutron and proton clusters) surrounded by a dilute free neutron gas is similar to the situation realized in cf-materials where lattice nuclei are surrounded by quasi-free band neutrons.

If the neutrons in a neutron band manipulated in the TNCF (trapped neutron catalyzed fusion) model interact with a radioactive nucleus, we can expect a drastic

change of the decay scheme rather larger than the case of the decay by orbital electron capture of ^{74}Be as discussed in another paper [Kozima 2014b].

3.1. Foreign Nucleus at its Ground State in a CF-Material

In a cf-material made of the superlattice composed of two sublattices of a host element (e.g. Ni or Pd) and a hydrogen isotope (e.g. H or D), neutron bands are formed by the super-nuclear interaction between lattice nuclei [Kozima 2006, Sec. 3.7]. The neutrons in a band correspond to the trapped neutrons assumed in the TNCF model and behave as Bloch waves without disturbance except thermal motion of the sublattices. The neutrons in a band (or the cf-matter) have similar nature to the free neutron gas in the neutron star matter and there may be nucleon clusters shown by simulation [Negele 1973]. When there is a foreign nucleus, the cf-matter (neutron Bloch waves) interacts with the nucleus and the interaction induces many events depending on the characteristics of the foreign nucleus.

If the foreign nucleus is at its ground state, we can naturally expect absorption of a neutron or a nucleon cluster (a group of neutrons and protons in the cf-matter) to form a new nucleus as assumed in our explanation of the cold fusion phenomenon (CFP) [Kozima 19998, 2006]. In the original TNCF model where a trapped neutron is supposed to behave similarly to that in free space, we could give semi-quantitative explanations of plural events observed simultaneously adjusting the single parameter of the model.

3.2. Foreign Nucleus at its Unstable State

There are several experimental data of the shortening of the decay constant in radioactive elements in the CFP [Monti 1995, Dash 2003, 2005, Goddard 2000]. The data sets obtained by Dash et al. have been explained by the TNCF model in another paper presented at this Conference [Kozima 2014b]. In this case, the radioactive nuclei exist in CF materials from the first and are foreign nuclei for the Bloch neutrons.

4. Explanation of Nuclear Transmutation in the CFP by the TNCF Model

To explain the nuclear reactions observed in solids at near room temperature without specific acceleration mechanisms, we have proposed a model with an adjustable parameter n_n (density of the assumed neutrons in cf-materials) and analyzed many experimental data sets successfully giving qualitative and sometimes semi-quantitative explanation for them [Kozima 1998, 2006, 2013b].

We have assumed existence of the trapped neutrons with a density n_n and thermal energy in materials where occur nuclear reactions (cf-materials). Furthermore, we assumed that the neutron reacts with foreign nuclei in a cf-material according to the same mechanism of the nuclear reactions in free space. Therefore, for a reaction between a nucleus ${}^A_Z\text{X}$ and a neutron n ;



the number of reactions N_{nX} per unit time and volume is expressed as;

$$N_{nX} = 0.35 n_n v_n n_X \sigma_{nX} \quad (4.2)$$

where $0.35 n_n v_n$ is the flow density of the trapped thermal neutrons per unit area and time, n_X is the density of the nucleus ${}^A_Z\text{X}$ where the reaction occurs, σ_{nX} is the cross section of the reaction determined in free space.

The concept of the trapped neutron in a cf-material assumed a priori in the TNCF model has been investigated quantum mechanically. It is shown that neutron bands are formed by an interaction between lattice nuclei mediated by occluded hydrogen isotopes (super-nuclear interaction) [Kozima 2006]. A cf-material is supposed to be a superlattice composed of two sublattices, one of the lattice nuclei (e.g. Pd or Ni) and another of the occluded hydrogen isotope (e.g. D or H). The occluded hydrogen isotope has extended wavefunction interacting with several lattice nuclei through the ordinary nuclear force thus mediating indirect interaction between these lattice nuclei. This interaction between neutrons in different lattice nuclei is the super-nuclear interaction of a new kind and results in formation of neutron bands. The neutrons in these bands behave as the trapped neutrons assumed in the TNCF model. We have proposed a name ‘‘cf-matter’’ to express the neutrons in the neutron bands formed by this super-nuclear interaction mediated by the occluded hydrogen isotopes.

The cf-matter defined above may have the same properties to the free neutron gas appeared in the neutron star matter. Using analogy between the cf-matter and the free neutron gas, we assume that the nuclear (or nucleon) cluster ${}^A_Z\Delta$ in the latter is also exists in the former.

The nuclear transmutations observed in cf-materials have been classified into several classes as explained in the next section. To explain some cases of the nuclear transmutation where new nuclei with large changes of nucleon numbers appear from that of nucleus existed in an original material, we can use the nucleon cluster instead of a single neutron:

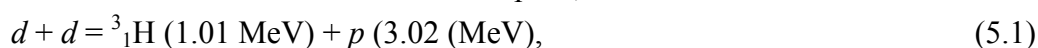


The reaction (4.4) expresses a case where the nucleon cluster ${}^A_Z\Delta$ transforms

automatically into a nucleus A_ZX in the cf-material.

5. Illustrative Examples of the Analysis of Experimental Data Sets showing Nuclear Transmutation (NT) in the CFP

The first experimental data showing the nuclear transmutation in the cold fusion phenomenon (CFP) in the deuterium systems is the data given by Morrey et al. [Morrey 1990] using the a sample provided by Fleischmann et al. They could measure the remaining helium in the surface region of the Pd sample which had shown excess heat. Their result had been accepted by many scientists as an negative evidence against the cold fusion proposed by Fleischmann et al. [Fleischmann 1989] due to the discrepancy between the amount of helium they observed in the surface region of the sample and the excess heat measured by the providers. The discrepancy was concluded based on the Fleischmann's hypothesis that there had been occurred nuclear reactions between two deuterons written down as follows in free space;



The discrepancy between the amount of the helium and the excess energy was resolved [Kozima 1997a] by a new idea based on the mechanism producing the nuclear products, different from reactions (5.1) – (5.3), according to the premises of the model (TNCF model) where was assumed existence of thermal neutrons in solids proposed by us [Kozima 1994].

On the other hand, the first experimental data showing the nuclear transmutation in protium systems was obtained by R.T. Bush [Bush 1992] in Ni/H₂O+K₂CO₃ (Na₂CO₃, Rb₂CO₃)/Pt systems. He observed production of Ca in an electrolytic system with a potassium electrolyte. This data had been explained semi-quantitatively by our model [Kozima 1997b, 1998 (Sec. 11.11b)].

To show the diversity of experimental data on the nuclear transmutation observed in the CFP, we cite here a figure showing variety of product nuclei given by Miley et al. [Miley 1996b] in Fig. 4.1. In this figure, they compiled data sets of the nuclear transmutation observed by Miley et al., Mizuno et al., and Bockris et al. Plotted are their data of PS/P microsphere (palladium Run #11), Mizuno's data and Bockris' data for Pd cathodes with D₂O electrolytic cell. (The PS/P microsphere means a microsphere of a polystyrene core with a coating of palladium by sputtering.)

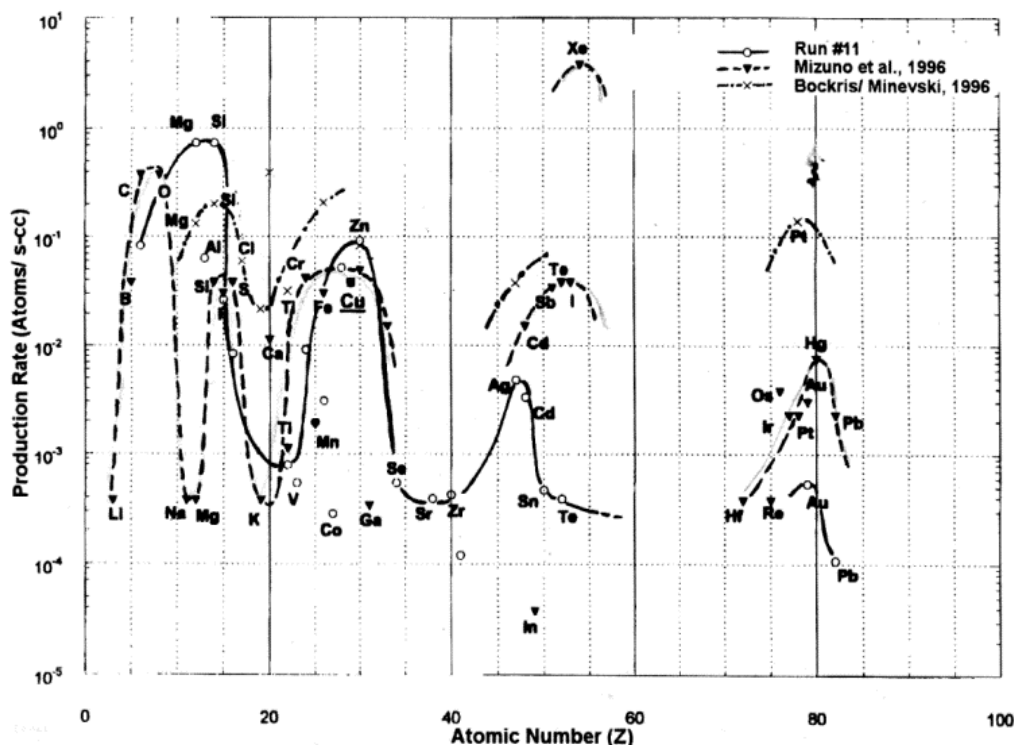


Fig. 5.1. Nuclei generated in cf-materials observed by Miley et al., Mizuno et al. and Bockris et al. [Miley 1996b, Fig. 4].

Before discussing the overall feature of the nuclear transmutation in the CFP, we give some examples of experimental data sets analyzed by the TNCF model in this Section. Extensive data of the nuclear transmutation in the CFP will be given in Section 6.

5.1. Nuclear transmutation supposed to be caused by single neutron absorption

In the course of the investigation of the CFP with the phenomenological TNCF model first proposed at ICCF4 [Kozima 1994], the model has been extended to include absorption of a nucleon cluster ${}^A_Z\Delta$ with Z protons and $(A - Z)$ neutrons by a nucleus ${}^{A'}_Z X$, in addition to the absorption of a single neutron assumed first, to treat several experimental data sets showing nuclear transmutations with large changes of nucleon numbers after the reaction [Kozima 2006].

The fundamental equation of the TNCF model to interpret the nuclear transmutation in the CFP is assumed to be the one showing the number of reactions N_{nX} in a time t between the trapped neutron with a density n_n and the nucleus ${}^A_Z X$:

$$n + {}^A_Z X = {}^{A+1}_Z X, \tag{5.4}$$

$$N_{nX} = 0.35 n_n v_n n_X V_{nX} t \tag{5.5}$$

where $(0.35 n_n v_n)$ is the flow density of the trapped thermal neutrons per unit area and time, n_X is the density of the nucleus A_ZX , V is the volume where the reaction occurs, and σ_{nX} is the cross section of the reaction defined in free space.

We summarize the analyses of several experimental data sets of the nuclear transmutation (NT) with variety of results obtained hitherto in this sub-section.

5.1.1. Shifts of isotope ratios of Ti and Pd

After an experiment with a duration time τ [Kropfenstein 1998], the density x_i ($i = 1 - 5$) of isotopes ${}^A_Z\text{Ti}$ ($[A = 46 - 50]$ [$i = 1 - 5$]) changed by the absorption of a neutron followed by a β^- -decay (or electron capture, EC) according to the following equations (cf. Eq. (5.5)):

$$x_1 = x_1^{(0)} - 0.35 n_n v_n \sigma_1 \tau x_1^{(0)}, \quad (5.6)$$

$$x_i = x_i^{(0)} + 0.35 n_n v_n \sigma_i \tau x_{i-1}^{(0)} - 0.35 n_n v_n \sigma_i \tau x_i^{(0)}, \quad (i = 2 - 5) \quad (5.7)$$

Solving this simultaneous equation, we could determine the theoretical ratios of $\eta_{5i|th} \equiv x_5/x_{i|th}$ to compare with the experimental ones. The coincidence is very good as seen in columns 6 and 7 in Table 5.1 [Kozima 2006 Appendix C7].

Table 5.1. Data about titanium isotopes ${}^A_Z\text{Ti}$ ($[A = 46 - 50] \equiv [i = 1 - 5]$) in cathodes. Absorption cross section σ_i , natural abundance $x_i^{(0)}$, nominal abundance ratio $\eta_{5i|nom}^{(0)} \equiv x_5^{(0)}/x_i^{(0)}|_{nom}$, measured ratios $\eta_{5i|exp}^{(0)} \equiv x_5^{(0)}/x_i^{(0)}|_{exp}$ before and $\eta_{5i|exp} \equiv x_5/x_{i|exp}$ after experiments, and their theoretical value $\eta_{5i|th}$ after experiments calculated using $\eta_{5i|exp}^{(0)} = x_5^{(0)}/x_i^{(0)}|_{nom}$.

Isotope	σ_i (b)	$x_i^{(0)} _{nom}$ (%)	$x_5^{(0)}/x_i^{(0)} _{nom}$	$x_5^{(0)}/x_i^{(0)} _{exp}$	$\eta_{5i exp}$	$\eta_{5i th}$
${}^{46}\text{Ti}$ ($i = 1$)	0.596	7.93	0.6734	0.6960	0.6683	0.6683
${}^{47}\text{Ti}$ ($i = 2$)	1.702	7.28	0.7335	0.8027	0.6978	0.771
${}^{48}\text{Ti}$ ($i = 3$)	7.844	73.94	0.0722	0.0785	0.0727	0.0846
${}^{49}\text{Ti}$ ($i = 4$)	2.214	5.51	0.969	1.0111	0.9358	0.402
${}^{50}\text{Ti}$ ($i = 5$)	0.179	5.34	1.000	(1.00)	(1.00)	(1.00)

Similarly, the changes of palladium isotopes observed by Silver et al. [Silver 1993] are analyzed successfully and the result is presented in Table 5.2.

Table 5.2. Data about palladium isotopes ${}^A_{46}\text{Pd}$ ($[A = 102 - 110] \equiv [i = 1 - 6]$) in cathodes. To calculate experimental values of relative composition, we used SIMS data at 0.09 μm from the surface (15 minutes from the beginning). Natural abundance $x^{(0)}_i$, nominal abundance ratio $\eta^{(0)}_{i1|\text{nom}} \equiv x^{(0)}_i/x^{(0)}_{1|\text{nom}}$, measured ratio $\eta^{(0)}_{i1|\text{exp}} \equiv x^{(0)}_i/x^{(0)}_{1|\text{exp}}$, before and $\eta_{i1|\text{exp}} \equiv x_i/x_{1|\text{exp}}$ after experiments, and their theoretical value $\eta_{i1|\text{th}}$ after experiments calculated using $\eta^{(0)}_{21|\text{exp}} \equiv x^{(0)}_2/x^{(0)}_{1|\text{exp}}$. Experimental data for $i = 4$ and 5 measured in Omega Analytical Services, Aloha, OR. in 1996, are interchanged to compare well with theoretical results.

Isotope (i)	σ_i (b)	$x^{(0)}_{i \text{nom}}$ (%)	$\eta^{(0)}_{i1 \text{nom}}$	$\eta^{(0)}_{i1 \text{exp}}$	$\eta_{i1 \text{exp}}$	$\eta_{i1 \text{th}}$
${}^{102}\text{Pd}$ ($i = 1$)	3.36	0.96	1.000	1.000	1.000	(1.000)
${}^{104}\text{Pd}$ ($i = 2$)	0.523	10.97	11.42	9.0	13.7	(13.7)
${}^{105}\text{Pd}$ ($i = 3$)	20.25	22.33	23.26	19.8	25.0	7.9
${}^{106}\text{Pd}$ ($i = 4$)	0.303	27.33	28.47	24.0	32.8	51
${}^{108}\text{Pd}$ ($i = 5$)	8.504	26.71	27.82	23.8	27.8	18
${}^{110}\text{Pd}$ ($i = 6$)	0.227	11.81	12.30	9.5	14.8	12

5.1.2. Production of Sr from Rb in CF Materials

Bush et al. investigated nuclear transmutation from Rb to Sr and the accompanied excess energy generation and X-ray emission in light water electrolytic systems [Bush 1992, 1993a, 1993b, 1994]. They used Rb_2CO_3 and RbOH as electrolytes in H_2O in electrolysis experiments with a Ni sponge cathode and a Pt anode [Bush 1994].

The nuclear transmutation of Rb into Sr is explained by the following reactions in our model (TNCF model). In the surface layer of the Ni cathode, there are absorbed and occluded Rb atoms. When there is a cf-matter formed by the neutron band mechanism, a ${}^A_{37}\text{Rb}$ ($A = 85, 87$) nucleus absorbs a neutron and the resulting compound nucleus ${}^{A+1}_{37}\text{Rb}$ ($A = 85, 87$) decays as follows:



where $\underline{\nu}_e$ is an antiparticle of the electron neutrino. The absorption cross section of the reaction (5.8) for a thermal neutron are 0.480 and 0.120 b and the energies Q in Eq. (5.9) are 1.774 and 5.316 MeV for nuclei with $A = 85$ and 87, respectively.

Using Eq. (5.5), we can write down the simultaneous equation for densities $n^{\text{R}*}_{86}$ and $n^{\text{R}*}_{88}$ of the isotopes ${}^{86}_{38}\text{Rb}^*$ and ${}^{88}_{38}\text{Rb}^*$, respectively, and n^{S}_{86} and n^{S}_{88} of the isotopes ${}^{86}_{38}\text{Sr}$ and ${}^{88}_{38}\text{Sr}$, respectively, as follows:

$$dn^{\text{R}*}_{86}/dt = 0.35 n_n v_n \sigma_{\text{nR}85} n^{\text{R}}_{85} - n^{\text{R}*}_{86}/\tau_{86}, \quad (5.10)$$

$$dn^{\text{R}*}_{88}/dt = 0.35 n_n v_n \sigma_{\text{nR}87} n^{\text{R}}_{87} - n^{\text{R}*}_{88}/\tau_{88}, \quad (5.11)$$

$$dn_{86}^S/dt = n_{86}^{R^*}/\tau_{86}, \quad (5.12)$$

$$dn_{88}^S/dt = n_{88}^{R^*}/\tau_{88}, \quad (5.13)$$

where τ_{86} and τ_{88} are decay constants of $^{86}_{37}\text{Rb}^*$ and $^{88}_{37}\text{Rb}^*$, respectively.

The excess energy production E_{86} (or E_{88}) is written down using the energies Q_{86} (or Q_{88}) in Eq. (5.9) for $A = 85$ (or 87):

$$dE_{86}/dt = (n_{86}^{R^*}/\tau_{86}) Q_{86}, \quad (5.14)$$

$$dE_{88}/dt = (n_{88}^{R^*}/\tau_{88}) Q_{88}. \quad (5.15)$$

In this approximation using constant densities of rubidium isotopes, the amount of excess energy is proportional to the density of transmuted nucleus as shown by Eqs. (5.12) and (5.14) (or by Eqs. (5.13) and (5.15)).

The equations (5.10) – (5.13) are easily solved when we can assume that n_{85}^R and n_{87}^R are constant. Then, the equations (5.10) and (5.11) are solved to give an equation

$$y = (e^x - 1) e^{-x} \quad (5.16)$$

where $y = n_{86}^{R^*}$ (or $n_{88}^{R^*}$) and $x = t/\tau_{86}$ (or t/τ_{88}). The curve of this function is plotted in Fig. 5.2.

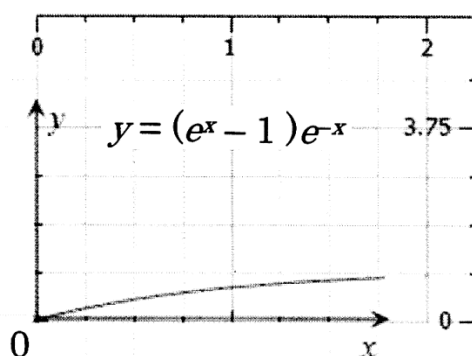


Fig. 5.2. Density (y) of the transmuted nucleus vs. time (x) in Eq. (5.16) according to the TNCF model for the situation of the experiment by Bush et al. [Bush 1994].

It was announced hesitantly in their paper that the excess energy E_1 observed in [Experiment I] with Rb_2CO_3 is about 5 times less than E_2 in [Experiment II] with RbOH (“For cell 56 (light water based RbOH), which had evidenced about five times as much excess heat as cell 53 (light water based Rb_2CO_3) based upon calorimetry.” [Bush 1994]): $E_2 \sim 5E_1$ or

$$(E_2/E_1)_{\text{exp}} \sim 5. \quad (5.17)$$

Theoretically, we can calculate the excess energy E_1 in [Experiment I] adding E_{86} and E_{88} determined by Eqs. (5.14) and (5.15) using appropriate parameters for the experiment. The most sensitive parameter will be the neutron density n_n in Eqs. (5.10)

and (5.11). Without further data to determine the parameter n_n , we have to satisfy ourselves assuming the same value of n_n in [Experiments I] and [Experiments II]. Then, we can estimate the ratio of excess energies using both values of transmuted nuclei;

$$(E_2/E_1)_{th} = (n_{86|2}^S / n_{86|1}^S) [\{Q_{86} + (n_{88}^S / n_{86}^S)|_2 Q_{88}\} / \{Q_{86} + (n_{88}^S / n_{86}^S)|_1 Q_{88}\}]. \quad (5.18)$$

From Fig. 6 of Bush et al. [Bush 1994], we can calculate $(n_{86|2}^S / n_{86|1}^S)$ to be 1.31. Using the values $Q_{86} = 1.774$ MeV and $Q_{88} = 5.316$ MeV in Eq. (5.9) and experimental data $(n_{88}^S / n_{86}^S)|_1 = 3.5$ and $(n_{88}^S / n_{86}^S)|_2 = 2.7$, we obtain theoretical excess energy ratio

$$(E_2/E_1)_{th} = 1.0, \quad (5.19)$$

to be compared with $(E_2/E_1)_{exp}$ given in Eq. (5.17).

This coincidence of $(E_2/E_1)_{exp}$ and $(E_2/E_1)_{th}$ in this case is within a factor ~ 5 .

5.2. Nuclear transmutation supposed to be caused by absorption of a nucleon cluster

The interesting experimental data sets obtained by Iwamura et al. [Iwamura 2002, 2006a, 2006b] give us information about a phase of the neutron-nucleus interaction in the CFP and also the local nature of the nuclear transmutation, especially the absorption of a nucleon cluster by a nucleus. They used a specific structure called ‘‘Pd complex,’’ made of a stratum structure Pd/[CaO/Pd]₅ in which the widths of layers are 400, 20 and 180 Å, respectively, as shown in Fig. 5.3.

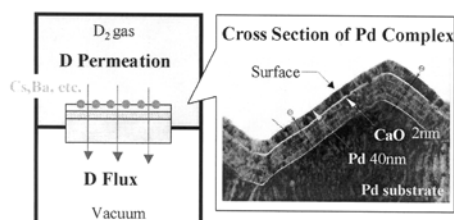


Fig. 5.3. Pd complex used in the experiments by Iwamura et al. [Iwamura 2006b]

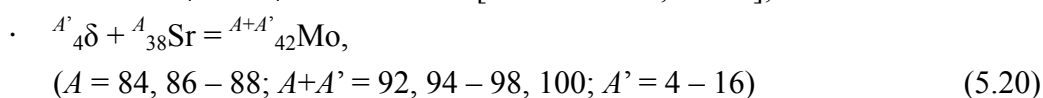
After adding alien elements Cs, Sr or Ba on the surface of the sample, D₂ gas was permeated through this structure as shown in Fig. 5.3, they investigated the surface of the complex and found nuclear transmutations of elements $^{A}_{55}\text{Cs}$ to $^{A+8}_{59}\text{Pr}$, $^{A}_{38}\text{Sr}$ to $^{A+A'}_{42}\text{Mo}$ and $^{A}_{56}\text{Ba}$ to $^{A+A'}_{62}\text{Sm}$. The production of Pr was confirmed by Hioki et al. [Hioki 2013] while the detected amount of Pr is two orders of magnitude less than that reported by Iwamura et al. [Iwamura 2002].

Table 5.4. Isotopic ratios of natural Sr and detected Mo in percent.

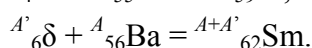
A	84	86	87	88			
${}^A_{38}\text{Sr}$ (%)	0.56	9.86	7.02	82.86			
A	92	94	95	96	97	98	100
${}^A_{42}\text{Mo}$ (%)	7	6	7	62	5	8	5

We tabulate their accumulated data of Mo production from Sr in Table 5.4 depicted in their data [Iwamura 2002, Fig. 10] to show the complex nature of the nuclear transmutation.

These results are clearly demonstrating the nuclear reactions catalyzed by a possible nucleon clusters ${}^4_4\delta$ to ${}^{16}_4\delta$ in our model [Kozima 2006, 2011a];



In the cases of Cs and Ba, the relevant reactions are written down as follow;



$$(A = 132, 134 - 138, A+A' = 144, 147 - 150, 152, 154; A' = 6 - 22) \quad (5.22)$$

In the case of the third reaction (5.22) [Iwamura 2006a], the transmutation from ${}^{137}_{56}\text{Ba}$ and ${}^{138}_{56}\text{Ba}$ to ${}^{149}_{62}\text{Sm}$ and ${}^{150}_{62}\text{Sm}$, respectively, are explained by the reaction associated with the nucleon cluster (or neutron drop) ${}^{12}_6\delta$. However, there remains possible participation of other nucleon clusters as noticed in the bracket of Eq. (5.22).

The data of Pr from Cs and abundance of ${}^{96}_{42}\text{Mo}$ correlated to the amount of ${}^A_{38}\text{Sr}$ suggest us the stability of ${}^8_4\delta$ in the cf-matter formed in their cf-materials, Pd complexes, at their boundary/surface region. The multi-neutron transfer is a problem discussed in the nuclear physics as we have discussed it in our paper presented at this Conference [Kozima 2014a]. This fact gives us a strong support to use the idea of the nucleon cluster ${}^A_Z\delta$ in the explanation of nuclear transmutations in the CFP.

In addition to the data of nuclear transmutations catalyzed by the nucleon cluster ${}^A_Z\delta$ in our analyses, they determined the locality of the positions where occur these NTs to generate Pr, Mo and Sm by using 100- and 500-micron X-ray beams [Iwamura 2006b].

The confirmation of occurrence of nuclear transmutations (I) only in D_2 permeation but not in H_2 and (II) necessity of CaO layer is interesting from our point of view.

The first point will be explained as follows. As we have often discussed, D in Pd and H in Ni are specific combination to assure formation of the cf-matter due to the neutron band by the super-nuclear interaction between lattice nuclei mediated by deuterons or protons in interstices. Therefore, it is reasonable to obtain positive results

only in PdD_x systems.

The second point will be explained as follows. The existence of CaO layer in the Pd complex used by Iwamura et al. is effective to form homogeneous distribution of deuterium in Pd lattice blocking the flow of deuteron through the complex thus making the superlattice of Pd and D more ideal. This is advantageous for realization of the super-nuclear interaction between lattice nuclei. Even then, there remains inhomogeneity along the surface of the complex resulting in the localization of products nuclei as detected by them [Iwamura 2006b].

6. Experimental Data Showing Nuclear Transmutations (NTs) by Absorption (NT_A), Decay (NT_D), Fission (NT_F), and Transformation (NT_T) and Their Explanation by the TNCF Model

The nuclear transmutations observed in the CFP show a variety of events difficult at first to investigate systematically. The phenomenological approach used by us, however, has given a powerful point of view to look at these complex events as have been performed in our investigation in these about 20 years as summarized in our books and papers [Kozima 1998, 2006, 2009b].

The typical data showing variety of the nuclear transmutation in the CFP has been given as the diagram of the frequency of observation vs. the atomic number of generated elements as shown in Fig. 6.1 [Kozima 2006 (Fig. 2.11), 2012a]. This figure shows also the empirical law of stability effect in the amount of resultant elements.

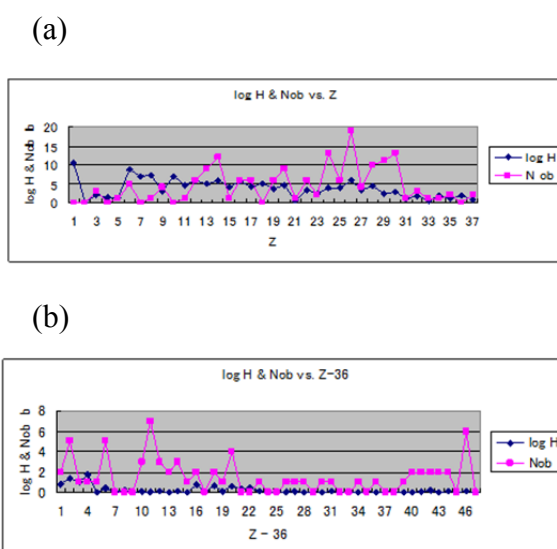


Fig. 6.1. Correspondence between the frequency N_{ob} observing elements in the CFP and the relative abundances $\log_{10}H$ of elements [Suess 1956] in the universe: (a) $Z = 3 - 38$ and (b) $Z = 39 - 83$ [Kozima 2006].

According to our experience, we can classify the nuclear transmutations (NT) in the CFP by the supposed mechanisms into four categories (1) NT_A, (2) NT_D, (3) NT_F and (4) NT_T and by relevant numbers of neutrons into two categories (I) single neutron and (II) nucleon cluster ${}^A_Z\Delta$. The nucleon cluster ${}^A_Z\Delta$ has been used in nuclear physics to explain neutron star formation [Negele 1972] and independently worked out in our investigation of NT's [Kozima 2006].

Keeping these concepts in our mind, we give a survey of experimental data sets of the nuclear transmutation in the CFP. Some of the data sets given below had been analyzed and published elsewhere [Kozima 1998, 2006, 2011c].

6.1. Nuclear Transmutation by Absorption (NT_A) of a Single Neutron

There are several data sets showing nuclear transmutations explained by simple absorption of single neutron by a nucleus preexisted in the cf-material.

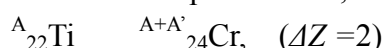
- (a) ${}^{12}_6\text{C} + n \rightarrow {}^{13}_6\text{C}$ [Mizuno 2008] [Kozima 2008d]
- (b) ${}^{56}_{26}\text{Fe} \rightarrow {}^{57}_{26}\text{Fe}$ [Iwamura 1998, Kumazawa 2005] [Kozima 2010b]
- (c) ${}^A_{24}\text{Cr} \rightarrow {}^{A+1}_{24}\text{Cr}$, [Mizuno 1996]
- (d) ${}^A_{22}\text{Ti} \rightarrow {}^{A+1}_{22}\text{Ti}$, [Kropfenstein 1998]
- (e) ${}^A_{46}\text{Pd} \rightarrow {}^{A+1}_{46}\text{Pd}$, [Dash 1996]
- (f) (1) Increase of Elements Ti, Cr, Co, As, Ir, and Tl and
(2) decrease of B, Sr, Pd and Ba. [Celani 2010] [Kozima 2011b]

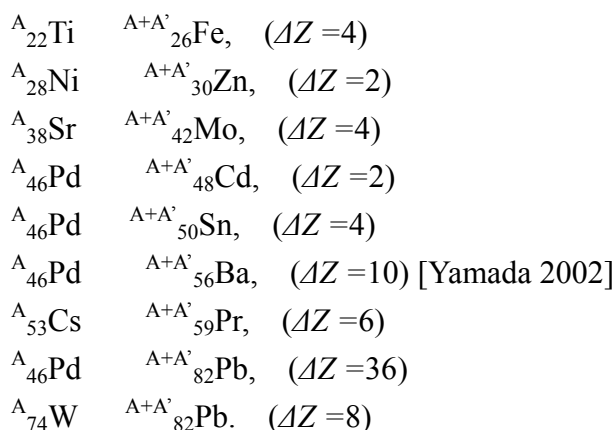
6.2. Nuclear Transmutation by Absorption (NT_A) of a nucleon cluster ${}^A_Z\Delta$

We can explain some data sets by using the concept of nucleon cluster [Kozima 2006, 2.5.2]

- (a) ${}^A_{26}\text{Fe} + {}^4_2\Delta \rightarrow {}^{A+4}_{28}\text{Ni}$ (A = 54, 56, 57, 58 with isotope ratios 5.82, 91.66, 2.19, 0.33 %) [Kumazawa 2005]
- (b) Fe from C [Sundaresan 1994][Hanawa 2002]
- (c) Cr in Ti/D/S system [Kopecek 1996]
- (d) Pb in Pd/Li/D [Mizuno 1996b, 1997]
- (e) Cs and Sr in Pd [Iwamura 2002]
- (f) Ba and Pb in Pd/D(H)/Na/Pt and Pd/(H₂O + Na₂CO₃)/Pt [Arapi 2002, Yamada 2002]

The data of these nuclear transmutations is tabulated as follows with changes of the proton number ΔZ in parentheses;





6.3. Direct Evidence of Nuclear Transmutation by Decay (NT_D) with Decay-Time Shortening

- (a) ${}^3_1\text{H} \rightarrow {}^3_2\text{He}, (\beta^-)$. ($\tau_d = 3.87 \times 10^4 \text{ s}$) [Reifenschweiler 1994]
- (b) ${}^{26}_{12}\text{Mg} \rightarrow {}^{27}_{13}\text{Al}, (\beta^-)$. [Kumazawa 2005]
- (c) ${}^{107}_{46}\text{Pd}^* \rightarrow {}^{107}_{47}\text{Ag}, (\beta^-)$. ($\tau_d = 1.3 \times 10^9 \text{ y}$) [Savvatimova 1994, Passell 2006]
- (d) ${}^{109}_{46}\text{Pd}^* \rightarrow {}^{109}_{47}\text{Ag}, (\beta^-)$. ($\tau_d = 13.7 \text{ h}$) [Savvatimova 1994, Passell 2006]
- (e) ${}^{40}_{19}\text{K}^* \rightarrow {}^{40}_{20}\text{Ca}, (\beta^-)$. ($\tau_d = 6.5 \times 10^6 \text{ y}$) [Bush 1992, Notoya 1993, Kumazawa 2005]
- (f) ${}^{235}_{92}\text{U}^* \rightarrow {}^{231}_{90}\text{Th}^*, (\alpha)$. ($\tau_d = 1.0 \times 10^9 \text{ y}$) [Dash 2003, 2005, Goddard 2000]
- (g) ${}^{238}_{92}\text{U}^* \rightarrow {}^{234}_{90}\text{Th}^*, (\alpha)$. ($\tau_d = 6.5 \times 10^9 \text{ y}$) [Dash 2003, 2005, Goddard 2000]
- (h) $\text{K} \rightarrow \text{Ca}$, $\text{Mg} \rightarrow \text{Al}$, and $\text{Fe} \rightarrow \text{Ni}$, are explained by single neutron absorption with a succeeding beta-decay to get final nuclides. [Kumazawa 2005] [Kozima 2010b]

6.4. Indirect Evidence of Nuclear Transmutation by Decay NT_D (or Fission NT_F)

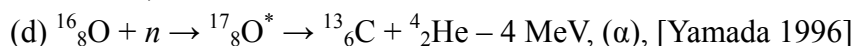
For cases of nuclear transmutation of nuclei with small proton numbers Z , the alpha decay is interpreted also as fission because the resulting nuclei have similar mass numbers A .

6.4.1. α -decay (NT_D) (or Fission NT_F) for small proton number nuclei

For nuclei with small proton numbers, NT_S are explained as NT_F or NT_A [Kozima 1998 Sec. 11.11, 2006 Secs. 2.5.1, 2.5.3]

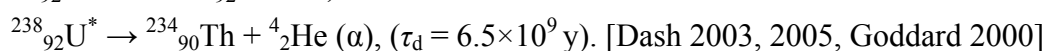
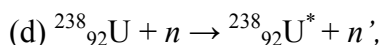
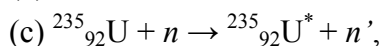
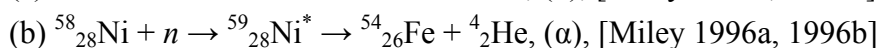
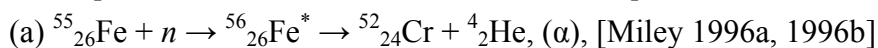
- (a) ${}^6_3\text{Li} + n \rightarrow {}^7_3\text{Li}^* \rightarrow {}^4_2\text{He} (+ {}^3_1\text{H}), (\alpha \text{ or fission})$ [Morrey 1990, Passell 2002] ([Hornyak 1948] p.192 II)
- (b) ${}^6_3\text{Li} + n \rightarrow {}^7_3\text{Li}^* \rightarrow {}^7_3\text{Li} \rightarrow {}^3_1\text{H} (+ {}^4_2\text{He}), (\alpha \text{ or fission})$ [Passell 2002]
- (c) ${}^{10}_5\text{B} + n \rightarrow {}^{11}_5\text{B}^* \rightarrow {}^7_3\text{Li} + {}^4_2\text{He}, (\alpha \text{ or fission})$ [Passell 1996] ([Hornyak 1948] p.

194 IX)



6.4.2. α -decay (NT_D) for large proton number nuclei

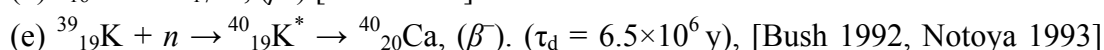
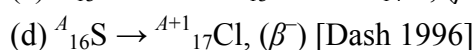
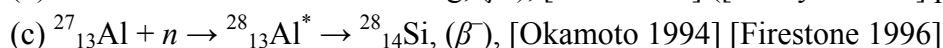
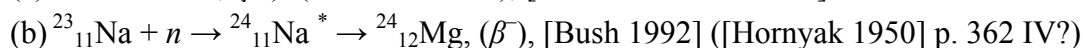
For nuclei with large proton numbers, the transmutation by alpha-decay is clearly identified [Kozima 1998 Sec. 11.11, 2006 Sec. 2.5.1].



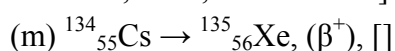
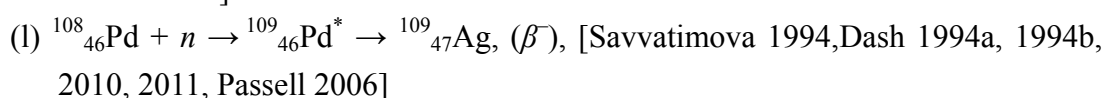
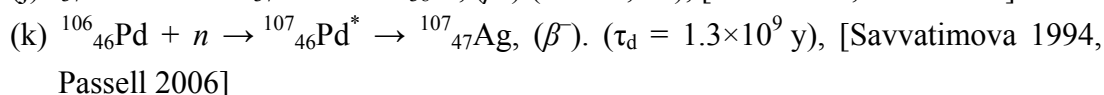
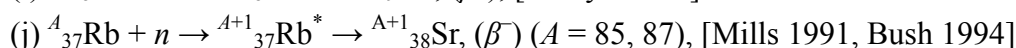
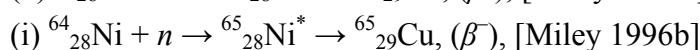
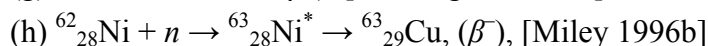
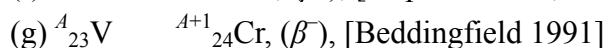
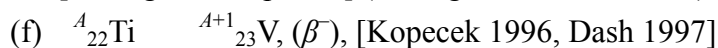
Details of the cases (c) and (d) are given in another paper [Kozima 2014b] presented at this Conference.

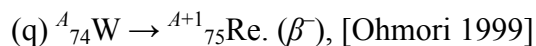
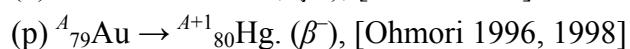
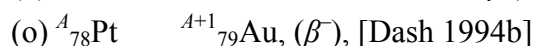
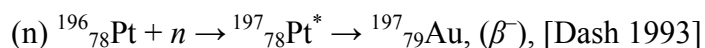
6.4.3. β -decay (NT_D)

There are many data sets showing that the observed nuclear transmutations are only explained by nuclear processes involving nuclear transmutation by beta-decay [Kozima 1998 Sec. 11.11, 2006 Sec. 2.5.1]. The extraordinarily long decay times in free space are given in parentheses after the reaction formulae.



[Alburger 1950 p. 381] (Alburger, $E_n = 0.02 \text{ MeV}$)





6.4.4. Nuclear Transmutation by Fission NT_F (or α -decay NT_D)

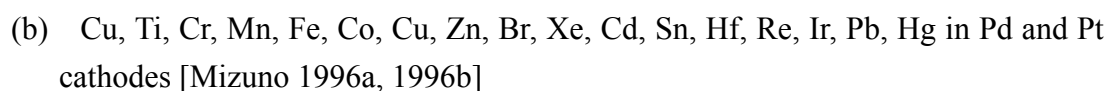
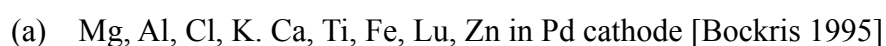
[Kozima 2006 (Section 2.5.3, 2.5.4)]

There are many data sets showing nuclear transmutations with large changes of mass numbers A from nuclei pre-existed in cf-materials before experiments. To understand the results in these cases, we have to assume existence of nucleon clusters in the cf-matter which have observed in the nuclear star matter [Kozima 2014a, Baym 1971, Negele 1973]. As noticed in Section 5.4.1, the nuclear transmutation by α -decay NT_D of a nucleus with a small proton number is considered also as nuclear transmutation by fission NT_F as noticed in Section 6.4.

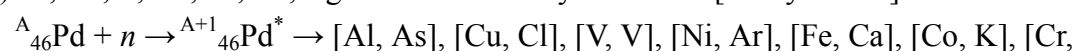
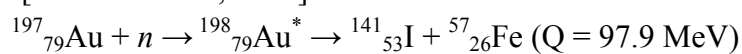
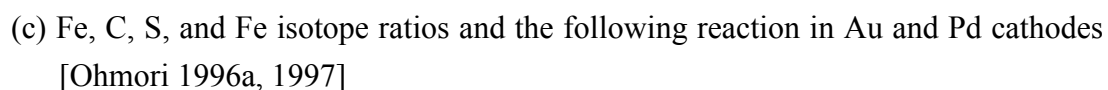
Fission caused by neutron absorption NT_F [Kozima 2006 Sec. 2.5.3]

The nuclear transmutation by fission of a nucleus with small proton number induced by absorption of a single neutron is known in nuclear physics and also observed in the CFP as explained in Section 6.4.

There are several data showing production of various elements most easily explained by a nuclear fission reaction by absorption of single neutron or a nucleon cluster. We summarize the data sets here not discriminating whether they are caused by absorption of a single neutron or of a nucleon cluster.

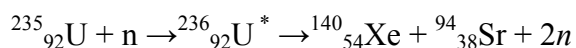


Generally speaking, abundances of heavier isotopes increase compared to the natural ratio, and those of lighter isotopes decrease. For example, ^{24}Mg went from 79% down to 74%, while ^{25}Mg went from 11 to 12%. This rule did not hold for some elements with few isotopes: ^{63}Cu increased while ^{65}Cu was absent, ^{47}Ti increased while ^{48}Ti decreased [Mizuno 1996b].



- Ti], [Zn, S], [Ag, e⁻]*.
- (e) ${}^A_{46}\text{Pd} + n \rightarrow {}^{A+1}_{46}\text{Pd}^* \rightarrow [\text{Zn, S}]$ [Li 1996] [Qiao 1998] [Kozima 1998 Sec. 11.12c]
- (f) Fe from C [Sundaresan 1994] [Hanawa 2000] [Bockris 1995] [Miley 1996 a – c] [Ohmori 1997]
- (g) Cr from Ti [Kopecek 1996]
- (h) Pb from Pd [Mizuno 1996b, 1997]
- (i) Pr, Mo from Cs/Pd, Sr/Pd [Iwamura 2002, 2006]
- (j) Pa, Pb from Pd [Arapi 2002, Yamada 2002]

**Foot note; The symbol [X, X'] means a possible fission product generating an observed element X with undetected element X'. For instance, a reaction*



is written as [Xe, Sr] in this symbol.

6.4.5. Nuclear transmutation by transformation NT_T [Kozima 2.5.4]

It is not certain whether the NT introduced in this subsection is caused by NT_T even if we put the explanation here by nuclear transmutation by transformation NT_T that is a generation of a nucleus ${}^A_Z\text{X}$ by a transformation of a nucleon cluster ${}^4_2\Delta$ in cf-matter in the solids. It should be remembered that there remains another explanation for the data by nuclear transmutation by fission NT_F.

- (a) Fe from C arcing. [Sundaresan 1994] [Hanawa 2000]
- (b) C on Pd [Mizuno 1996c][Yamada 1996][Chicea 2002, 2005]
- (c) C on W [Ohmori 1998]
- (d) Cl on Pd [Dash 1994]

6.5. Explanation of the “Decay Time Shortening” by Nuclear Physics

As listed up in Secs. 6.4.2 and 6.4.3, we have observed various product nuclei generated by the nuclear transmutations in the CFP possible to understand by assuming drastic shortening of decay times of compound nuclei formed by neutron absorption. As we have shown in our paper presented at this Conference [Kozima 2014a], the explanation of the shortening is different for the alpha decay and the beta decay. We give a brief explanation of the mechanisms for them below.

6.5.1. A Simple explanation of the Beta Decay in the CFP

The half-life t_{-} of the beta-decay is defined by the total probability of the disintegration of a beta-active nucleus per unit time given by integration of $P(p)dp$ over all electron momenta in the beta-spectrum [Blatt 1952 XIII 4 (4.1), Kozima 2014a]:

$$\beta\text{-decay probability} = \ln 2 / t_{-} = C f_{-}(Z, E_0) \quad (6.1)$$

where $f_{-}(Z, E_0)$ is the integral

$$f_{-}(Z, E_0) = \int_0^{p_0} F(Z, E) p^2 (E_0 - E)^2 dp \quad (6.2)$$

The upper limit of integration, $p_0 = (E_0^2 - 1)^{1/2}$, is the maximum value of the electron momentum measured by the unit mc .

The integral of (6.2) can be evaluated explicitly for $Z = 0$, i.e., if the Coulomb effect on the spectrum is neglected. The result is

$$f_{-}(0, E_0) = (1/60)(E_0^2 - 1)^{1/2} (2E_0^4 - 9E_0^2 - 8) + (1/4)E_0 \ln[E_0 + (E_0^2 - 1)^{1/2}] \quad (6.3)$$

For very large E_0 this function is proportional to E_0^5 . However, in the energy region of interest, $1.1 \leq E_0 \leq 10$, f_{-} does not follow the E_0^5 law but is more nearly proportional to $(E_0 - 1)^4$.

For Z not equal 0, the integral (6.2) must be evaluated numerically.

Anyway, the beta-decay probability depends strongly on the total energy liberated by the nuclear transition of the beta decay. The absorption of a thermal neutron gives energy to the nucleus of about 8 MeV that may increase E_0 by an amount about this value resulting in the half-life shortening such as that observed in the CFP [Kozima 2014a, Sec. 2.6].

This may give the explanation of the decay time shortening of beta decay we have had in the CFP.

6.5.2. Simple Explanation of the Alpha Decay in the CFP

A possible result of the existence of surface boundary with a surface energy E_{surf} and a thickness λ_c between nuclear matter in the nucleus and outside neutron sea may be related to the acceleration of alpha decay (or the decay-time shortening) of a quasi-stable radioactive nuclei by formation of the cf-matter (or neutron star matter) in the case of the CFP surrounding them [Kozima 2014a]. The nucleon cluster ${}^4_2\Delta$ formed in a nucleus transmits with a larger probability through the boundary resulting in the alpha-decay of the nucleus [Kozima 2014a, Sec. 2.9].

6.5.3. Decay Time Shortening

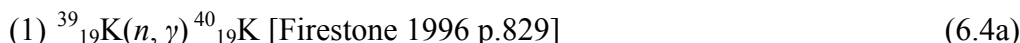
The product nuclei by the nuclear transmutation in the CFP have shown wide

diversity in their species challenging appropriate explanation based on the knowledge of nuclear physics. We have tried to explain some of these product nuclei in our phenomenological approach assuming drastic change of the decay times for compound nuclei produced by neutron absorption. Checking nuclear data minutely, however, we have realized that it is necessary to add a few factor in our explanation of the process given above to conclude the “decay time shortening” especially in the case of beta decay.

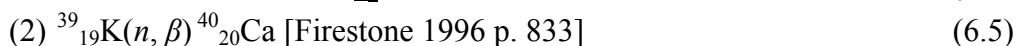
We discuss the problem in this subsection.

(a) “Decay-time shortening” in the case of beta-decay

The problem (e.g. decay of $^{40}_{19}\text{K}$ after the absorption of a neutron by $^{39}_{19}\text{K}$) is caused by the competition of two processes after the absorption of a thermal neutron;



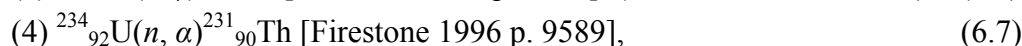
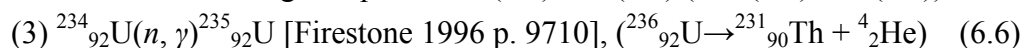
followed by a reaction



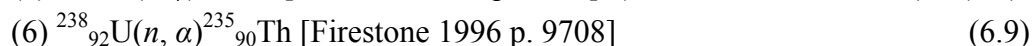
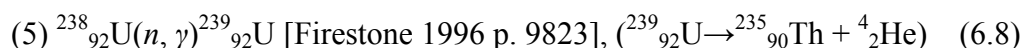
The explanation by the change of decay constants of $^{40}_{19}\text{K}$ given in Section 6.5.1 and in former papers and books [e.g. Kozima 2006] should be altered to take into consideration of the existence of the reaction (6.5) in addition to the (6.4a) and (6.4b) [Firestone 1996]. Apparently, the experimental data sets used in the explanation of “decay time shortening” include the both process (6.4) and (6.5). The apparent shortening of the decay time is assumed to explain the experimental data where a new nuclide $^{40}_{20}\text{Ca}$ appeared and assumed reaction was (6.4). If we can determine the ratio of $^{40}_{19}\text{K}$ and $^{40}_{20}\text{Ca}$, it is possible to determine one of the decay times of two processes (6.4) and (6.5) in the cf-materials knowing another one.

(b) “Decay-time shortening” in the case of alpha-decay

(i) The same consideration as that given above for the beta-decay is also applicable to the alpha-decay. The cases of heavy nucleus as $^{234}_{92}\text{U}$ (and $^{238}_{92}\text{U}$), the competitions are between the following two processes (6.6) and (6.7) (and (6.8) and (6.9)):



and



The apparent decrease of the decay time of $^{234}_{92}\text{U}$ (and $^{238}_{92}\text{U}$) is observed by the decrease of uranium due to the reaction (6.6) (and (6.8)) if we did not measure

appearance of thorium which is the case of the measurements. Variation of the half-life of $^{232}_{90}\text{Th}$ ($\tau_d = 1.41 \times 10^{10}$ y) was measured by R.A. Monti [Monti 1995] with insufficient data to analyze it with certainty.

In the case of co-deposition of U_3O_8 and H on Ni cathodes done by Goddard et al. [Goddard 2000], they measured increase of the radiation from their sample measured by a G-M counter for the same amount of U_3O_8 from 2900 (control) to 3700 counts (co-deposit sample). In this case, the co-deposition was performed with electrolysis by Ni cathode, Pt anode and acidic electrolyte. There are observed also existence of Cs, Fe and Ni on the nickel cathode and also topography change of the surface forming donut-like eruptions.

(ii) In the case of glow discharge by Dash et al. [Dash 2003], they used the gamma ray spectroscopy to confirm that there are thorium isotopes identified as $^{234}_{90}\text{Th}$ and $^{231}_{90}\text{Th}$ which are assumed to be generated from $^{238}_{92}\text{U}$ and $^{235}_{92}\text{U}$ by alpha decay, respectively. This is a typical example of the “decay-time shortening” of the alpha decay expressed as following equations by participation of the cf-matter:



The mechanism to realize the decay-time shortening for the alpha disintegration by the cf-matter is discussed in our paper [Kozima 2014a]. It is expected a decay-time shortening when there is the neutron star matter (or the cf-matter in the case of the CFP) surrounding the quasi-stable nuclei disintegrating by alpha emission as explained briefly in Section 6.5.2.

However, there remains some ambiguity if the gamma spectra used to identify the thorium isotopes are due to $^{235}_{90}\text{Th}$ and $^{232}_{90}\text{Th}$ which are consistent with the mechanism of alpha decay after single neutron absorption by $^{238}_{92}\text{U}$ and $^{235}_{92}\text{U}$, respectively.



The confirmation of $^{234}_{90}\text{Th}$ [Dash 2003] seems credible and the reaction (6.11) is reliable for the case of glow discharge experiment.

Then, we have to know two possibilities of the nuclear transmutation of $^{235}_{92}\text{U}$ (or $^{238}_{92}\text{U}$) by Eq. (6.10) (or Eq. (6.11)) and by Eq. (6.12) (or Eq. (6.13)) similar to that given in Section (a). In the beta decay, for instance, the generation of $^{40}_{20}\text{Ca}$ from $^{39}_{19}\text{K}$ is explained by the real “decay-time shortening” in the reaction (6.4) and by the “apparent shortening” by (6.5) explained above.

In conclusion of Section (b), we list up the data sets obtained by Dash et al. [Goddard 2000, Dash 2003, 21005]

1. Goddard et al. U_3O_8 and H on Ni. G-M counter detection of radiation increase by electroplating of U_3O_8 on Ni. Surface morphology change with voids surrounded by raised circular rimes. Detection of Cs, Fe (and Fm) on the surface by EDS.
2. Dash 2003. Discs of natural uranium were exposed to hydrogen and deuterium glow discharge plasmas. Alpha radiation, beta radiation, gamma spectra were observe. Increases of these radiations were determined. Gamma spectra revealed decrease of $^{238}_{92}U$ and increase of $^{234}_{90}Th$. Surface topography and concentration changes were observed b SEM and EDS. Erosion has occurred in the exposed area. Thorium was observed on the surface.
3. Dash 2005. Natural uranium foils were loaded by hydrogen by electrolysis with an electrolyte H_2SO_4 and a Pt anode. Increase of alpha, beta and gamma rays were observed. Gamma ray spectroscopy has shown increase of $^{234}_{90}Th$ and $^{235}_{92}U$.

It is interesting to notice that there exist two crystal modifications of uranium hydride, both cubic: an α form that is obtained at low temperatures and a β form that is grown when the formation temperature is above 250 °C. After growth, both forms are metastable at room temperature and below, but the α form slowly converts to the β form upon heating to 100 °C [Wikipedia, *Uranium hydrides*]. This lack of stability of UH_3 crystals may induce low reproducibility of experimental data of the CFP in the experiments discussed above.

7. Conclusions

The nuclear transmutations observed in the CFP have a diverse perspective beyond ordinary scopes formed in modern physics. Even in researchers in this field, there are many who do not want to accept the facts showing transmutations with large changes of nucleon numbers from those of nuclei preexisted in the cf-materials, the system composed of a host element and a hydrogen isotope. The host element is mainly a transition metal (Ti, Ni or Pd) or carbon (C) and the hydrogen isotope is not only deuterium but also protium (light hydrogen)

It is possible to take many ways of approach to the problem in this field from a microscopic to a phenomenological. We have tried a phenomenological approach using a model (TNCF model) where assumed existence of quasi-stable thermal neutrons in cf-materials where occurs the cold fusion phenomenon (CFP). The density of the assumed neutrons (trapped neutrons) n_n is a single adjustable parameter determined by an experimental value of an observable according to Premises of the model. Therefore, if there are more than two observables determined simultaneously, we can use an observable to determine n_n and then calculate another observable theoretically to

compare with an experimentally determined value of the observable. This gives us an evaluation of the effectiveness of our model.

Fortunately, we could give semi-quantitative accordance of the experimental and theoretical values thus calculated [Kozima 1998, 2006]. This result has suggested that the Premises of the TNCF model including existence of the trapped neutrons in the cf-material may have some reality behind them.

The nuclear transmutation observed in the CFP have been classified into four categories NT_A , NT_D , NT_F and NT_T and they have been explained qualitatively, sometimes semi-quantitatively, using the TNCF model.

Possible explanation of the existence of the quasi-stable trapped neutrons in cf-materials has been looked after in properties of transition metal hydrides and also in properties of exotic nuclei (recently developed new kinds of nuclei with extended neutron distribution) [Kozima 2006]. The characteristic of cf-materials composed of interlaced sublattices of a host element and a hydrogen isotope is used to show that there appears the super-nuclear interaction between lattice nuclei mediated by interstitial deuterons or protons. The super-nuclear interaction results in neutron bands in the cf-materials and the neutrons in the bands form the cf-matter composed of quasi-free neutrons and a few protons and electrons compensating charge neutrality as a whole. This cf-matter plays a decisive role to realized nuclear reactions in the CFP similar to the role of the free neutron sea in the physics of neutron star matter [Baym 1971, Negele 1973].

It is interesting to notice that there is a solid state phase of the super-nuclear interaction, i.e. its effect on the state of hydrogen isotopes in cf-materials. The protons or deuterons occluded in Ni or Pd lattice are in a lower energy state when their wavefunctions are not localized than that when they are localized, as experimental data have shown. Therefore, the wavefunctions of hydrogen isotopes and the diffusion properties of hydrogen isotopes should be strongly influenced by the nuclear force between the interstitial hydrogen isotope and the lattice nucleus. This fact is not noticed in solid state physics until now and the relation of wavefunctions and diffusion properties is not explained properly.

The experimental data sets on the nuclear transmutation in the CFP have been too diverse to be explained from a unified point of view. We have given in this paper a consistent explanation of almost all experimental data sets using our TNCF model (and its extended version of the nucleon cluster model).

We can give some expectations about possible CFP in materials not found yet based on the knowledge in experimental data we have obtained hitherto. Candidates are cobalt

($^{59}_{27}\text{Co}$) and copper ($^{63}_{29}\text{Cu}$ and $^{65}_{29}\text{Cu}$). These transition metals are able to occlude hydrogen isotopes and the nuclei have neutron levels at around the neutron evaporation level. Then, we can expect formation of the cf-matter according to the super-nuclear interaction and therefore the CFP in CoH_x (or CoD_x) and CuH_x (or CuD_x).

The whole data sets in the CFP extend from excess energy production to nuclear transmutations through emissions of neutron and charged particles. Application of these events to technology is possible but out of our imagination at present. At least, we can expect a new energy source and a radioactivity distinguisher by the nuclear reactions occurring in the cf-materials in which we can use fairly abundant elements on the earth. Deterioration of the cf-materials by the CFP observed every time in experiments is perhaps the most serious problem to overcome for the application of the CFP.

Acknowledgement

The author would like to express his thanks to Dr. Y. Iwamura for his kindness to send him their detailed data of the nuclear transmutation from Sr to Mo.

References

- [Alburger 1950] D.E. Alburger and E.M. Hafner, "Nuclear Energy Levels, $Z = 11 - 20$," *Rev. Mod. Phys.*, **22**, 373 - 385 (1950).
- [Baym 1971] G. Baym, H.A. Bethe and C.J. Pethick, "Neutron Star Matter," *Nuclear Phys.* **A175**, 225 - 271 (1971).
- [Beddingfield 1991] D.H. Beddingfield, F.E. Cecil, C.S. Galovich, H. Liu and S. Asher, "Characterization of Charge Particle Bursts from Deuterium Loaded Thin Titanium Foils," *Proc. ICCF2*, pp. 99 - 103 (1991).
- [Blatt 1952] J.M. Blatt and V.F. Weisskopf, *Theoretical Nuclear Physics*, John Wiley & Sons, New York, 1952. ISBN-10: 0-471-08019-5
- [Bockris 1995] J.O'M. Bockris and Z. Minevski, "Two Zones of 'Impurities' Observed after prolonged Electrolysis of Deuterium on Palladium," *Infinite Energy*, **5 & 6**, pp. 67 - 69 (1995).
- [Burbidge 1957] E.M. Burbidge, G.R. Burbidge, W.A. Fowler and F. Hoyle, "Synthesis of the Elements in Stars," *Rev. Mod. Phys.*, **29**, pp. 547 - 656 (1957).
- [Bush, R.T. 1992] R.T. Bush, "A Light Water Excess Heat Reaction Suggests that 'Cold Fusion' May Be 'Alkali-Hydrogen Fusion'," *Fusion Technol.*, **22**, pp. 301 - 322 (1992).
- [Bush 1993a] R.T. Bush and D.R. Eagleton, "Experiments Supporting the Transmission Resonance Model for Cold Fusion in Light Water: I. Correlation of Isotopic and

- Elemental Evidence with Excess Heat,” *Proc. ICCF3*, pp. 405 – 408 (1993).
- [Bush 1993b] R.T. Bush and D.R. Eagleton, “Experiments Supporting the Transmission Resonance Model for Cold Fusion in Light Water: II. Correlation of X-ray Emission with Excess Power,” *Proc. ICCF3*, pp. 409 – 416 (1993).
- [Bush 1994] R.T. Bush and D.R. Eagleton, “Evidence for Electrolytically Induced Transmutation and Radioactivity Correlated with Excess Heat in Electrolytic Cells with Light Water Rubidium Salt Electrolytes,” *Trans. Fusion Technol.* **26**, 344 – 354 (1994).
- [Celani 2010] F. Celani, P. Marini, et al., “First measurement on Nano-coated Ni Wire, at Very High Temperature, under He, Ar, H₂, D₂ Atmosphere and Their Mixtures,” Paper presented at 9th International Workshop on Anomalies in Hydrogen/Deuterium Loaded Metals (Certosa di Pontignano, Siena-Italy; Sept. 17 – 19, 2010).
- [Chicea 2002] D. Chicea, “On New Elements on Cathode Surface after Hydrogen Isotopes Absorption,” *Proc. ICCF9*, pp. 53 – 56 (2002). ISBN 7-302-06489-X/O·292
- [Chicea 2005] D. Chicea, “Comment on Carbon Production in Deuterium-Metal Systems,” *Proc. ICCF10*, 475 – 481 (2000). ISBN 981-256-564-7
- [Dash 1993] J. Dash, G. Noble and D. Diman, “Surface Morphology and Microcomposition of Palladium Cathodes after Electrolysis in Acidified Light and Heavy Water: Correlation with Excess Heat,” *Trans. Fusion Technol.*, **26**, 299 – 306 (1993).
- [Dash 1994a] J. Dash, G. Noble and D. Diman, “Changes in Surface Topography and Microcomposition of a Palladium Cathode caused by Electrolysis in Acidified Light Water,” *Proc. Int. Sym. Cold Fusion and Advanced Energy Sources* (Minsk, Belarus, May 25 – 26, 1994) pp. 172 – 183 (1994).
- [Dash 1994b] J. Dash, G. Noble and D. Diman, “Surface Morphology and Microcomposition of Palladium Cathodes after Electrolysis in Acidified Light and Heavy Water: Correlation with Excess Heat,” *Proc. ICCF4*, **2**, pp. 25-1 – 25-11 (1994).
- [Dash 1996] J. Dash, “Chemical Changes and Excess Heat caused by Electrolysis with H₂SO₄ – D₂O Electrolyte,” *Proc. ICCF6*, pp. 477 – 481 (1996).
- [Dash 1997] J. Dash, R. Kopecek and S. Miguet, “Excess Heat and Unexpected Elements from Aqueous Electrolysis with Titanium and Palladium Cathodes,” *Proc. 32th Intersociety Energy Conversion Engineering Conference*, **2**, pp. 1350 – 1355 (1997).
- [Dash 2003a] J. Dash, I. Savvatimova, S. Frantz, E. Weis and H. Kozima, “Effects of

- Glow Discharge with Hydrogen Isotope Plasmas on Radioactivity of Uranium,” *Proc. ICCF9*, pp.77 – 81 (2003). ISBN 7-302-06489-X/O·292
- [Dash 2003b] J. Dash, H. Kozima, I. Savvatimova, S. Frantz and E. Weis, “Effects of Glow Discharge with Hydrogen Isotope Plasmas on Radioactivity of Uranium,” *Proc. 11th Intern. Conf. Emerging Nuclear Energy Systems*, p.122 – 126 (2003).
- [Dash 2005] J. Dash and D. Chicea, “Changes in the Radioactivity, Topography, and Surface Composition of Uranium after Hydrogen Loading by Aqueous Electrolysis,” *Proc. ICCF10* pp. 463 – 474 (2005). ISBN 981-256-564-7
- [Dash 2010] J. Dash and Q. Wang, “Anomalous Silver on the Cathode Surface after Aqueous Electrolysis,” *Proc. ICCF15*, pp. 38 – 40 (2010). This paper is posted at New Energy Times website:
<http://newenergytimes.com/v2/conferences/LENRConferenceProceedings.shtml>
- [Dash 2011] J. Dash and J. Solomon, “Effect of Recrystallization on Heat Output and Surface Composition of Ti and Pd Cathodes,” *Preprints of Proc. ICCF17* (2011).
- [DOE Report 2004] “*Report of the Review of Low Energy Nuclear Reactions.*”
http://www.science.doe.gov/Sub/Newsroom/News_Releases/DOE-SC/2004/low_ene_rgy/CF_Final_120104.pdf
<http://newenergytimes.com/v2/government/DOE2004/7Papers.shtml>
- [Firestone 1996] R.B. Firestone, *Table of Isotopes*, CD-ROM 8th edition, v. 1.0, Wiley-Interscience, 1996.
- [Fleischmann 1989] M. Fleischmann, S. Pons and M. Hawkins, “Electrochemically induced Nuclear Fusion of Deuterium,” *J. Electroanal. Chem.* **261**, pp. 301 – 308 (1989).
- [Goddard 2000] G. Goddard, J. Dash and S. Frantz, “Characterization of Uranium Codeposited with Hydrogen on Nickel Cathodes,” *Transactions of American Nuclear Soc.* **83**, 376 – 378 (2000).
- [Hanawa 2000] T. Hanawa, “X-ray Spectrometric Analysis of Carbon Arc Products in Water,” *Proc. ICCF8*, pp. 147 – 152 (2000). ISBN 88-7794-256-8
- [Hora 1998] H. Hora, G.H. Miley, J.C. Kelly and Y. Narne, “Nuclear Shell Magic Numbers agree with Measured Transmutation by Low-Energy Reactions,” *Proc. ICCF7*, pp. 147 – 151 (1998).
- [Iwamura 1998] Y. Iwamura, T. Itoh, N. Gotoh, M. Sakano and I. Toyoda, "Detection of Anomalous Elements, X-ray and Excess Heat induced by Continuous Diffusion of Deuterium through Multi-layer Cathode (Pd/CaO/Pd)," *Proc. ICCF7*, pp. 167 – 171, ENECO Inc. Utah, USA, 1998.
- [Iwamura 2002] Y. Iwamura, Y. Sakano and T. Itoh, “Elemental Analysis of Pd

- Complexes: Effects of D₂ Gas Permeation,” *Jpn. J. Appl. Phys.*, **41**, 4642 – 4650 (2002).
- [Iwamura 2006a] Y. Iwamura, T. Itoh, M. Sakano, N. Yamazaki, S. Kuribayashi, Y. Terada, T. Ishikawa and J. Kasagi, “Observation of Nuclear Transmutation Reactions induced by D₂ Gas Permeation through Pd Complexes” *Proc. ICCF11*, pp. 339 – 349 (2006). ISBN 981-256-640-6.
- [Iwamura 2006b] Y. Iwamura, T. Itoh, M. Sakano, N. Yamazaki et al., “Observation of Surface Distribution of Products by X-ray Fluorescence Spectrometry during D₂ Gas Permeation through Pd Complexes” *Proc. ICCF12* pp. 178 – 187 (2006). ISBN 981-256-901-4.
- [Kanungo 2011] R. Kanungo, A. Prochazka, W. Horiuchi et al., “Matter Radii of ³²⁻³⁵Mg,” *Phys. Rev.* **C83**, 021302-1 – 4 (2011).
- [Klopfenstein 1998] M.K. Klopfenstein and J. Dash, “Thermal Imaging during Electrolysis of Heavy Water with a Ti Cathode,” *Proc. ICCF7*, pp. 98 – 102 (1998).
- [Kopecek 1996] R. Kopecek and J. Dash, “Excess Heat and Unexpected Elements from Electrolysis of Heavy Water with Titanium Cathodes,” *J. New Energy, Proc. 2nd International Low Energy Nuclear Reactions Conference*, pp. 46 – 53 (1996).
- [Kozima 1994] H. Kozima, “Trapped Neutron Catalyzed Fusion of Deuterons and Protons in Inhomogeneous Solids,” *Trans. Fusion Technol.* **26-4T**, pp. 508 – 515 (1994). ISSN: 0748-1896.
- [Kozima 1997a] H. Kozima, W. Watanabe, K. Hiroe, M. Nomura, M. Ohta and K. Kaki, “Analysis of Cold Fusion Experiments Generating Excess Heat, Tritium and Helium,” *J. Electroanal. Chem.*, **425**, 173 – 178 (1997) and **445**, 223 (1998).
- [Kozima 1997b] H. Kozima, “Nuclear Transmutation in Cold Fusion,” *Cold Fusion*, **23**, 54 – 64 (1997). And also *Symposium on the Nuclear Transmutation in Solids* (June 20, 1997, Iwate Univ., Morioka, Japan). pp. 82 – 88 (1997).
- [Kozima 1998] H. Kozima, *Discovery of the Cold Fusion Phenomenon*, Ohtake Shuppan Inc., Tokyo, Japan, 1998. ISBN 4-87186-044-2.
- [Kozima 2000] H. Kozima, “Electroanalytical Chemistry in Cold Fusion Phenomenon,” in *Recent Research Developments in Electroanalytical Chemistry*, Edited by S.G. Pandalay, Vol. 2, pp. 35 – 46 (2000). ISBN; 81-86846-94-8.
And also *Reports of CFRL (Cold Fusion Research Laboratory)*, **12-2**, 1 – 11 (2007).
<http://www.geocities.jp/hjrfq930/Papers/paperr/paperr.html>
- [Kozima 2004] H. Kozima, “Quantum Physics of Cold Fusion Phenomenon,” in *Developments in Quantum Physics Researches – 2004*, pp. 167 – 196, Ed. F. Columbus and V. Krasnoholovets, Nova Science Publishers, Inc., New York, 2004.

ISBN 1-59454-003-9

- [Kozima 2006] H. Kozima, *The Science of the Cold Fusion Phenomenon*, Elsevier Science, 2006. ISBN-10: 0-08-045110-1.
- [Kozima 2007] H. Kozima, “Six Sketches on Complexity and Wavefunctions in the Cold Fusion Phenomenon,” *Reports of CFRL (Cold Fusion Research Laboratory)*, **5-1**, 1 (2007). <http://www.geocities.jp/hjrfq930/Papers/paperr/paperr.html>
- [Kozima 2008a] H. Kozima, “The Cold Fusion Phenomenon as a Complexity (2) – Parameters Characterizing the System where occurs the CFP –” *Proc. JCF8* (Nov. 29 – 30, 2007, Kyoto, Japan), pp. 79 – 84 (2008). <http://jcfrs.org/file/jcf8-proceedings.pdf>
- [Kozima 2008b] H. Kozima, “The Cold Fusion Phenomenon as a Complexity (3) – Characteristics of the Complexity in the CFP –,” *Proc. JCF8* (Nov. 29 – 30, 2007, Kyoto, Japan), pp. 85 – 91 (2008). <http://jcfrs.org/file/jcf8-proceedings.pdf>
- [Kozima 2008c] H. Kozima, W.W. Zhang and J. Dash, “Precision Measurement of Excess Energy in Electrolytic System Pd/D/H₂SO₄ and Inverse-Power Distribution of Energy Pulses vs. Excess Energy,” *Proc. ICCF13*, pp. 348 – 358 (2008). ISBN 978-5-93271-428-7.
- [Kozima 2008d] H. Kozima and T. Mizuno, “Nuclear Transmutations in Hydrocarbons; Polyethylene (XLPE) Films and Phenanthrene on Pt Mesh Substrate,” *Reports of CFRL (Cold Fusion Research Laboratory)*, **8-4**, pp. 1 – 18 (October, 2008): <http://www.geocities.jp/hjrfq930/Papers/paperr/paperr.html>
- [Kozima 2009a] H. Kozima, “On the Methodology of the Cold Fusion Research” *Reports of Cold Fusion Research Laboratory (CFRL)* **9-5**, pp. 1 – 39 (November, 2009). <http://www.geocities.jp/hjrfq930/Papers/paperr/paperr.html>
- [Kozima 2009b] H. Kozima and T. Mizuno, “Investigation of the Cold Fusion Phenomenon in the Surface region of Hydrogen Non-occlusive Metal Catalysts; W, Pt and Au,” *Proc. JCF9*, pp. 52 – 58 (2009): <http://jcfrs.org/file/jcf9-proceedings.pdf>
And also *Reports of CFRL (Cold Fusion Research Laboratory)*, **9-2**, pp. 1 – 11 (October, 2009); <http://www.geocities.jp/hjrfq930/Papers/paperr/paperr.html>
- [Kozima 2010a] H. Kozima, “Complexity in the Cold Fusion Phenomenon,” *Proc. ICCF14* (August 10 – 15, 2008, Washington D.C., USA), Eds. J. Nagel and M.E. Melich, pp. 613 – 617 (2010). ISBN 978-0-578-06694-3.
- [Kozima 2010b] H. Kozima and T. Date, “Nuclear Transmutations in Polyethylene (XLPE) Films and Water Tree Generation in Them” *Proc. ICCF14* (August 10 – 15, 2008, Washington D.C., U.S.A.) pp. 618 – 622 (2010). ISBN: 978-0-578-06694-3
And also *Reports of CFRL (Cold Fusion Research Laboratory)*, **8-2**, pp. 1 – 15

- (2010): <http://www.geocities.jp/hjrfq930/Papers/paperr/paperr.html>
- [Kozima 2011a] H. Kozima, “Localization of Nuclear Reactions in the Cold Fusion Phenomenon,” *Proc. JCF11* pp. 59 – 69 (2011)
<http://jcf11-proceedings.pdf>
And also *Reports of CFRL (Cold Fusion Research Laboratory)*, **11-2**, pp. 1 – 19 (2011)
<http://www.geocities.jp/hjrfq930/Papers/paperr/paperr.html>
- [Kozima 2011b] H. Kozima and F. Celani, “Brief Explanation of Experimental Data Set on Excess Heat and Nuclear Transmutation in Multiply Nanocoated Ni Wire” *Proc. JCF11* pp. 53 - 58 (2011): <http://jcf11-proceedings.pdf>
And also *Reports of CFRL*, **11-1**, pp. 1 – 8 (2011)
<http://www.geocities.jp/hjrfq930/Papers/paperr/paperr.html>
- [Kozima 2011c] H. Kozima, “Physics of the Cold Fusion Phenomenon,” *Reports of CFRL*, **11-4**, pp. 1 – 21 (2011).
<http://www.geocities.jp/hjrfq930/Papers/paperr/paperr.html>
- [Kozima 2012a] H. Kozima, “Three Laws in the Cold Fusion Phenomenon and Their Physical Meaning,” *Proc. JCF12*, pp. 1 – 14 (2012).
<http://jcf12-proceedings.pdf>
And also *Reports of CFRL (Cold Fusion Research Laboratory)*, **11-6**, 1 – 14 (2011).
<http://www.geocities.jp/hjrfq930/Papers/paperr/paperr.html>
- [Kozima 2012b] H. Kozima, “Cold Fusion Phenomenon in Open, Non-equilibrium, Multi-component Systems,” *Reports of CFRL (Cold Fusion Research Laboratory)*, **12-1**, 1 – 14 (2012). <http://www.geocities.jp/hjrfq930/Papers/paperr/paperr.html>
- [Kozima 2013a] H. Kozima and M. Tada, “Emission of Charged Particles in the Cold Fusion Phenomenon,” *Proc. JCF13*, (to be published) and to be posted at JCF website: <http://jcf13-proceedings.pdf>
- The paper is also published as *Reports of CFRL* **13-2**, pp. 1 – 32 (2013) and posted at CFRL website: <http://www.geocities.jp/hjrfq930/Papers/paperr/paperr.html>
- [Kozima 2013b] H. Kozima, “Cold Fusion Phenomenon in Open, Nonequilibrium, Multi-component Systems – Self-organization of Optimum Structure,” *Proc. JCF13*, 13-19, pp. 134 – 157 (2013) and to be posted at JCF website:
<http://jcf13-proceedings.pdf>
- The paper is also published as *Reports of CFRL* **13-3**, pp. 1 – 24 (2013) and posted at CFRL website: <http://www.geocities.jp/hjrfq930/Papers/paperr/paperr.html>
- [Kozima 2013c] H. Kozima, “Trapped Neutron Catalyzed Fusion Model with an Adjustable Parameter,” *Infinite Energy*, **112** (November/December 2013), pp. 39 – 40 (2013)

- [Kozima 2014a] H. Kozima and K. Kaki, “Atomic Nucleus and Neutron — Nuclear Physics Revisited with the Viewpoint of the Cold Fusion Phenomenon,” *Proc. JCF14*, **14-6**, pp. xx – yy (2014) (to be published) and posted at JCF website: <http://jcfrs.org/file/jcf14-proceedings.pdf>. And also *Reports of CFRL 14-1*, 1 – 10 (March, 2014) that is posted at CFRL website: <http://www.geocities.jp/hjrfq930/Papers/paperr/paperr.html>.
- [Kozima 2014b] H. Kozima, “Nuclear Transmutation in Actinoid Hydrides and Deuterides,” *Proc. JCF14*, **14-15**, pp. xx - yy (2014) (to be published) and posted at JCF website: <http://jcfrs.org/file/jcf14-proceedings.pdf>. And also *Reports of CFRL 14-2*, 1 – 10 (March, 2014) that is posted at CFRL website: <http://www.geocities.jp/hjrfq930/Papers/paperr/paperr.html>
- [Kozima 2014c] H. Kozima, “The Cold Fusion Phenomenon – What is It?” *Proc. JCF14*, **14-16**, pp. xx - yy (2014) (to be published) and posted at JCF website: <http://jcfrs.org/file/jcf14-proceedings.pdf>. And also *Reports of CFRL 14-4*, 1 – xx (March, 2014) which is posted at CFRL website:; <http://www.geocities.jp/hjrfq930/Papers/paperr/paperr.html>
- [Kropfenstein 1997] M.K. Kropfenstein and J. Dash, “Thermal Imaging during Electrolysis of Heavy Water with a Ti Cathode,” *Proc. ICCF7*, pp. 98 – 102 (1998).
- [Kumazawa 2005] T. Kumazawa, W. Nakagawa and H. Tsurumaru, “A Study on Behavior of Inorganic Impurities in Water Tree” *Electrical Engineering in Japan* **153**, 1 – 13 (2005).
- [Li 1991] X.Z. Li, “Chinese Effort in Understanding the ‘Cold Fusion’ Phenomena,” *The Science of Cold Fusion (Proc. ICCF2)*, Conference Proceedings Vol. 33, pp. 309 – 317 (1991). ISBN 88-7794-045-X.
- [Lu 2013] Z.-T. Lu, P. Mueller, G.W. F. Drake, W. Nörtershäuser, S.C. Pieper and Z.-C. Yan, “Colloquium: Laser probing of neutron-rich nuclei in light atoms,” *Rev. Mod. Phys.*, **85**, 1383 – 1400 (2013).
- [Miles 1993] M.H. Miles, R.A. Hollins, B.F. Bush and J.J. Lagowski, *J. Electroanal. Chem.* **346**, pp. 99 – 115 (1993).
- [Miles 1994] M.H. Miles, B.F. Bush and J.J. Lagowski, *Fusion Technol.*, **25**, pp. 478 – 486 (1994).
- [Miley 1996a] G.H. Miley and J.A. Patterson, “Nuclear Transmutations in Thin-Film Nickel Coatings undergoing Electrolysis,” *J. New Energy (Proc. 2nd International Low Energy Nuclear Reactions Conference)*, **1 – 3**, pp. 5 – 30 (1996).
- [Miley 1996b] G.H. Miley and J.A. Patterson, “Quantitative Observation of Transmutation Products occurring in Thin-Film Coated Microspheres during

- Electrolysis," *Proc. ICCF6*, pp. 629 – 644 (1996).
- [Mizuno 1996a] T. Mizuno, T. Ohmori, T. Akimoto et al., "Isotope Distribution for the Elements Evolved in Palladium Cathode after Electrolysis in D₂O Solution," *Proc. ICCF6*, pp. 665 – 669 (1996).
- [Mizuno 1996b] T. Mizuno, T. Ohmori and M. Enyo, "Anomalous Isotopic Distribution in Palladium Cathode after Electrolysis," *J. New Energy*, **1-2**, pp. 37 – 44 (1996)
- [Mizuno 1996c] T. Mizuno, T. Ohmori and M. Enyo, "Isotopic Changes of the Reaction Products induced by Cathodic Electrolysis in Pd," *J. New Energy*, **1-3**, pp. 31 – 45 (1996)
- [Mizuno 2008] T. Mizuno and S. Sawada, "Anomalous Heat Generation during Hydrogenation of Carbon (Phenanthrene)," *Proc. ICCF14*, pp. 147 – 168 (2008). ISBN: 978-0-578-06694-3.
- [Monti 1995] R.A. Monti, "Variations of the Half-Lives of Radioactive Elements and Associated Cold Fusion and Cold Fission Reactions," *J. New Energy*, **1-1**, pp. 119 – 125 (1995).
- [Morrey 1990] J.R. Morrey, M.R. Caffee, H. Farrar, IV, N.J. Hoffman, G.B. Hudson, R.H. Jones, M.D. Kurz, J. Lupton, B.M. Oliver, B.V. Ruiz, J.F. Wacker and A. Van, "Measurements of Helium in Electrolyzed Palladium," *Fusion Technol.* **18**, 659 (1990).
- [Negele 1973] J.W. Negele and D. Vautherin, "Neutron Star Matter at Sub-nuclear Densities," *Nuclear Physics*, **A207**, 298 - 320 (1973).
- [Notoya 1993] R. Notoya, "Cold Fusion by Electrolysis in a Light Water-Potassium Carbonate Solution with a Nickel Electrode," *Fusion Technol.* **24**, 202 – 204 (1993).
- [Ohmori 1996a] T. Ohmori, T. Mizuno and M. Enyo, "Isotopic Distributions of Heavy Metal Elements produced during the Light Water Electrolysis on Gold Electrode," *J. New Energy*, **1-3**, pp. 90 – 99 (1996).
- [Ohmori 1996b] T. Ohmori, T. Mizuno and M. Enyo, "Production of Heavy Metal Elements and Anomalous Surface Structure of the Electrode produced during the Light Water Electrolysis on Au Electrode," *Proc. ICCF6*, pp. 670 - 674 (1996).
- [Ohmori 1997] T. Ohmori, M. Enyo, T. Mizuno, Y. Nodasaka and H. Minagawa, "Transmutation in the Electrolysis of Light Water – Excess Energy and Iron Production in a Gold Electrode," *Fusion Technol.*, **31**, 210 – 218 (1997).
- [Ohmori 1998] T. Ohmori, T. Mizuno, Y. Nodasaka and M. Enyo, "Transmutation in a Gold-Light Water Electrolysis System," *Fusion Technol.*, **33**, pp. 367 – 382 (1998).
- [Ohmori 1999] T. Ohmori and T. Mizuno, "Nuclear Transmutation Reaction Caused by Light Water Electrolysis on Tungsten Cathode under Incandescent Conditions,"

- Infinite Energy*, **27**, pp. 34 – 39 (1999).
- [Ohtsuki 2004] T. Ohtsuki, H. Yuki, M. Muto, J. Kasagi and K. Ohno, “Enhanced Electron-Capture Decay Rate of ^7Be Encapsulated in C_{60} Cages,” *Phys. Rev. Lett.* **93**, 112501-1 – 112501-4 (2004).
- [Okamoto 1994] M. Okamoto, H. Ogawa, Y. Yoshinaga, T. Kusunoki and O. Odawara, “Behavior of Key Elements in Pd for the Solid State Nuclear Phenomena Occurred in Heavy Water Electrolysis,” *Proc. ICCF4* (Hawaii, USA, Dec. 6 — 9, 1993), Vol.3, p.14 (1994), EPRI, Palo Alto, California, USA.
- [Passell 1996] T.O. Passell, “Search for Nuclear Reaction Products in Heat-Producing Palladium,” *Proc. ICCF6*, pp. 282 – 290 (1996).
- [Passell 1997] T.O. Passell, “Search for Nuclear Reaction Products in Heat-Producing Pd,” *Proc. ICCF7*, pp. 309 – 313 (1998).
- [Passell 2002] T.O. Passell, “Evidence for Lithium-6 Depletion in Pd Exposed to Gaseous Deuterium and Hydrogen,” *Proc. ICCF9*, pp. 299 – 304 (2002). ISBN 7-302-06489-X/O-292 Time-of-Flight secondary ion mass spectrometry (TOF SIMS).
- [Passell 2006] T.O. Passell, “Pd-110/Pd-108 Ratios and Trace Element Changes in Particulate Palladium Exposed to Deuterium Gas,” *Proc. ICCF10*, pp. 399 – 403 (2006). ISBN 981-256-564-7.
- [Qian 2003] Y.-Z. Qian, “The Origin of the Heavy Elements: Recent Progress in the Understanding of the *r*-Process,” *Prog. Part. Nucl. Phys.*, **50**, 153 – 199 (2003).
- [Qiao 1998] G.S. Qiao, X.L. Han, L.C. Kong and X.Z. Li, “Nuclear Products in a Gas Loading D/Pd and H/Pd System,” *Proc. ICCF7*, pp. 314 – 318 (1998).
- [Reifenschweiler 1995] O. Reifenschweiler, “Some Experiments on the Decrease of the Radioactivity of Tritium Sorbed by Titanium,” *Proc. ICCF5*, pp. 163 – 172 (1995).
- [Savvatimova 1994] I.B. Savvatimova, Y.R. Kucherov and A.B. Karabut, “Cathode Material Change after Deuterium Glow Discharge Experiment,” *Trans. Fusion Technol.* **26**, 389 - 394 (1994).
- [Segre 1949] E. Segre and C.E. Wiegand, “Experiments on the Effect of Atomic Electrons on the Decay Constant of Be^7 ,” *Phys. Rev.* **75**, 39 – 43 (1949).
- [Silver 1993] D.S. Silver, J. Dash and P.S. Keefe, “Surface Topology of a Palladium Cathode after Electrolysis in Heavy Water,” *Fusion Technol.*, **24**, 423 – 430 (1993).
- [Storms 2007] E. Storms, *The Science of Low Energy Nuclear Reaction – A Comprehensive Compilation of Evidence and Explanations about Cold Fusion*, World Scientific, Singapore, 2007. ISBN-10 981-270-620-8
- [Suess 1956] H.E. Suess and H.C. Urey, “Abundances of the Elements,” *Rev. Mod. Phys.*

28, pp. 53 – 74 (1956).

- [Sundaresan 1994] R. Sundaresan and J.O'M. Bockris, "Anomalous Reactions during Arcing between Carbon Rods in Water," *Fusion Technol.*, **26**, 261 – 265 (1994).
- [Wiedenhöver 2007] Ingo Wiedenhöver, "Exotic Nuclei" Lecture note given at National Nuclear Physics Summer School, 7/16/2007 Tallahassee, Florida.
- [Yamada 1996] H. Yamada, H. Nonaka, A. Dohi, H. Hirahara, T. Fujiwara, X. Li and A. Chiba, "Carbon Production on Palladium Point Electrode with Neutron Burst under DC Glow Discharge in Pressurized Deuterium Gas," *Proc. ICCF6*, pp. 610 – 614 (1996).
- [Yamada 2002] H. Yamada, S. Narita, Y. Fujii, T. Sato, S. Sasaki and T. Ohmori, "Production of Ba and Several Anomalous Elements in Pd under Light Water Electrolysis," *Proc. ICCF9*, pp. 420 – 423 (2002). ISBN 7-302-06489-X/O-292.
- [Zdenek 2006] Zdenek Dlouhy, "Structure and Properties of Exotic Nuclei using Radioactive Nuclear Beams," (doctoral theses) Praha, Listopad, 2006
- [Zukai 1974] Zukai Genshiryoku Yogo Ziten (1974). (Illustrated Dictionary of Atomic Power Terms, in Japanese) Nikkan Kogyo Shinbunsha, Tokyo, 1974. NDC 429.03

The Cold Fusion Phenomenon – What is It?

Hideo Kozima

Cold Fusion Research Laboratory
597-16, Yatsu, Aoi, Shizuoka, 421-1202 Japan

Abstract

Present status of the cold fusion (CF) research is reviewed from our point of view to make this field a common heritage of modern science. Various events observed in this field specified by a generic name “cold fusion phenomenon (CFP)” are investigated as a whole from a point of view using a phenomenological model (TNCF model) with a parameter n_n based on the whole experimental facts obtained in materials composed of various host solids and hydrogen isotopes not only deuterium but also protium (cf-materials). The parameter n_n is assumed to be the density of the quasi-stable trapped neutrons (cf-matter) formed in the cf-material. Events used to construct the model include generation of excess energy, emissions of neutrons and charged particles, generation of tritium and helium, and the nuclear transmutation at boundary regions of materials. Numerical relations between numbers of multiple events are explained semi-quantitatively by the model. Empirical laws for observables found in experiments have been used to discuss the cold fusion phenomenon as a complexity thus explaining irreproducibility and sporadicity of events as fundamental natures of the CFP. Bases of the premises assumed in the model, especially the existence of the trapped neutrons, have been investigated quantum mechanically in terms of characteristics of cf-materials. A possible mechanism of an indirect nuclear interaction between lattice nuclei mediated by interstitial hydrogen isotopes (super-nuclear interaction) was proposed. The neutron bands formed by this super-nuclear interaction contribute to formation of the trapped neutrons and even further of the cf-matter. Recent knowledge in nuclear physics and solid state physics is used to give some predictions of possible experiments not known until now. The copper (Cu) is a metal that show high mobility of hydrogen isotopes at higher temperatures than 450 °C and the nucleus has neutron energy levels at around evaporation level (zero level). These characteristics suffice necessary conditions for formation of the neutron bands by the super-nuclear interaction between lattice nuclei in copper hydrides at higher temperatures than 450 °C. So, we may be able to obtain positive data for the CFP in CuH_x and/or CuD_x there. Possible applications of the CFP are proposed. Though the answer to the question “What is the CFP” is not given at present, we have many materials to solve this riddle in near future. Recent knowledge on atomic nuclei and transition-metal hydrides related to the CFP from our point of view is summarized in Appendix.

1. Introduction

How is it possible to give an evidence of reality for a phenomenon lacking many essential factors common to conventional science developed in the 20th century? This is a question caused by disputes (e.g. [Krivit 2013]) on the article by E. Storms [Storms 2010] published in the *Naturwissenschaften*. In a field where principles governing events are not established such as the cold fusion phenomenon (CFP), the meaning of this term CFP will be explained below, a discussion has to be based on facts with explicit exhibition of a point of view on which the dispute stands. The cold fusion phenomenon (CFP) is the theme at hand originating in the work published almost a quarter of a century ago by Fleischmann et al. [Fleischmann 1989, Kozima 2014]. We will make a trial to open a common field among people with different feelings and opinions to the CFP to discuss this controversial problem positively with each other. Our fundamental point of view is a phenomenological approach based on the experimental data sets as presented by researchers who are reliable to the data. We will not restrain ourselves to such an assumption as *d-d* fusion reactions in solids as the fundamental mechanism for the CFP which restrict our eyes only to the deuterium system neglecting the protium system where are also observed various events supposed to belong to the CFP.

2. Cold fusion phenomenon, cf-materials, and experimental data sets

It is better to define our terminology at first to discuss this complicated and controversial theme, the cold fusion phenomenon (CFP). The “cold fusion phenomenon” is the term we call the events as a whole related to the field originally called “cold fusion” by the pioneering researchers who expected *d-d* fusion reactions in solids composed of host metal (Pd) and deuterium (a kind of hydrogen isotopes). The term “cold fusion phenomena” was first used by Chinese researchers (e.g. [Li 1991]) in the papers presented at ICCF2 in 1991. To clarify the meaning of the term, we redefine it as follows;

The CFP (Cold Fusion Phenomenon) stands for “nuclear reactions and accompanying events occurring in open (with external particle and energy supplies), non-equilibrium system composed of solids with high densities of hydrogen isotopes (H and/or D) in ambient radiation” belonging to Solid-State Nuclear Physics (SSNP) or Condensed Matter Nuclear Science (CMNS). (CFRL News No.81, <http://www.geocities.jp/hjrfq930/>).

The cold fusion phenomenon does surely belong to solid-state nuclear physics (SSNP) or condensed matter nuclear science (CMNS) as the superconductivity belongs

to conductor physics. However, the SSNP or CMNS is too wide to properly define our meaning included in the CFP that is rather expressed as solid-state nuclear reactions or condensed matter nuclear reactions. We like to clear cut the CFP from such events resulting from the interaction of neutrons or atomic nuclei with atoms without induced nuclear reactions as Knight shift [Knight 1949], Moessbauer effect [Moessbauer 1958], the change of K-capture probability by environment [Ohtsuki 2004], neutron guide [Kruegler 1980], neutron trap [Hino 1998, Huffman 2000], etc. belonging also to the SSNP or CMNS. It is necessary to add a comment on the limitation of our research field of the CFP in which there is no artificial acceleration with energies more than 1 keV which adds surplus factors to the events in the CFP.

It is also convenient to define “cf-material” which is the substance where occurs the CFP. The cf-material is composed mainly of a host material (transition metals and alloys) occluding hydrogen isotopes, i.e. protium or/and deuterium, and sometimes of noble and other metals in contact with hydrogen isotopes, and of carbon compounds including hydrogen (e.g. XLPE or cross-linked polyethylene). The composition of the cf-material is various with only a common characteristic of occlusion of hydrogen isotopes with a high density.

We will not describe detailed experimental data sets as far as possible which have been extensively given in books [Kozima 1998, 2006, Storms 2007] and papers cited there*.

Footnote

Papers on the CFP have been published in several journals and also published in Proceedings of Conferences. Many important papers have been cited in the References of the referred books. Papers published in Proceedings of ICCF (International Conference on the Cold Fusion) are printed in the “Contents of Proceedings “posted at CFRL website: <http://www.geocities.jp/hjrfq930/Cfcom/Histry/Histry.html>.

Papers published in Proceedings of JCF (Japan CF-research Society) are posted at the JCF website: <http://jcfrs.org/pubs.html>

Some papers published in Conferences are posted at the New Energy Times website: <http://newenergytimes.com/v2/conferences/LENRConferenceProceedings.shtml>

Many papers published in many places have posted at the following LENR-CANR.ORG website even if its editorial responsibility is ambiguous: <http://lenr-canr.org/>

For convenience of readers, we show here tables of experimental data sets given in my book [Kozima 1998 (Tables 11.2 and 11.3)] and cited in the next book [Kozima 2006 (Tables 2.2 and 2.3)] as Tables 2.1 and 2.2. The data obtained by the analyses based on the TNCF model first presented at ICCF4 held in Hawaii, USA in December 1993 [Kozima 1994] are also given in the last two columns of the Tables.

We also will not give evaluation of experimental data sets which is one of targets of the dispute of whether the CFP is real or not. Our point of view about this problem is that we accept data sets as they were presented even if there are some mistakes or misunderstandings in some of many data sets expecting compensation of defects by accumulating a great number of data sets worked out in the period of about a quarter of a century. However, the interpretation of the data given in a paper is a completely different thing from what the data itself tells us. We listen in the experimental data sets themselves even if they show us curious feature but do not necessarily follow the interpretation given there.

Authoritative evaluations of papers of experimental data sets in the CFP have been given in two reports of DOE committees [DOE Report 1989, DOE Report 2004] but with limitations imposed by the requirement to work with the corresponding object papers. The DOE Report 1989 was hasty to deny the occurrence of $d-d$ fusion reactions in cf-materials that was the main theme of the CF research at that time. Generation of excess energy by the $d-d$ fusion reactions was denied due to the irreproducibility and inconsistency among observed quantities. On the other hand, the DOE Report 2004 was intended to evaluate a paper presented by a group of researchers to show occurrence of a new type of the $d-d$ reaction generating excess heat and helium in cf-materials with deuterium. Accordingly, it had a limitation in the scope of its investigation on the CFP. The proposed mechanism of the $d-d$ fusion in solids was criticized but the experimental data sets after 1989 were evaluated positively.

The most important fields of the CFP developed after the initial discovery in 1989 are various kinds of events in protium systems and the nuclear transmutations both in deuterium and protium systems which have not been in their targets of the evaluation of the two DOE Reports [DOE Reports 1989, 2004].

Table 2.1. Pd/D(H)/Li System. Neutron density n_n and relations between the numbers N_x of event X obtained by theoretical analysis of experimental data on the TNC model ($N_Q=Q(\text{MeV})/5$ (MeV)) [Kozima 2006, Table 2.2]. Typical value of the surface vs. volume ratio S/V (cm^{-1}) of the sample is tabulated, also. As we see here, there are several data sets of the CFP in Pd/H/Li(S) systems even if the combination Pd/D/Li is overwhelmingly preferable for the phenomenon.

Authors	System	S/V cm^{-1}	Measured Quantities	n_n cm^{-3}	Other Results (Remarks)
Fleischmann et al. ¹⁾	Pd/D/Li	6 ~40	Q, t, n $N_t/N_n \sim 4 \times 10^7$ $N_Q/N_t \sim 0.25$	$\sim 10^9$	($Q=10\text{W}/\text{cm}^3$) $N_t/N_n \sim 10^6$ $N_Q/N_t = 1.0$
Morrey et al. ¹⁻⁴⁾	Pd/D/Li	20	$Q, {}^4\text{He}$ ${}^4\text{He}$ in $\ell \leq 25\mu\text{m}$	4.8×10^8	$N_Q/N_{\text{He}} \sim 5.4$ (If 3% ${}^4\text{He}$ in Pd)
Roulette ^{1''')}	Pd/D/Li	63	Q	$\sim 10^{12}$	
Storms ⁴⁾	Pd/D/Li	9	$t(1.8 \times 10^2 \text{Bq}/\text{ml})$	2.2×10^7	($\tau=250\text{h}$)
Storms ⁴⁾	Pd/D/Li	22	Q ($Q_{\text{max}}=7\text{W}$)	5.5×10^{10}	($\tau=120\text{h}$)
Takahashi et al. ⁵⁾	Pd/D/Li	2.7	t, n $N_t/N_n \sim 6.7 \times 10^4$	3×10^5	$N_t/N_n \sim$ 5.3×10^5
Miles et al. ^{18')}	Pd/D/Li	5	$Q, {}^4\text{He}$ ($N_Q/N_{\text{He}}=1\sim 10$)	$\sim 10^{10}$	$N_Q/N_{\text{He}} \sim 5$
Okamoto et al. ^{12')}	Pd/D/Li	23	Q, NT_D $\ell_0 \sim 1\mu\text{m}$	$\sim 10^{10}$	$N_Q/N_{\text{NT}} \sim 1.4$ (${}^{27}\text{Al} \rightarrow {}^{28}\text{Si}$)
Oya ¹²⁻⁵⁾	Pd/D/Li	41	Q, γ spectrum	3.0×10^9	(with ${}^{252}\text{Cf}$)
Arata. et al. ¹⁴⁾	Pd/D/Li	7.5 $\times 10^4$	$Q, {}^4\text{He}$ ($10^{20} \sim 10^{21}$ cm^{-3}) $N_Q/N_{\text{He}} \sim 6$	$\sim 10^{12}$	(Assume t channeling in Pd wall)
McKubre ³⁾	Pd/D/Li	125	Q (& Formula)	$\sim 10^{10}$	Qualit.explan.
Passell ^{3''')}	Pd/D/Li	400	NT_D	1.1×10^9	$N_{\text{NT}}/N_Q=2$
Cravens ^{24''')}	Pd/H/Li	4000	Q ($Q_{\text{out}}/Q_{\text{in}}=3.8$)	8.5×10^9	(If PdD exists)
Bockris ⁴³⁾	Pd/D/Li	5.3	$t, {}^4\text{He}; N_t/N_{\text{He}} \sim 240$	3.2×10^6	$N_t/N_{\text{He}} \sim 8$
Lipson ¹⁵⁻⁴⁾	Pd/D/Na	200	γ ($E_\gamma=6.25\text{MeV}$)	4×10^5	If effic. =1%
Will ⁴⁵⁾	Pd/D ₂ SO ₄	21	$t(1.8 \times 10^5/\text{cm}^2\text{s})$	3.5×10^7	(If $\ell_0 \sim 10\mu\text{m}$)
Cellucci et al. ^{51''')}	Pd/D/Li	40	$Q, {}^4\text{He}$ $N_Q/N_{\text{He}}=1\sim 5$	2.2×10^9	(If $Q=5\text{W}$) $N_Q/N_{\text{He}}=1$
Celani ^{32''')}	Pd/D/Li	400	Q ($Q_{\text{max}}=7\text{W}$)	1.0×10^{12}	(If 200% output)
Ota ⁵³⁾	Pd/D/Li	10	Q (113%)	3.5×10^{10}	($\tau=220\text{h}$)
Gozzi ^{51''')}	Pd/D/Li	14	$Q, t, {}^4\text{He}$	$\sim 10^{11}$	($\tau \sim 10^3\text{h}$)
Bush ²⁷⁾	Ag/PdD/Li	2000	Q ($Q_{\text{max}}=6\text{W}$)	1.1×10^9	($\tau=54\text{d}$, Film)
Mizuno 26-4)	Pd/D/Li (If Cr in Pd)	3.4	Q, NT_D $\ell \leq 2\mu\text{m}$)	2.6×10^8	$\tau=30\text{d}$, Pd $1\text{cm}\phi \times 10\text{cm}$
Iwamura ¹⁷⁾	PdD _z	20	n (400/s), t	3.9×10^8	$4.4 \times 10^6\text{t/s}$
Itoh ¹⁷⁾	PdD _z	13.3	n (22/m), t	8.7×10^7	$7.3 \times 10^{10}\text{t/s}$
Itoh ^{17''')}	PdD _z	13.3	n ($2.1 \times 10^3/\text{s}$)	3.9×10^8	
Iwamura 17''')	PdD _z	20	Q (4 W) NT_F (Ti, Cr etc.)	3.3×10^{10}	($\text{NT}_F?$ unexplained)
Miley ⁶⁵⁾	Pd/H/Li	150	NT_F (Ni, Zn,)	4.5×10^{12}	
Dash ⁵⁹⁾	Pd/D, H ₂ SO ₄	57	Q, NT_D	$\sim 10^{12}$	Pt \rightarrow Au
Kozima ²⁰³⁾	Pd/D, H/Li	200	n ($2.5 \times 10^{-4}/\text{s}$)	2.5×10^2	Effic. =0.44%

Table 2.2. Ni/H/K System and others. Neutron density n_n and relations between the numbers N_x of event X obtained theoretical analysis of experimental data on TNCF model ($N_Q \equiv Q(\text{MeV})/5$ (MeV)) [Kozima 2006, Table 2.3]. Typical value of the surface vs. volume ratio S/V (cm^{-1}) of the sample is tabulated, also. As we see here, there are several data sets of the CFP in Ni/D/K systems even if the combination Ni/H/K is overwhelmingly preferable for the phenomenon.

Authors	System	S/V cm^{-1}	Measured Quantities	n_n cm^{-3}	Other Results (Remarks)
Jones ²⁾	Ti/D/Li	8.1	n (2.45 MeV)	3.1×10^{11}	
Mills ²⁵⁾	Ni/H/K	160	Q (0.13 W)	3.4×10^{10}	
Bush ^{27')}	Ni/H/K	~ 160	$NT_D(\text{Ca})$	5.3×10^{10}	$N_Q/N_{NT} \sim 3.5$ ($^{40}\text{K}\tau=0$)
	Ni/H/Na	~ 160	$NT_D(\text{Mg})$	5.3×10^{11}	
Bush ^{27'')}	Ni/H/Rb	$\sim 10^4$	$NT_D(\text{Sr})$	1.6×10^7	$N_Q/N_{NT} \sim 3$
Savva- timova ^{34'')}	Pd/D ₂	100	$NT_D(\text{Ag})$	9×10^{10}	
Alekseev ^{44')}	Mo/D ₂	4.1	t ($\sim 10^7/\text{s}$)	1.8×10^7	(If MoD)
Romodanov ^{44''')}	TiC/D	4.1	t ($\sim 10^6/\text{s}$)	$\sim 10^6$	(D/Ti \sim 0.5 assumed)
Reifenschweiler ^{38')}	TiT _{0.0035}	7×10^5	β decay reduction	1.1×10^9	($T=0\sim 450^\circ\text{C}$)
Dufour ⁷⁾	Pd,SS/D ₂ Pd,SS/H ₂	48	Q, t, n	9.2×10^{11} 4.0×10^9	(D(H)/Pd \sim 1 is assumed)
Claytor ⁹⁾	Pd/D ₂	400	t (12.5 nCi/h)	1.6×10^{13}	(If D/Pd \sim 0.5)
Srinivasan ¹⁶⁾	Ti/D ₂	1500	t ($t/d \sim 10^{-5}$)	1.9×10^8	(Aged plate)
De Ninno ^{6')}	Ti/D ₂	440	n, t	1.2×10^6	(D/Ti=1,1w)
Focardi ²³⁾	Ni/H ₂	8.2	Q	3.0×10^{12}	(If $N_p=10^{21}$)
Oriani ⁵²⁾	SrCeO ₃ /D ₂	22	$Q \sim 0.7\text{W}$	4.0×10^{10}	$V=0.31\text{cm}^3$
Notoya ^{35'')}	Ni/D,H/K	3.4 $\times 10^4$	Q (0.9 W), t	2.4×10^{13}	(If 1/2 t is in liquid)
Notoya ³⁵⁻⁴⁾	Ni/D,H/K	same	$NT_D(\text{Ca})$	1.4×10^9	(Sintered Ni)
Yamada ⁵⁴⁾	Pd/D ₂	185	$n, NT_D(\text{C})$	2.0×10^{12}	
Cuevas ⁵⁵⁾	TiD _{1.5}	134	n (102 n/s)	5.4×10^{11}	
Niedra ⁵⁶⁾	Ni/H/K	80	Q (11.4 W)	1.4×10^9	5km \times 0.5mm ϕ
Ohmori ^{22'')}	Au/H/K	200	$Q, NT_F(\text{Fe})$	$\sim 10^{11}$	(Au plate)
Li ⁵⁷⁾	Pd/D ₂	185	Q	1.6×10^{12}	(Pd wire)
Qiao ^{57')}	Pd/H ₂	185	$NT_F(\text{Zn})$	3.8×10^{10}	(40%NT in 1y)
Bressani ^{58')}	Ti/D ₂	$\leq 10^3?$	n (ϵ)	$10^5 - 10^6$	(Ti shaving)
Miley ^{65')}	Ni/H/Li	50	$NT_D(\text{Fe,Cr},\dots)$	1.7×10^{12}	

It should be emphasized first that the CFP occurs not only in deuterium but also in protium systems. For a long period after 1989, there remained people even in the CF researchers who are reluctant to recognize the occurrence of the CFP in protium systems persisting in the reactions (2.1) – (2.3) below (in the free space) generating excess energy Q (in MeV);





It is regrettable to know that there are scientists who are restricting their sight themselves by the negligence of the unexpected facts betraying their expectation. If we want to find a common cause of peculiar events in both deuterium and protium systems, we have to open our eyes to experimental facts themselves obtained in both systems.

3. Irreproducibility, sporadicity, and conceptual incoherence

Now, we would like to discuss several causes of discrepancy between pros and cons in evaluation of works in the CFP; irreproducibility, sporadicity, and conceptual incoherence.

3.1. Irreproducibility

In general, reproducibility of an event is a characteristic in simple systems governed by differential equations while it is not in complex systems where events are described by nonlinear dynamics.

The phase transition of transition-metal hydrides and deuterides, e.g. PdH_x, is the manifestation of nonlinear interaction of hydrogen atoms and host metals. The palladium hydride PdH_x makes transition from the *fcc* ($\alpha + \beta$) phase solution to the *fcc* β phase hydride at $x = 0.63$. (The α phase is a solution made of H in an octahedral site of *fcc* Pd lattice and the β phase is a hydride where H⁺ occupies at an octahedral site) [Flanagan 1978].

The super-lattice composed of the host lattice and the interstitial lattice of hydrogen (or deuterium) is governed by the atomic process of the hydrogen migration through the host lattice which is influenced by the occupation rate of interstitial sites. Furthermore, if our speculation is correct, the formation of the super-lattice PdH is influenced by the super-nuclear interaction of lattice nuclei mediated by interstitial protons. This interaction has nonlinear character due to its origin depending on the geometric arrangement of protons in the interstices. The formation of the cf-matter in surface regions of a cf-material where the superlattice is realized is determined by nonlinear processes as discussed in our papers [Kozima 2012, 2013].

In addition to this atomic characteristic of transition-metal hydrides deuterides, it is our common sense that events in nuclear physics are statistical and not deterministic as the simple example of the alpha-decay shows. If an event is caused by an uncontrollable microscopic change in a nuclear system and is directly combined to the cause, then the effect observed macroscopically is governed by the microscopic process and is therefore

statistical. The detection of the effect is inevitably stochastic and not reproducible individually. Simple example is useful to elucidate the situation; if the effect is observed separately for an individual event but not as an averaged quantity over many events (as many nuclear processes are the cases); the stochastic nature of the event should be emphasized. Sudden bursts of excess heat and neutron emission observed in several experiments have showed such stochastic and sporadic nature in the CFP.

These two phases of the CFP, one the nonlinear nature of cf-matter formation and another statistical nature of the nuclear reactions, result in irreproducibility of the events in the CFP.

3.2. Sporadicness (Sporadicity)

Sporadic occurrence of events in the CFP is another characteristic of this field. To express sporadic character of events, we would like to propose to use new word “sporadicity” while there is lengthy word “sporadicness” in a dictionary. Then, sporadicity of the events in the CFP is explained by statistical formation of optimum conditions for the occurrence of a microscopic situation where caused events observed as a macroscopic observable such as excess energy and neutron emission explained above in relation to the irreproducibility.

3.3. Conceptual incoherence

The most subtle and difficult problem to explain is consistency of experimental facts as a whole with the framework of the modern science developed in 20th century. A point of view to investigate experimental data sets of observables in the CFP is decisively important in relation to this problem. It is necessary to take whole experimental facts into consideration not discarding data sets unfavorable for a point of view to construct a science based on the facts. It is difficult to distinguish the simple system described by differential equations that is we have used to study in nuclear physics from the complex system described by nonlinear dynamics in which the CFP belongs to. As we have suggested in our papers [Kozima 2012, 2013] and will show below, events in the CFP seem to be characterized by complexity. The irreproducibility and the sporadicity explained above is a natural conclusion of the complexity if cf-materials are essentially the proper object which should be treated by the nonlinear dynamics.

4. Experimental facts and cf-materials in general

We summarize experimental systems and observed facts in Table 4.1 to show vast amount of information obtained in the CFP in these about 25 years.

This table shows that the cold fusion phenomenon (CFP) occurs in various solids with various agents and its contents are very complex.

Agents necessary for CFP known by now are hydrogen isotopes, i.e. hydrogen H (proton p) and deuterium D (deuteron d), neutron n , lithium-6 (${}^6\text{Li}$), boron-10 (${}^{10}\text{B}$), potassium-39 (${}^{39}\text{K}$), rubidium-85 and -87 (${}^{85}\text{Rb}$ and ${}^{87}\text{Rb}$). It is, however, not well known what is actually necessary for the host solids and the agents to induce the CFP, i.e. the necessary conditions of the CFP are not quantitatively determined at all.

Tending to be overlooked is the existence of background neutrons which is one of the necessary conditions to induce the CFP as several experimental data sets had clearly shown; when there are no background neutrons, no CFP is observed and when artificial thermal neutrons are irradiated, the CFP is intensified as explained in Section 2.2 (d) of the book [Kozima 2006].

Table 4.1. System and Obtained Evidence of the CFP: Host solids, agents, experimental methods, direct and indirect evidence, cumulative and dissipative observables are tabulated. Q and NT express excess energy and the nuclear transmutation, respectively. Direct evidence of nuclear reactions in the CFP are dependences of reaction products on their energy (ϵ) and position (\mathbf{r}), decrease of decay constants of radioactive nuclides, decrease of fission threshold energy of compound nuclei.

Host solids	Pd, Ti, Ni, KCl + LiCl, ReBa ₂ Cu ₃ O ₇ , Na _x WO ₃ , KD ₂ PO ₄ , TGS (triglycinesulfate), SrCe _a Y _b Nb _c O _d , XLPE (cross linked polyethylene)
Agents	$n, d, p, {}^6_3\text{Li}, {}^{10}_3\text{B}, {}^{39}_{19}\text{K}, {}^{85}_{37}\text{Rb}, {}^{87}_{37}\text{Rb}$
Experiments	Electrolysis, Gas discharge, gas contact
Direct evidences of nuclear reaction	Gamma ray spectrum $\gamma(\epsilon)$, Neutron energy spectrum $n(\epsilon)$, Space distribution of NT products NT(\mathbf{r}), Decrease of decay constants, lowering of fission threshold energy
Indirect evidences of nuclear reaction	Excess energy Q , Number of neutrons N_n , Amounts of tritium atom N_t , helium-4 atom* N_{He4} , NT products (NT _D , NT _F , NT _A), X-ray spectrum X(ϵ)
Cumulative observables	NT(\mathbf{r}), amount of tritium atom N_t , helium-4* N_{He4} ,
Dissipative observables	Excess energy Q , neutron energy spectrum $n(\epsilon)$, number of neutrons N_n , Gamma ray spectrum $\gamma(\epsilon)$, X-ray spectrum X(ϵ),

*It should be given a comment on the observation of helium-4. The quantitative observation of helium-4 is extremely difficult as an expert of helium measurement once pointed out [Kozima 2002]. So, we have to be careful to interpret an experimental data set when they include a quantitative detection of helium.

Direct evidence of nuclear reactions is events clearly resulting from nuclear reactions from common sense of present physics. The following events belong in this category; emission of gamma ray, neutrons with definite energy, generation of new nuclides (including possible occurrence of nuclear fission), changes of decay constants of radiative nuclides.

Indirect evidence of nuclear reactions are events most appropriately explained by nuclear reactions; excess energy of huge amount inexplicable by chemical reactions or physical processes, extraordinary increase of number of neutrons, increase of tritium amount, increase of helium-4, appearance of X-ray radiation, and so on.

The cumulative and dissipative observables give a measure of reliability of experimental data on them. Generally speaking, cumulative observables have higher reliability on the measured values than the dissipative ones have.

It should be noticed that events classified in direct and indirect evidences in Table 4.1 are not necessarily observed at the same time. Rather, it is rarely the case that two or more events are observed simultaneously. Some examples of these rare cases are tabulated in the book [Kozima 1998, 2006]. Usually, excess heat is observed along with some other events, e.g. tritium and neutron, or nuclear transmutation (NT). In such lucky cases where measured several observables simultaneously, we can have an important clue to determine the mechanism for reactions resulting in these observables.

As explained in the next section, we have determined the numbers of reactions giving two or three observables using an adjustable parameter to give satisfactory coincidence with corresponding numbers obtained by experiments [Kozima 1998 (Section 11.1b), 2006 (Section 3.3.1)].

5. A phenomenological model (TNCF model)

The TNCF model [Kozima 1998, 2006] with a single adjustable parameter n_n is based on the whole experimental facts obtained in materials composed of various host solids and hydrogen isotopes not only deuterium but also protium. Events used to construct the model include generation of excess energy, emission of neutrons, emission of charged particles, generation of tritium and helium, and nuclear transmutation at boundary regions of materials. When we analyze experimental data sets of several observables determined simultaneously, we could determine the parameter n_n by an observable and then calculates another observable by the recipe of the model using the determined parameter to compare with its experimental data. The comparisons have been successful semi-quantitatively.

One of the most interesting results explained by the TNCF model is the ratios of

numbers N_x 's of plural events X 's observed simultaneously. Determining the parameter n_n by the data of the number N_x of an event X , we can calculate the number N_y of another event Y using the model and compare the theoretical ratio $(N_x/N_y)_{th}$ thus calculated with the experimental value $(N_x/N_y)_{ex}$. We have obtained fairly good coincidence of these values in a factor about 3 as expressed by the following relation [Kozima 2006, Sec. 3.3.1]:

$$(N_x/N_y)_{th} = \alpha(N_x/N_y)_{ex} \quad (5.1)$$

with $\alpha \sim 3$. The events X 's used are excess energy Q (N_Q), amounts of generated tritium (N_t) and helium-4 (N_{He4}) and product nucleus of nuclear transmutation (N_{NT}).

Details of the model are explained in the books [Kozima 1998, 2006] and papers (for example [Kozima 2008a]). The success of this approach substantiated the assumption of the trapped neutrons in cf-materials and the basis of the assumption has been investigated quantum mechanically which is left for the references (e.g. [Kozima 2008c]). The cf-matter is the concept worked out in relation to the neutron bands formed by the super-nuclear interaction between lattice nuclei mediated by interstitial hydrogen isotopes corresponding to the assumed trapped neutrons in the TNCF model [Kozima 2006, Sec. 3.7.5]. Necessary conditions for realization of the cf-matter are given in Appendix to this paper.

6. Three empirical laws in the CFP

The three empirical laws (or regularities) [Kozima 2012] found in our course of research show that the CFP is a phenomenon belonging to complexity. The irreproducibility of events in the CFP discussed in Sec. 3 is closely related to the complexity in this phenomenon. We explain them below as a material for discussion.

6.1. $1/f$ dependence of excess energy production (“inverse-power law”)

In several experimental data sets, we are able to count numbers (frequency) N_Q of an event with a specific amount of excess energy Q (or an excess power P) and plot them as a function of Q (or P) obtaining N_Q vs. Q (or P) plot [Kozima 2006, Sec. 2.12]. The first plot was obtained for the data by McKubre et al. [McKubre 1993]. This plot clearly shows that there is an inverse-power relation of frequency vs. intensity with an exponent p of 1, famous in complexity. This regularity may be called the inverse-power dependence of frequency on intensity of the excess energy production (“inverse-power law”). The inverse-power law has been shown also for a data set obtained by Kozima et al. (with $p = 2$) [Kozima 2008b] and those compiled by Storms ⁸⁾(with $p = 1.0$) [Lietz 2008] as shown in Fig. 6.1.

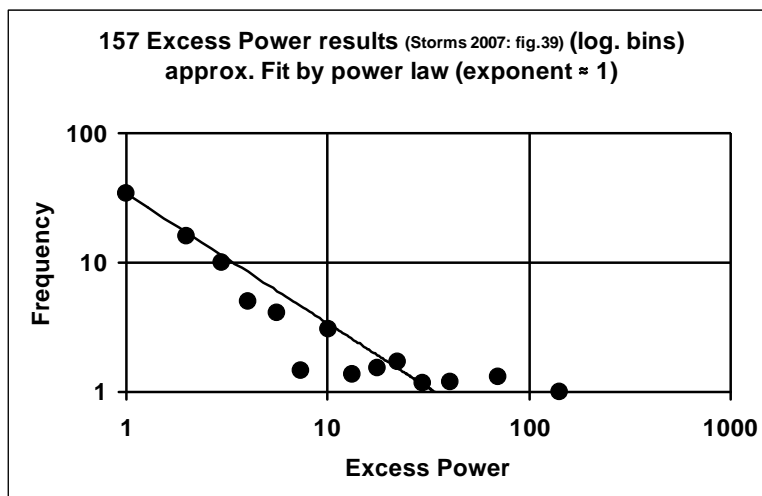


Fig. 6.1. Distribution of 157 excess energy results by Lietz [Lietz 2008] using the data collected by Storms [Storms 2007]. Values have been stored in bins of size 10. The line shows a power-law fit to the binned data with an exponent of 1.0 ($r^2 = 90\%$) (Fig. 3 of [Lietz 2008])

6.2. Stability effect on the nuclear transmutation products (“stability law”)

If we survey numbers of elements produced by the nuclear transmutation in the CFP, we notice the frequency obtaining an element has a positive correlation with the amount of the element in the universe [Kozima 2006, Sec. 2.11]. Plotting out (i) the number of experiments where observed an elements ${}_Z\text{X}$ together with (ii) the amount in the universe compiled by Suess and Urey [Suess 1956] against its proton number Z , we obtain a diagram showing the coincidence of the peaks of (i) and (ii), which gives the stability effect for nuclear transmutation products [Kozima 2010a] as shown in Fig. 6.2. We may call this regularity the “stability law” for nuclear transmutation in the CFP.

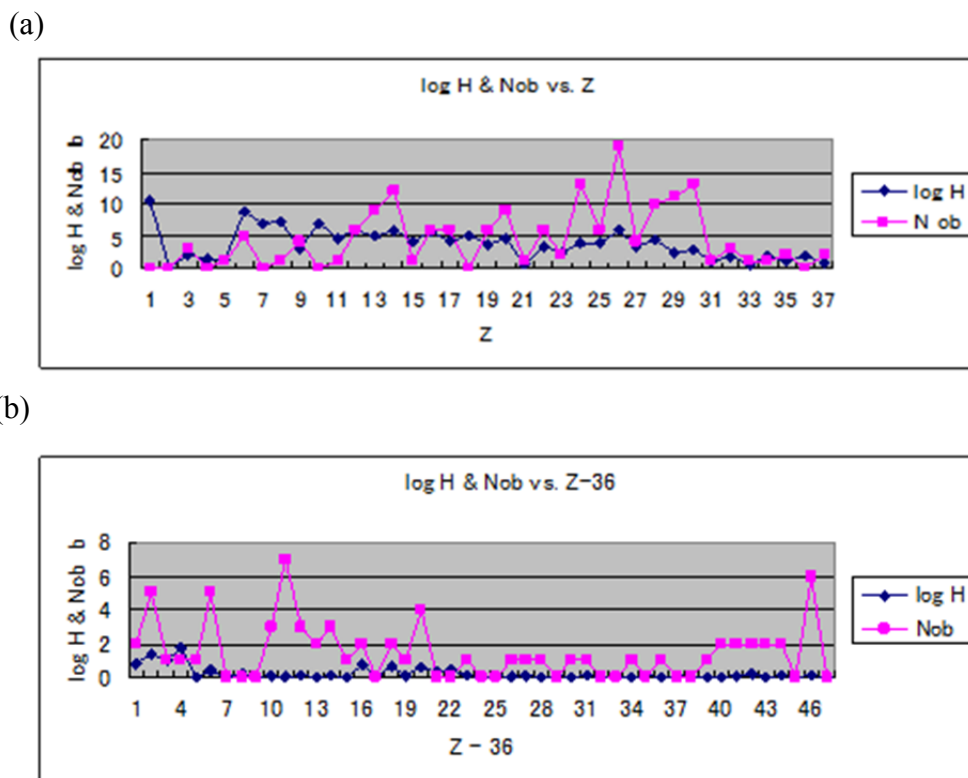


Fig. 6.2. Correspondence between the frequency $N_{ob}(Z)$ observing elements in the CFP and the relative abundances $\log_{10}H(Z)$ of elements in the universe [Suess 1956]: (a) $Z = 3 - 38$ and (b) $Z = 39 - 83$ [Kozima 2006]

6.3. Complexity of events (“bifurcation law”)

The third law in the CFP is a little subtle to show it compared with the former two. Even if the number of examples is scarce, we have several fortunate data sets of temporal evolution of effects in the CFP. The first one is that of neutron emission from TiD_x by De Ninno et al. published in 1989 [De Ninno 1989]. Another data set is the excess heat generation observed by McKubre et al. in 1993 [McKubre 1993]. Furthermore, we can cite another example of the temporal evolution of excess energy generation measured by Kozima et al. in 2008 [Kozima 2008b]. The data by McKubre et al. is shown in Fig. 6.3. The empirical feature of these temporal evolutions of observables is similar to the bifurcation of the solutions of an equation in nonlinear dynamics shown in Fig. 6.4 [Kozima 2012]. This is what we call the “bifurcation law”.

By the nature of events in complexity, we can give only qualitative explanation of an experimental result in analogy to the mathematical results of numerical simulations for the logistic difference equation. The analogical explanations of the laws observed in the CFP have been given using the Feigenbaum’s theorem describing a nature of an equation of nonlinear dynamics [Kozima 2012, 2013].

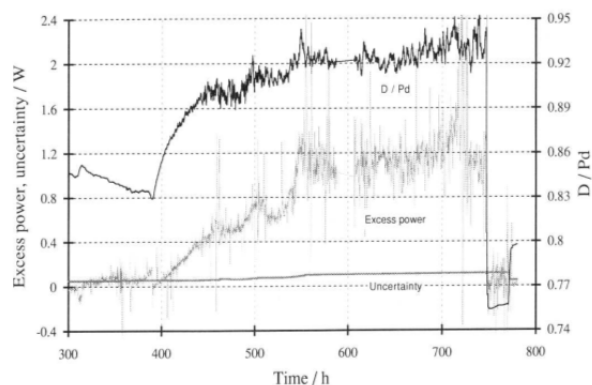


Fig. 6.3. Variation of Excess Power, Uncertainty and Loading ratio [McKubre 1993].

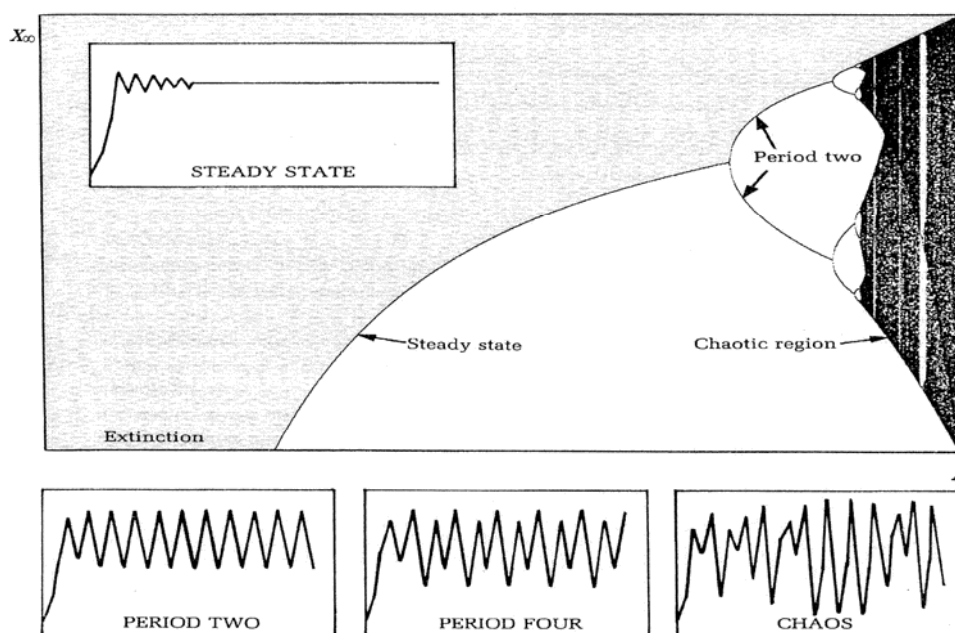


Fig. 6.4. Bifurcation diagrams ([Gleick 1987], page 71).

7. Conclusions

The cold fusion phenomenon (CFP) has been a controversial theme in the interdisciplinary region between solid state physics and nuclear physics. As has been shown above, the CFP observed in cf-materials containing hydrogen isotopes (deuterium or/and protium) is too complicated to be explained only by some simple extrapolations of knowledge established in solid-state nuclear physics (or condensed matter nuclear science) developed in 20th century. If it is reflecting something real in entity not noticed before 1989, there should be a fundamentally new physics hidden under the cloud of various events observed in the CFP and in turn the physics should

reveal the existence of new events in solid state physics and nuclear physics. Our effort in this field should also be in the direction to find out what we can say about these new phenomena reflected from the CFP in the traditional research fields of physics.

On the other hand, the TNCF model fairly successful to explain the CFP as a whole at present will serve as a first step in the right direction to the science of this new field. The model shows that the new physics should be a science including a new state of neutrons in cf-materials. Furthermore, if we notice that the CFP is characterized by complexity, we have to treat the cf-material, the superlattice composed of a host sublattice (host nuclei at the lattice points) and a proton (deuteron) sublattice (protons (deuterons) at the interstitials) as a whole taking into nuclear reactions among host nuclei and interstitial protons (deuterons).

From our point of view using a phenomenological approach [Kozima 1994, 1998, 2004, 2006], the idea of the cf-matter resembling to the neutron sea appeared in the investigation of the neutron star matter is the most hopeful entity having close connection with neutron physics developing in nuclear physics. We have a lot novel knowledge of neutron interaction in isolated exotic nuclei behaving differently from the traditional concept of nuclear force in the nucleus [Kozima 2014a]. Furthermore, when a nucleus is not isolated and connected with other nuclei through the super-nuclear interaction, nuclear force between lattice nuclei mediated by protons or deuterons at interstitials with wavefunctions extended over lattice points as figured out in our model, we may have a new perspective of neutron physics in hydrogenated solids resulting in new features of nuclear physics not found in isolated particles considered by now.

Some new materials supporting our model are presented in Appendix to supplement our explanation given in papers and books published before [Kozima 2006, 2008c] and briefly discussed their relation to the TNCF model.

In conclusion, the answer we can give to the question “What is the cold fusion phenomenon (CFP)?” is “It is a riddle” at present when we do not know the complete necessary and sufficient conditions for the CFP. If the science of the CFP is established on the line suggested by our phenomenological approach, the vista of future science as the physics of neutrons in hydrogenated solids is wide and endless. We can not overview its development in future correctly at present.

It should be discussed briefly possible applications of the CFP. The events observed in the CFP, e.g. excess energy production and nuclear transmutation, are naturally considered to be used in commercial devices. There, however, remain several limitations for their effective application due to the essential characteristics of this phenomenon. One is the sporadicity of the events and another is the short durability of

working cf-materials which has been shown as defects generated at the surface of cf-materials where have occurred events of the CFP. Furthermore, we have to care emergence of radioactive emissions of neutrons and charged particles in the cf-materials. The sporadicity of the events will be overcome if we know the necessary and sufficient conditions for the events by development of science of the CFP. The durability of the working materials will be improved by the science of the CFP or remedied by such a technical invention to replace new working elements regularly. The hazardous radioactivity could be prevented by appropriate protection facilities.

Appendix

Some Characteristics of Lattice Nuclei and Interstitial Hydrogen Isotopes in CF-Materials related to the Formation of the CF-Matter for the Cold Fusion Phenomenon

As we have investigated hitherto, the cold fusion phenomenon (CFP) has close relation with the property of lattice nuclei on one hand and with the property of interstitial hydrogen isotopes on the other.

First of all, it is necessary to have a cf-material where is a superlattice composed of a sublattice of a host element and another of a hydrogen isotope. In addition to this condition, there are some necessary conditions on the lattice nucleus and the interstitial hydrogen isotope to realize the super-nuclear interaction between lattice nuclei for formation of the neutron bands and accordingly of the cf-matter in a cf-material. The nucleus of a host element on the lattice points of a cf-material (lattice nucleus) should have a neutron wavefunction with large extension. The interstitial hydrogen isotope (proton or deuteron on interstitial sites), on the other hand, should have a wavefunction extending over nearest neighbor lattice points. Then, we can expect the super-nuclear interaction between neutrons in lattice nuclei mediated by interstitial hydrogen isotopes. This scenario for the CFP has supports from recent knowledge of nuclear physics and solid state physics as briefly explained below in addition to the data we have used in our former books and papers [Kozima 2006, 2008c, 2013].

In this appendix, we give this recent knowledge as follows:

A1. Neutron levels at around evaporation level (zero level)

A1-1 Cross-linked Polyethylene (XLPE) $[\text{CH}_2]_n$

A1-2 ${}^A_{24}\text{Cr}$ ($A = 50 - 54$)

A1-3 ${}^{63}_{29}\text{Cu}$ and ${}^{65}_{29}\text{Cu}$

A1-4 ${}^A_{30}\text{Zn}$ ($A = 64 - 70$)

- A1-5 Al_2CuH_x
- A2. Exotic nucleus with a large excess number of the neutron
- A3. Diffusion coefficient of isotopes of hydrogen in Pd, Ni, and Cu
- A4. Mean-square displacements of hydrogen atoms in V, Nb, Ta and Pd

A1. Neutron levels at around evaporation level (zero level)

The super-nuclear interaction between lattice nuclei mediated by interstitial protons or deuterons may have a close relation to the neutron energy levels at around the evaporation levels (levels at around zero) which have wide-spread wavefunctions. Energies of neutron orbits in a nucleus with a nucleon number A calculated by C.J. Veje [Bohr 1969] are shown in Fig. A1 (for $A = 18 - 210$). Many examples for modification of shell structure in neutron-rich nuclei have been known recently [Wiedenhover 2007]. Therefore, the energies of neutron orbits at around zero energy shown in Fig. A1 may be altered by formation of neutron-rich exotic states of relevant nuclei. We use this figure, however, for our investigation of the CFP because we have no data of recent information about them at present.

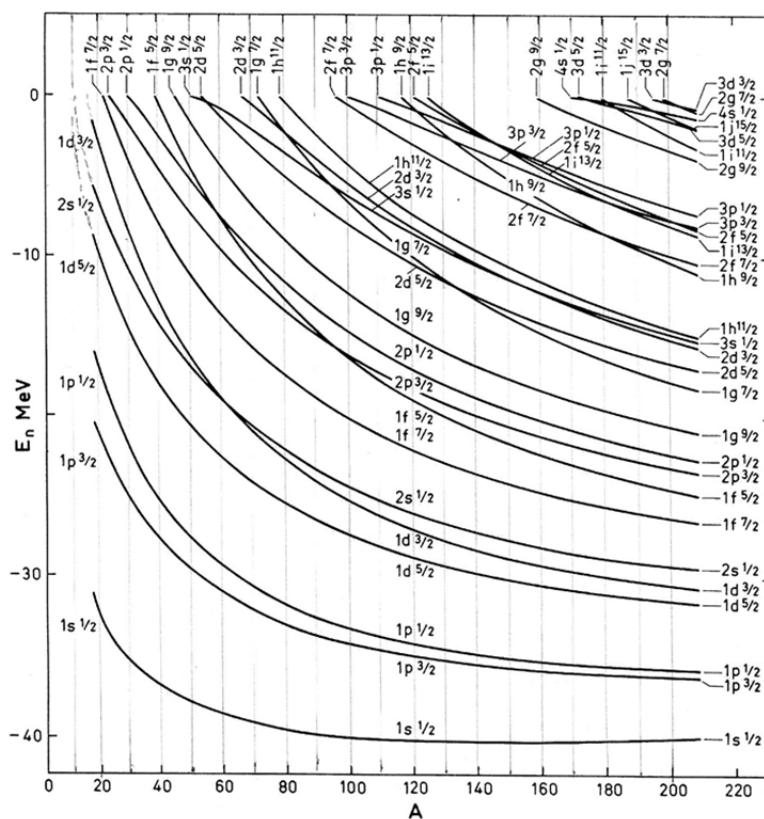


Fig. A1. Energies of neutron orbits in nuclei calculated by C.J. Veje [Bohr 1969]

The CFP is most frequently observed in transition-metal deuterides and hydrides, especially in TiD (H), NiH (D), and PdD (H). Furthermore, these transition-metal nuclei have a common characteristic; existence of excited neutron levels near zero in an isolated nucleus, $3s_{1/2}$ in ${}^A_{22}\text{Ti}$ ($A = 46 \sim 50$), $3s_{1/2}$ in ${}^A_{28}\text{Ni}$ ($A = 58 \sim 64$), and $3p_{3/2}$ and $3p_{1/2}$ in ${}^A_{46}\text{Pd}$ ($A = 102 \sim 110$) as shown in Fig. A1 [Bohr 1969]. As discussed in books and papers [Kozima 2006 (Sec. 3.6), 2012] and in Secs. A3 and A4 in this Appendix, the wavefunctions of protons and deuterons in these compounds show extended nature asked for the super-nuclear interaction.

Therefore, the CFP observed in PdH (D), TiD (H) and NiH (D) is a typical illustration of the mechanism proposed by our model.

Interesting cases of XLPE ($[\text{CH}_2]_n$), CrH_x , CuH_x , ZnH_x and Al_2CuH_x are discussed successively in this Section.

A1-1. Cross-linked Polyethylene (XLPE) $[\text{CH}_2]_n$

A wonderful experimental data of water-tree formation had been obtained in XLPE used for shielding of wires to transmit the electric power and explained by the TNCF model as a phenomenon showing nuclear transmutations at boundary regions of spherulite and amorphous phase [Kozima 2010b]. This data has shown that carbon is responsible to the CFP if regular arrays of carbon and hydrogen isotopes are formed. From our point of view that the CFP is realized when there is the super-nuclear interaction between lattice nuclei (in this case C) mediated by interstitial protons or deuterons. Looking into Fig. A1, we see there may be a neutron level $1d_{3/2}$ and possibly another one $2s_{1/2}$ for a ${}^{12}_6\text{C}$ nucleus extrapolating the curve at $A = 20$ to left. If this extrapolation is permissible, the explanation of the data obtained in XLPE by the CFP will have another support from knowledge of nuclear physics.

A1-2. ${}^A_{24}\text{Cr}$ ($A = 50 - 54$)

In this case, we see there is a level $3s_{1/2}$ at around $A = 50 - 53$. Chromium (Cr) crystalizes in a *bcc* lattice and becomes *hcp* and *fcc* lattices as a high-temperature phase at high pressures by absorption of hydrogen isotopes [Fukai 2005, Tables 2.4 and 2.5]. Therefore, CrH_x or CrD_x will be a cf-material at high temperatures where these hydrides are realized by the mechanism (the super-nuclear interaction) explained in A1-1.

A1-3. ${}^{63}_{29}\text{Cu}$ and ${}^{65}_{29}\text{Cu}$

As we see in Fig. A8, copper (Cu) has similar characteristic of hydrogen diffusion to

Pd at a high temperature region above 450 °C. From only this property of a large diffusion constant for hydrogen diffusion (suggesting extended proton wavefunctions), we can expect that the CFP will occur in Cu in this temperature region inconsistent with the experimental facts. This contradiction will be understood by the absence of neutron levels at zero energy for copper nuclei with $A = 63$ and 65 as we see in Fig. A1.

A1-4. ${}^A_{30}\text{Zn}$ ($A = 64 - 70$)

In this case, we see there is a level $2d_{3/2}$ at around $A = 66 - 70$ for zinc (Zn). This state is responsible to the super-nuclear interaction if there are occluded hydrogen isotopes at interstitial sites. However, we do not know if Zn is responsible for hydrides formation. This fact excludes Zn from a host element for a cf-material.

A1-5. Al_2CuH_x

It is reported in a recent paper by Saitoh et al. [Saitoh 2013] that an interstitial alloy Al_2CuH_x is a good material for storage of hydrogen isotopes. The structure is shown in Fig. A2. As explained above, Cu is not possible to give a neutron state at zero energy. On the other hand, ${}^{27}_{13}\text{Al}$ has no zero energy states as we see in Fig. A1. So, this material will not show the CFP and stable against nuclear reactions. This property will be preferable for a material to store hydrogen in it.

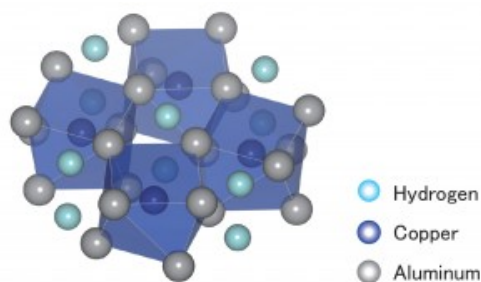


Fig. A2. Structure of the interstitial alloy Al_2CuH_x [Saitoh 2013].

A2. Exotic nucleus with a large excess number of the neutron

It is well known that exotic nuclei with large excess numbers of the neutron over that of the proton have neutron halos around the nuclear core. One example of these halo structure of ${}^{11}_4\text{Be}$ is shown in Fig. A3.

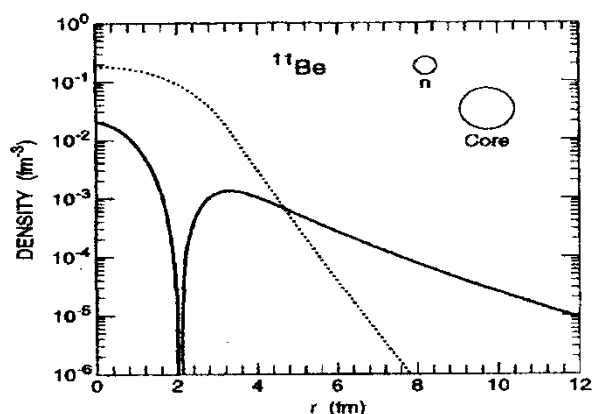


Fig. A3. Plot of the ^{11}Be density [Riisager 1994]. The upper right corner shows the simplified picture of a halo nucleus as a two-body system with an inert core and a halo neutron. Dotted line, core density as a function of radius; solid line, the density obtained in a Hartree –Fock calculation with the neutron in a $2s_{1/2}$ orbital and a single-neutron separation energy adjusted (to agree better with experiment) to 0.51 MeV. Note the very far-extended, dilute tail that is the characterizing feature of a halo [Riisager 1994].

Recent investigations of the exotic nucleus have shown characteristic interactions between neutrons different from that between neutron and proton [Kanungo 2011, Lu 2013]. These features of exotic nuclei about neutron behavior at a relatively thin density may have some relation with peculiar properties of the cf-matter worked out by the investigation of the CFP using the TNCF model

It is not known the relation between these excited neutron levels at around the zero energy level (cf. Fig. A1) and the neutron halo in exotic nuclei at present even if we know that “Neutron-rich nuclei have shell structure different from their “stable” siblings and their proton-rich mirrors!” [Wiedenhover 2007]. From the viewpoint of the CFP, the relation of the excited neutron levels and the neutron halo should be very close and these neutron levels are contributing to the stabilization of the exotic nuclei of the corresponding nuclides in cf-materials. Therefore, the investigations on the CFP in PdH(D), TiD(H) and NiH(D) systems will give information about neutron halo in exotic nuclei at lattice points, the wavefunction of protons or deuterons at interstices, and their interaction if our expectation is true.

Another example of neutron halos of ^6_2He and ^8_2He is given in Fig. A4. In this figure, we can see a fairly good coincidence between theory and experiment showing advance in theoretical understanding of nuclear structure.

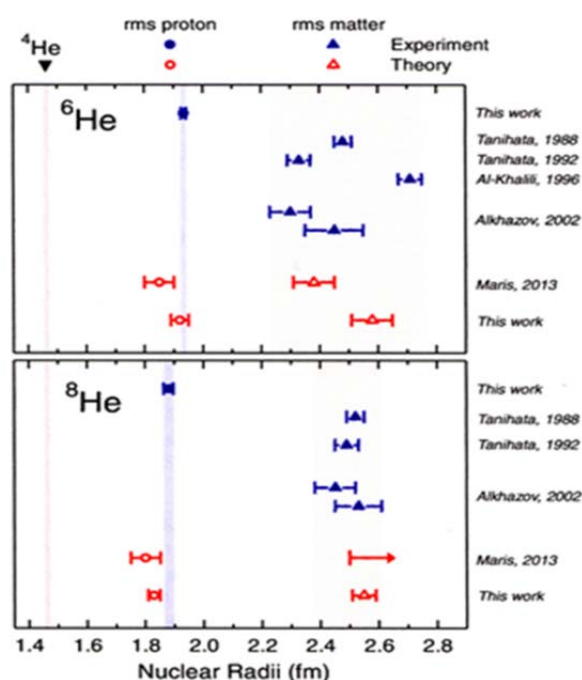


Fig. A4. Comparison between experimental and theoretical values of point-proton and matter radii for ${}^6\text{He}$ (top panel) and ${}^8\text{He}$ (bottom panel) [Lu 2013, Fig. 8]

The investigation of exotic nuclei is not limited to the structure of neutron halo but gives us much information about the nucleus. The data shown in Fig. A5 is the two-neutron separation energy S_{2n} as a function of the neutron number N of exotic nuclei.

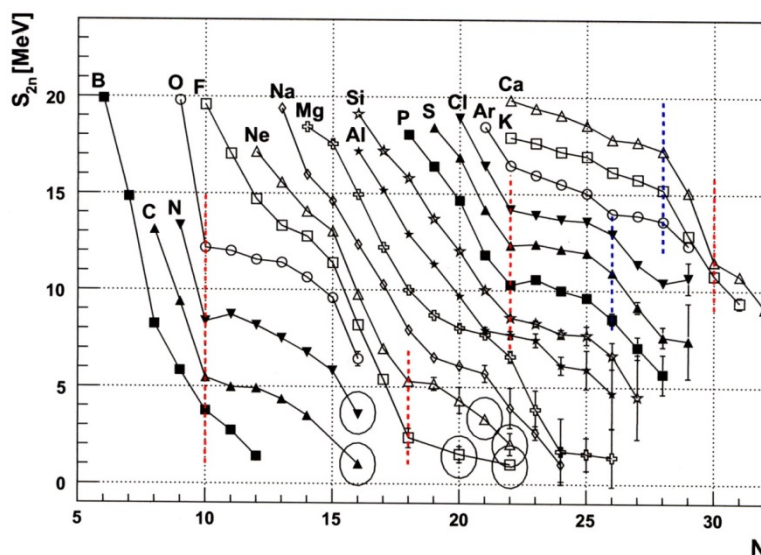


Fig. A5. Two-neutron separation energy S_{2n} vs. N – the drop points are visualized by vertical dotted red lines [Zdenek 2006, Fig. 8].

Figure A5 shows a strong effect of the magic number on S_{2n} and also reality of

two-neutron transfer of exotic nuclei to outside and from surrounding neutron sea (cf-matter) if there it is. The nuclear transmutation induced by absorption of a nucleon cluster ${}^A_Z\Delta$ considered in the explanation of the CFP will be closely related to the two-neutron separation observed in nuclear physics.

A3. Diffusion coefficient of isotopes of hydrogen in Pd, Ni, and Cu

Diffusion constants may have close relation to the occurrence of the CFP.

In palladium (Pd), deuterium (D) has larger values of diffusion constant than protium (H) at a temperature region below 100°C as shown in Fig. A6, while a reversal occurs in higher temperature region than 500°C [Voelkl 1978 (Fig. 12.20), Fukai 1982, Fig. 4 and Table 2]. So, we can expect PdH_x is preferable than PdD_x for the CFP at the higher temperature region according to the mechanism based on the super-nuclear interaction proposed by us [Kozima 2006].

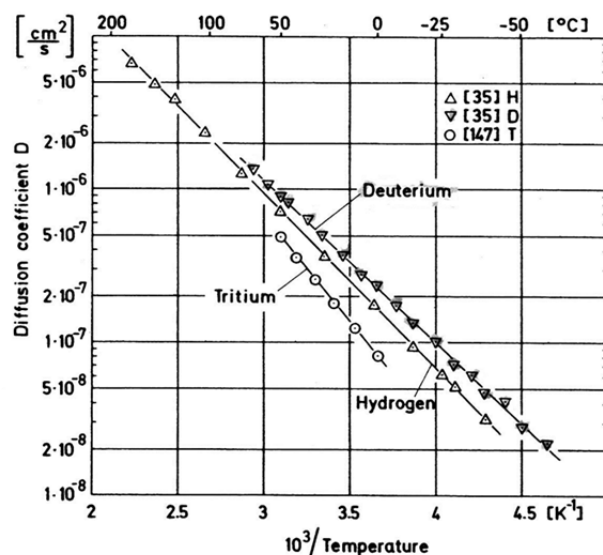


Fig. A6. Diffusion coefficient of isotopes of hydrogen in Pd (Numbers in brackets refer to References of original paper) [Voelkl 1978].

In Ni, the diffusion coefficients of H and D are normal, i.e. the light isotope diffuses faster than the heavy one as we see in Fig. A7. We observe the CFP in NiH_x easily than in NiD_x.

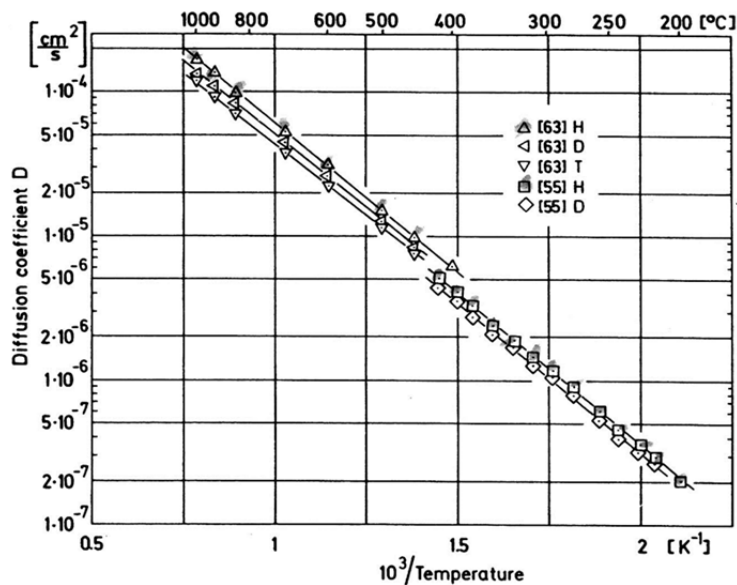


Fig. A7. Diffusion coefficient of isotopes of hydrogen in Ni (Numbers in brackets refer to References of original paper) [Voelkl 1978].

It is interesting to look into the diffusion data in Cu. As shown in Fig. A8, the diffusion coefficients of hydrogen isotopes in Cu is normal but measured only at a higher temperature region than 400 °C.

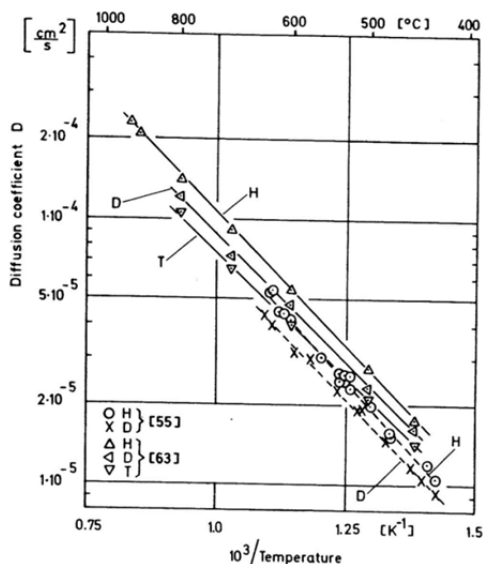
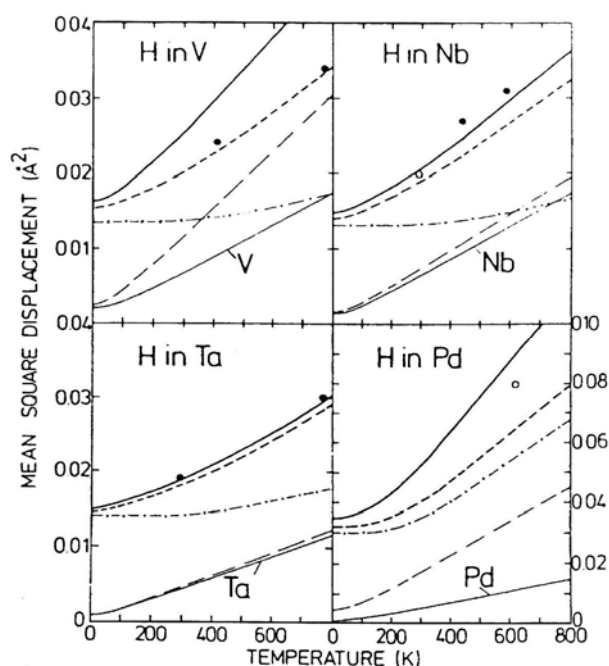


Fig. A8. Diffusion coefficient of isotopes of hydrogen in Cu (Numbers in brackets refer to References of original paper) [Voelkl 1978].

A4. Mean-square displacements of hydrogen atoms in V, Nb, Ta and Pd

The non-local characteristic of wavefunctions of hydrogen isotopes in cf-materials

has been discussed in our papers and books and in Sec. A3 using the diffusion properties of D and H in them. The same tendency of hydrogen isotopes in cf-materials is also exhibited by using vibration amplitudes of D and H in them. The data sets shown in Fig. A9 are just only for protium H (not for deuterium D) in V, Nb, Ta and Pd but shows the non-localized characteristic of wavefunctions of H in Pd which is closely connected to the appearance of the CFP in Pd but not in other metals (V, Nb and Ta), from our point of view. The sharp increase of the vibration amplitude with temperature in Pd clearly shows the favor of higher temperatures for the CFP recognized and pointed out by many researchers hitherto.



Mean-square displacements. —: $\langle u^2 \rangle^H$ model I. ---: $\langle u^2 \rangle^H$ model II. ---: $\langle u^2 \rangle_{\text{band}}^H$ model I. ····: $\langle u^2 \rangle_{\text{loc}}^H$ model I. —: $\langle u^2 \rangle_{\text{host}}$ [5.95]. Experimental values: ● [5.96], Nb ○ [5.97], Pd ○ [5.98]

Fig. A9. The mean-square displacements for H in V, Nb, Ta, and Pd, consist of contributions from the localized and the band modes, $\langle u^2 \rangle^H = \langle u^2 \rangle_{\text{loc}}^H + \langle u^2 \rangle_{\text{band}}^H$, and each of these contributions can be calculated separately [Fukai 2005, Fig. 5.33]. The reference symbol as [5.95] etc. in the figure are those of original ones. Model I and II there are two models used to calculate the frequency spectrum of the hydrogen vibration from which $\langle u^2 \rangle^H$ was calculated.

Acknowledgement

The author would like to express his thanks to S.B. Krivit and E. Storms for their kindness for sending him their papers published in Naturwissenschaften. He is also thankful to Prof. K. Kaki for valuable discussions on the properties of nuclei through this work.

References

- [Bohr 1969] A. Bohr and B.R. Mottelson, *Nuclear Structure I*, Benjamin, New York, 1969.
- [De Ninno 1989] A. De Ninno, A. Frattolillo, G. Lollobattista, G. Martinio, M. Martone, M. Mori, S. Podda and F. Scaramuzzi, "Evidence of Emission of Neutrons from a Titanium-Deuterium System," *Europhys. Lett.* **9**, 221 (1989).
- [DOE Report 1989] *Cold Fusion Research*, November 1989 - A Report of the Energy Research Advisory Board to the United States Department of Energy - , DOE/S-0071 (August, 1989) and DOE/S--0073, DE90, 005611. This report is posted at the *New Energy Times* website;
<http://newenergytimes.com/v2/government/DOE/DOE.shtml>
- [DOE Report 2004] "Report of the Review of Low Energy Nuclear Reactions."
http://www.science.doe.gov/Sub/Newsroom/News_Releases/DOE-SC/2004/low_energy/CF_Final_120104.pdf. This report is posted at the *New Energy Times* website:
<http://newenergytimes.com/v2/government/DOE2004/7Papers.shtml>
- [Flanagan 1978] T.B. Flanagan, "Palladium-Hydrogen: The Classical Metal-Hydrogen System," in R. Bau Ed., *Transition Metal Hydrides*, American Chemical Society, Advances in Chemistry Series No. 67. 1978.
- [Fleischmann 1989] M. Fleischmann, S. Pons and M. Hawkins, "Electrochemically induced Nuclear Fusion of Deuterium," *J. Electroanal. Chem.*, **261**, 301 – 308 (1989).
- [Fukai 1982] Y. Fukai, "Properties of Metal Hydrides (II)," *Solid State Physics* **17**, 701 – 716 (1982) (in Japanese).
- [Fukai 2005] Y. Fukai, *The Metal-Hydrogen System – Basic Bulk Properties*, Springer, Berlin, 2005. USBN-10 3-540-00494-7.
- [Gleick 1987] J. Gleick *Chaos – Making a New Science*, Penguin Books, 1987. ISBN 0-14-00.9250-1.
- [Hino 1998] M. Hino, N. Achiwa, S. Tasaki, T. Ebisawa, T. Kawai and T. Akiyoshi, "Observation of Quasibound States of Neutron in Fabry-Perot Magnetic Thin-Film Resonator using Larmor Precession," *Physica* **B241-243**, 1083 – 1085 (1998).
- [Huffman 2000] P. R. Huffman, C. R. Brome, J. S. Butterworth, et al., "Magnetic Trapping of Neutrons," *Nature* **403**, 62-64 (6 January 2000).
- [Kanungo 2011] R. Kanungo, A. Prochazka, W. Horiuchi et al., "Matter Radii of ^{32}Mg ," *Phys. Rev.* **C83**, 021302-1 – 4 (2011).
- [Knight 1949] W. D. Knight, "Nuclear Magnetic Resonance Shift in Metals," *Phys. Rev.*, **76**, 1259 – 1260 (1949).

- [Kozima 1994] H. Kozima, “Trapped Neutron Catalyzed Fusion of Deuterons and Protons in Inhomogeneous Solids,” *Trans. Fusion Technol.* **26**, 508 – 515 (1994).
- [Kozima 1998] H. Kozima, *Discovery of the Cold Fusion Phenomenon* (Ohtake Shuppan Inc., 1998). ISBN 4-87186-044-2.
- [Kozima 2002] H. Kozima, “An Explanation of Data Sets obtained by McKubre et al. (Excess Heat), Clarke (Null Results of ^4He and ^3He) and Clarke et al. (Tritium) with ‘Arata Cell,’” *Proc. ICCF9*, pp. 182 – 185 (2002). ISBN 7-302-06489-X/O ·292
- [Kozima 2004] H. Kozima, “Quantum Physics of Cold Fusion Phenomenon,” in *Developments in Quantum Physics Researches – 2004*, pp. 167 – 196, Ed. F. Columbus and V. Krasnoholovets, Nova Science Publishers, Inc., New York, 2004. ISBN 1-59454-003-9
- [Kozima 2006] H. Kozima, *The Science of the Cold Fusion Phenomenon*, Elsevier Science, 2006. ISBN-10: 0-08-045110-1.
- [Kozima 2008a] H. Kozima, “Phenomenology of the Cold Fusion Phenomenon,” *Reports of CFRL (Cold Fusion Research Laboratory)*, **8-3**, pp. 1 – 23 (September, 2008); <http://www.geocities.jp/hjrfq930/Papers/paperr/paperr.html>
- [Kozima 2008b] H. Kozima, W.W. Zhang and J. Dash, “Precision Measurement of Excess Energy in Electrolytic System Pd/D/H₂SO₄ and Inverse-Power Distribution of Energy Pulses vs. Excess Energy,” *Proc. ICCF13*, pp. 348 – 358 (2008). ISBN 978-5-93271-428-7.
- [Kozima 2008c] H. Kozima, “Physics of the Cold Fusion Phenomenon,” *Proc. ICCF13* (June 25 – July 1, 2007, Dagomys, Sochi, Russia) pp. 690 – 703 (2008). And also *Reports of CFRL (Cold Fusion Research Laboratory)* **11-4**, 1 – 21 (January, 2011). <http://www.geocities.jp/hjrfq930/Papers/paperr/paperr.html>
- [Kozima 2010a] H. Kozima, “Complexity in the Cold Fusion Phenomenon,” *Proc. ICCF14*, pp. 613 – 617 (2010).
- [Kozima 2010b] H. Kozima and H. Date, “Nuclear Transmutations in Polyethylene (XLPE) Films and Water Tree Generation in Them,” *Proc. ICCF14*, pp. 618 – 622 (2010). And also *Reports of CFRL*, **8-2**, pp. 1 – 15 (August, 2008); <http://www.geocities.jp/hjrfq930/Papers/paperr/paperr.html>
- [Kozima 2012] H. Kozima, “Three Laws in the Cold Fusion Phenomenon and Their Physical Meaning,” *Proc. JCF12*, pp. 101 – 114 (2012). <http://jcf12.org/file/jcf12-proceedings.pdf>.
And also *Reports of CFRL (Cold Fusion Research Laboratory)*, **11-6**, 1 – 14 (2011). <http://www.geocities.jp/hjrfq930/Papers/paperr/paperr.html>
- [Kozima 2013] H. Kozima, “Cold Fusion Phenomenon in Open, Non-equilibrium,

- Multi-component Systems,” *Proc. JCF13*, pp. 134 - 157 (2013).
<http://jcf13-proceedings.pdf>
And also *Reports of CFRL (Cold Fusion Research Laboratory)*, **12-1**, 1 – 14 (2012).
<http://www.geocities.jp/hjrfq930/Papers/paperr/paperr.html>
- [Kozima 2014] H. Kozima, “Nuclear Transmutations (NTs) in Cold Fusion Phenomenon (CFP) and Nuclear Physics,” *Proc. JCF14*, **14-15**, (2014) (to be published) and posted at JCF website: <http://jcf14-proceedings.pdf>.
And also *Reports of CFRL* **14-3**, 1 – 38 (March, 2014) that is posted at CFRL website: <http://www.geocities.jp/hjrfq930/Papers/paperr/paperr.html>.
- [Krivit 2013] S.B. Krivit, “Nuclear phenomena in low-energy nuclear reaction research,” *Naturwissenschaften* (2013) DOI 10.1007/s00114-013-1080-z.
- [Kruegler 1980] K.-J. Kruegler, W. Paul and U. Trinks, “Properties of Straight and Curved Neutron Guide Tubes,” *Zeit. Physik*, **B39**, 361 – 370 (1980).
- [Li 1991] X.Z. Li, “Chinese Effort in Understanding the ‘Cold Fusion’ Phenomena,” *The Science of Cold Fusion (Proc. ICCF2) – Conference Proceedings* Vol. **33**, Italian Phys. Soc., pp. 309 – 317 (1991). ISBN 88-7794-045-X.
- [Lietz 2008] H. Lietz, "Status of the Field of Condensed Matter Nuclear Science", Working Paper, Mittweida University, August 2008.
- [Lu 2013] Z.-T. Lu, P. Mueller, G.W. F. Drake, W. Nörtershäuser, S.C. Pieper and Z.-C. Yan, “Colloquium: Laser probing of neutron-rich nuclei in light atoms,” *Rev. Mod. Phys.*, **85**, 1383 – 1400 (2013).
- [McKubre 1993] M.C.H. McKubre, S. Crouch-Baker, A.M. Riley, S.I. Smedley and F.L. Tanzella, "Excess Power Observed in Electrochemical Studies of the D/Pd System," *Proc. ICCF3*, pp. 5 - 19 (1993). ISBN 4-946443-12-6.
- [Mössbauer 1958] R.L. Mössbauer, "Kernresonanzfluoreszenz von Gammastrahlung in Ir¹⁹¹." *Zeitschrift für Physik A* **151** (2): 124–143 (1958).
- [Ohtsuki 2004] T. Ohtsuki, H. Yuki et al., “Enhanced Electron-Capture Decay Rate of ⁷Be Encapsulated in C₆₀ Cages,” *Phys. Rev. Lett.*, **93**, 112501-1 – 4 (2004).
- [Riisager 1994] K. Riisager, “Neutron Halo States,” *Rev. Mod. Phys.*, **68**, 1106 – 1116 (1994).
- [Saitoh 2013] H. Saitoh, S. Takagi, N. Endo, A. Machida, K. Aoki, S.-I. Orimo, and Y. Katayama, “Synthesis and formation process of Al₂CuH_x: A new class of interstitial aluminum-based alloy hydride,” *APL Materials* **1**, 032113 (2013); doi: 10.1063/1.4821632
- [Storms 2007] E. Storms, *The Science of Low Energy Nuclear Reaction*, World Scientific, Singapore, 2007, ISBN-10; 981-270-620-8.

- [Storms 2010] E. Storms, “Status of Cold Fusion (2010),” *Naturwissenschaften* (2010) **97**: 861–881 DOI 10.1007/s00114-010-0711-x
- [Storms 2013] E. Storms, “Efforts to explain low-energy nuclear reactions,” *Naturwissenschaften* (2013) Published online, 30 Oct. 2013. DOI 10.1007/s00114-013-1101-y
- [Suess 1956] H.E. Suess and H.C. Urey, “Abundances of the Elements,” *Rev. Mod. Phys.* **28**, pp. 53 – 74 (1956).
- [Voelkl 1978] J. Voelkl and G. Alefeld, “Diffusion of Hydrogen in Metals,” in *Hydrogen in Metals I*, G. Alefeld and J. Voelkl ed., pp. 321 – 348. Springer, Berlin, 1978.
- [Wiedenhöver 2007] I. Wiedenhöver, “Exotic Nuclei,” *Lecture note given at National Nuclear Physics Summer School*, 7/16/2007 Tallahassee, Florida.
- [Zdenek 2006] Zdenek Dlouhy, “Structure and Properties of Exotic Nuclei using Radioactive Nuclear Beams,” (doctoral theses), Praha, Listopad, 2006.